
The large-scale environments of radio-loud active galactic nuclei and their evolution across cosmic time

Dominika Wylezalek



München 2014

The large-scale environments of radio-loud active galactic nuclei and their evolution across cosmic time

Dominika Wylezalek

Dissertation
an der Fakultät für Physik
der Ludwig–Maximilians–Universität
München

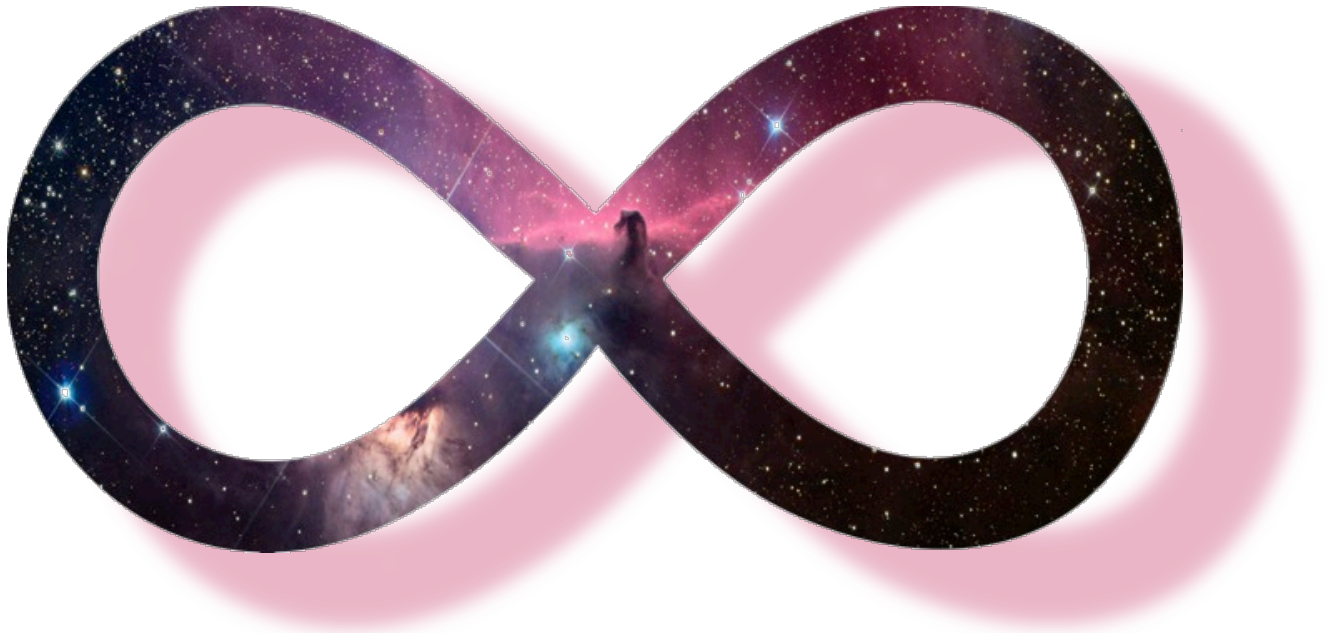
vorgelegt von
Dominika Wylezalek
aus Aschaffenburg

München, den 29. April 2014

Erstgutachter: Prof. Dr. Andreas Burkert

Zweitgutachter: Prof. Dr. Werner Becker

Tag der mündlichen Prüfung: 3. Juli 2014



*Selbst wenn wir tausendfach das
'Nichts' an die Außenwände des Uni-
versums geschrieben hätten, würden
wir uns letztlich dennoch fragen, was
hinter diesen Grenzen liegt.*

– B. Schüll, fast identisch zu DW,
für Mum & Dad

*Der Mensch muss bei dem Glauben
verharren, dass das Unbegreifliche
begreiflich sei; er würde sonst nicht
forschen.*

– J. W. v. Goethe

This thesis has been carried out at the European Southern Observatory under the supervision of Dr. Carlos De Breuck and Dr. Joël Vernet.

Contents

Zusammenfassung	xv
Abstract	xvii
1 Introduction	1
1.1 Motivation	1
1.2 Galaxy Clusters	3
1.2.1 Formation and Evolution	5
1.2.2 Observed Properties	8
1.2.3 Galaxy Clusters as Cosmological Probes	11
1.3 Radio-loud active galactic nuclei	14
1.3.1 Radio Galaxies	14
1.3.2 Radio-loud Quasars	17
1.3.3 Large-scale environments	18
1.4 High-redshift galaxy clusters	18
1.5 This Thesis	21
2 High-redshift galaxy clusters around radio-loud AGN	23
2.1 Introduction	24
2.2 The CARLA Sample	26
2.3 Data	27
2.3.1 Observations	27
2.3.2 Data Reduction	29
2.3.3 Source Extraction	29
2.3.4 Completeness Limit	30
2.4 The Environments of Radio-Loud AGN	31
2.4.1 IRAC-Selected Sources	31
2.4.2 Comparison to Blank Fields	31
2.4.3 Radial Distribution of IRAC-Selected Sources	34
2.4.4 Dependence on AGN Type	38
2.4.5 Dependence on Redshift	38
2.4.6 Dependence on Radio Luminosity	40
2.5 The environments of HzRGs and RLQs	41
2.6 Summary	43

3	The Galaxy Cluster Mid-Infrared Luminosity Function at $1.3 < z < 3.2$	45
3.1	Introduction	46
3.2	Data	48
3.2.1	Observations and Data Reduction	48
3.2.2	Cluster Sample	48
3.3	The Luminosity Function for Galaxy Clusters at $z > 1.3$	52
3.3.1	Method	52
3.3.2	Background Subtraction	53
3.3.3	Fitting Details	58
3.3.4	Uncertainty and Confidence Region Computation	60
3.4	Robustness Tests	60
3.4.1	Stability of the IRAC Color Criterion with Redshift	60
3.4.2	Validation of Luminosity Function Measurement Method	62
3.5	The Redshift Evolution of m^*	63
3.5.1	Comparison to Galaxy Evolution Models	63
3.5.2	Dependence on Cluster Richness	65
3.5.3	Difference between $\alpha = free$ and $\alpha = -1$ fits	65
3.6	Discussion	66
3.6.1	Alternatives to pure passive Evolution Models	66
3.6.2	Biases of the CARLA cluster sample	68
3.7	Summary	70
4	Why $z > 1$ radio-loud galaxies are located in dense environments	73
4.1	Introduction	73
4.2	Method	75
4.2.1	Data	75
4.2.2	Obtaining a mass- and redshift-matched galaxy control sample	77
4.2.3	Measuring environment	79
4.2.4	Properties of CARLA RLAGN	79
4.3	Results	80
4.3.1	Are RLAGN in dense environments because they are massive?	80
4.3.2	Environmental selection bias due to radio properties	85
4.4	Implications of results	87
4.4.1	Maximum fraction of massive galaxies that become RLAGN	87
4.4.2	Total lifetime of the radio emitting phase	88
4.4.3	Heating the intracluster medium	89
4.5	Conclusions	89

5	A Herschel view of the environment of the radio galaxy 4C+41.17 at $z = 3.8$	91
5.1	Introduction	92
5.1.1	High-Redshift Radio Galaxies as Tracers of Protoclusters	92
5.1.2	The HeRGÉ Project	92
5.1.3	4C+41.17	93
5.2	Observations and Data Reduction	94
5.2.1	Far-Infrared Observations	94
5.2.2	Mid-Infrared Data	94
5.2.3	(Sub)millimetre Data	95
5.3	Source Extraction and Cross-correlation Analysis	95
5.3.1	Source Extraction	95
5.3.2	Cross-Correlation Between Bands	98
5.4	Analysis	100
5.4.1	Photometric Redshifts	100
5.4.2	<i>Herschel</i> non-detections	104
5.4.3	Far-IR Luminosities, Star-Formation Rates and Limits	105
5.4.4	Number Density	105
5.5	Summary and Conclusions	107
6	Outlook	109
A	The full CARLA sample	113
B	Results for $3.6\mu\text{m}$ luminosity functions	121
C	Notes on individual sources in the field of 4C41.17	123
	Curriculum Vitae	145
	Acknowledgements – Danksagung	147

List of Figures

1.1	Cosmic Web	2
1.2	The galaxy cluster Abell 1689	4
1.3	The distribution of clusters in Abell's catalog	5
1.4	Evolution of the dark matter density field	7
1.5	Illustration of the Sunyaev-Zel'dovich Effect	11
1.6	Illustration of gravitational lensing	12
1.7	Cosmology with cluster counts	13
1.8	Radio galaxy components	15
1.9	AGN unification scheme	19
2.1	Rest-frame 500 MHz luminosity vs. redshift for the CARLA sample	28
2.2	Number counts for the SpUDS and CARLA surveys.	30
2.3	Illustration of the IRAC color criterion.	32
2.4	Histogram/cumulative number counts of densities of IRAC-selected sources	35
2.5	Postage stamps of the fields of MRC1217-276 and J105231.82+08060	36
2.6	Radial surface density distribution of IRAC-selected sources	37
2.7	Histogram of IRAC-selected sources for HzRG and RLQ	39
2.8	Surface density distribution as function of redshift	40
2.9	Surface density distribution as function of radio luminosity	42
3.1	IRAC1 vs. IRAC2 flux density for color-selected sources	49
3.2	Density histogram of CARLA and SpUDS	51
3.3	CARLA cluster Schechter function fits at $4.5 \mu\text{m}$	54
3.4	Number counts for the SpUDS and SERVS survey	56
3.5	Distribution of IRAC-selected sources in the SpUDS and SERVS surveys.	57
3.6	Median best-fit $m_{4.5}^*$ with $\alpha = -1$ as a function of galaxy cluster richness	58
3.7	Confidence regions for α vs. m^*	59
3.8	Stability of the IRAC color criterion with redshift	62
3.9	Evolution of $m_{4.5\mu\text{m}}^*$ with redshift	64
3.10	Model predictions for the evolution of m^*	69
4.1	Redshift, Color, Magnitude Histograms	76
4.2	Comparison between CARLA and UDS fields matched in color	81
4.3	Comparison between CARLA and UDS fields matched in mass	82
4.4	Radial densities of CARLA and UDS fields	84

4.5	Radio properties as function of CARLA density	85
4.6	Scaled CARLA and UDS density histograms	88
5.1	0.6' × 0.6' postage stamps of 4C+41.17 and source 16	98
5.2	Coverage map and spatial distribution of sources, centered on 4C+41.17 .	104
6.1	Three-color image of the field of 7C1753 at $z = 1.9$	110
B.1	Schechter fits to the 3.6 μm CARLA cluster luminosity function	122
C.1	Multi-wavelength postage stamps, SED and χ^2 curve for source 2	123
C.2	Multi-wavelength postage stamps, SED and χ^2 curve for source 5	124
C.3	Multi-wavelength postage stamps, SED and χ^2 curve for source 7	125
C.4	Multi-wavelength postage stamps, SED and χ^2 curve for source 9	126
C.5	Multi-wavelength postage stamps, SED and χ^2 curve for source 11	127
C.6	Multi-wavelength postage stamps, SED and χ^2 curve for source 13	128
C.7	Multi-wavelength postage stamps, SED and χ^2 curve for source 16	129
C.8	Multi-wavelength postage stamps, SED and χ^2 curve for source 17	130
C.9	Multi-wavelength postage stamps, SED and χ^2 curve for source 19	131
C.10	Multi-wavelength postage stamps, SED and χ^2 curve for source 21	132
C.11	Multi-wavelength postage stamps, SED and χ^2 curve for source 29	133

List of Tables

2.1	The CARLA sample (in R.A. order).	31
2.2	Comparison to previous work on type-1 and type-2 AGN environments. . .	41
3.1	Schechter fit results for 4.5 μm luminosity functions	61
4.1	Results from Spearman rank correlation tests	83
5.1	HIPE parameters for <i>Herschel</i> reduction	96
5.2	Flux densities of sources with at least two <i>Herschel</i> detections	97
5.3	Astrometry of the <i>Herschel</i> sources in the 4C+41.17 field	99
5.4	Multi-wavelength cross-correlation statistics	101
5.5	Summary of the templates used for deriving photometric redshifts	103
5.6	Summary of photometric redshifts	103
5.7	Far-IR properties of sources in the 4C+41.17 field	106
A.1	The CARLA sample (in R.A. order).	113
B.1	Schechter fit results for 3.6 μm luminosity functions	121

Zusammenfassung

Galaxienhaufen sind die massereichsten und größten Strukturen im Universum, die gravitativ gebunden sind. Sie sind vor 10 bis 11 Milliarden Jahren (das entspricht einer Rotverschiebung von $2 < z < 3$) entstanden und helfen deswegen zu verstehen, wie sich die großräumige Struktur des Universums entwickelt hat und welche physikalischen Prozesse die Entwicklung von Galaxien beeinflusst haben. Insbesondere ist die Zeit, die Rotverschiebungen von $1 < z < 3$ entspricht, eine wichtige Epoche. Denn obwohl Beobachtungen zeigen, dass Sternentstehung die Zentren von Galaxienhaufen bei $z > 1.5$ dominiert, scheint sie ab $z < 1.5$ zunehmend unterdrückt zu sein. Dann beginnen elliptische Galaxien die Zentren der Haufen zu dominieren. Es ist allerdings nicht klar, wie die Entstehung und Entwicklung dieser massereichen elliptischen Galaxien von den Eigenschaften des sie umgebenden Haufens abhängt und wann genau dieser Übergang passiert. Insbesondere Galaxienhaufen mit $z > 1.5$ können darüber Aufschluss geben. Zur Zeit ist über diese hoch rotverschobenen Galaxienhaufen jedoch noch nicht viel bekannt, da die Suche nach ihnen bisher nur wenig erfolgreich war und nur wenige Haufen mit $z > 1.5$ gefunden wurden. Es war bisher sehr schwer, diesen Bereich der Rotverschiebung mit zur Verfügung stehenden Teleskopen und Instrumenten zu beobachten und er wurde daher auch 'redshift desert' genannt.

Die Arbeit, die in dieser Dissertation vorgestellt wird, hat viel dazu beigetragen, hoch rotverschobene Galaxienhaufen zu finden und zu analysieren. Das Projekt CARLA ('Clusters around radio-loud AGN') hat 420 radiolaute AGN (aktive galaktische Nuklei), die über die ganze Himmelskugel verteilt sind und Rotverschiebungen von $1.3 < z < 3.2$ haben, mit Hilfe des *Spitzer Weltraumteleskops* beobachtet. Aus früheren Beobachtungen ging hervor, dass sich radiolaute AGN in dichten Galaxienumgebungen befinden und sich dafür eignen Galaxienhaufen oder -gruppen zu finden. Mit Hilfe von CARLA wurden nun die Umgebungen einer großen Anzahl von radiolauten AGNs systematisch untersucht, in dem nach dichten Ansammlungen von Galaxien mit bestimmten Farben um den AGN gesucht wurde. So konnten mit Hilfe dieses Programms über 200 Galaxienhaufenkandidaten gefunden werden.

Helligkeitsfunktionen der CARLA Galaxienhaufenkandidaten zeigten außerdem, dass die Unterdrückung der Sternentstehung in Galaxienhaufen um radiolaute AGN früher stattfindet als in Galaxienhaufen, die in anderen Himmelsdurchmusterungen gefunden wurden. Dies weist darauf hin, dass die CARLA Galaxienhaufen zu den massereichsten und am weitesten entwickelten Strukturen bei $z > 1.5$ gehören könnten. Wir zeigten auch, dass sich radiolaute AGN in noch dichteren Umgebungen befinden als Galaxien, die ähnlich massereich sind. All dies macht Galaxienhaufen um radiolaute AGN zu sehr interessanten Objekten, die helfen können zu verstehen, wie sich Galaxien in den dichtesten Gebieten des Universums entwickelt und angesammelt haben.

Ein ergänzendes Projekt, HERGE, beobachtete 71 Radiogalaxien mit $1 < z < 5$ im fernen Infrarot mit Hilfe des *Herschel Weltraumteleskops*. Weitere Daten im mittleren Infrarot, teilweise im nahen Infrarot und im sub-Millimeter Bereich ermöglichten es, einzelne Galaxienhaufen detaillierter zu untersuchen. Ein Pilotprojekt für einen einzelnen Galaxienhaufenkandidaten zeigte, dass es möglich ist herauszufinden, welche Galaxien zum Haufen gehören und deren Sternentstehungseigenschaften zu untersuchen.

Diese Projekte haben essentielle Grundlagen für zukünftige Arbeit gelegt, die Entstehung und Entwicklung der massereichsten Strukturen im Universum über einen Zeitraum von mehreren Milliarden Jahren besser zu verstehen.

Abstract

Emerging from the cosmic web, galaxy clusters are the most massive gravitationally bound structures in the universe. Thought to have begun their assembly at $2 < z < 3$, i.e. 10 to 11 billion years ago, clusters provide insights into the growth of large-scale structure as well as the physics that drives galaxy evolution. The redshift range $1 < z < 3$ is a key epoch in their evolution. At $z \sim 1.5$, elliptical galaxies start to become the dominant population in cluster cores, and star formation in spiral galaxies is being quenched. But there is also evidence for a progressive increase in the amount of star formation that occurs in galaxy cluster cores at $z \gtrsim 1.5$. To understand the dependence of the formation mechanisms of massive galaxies with environment, we must focus on clusters at relatively unexplored redshifts $z > 1.5$ where major assembly is in progress. The search for galaxy clusters at high redshift, so far, has been mildly successful and only a handful of clusters at $z > 1.5$ have been confirmed. Because this redshift range was essentially unreachable with previous instrumentation, it was dubbed a 'redshift desert'.

The work presented in this thesis has made a major contribution to this field. The Clusters Around Radio- Loud AGN (CARLA) survey, a 400 hr targeted *Warm Spitzer* program, observed 420 radio-loud AGN (active galactic nuclei) at $1.3 < z < 3.2$ across the full sky. Extensive literature over several decades shows that powerful radio-loud AGN preferentially reside in overdense environments. From this survey, we have identified a sample of ~ 200 galaxy cluster candidates by selecting strong overdensities of color-selected sources. By studying the luminosity function of the CARLA cluster candidates, we showed that quenching is happening much earlier in clusters around radio-loud AGN than in field galaxy samples. This suggests that our targets may well be the most massive and evolved structures known to date at $z > 1.5$. We also showed that radio-loud AGN reside in denser environments than similarly massive galaxies. This makes high-redshift clusters around radio-loud AGN particularly interesting as they can reveal how galaxies in the most massive dark matter halos assembled.

A complementary project, HERGE (*Herschel* Radio Galaxy Evolution Project) observed a sample of 71 radio galaxies at $1 < z < 5$ at far-IR wavelengths with the *Herschel Space Observatory*. Supporting data in the mid-IR, partially in the near-IR and at sub-mm wavelengths allow to study cluster fields in more detail. A pilot project on a single field showed that we can identify cluster members and constrain their star-formation properties.

These projects laid the foundation for future work, which will make a significant impact on understanding the formation of the most massive structures over several billion years.

Chapter 1

Introduction

1.1 Motivation

Since the beginning of humankind, people have looked up on the skies and admired the beauty and complexity of the rising and setting sun, moon and stars. Originally, stars and planets were associated with gods and it was believed the heavens determined the fate of earthy existence. In the last centuries, however, when first telescopes were developed and astronomy disentangled itself from mythological and religious influences, it became clear that there are millions of stars and galaxies with the earth being just a small 'pale blue dot' among them. It is this vastness and apparent infinity of the Universe that makes people wonder about their place and purpose and keeps them wanting to find the answers to the many questions about its nature and origin.

The fact that the Universe most likely originated 13.8 billion years ago in a Big Bang is probably one of the most striking discoveries of the last century. Since then, it has been evolving and building up the structures that we can observe today. Large sky surveys have revealed that matter is not distributed uniformly across space, but organised in clustered structures, called the 'cosmic web' (Fig. 1.1). Stars are organised into galaxies, which form galaxy groups, clusters, superclusters and filaments. Above the scale of filaments, the Universe seems to be finally homogenised with a smooth distribution of structure. This scale is often referred to as the 'End of Greatness'.

The shape, size and distribution of the cosmic web is closely linked to the initial conditions and density perturbations $\sim 10^{-33}$ s after the Big Bang (Peebles, 1980) that were presumably imprinted during the inflationary period of the Universe¹. These perturbations

¹The inflationary epoch of the Universe is a rapid, much faster than the speed of light, expansion of space in the early Universe happening sometime between 10^{-36} to 10^{-32} s after the Big Bang. In March 2014, the BICEP2 collaboration announced they detected inflationary gravitational waves, apparently proving the theory of inflation (BICEP2 Collaboration et al., 2014).

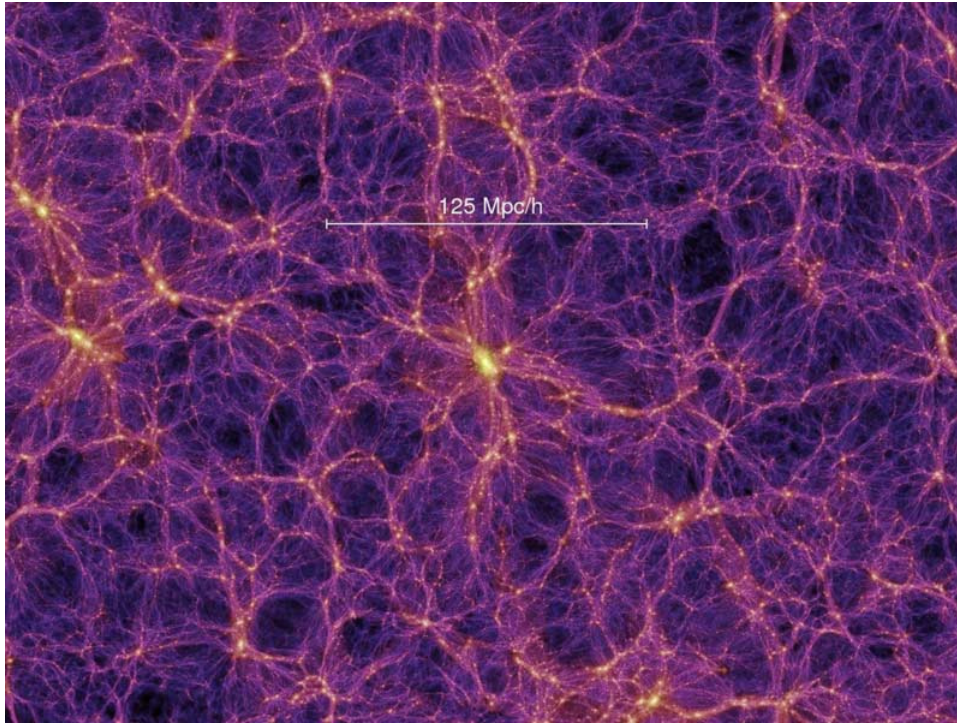


Figure 1.1: The Cosmic Web - Distribution of dark matter in the Universe as revealed by the Millennium simulation. Credit: V. Springel

are considered to be the seeds of all structures today. Galaxy clusters, large collections of galaxies, that formed in the densest regions, represent the most massive collapsed and gravitationally bound structures. They are thus at the cross-roads between cosmology and astrophysics and are unique laboratories for studying the growth of structures over cosmic time. Especially the most distant clusters are crucial for understanding and testing different models of structure formation and evolution.

An essential step towards this goal is to find these structures and to build large samples at the highest redshifts. The search for galaxy clusters at high redshift, so far, has been mildly successful and only a handful of clusters at $z > 1.5^2$, corresponding to a look-back time of more than 9 billion years, could be confirmed. We therefore need to develop and use better search techniques to find and investigate the most distant clusters.

The following chapters summarise our current knowledge about the properties of clusters and their role in understanding the evolution of the growth of structure. They also explain how a specific, very massive type of galaxies hosting a radio-loud active galactic nucleus

² z denotes the cosmological redshift that is due to the expansion of the Universe. The larger z the farther away the observed object and the further back in time we look. The redshift does not linearly increase with look-back time, e.g. $z = 1$ corresponds to a look-back time of 8 Gyrs, $z = 2$ to about 10.5 Gyrs and $z = 3$ to about 11.7 Gyrs. $z = 0$ corresponds to the present time.

(RLAGN) can be used to trace the most massive and distant structures and what we can learn from studying their large-scale environments.

1.2 Galaxy Clusters

Galaxy clusters are the largest gravitationally bound structures in the Universe, consisting of hundreds of galaxies, with total masses up to a few $10^{15} M_{\odot}$ ³ and sizes of 2 to 10 Mpc⁴. About 90 % of the total mass in clusters is dark matter, while $\sim 9\%$ is made up of the hot intracluster medium (ICM), a hot X-ray emitting plasma between the cluster galaxies. The galaxies and their stars themselves only contribute to only about 1% of the total mass of a cluster. Figure 1.2 shows a multi-wavelength image of the massive galaxy cluster Abell 1689 at $z = 0.18$ and illustrates the main components of a cluster. The luminous galaxies and stars are bright at optical wavelengths, the hot ICM can be observed via its extended X-ray emission and the dark matter is indirectly observable through the gravitational lensing effect, distorting the shape of background galaxies, even creating arcs and rings (so called Einstein rings) in extreme cases.

The first evidence for the tendency of ‘nebulae’, i.e. galaxies, to cluster was discovered by Charles Messier and William Herschel in the 18th century. This was the time when first systematic catalogs of objects were constructed, like Messier’s catalog *Catalogue des nébuleuses et des amass d’étoiles que l’on découvre parmi les étoiles fixes, sur l’horizon de Paris* (Messier, 1781). Messier noted the trend of concentration of nebulae in the Virgo constellation, while Herschel suggested that the *sidereal system we inhabit*, the Milky Way galaxy, is only one among other nebulae and that therefore the other nebulae must be outside our own system. He was also one of the first ones to describe the Coma cluster as *a remarkable collection of many hundreds of nebulae* (Herschel, 1785).

But it was not until the early 1920’s that the extragalactic nature of nebulae was proven which implied that clusters of galaxies were massive and gigantic systems (Hubble, 1925, 1926). In the following decades, systematic searches were carried out to find galaxies and increasing evidence for the tendency of galaxies to cluster was collected. Catalogs, such as the *Catalogue of Galaxies and Clusters of Galaxies* (Herzog et al., 1957) and Abell’s catalog *The distribution of rich clusters of galaxies* (Abell, 1958, see Fig. 1.3) were published. Especially the latter one has become a milestone in galaxy cluster science. Extensive redshift surveys revealed the three-dimensional structure of clusters and identified filaments connecting clusters and voids. Clusters were being used to identify the large-scale structure of the Universe.

³ M_{\odot} is the mass of the sun (1.99×10^{30} kg)

⁴1 parsec (pc) corresponds to 3.09×10^{16} m and 3.26 light years

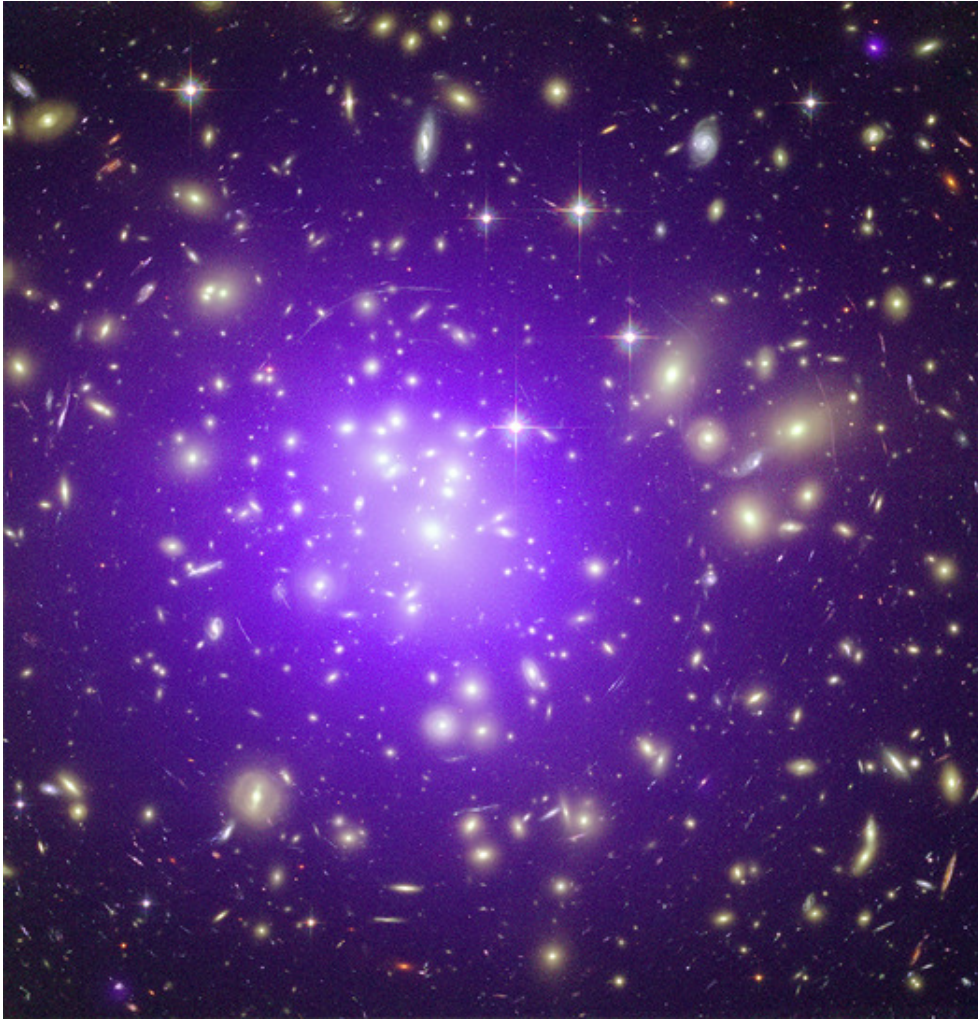


Figure 1.2: Composite image of the massive cluster Abell 1689 at $z = 0.18$ illustrating the various components of a galaxy cluster. Galaxies, observed at optical wavelengths, are colored in yellow, while the hot ICM can be traced through diffuse X-ray emission, shown in purple. The arcs and distorted shapes of background galaxies in the optical image are a result of the gravitational lensing effect, an indirect observation of the large dark matter mass in this system. Credits: X-ray: NASA/CXC/MIT/E.-H Peng et al; Optical: NASA/STScI

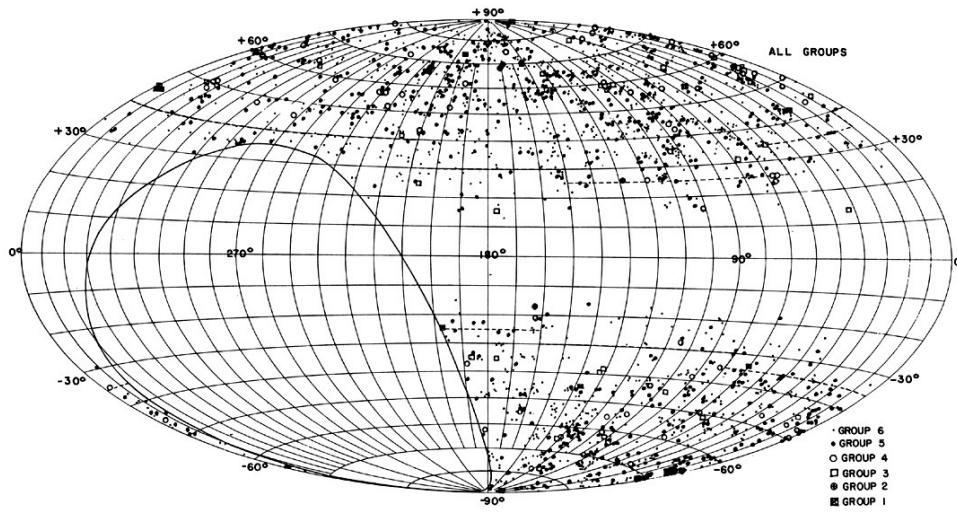


Figure 1.3: The distribution of galactic coordinates of the clusters in Abell's catalog (Abell, 1958)

These catalogs laid the foundation of galaxy cluster science as they provided the community with a collection of clusters. For the first time, astronomers were able to study this phenomenon as a population. The analyses started to cover various aspects such as galaxy cluster distribution, formation and evolution. In 1933, Fritz Zwicky was the first one to infer the total mass of the Coma cluster by using the virial theorem and measure velocity dispersions. The large mass he inferred exceeded the one of combined mass of stars in the cluster by far which led Zwicky to the assumption of unseen *dark matter* inventing this widely used term (Zwicky, 1933).

Given the remarkable properties of galaxy clusters it is no surprise that the interest in clusters increased so much that in 1959 the journal *Astronomischer Jahresbericht* (Astronomical annual report) devoted a new section to galaxy clusters. Galaxy clusters have become a main research topic in astronomy and have developed into one of the central efforts of modern astrophysics.

1.2.1 Formation and Evolution

Galaxy clusters are thought to have formed through the collapse of peaks in the primordial dark matter density field that exceed the mean density of the rapidly expanding Universe and baryonic structures, e.g. galaxies, emerge in these dark matter peaks. This process of collapsing dark matter overdensities that are gravitationally amplified has been studied into the non-linear regime, i.e. the regime where the growth of structure cannot be described by linear perturbation theory anymore, with N-body simulations. The build-up of structure happens hierarchically with a combination of infalling mass and merging leading to increas-

ingly larger dark matter halo masses (see Fig. 1.4). Clusters emerge from the densest and most massive of these density peaks and are a result of this 13 Gyr⁵ long process. Over time matter settles into an equilibrium configuration. But as the gravitational collapse is an extended process and matter is being accreted constantly and minor mergers happen regularly, even low-redshift clusters may not have reached this equilibrium state yet (for a review see Kravtsov & Borgani, 2012).

The initial conditions of the primordial density field and the processes occurring during the collapse and merging determine the internal structure of the halo. The dark matter density profile of the halo, for example, has been shown to be commonly best represented by a Navarro-Frenk-White profile (NFW, Navarro et al., 1995):

$$\rho_{NFW}(r) = \frac{4\rho_s}{x(1+x^2)}, \quad x = r/r_s \quad (1.1)$$

where r_s is the scale radius, at which the logarithmic slope of the profile is equal to -2 and ρ_s is the characteristic density at $r = r_s$. This profile arises due to the shape and density of the initial density peak and due to thermodynamic processes happening during the collapse. Measuring this density profile, the velocity dispersion profile or the shape of the dark matter halo allow to set important constraints on structure formation scenarios and paradigms (see also Section 1.2.3, for a review see Allen et al., 2011).

During halo formation, various astrophysical processes play an important role shaping the baryonic structures emerging in the dark matter halos. The kinetic energy of diffuse gas falling into the dark matter potential well is converted into thermal energy via shocks and compression. As the gas settles its temperature reaches about 10^6 - 10^8 K, values that are close to the virial temperature corresponding to the cluster mass (Kravtsov & Borgani, 2012). The presence of stars and galaxies in clusters, however, proves that gas has cooled during cluster formation. Radiative cooling is the primary cooling mechanism as the intracluster plasma is mostly optically thin.

The first generation of stars formed only about 100 million years after the Big Bang when gas cooled mainly through molecular hydrogen line emission. About 500 million years after the Big Bang, atomic line cooling allows the first galaxies to form and grow hierarchically with cosmic time. Supermassive black holes (SMBHs) grow through mergers and accreting mass in cluster cores. Observations of the most distant quasars⁶ indicate that supermassive black holes of one billion solar masses must have already existed 750 million years after the Big Bang (Fan, 2006). Mechanical and radiative feedback from jets driven by the black

⁵1 Gyr = 1 gigayear = 10^9 yrs

⁶Quasars belong to the most luminous objects in the universe and are galaxies hosting a very powerful black hole. The emission powered by the black hole outshines the light of the host galaxy making them appear as point-like (quasi stellar) objects.

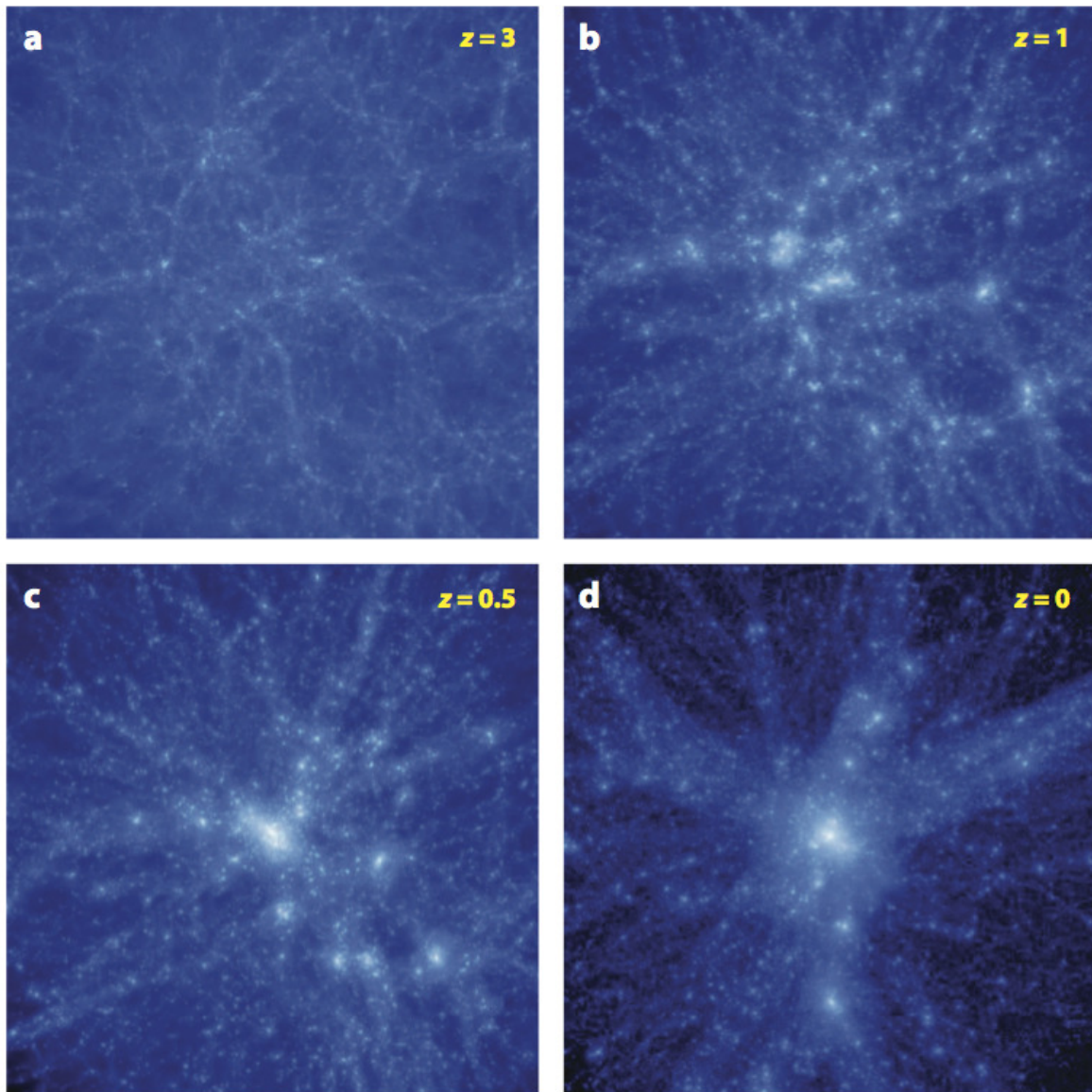


Figure 1.4: Simulated evolution of the dark matter density field in a density peak where a cluster is forming. The panels a, b and c correspond to look-back times of ~ 11.5 , 8 and 5 Gyrs, respectively, panel d shows the situation today. The figure illustrates the complexity of structure formation: deviation from spherical symmetry, presence of substructures and filaments (from Kravtsov & Borgani, 2012).

hole re-heat the gas and can stop star-formation and limit the maximum size of the galaxy.

Although the classical physics governing the hydrodynamic, magnetohydrodynamic or radiative transfer affects are known, the complex interplay, their 3D shape, non-linear evolution and couplings make baryon evolution a highly complex phenomenon and a lot of the details are still under debate or unknown.

1.2.2 Observed Properties

This Gyr-long process leads to the structures we observe today. Some of their most important properties are summarised in the following section.

Galaxies

Galaxy clusters, and specifically cluster cores, are found to preferentially host passive, early-type galaxies with the brightest cluster galaxy (BCG) generally found at the geometrical and kinematical centre of the hosting cluster. BCGs belong to the most massive galaxies in the Universe and are typically elliptical galaxies with old stellar populations and relatively low star-formation rates. This observed relationship between galaxy type and environments is known as morphology-density relation (Dressler, 1980). Spiral galaxies, i.e. late-type galaxies, are preferentially located in low-density environments and are rare in clusters, while elliptical galaxies, i.e. early-type galaxies⁷, are rarely found in isolation. Massive galaxies tend to be located in rich environments and local clusters host larger than the field populations of red sequence galaxies⁸ with little or no star formation. These observations are an indication that the cluster environment must play a crucial role in the evolution of cluster galaxies. Specifically, there is strong evidence that star formation in clusters is suppressed (known as star-formation-rate-density relation) and that this so-called environmental quenching is so effective that the fraction of star-forming galaxies is still below that in the field at low redshift ($z < 0.1$, e.g. Kauffmann et al., 2004; Peng et al., 2010; Chung et al., 2011).

Several processes have been proposed to account for this suppression of star-formation such as ‘ram pressure stripping’, ‘galaxy strangulation’ and ‘galaxy harassment’. Each of these processes act on different timescales and on different spatial scales while the relative importance of each individual one is still not fully understood (e.g. Moran et al., 2007).

⁷The terms ‘early-type’ and ‘late-type’ do not refer to the evolutionary state of a galaxy. The origin of the terms comes from the original interpretation that elliptical galaxies (early-types) evolved into spiral galaxies (late-types). Today we know that this interpretation is not correct and now these terms only refer to galaxy shapes.

⁸Galaxies with little star formation are called red (and dead) galaxies, due to their rest-frame optical colors. Since clusters host large fractions of those red galaxies, they are referred to as the red sequence population.

Ram pressure stripping occurs as galaxies move within the cluster environment that is filled with intra-cluster gas. While moving, they experience this gas as a wind that can become strong enough to remove the galaxy's gas, its fuel for star-formation. Cluster infalling galaxies can be strangled as the gravitational potential of the cluster, that they experience for the first time during the infall, creates tidal effects that allows the gas within the galaxy to escape. High speed galaxy encounters that can change and disturb the morphologies of the interacting galaxies and that lead to asymmetric galaxies or tidal tails are referred to as galaxy harassment.

So while it is well known that galaxy properties are dependent on environment the exact mechanisms and evolutionary histories are still a matter of debate. Is the role of the environment direct, i.e. are there processes that are specific to dense regions, or is it indirect, i.e. are internal galaxy processes governing galaxy evolution and is environment just tracing these particular internal processes (Alberts et al., 2014)? Most observations and models are consistent with a scenario in which cluster galaxies form in a short burst of star formation at high redshift ($z_f > 2$) and then undergo passive evolution. Local scaling relations such as the morphology-density relation and star-formation-rate density relation seem to be mainly in place by $z = 1$. However, recent studies in the mid-infrared have shown significant ongoing star-formation in the cores of clusters, as well as signs for a reversal of the star-formation-rate-density relation (Brodwin et al., 2013; Ziparo et al., 2014).

Especially studies of galaxy clusters at high redshift ($z > 1$) are important to reveal how cluster galaxies evolved from young, highly-star forming systems to the passive, old and star-formation suppressed systems that we observe at low redshift. Based on a single high-redshift cluster sample, several independent analyses have shown, that this epoch might have occurred at $z \sim 1.4$. But as I will show in this thesis, this might not be generally the case (see Wylezalek et al., 2014).

Intra-Cluster Medium (ICM)

The ICM is a hot, $T \sim 10^6$ - 10^8 K, low density, $n_e \sim 10^{-4}$ - 10^{-2} cm⁻³, diffuse X-ray emitting gas between the cluster galaxies. Through shocks, kinetic energy from the gravitational field is converted to thermal energy during cluster formation, which is responsible for the gas heating. The gas mass of the ICM is about 10 times larger than the mass in stars and is therefore the main contributor to the baryonic mass content of galaxy clusters. Since hydrogen is the most abundant element in the Universe, the ICM mainly consists of protons and electrons and a small fraction of helium nuclei. Many properties of the ICM and the cluster galaxies are tightly correlated, such as the ICM's temperature being consistent with the velocities of the cluster galaxies. This indicates that the gas and the galaxies share a common potential well and are nearly in equilibrium (Oegerle et al., 1990).

Many clusters show a strongly peaked X-ray emission in their core, primarily due to thermal bremsstrahlung, indicating that effective cooling of the gas is taking place there. But this radiative cooling would lead to a ‘cooling catastrophe’, meaning that the gas would cool down to very low temperatures and high star-formation rates (e.g. Fabian, 1994). However, the contrary is observed. Despite the strong X-ray emission, very little of the gas is actually cooling down to very low temperatures, consistent with low star-formation rates in the centre of galaxy clusters. This suggests that a heating mechanism prevents the gas from cooling down to low temperature. Today it is believed that the feedback by supermassive black holes (SMBHs) at the centre of many galaxies are responsible for this heating. The enormous energy output of the SMBH, e.g. collimated in galactic jets, re-heats the cluster gas.

One of the most important applications of studying the ICM is the correlation of different observable quantities of the ICM and properties of the cluster. Assuming the ICM is in hydrostatic equilibrium and the cluster is spherically symmetric, the total cluster mass can be derived (e.g. Sarazin, 1988). Such independent scaling relations are extremely important for e.g. cosmological uses of clusters where a small scatter of such relations is desired and independency from other properties of the cluster.

The ICM also influences the Cosmic Microwave Background (CMB)⁹. The CMB photons are scattered off the high energy electrons of the ICM through inverse Compton scattering. This leads to a small distortion ($< 1mK$) of the CMB spectrum and boosts the energy of the CMB photons. This effect is called the Sunyaev-Zel’dovich effect (SZE, Sunyaev & Zeldovich, 1980). The SZE results in a decrease of the CMB intensity below observed frequencies of 218 GHz and in an increase above 218 GHz (see Fig. 1.5). Since the SZ signal is independent of redshift, it is a powerful probe to find clusters. Measuring the amplitude of the SZ signal is particularly important as the integrated SZE is a measure for the total thermal energy of a cluster and the line-of-sight integrated electron density. The SZE map can therefore be converted into an accurate map of the total baryon content of a cluster and can provide a robust measure of the cluster mass (e.g. Myers et al., 1997). One of the difficulties with determining a precise mass estimate arises if a radio-loud source within the field of view is contaminating the signal.

Dark Matter

About 90% of the total mass of a cluster consists of dark matter that does not emit any electromagnetic radiation. Its existence is inferred from its gravitational effects on

⁹The CMB is a thermal background radiation assumed to be left-over from the Big Bang, it is thus the oldest light in the Universe. It is almost exactly the same in every observed direction and has a thermal black body spectrum with a temperature of $T_{CMB} = 2.73$ K.

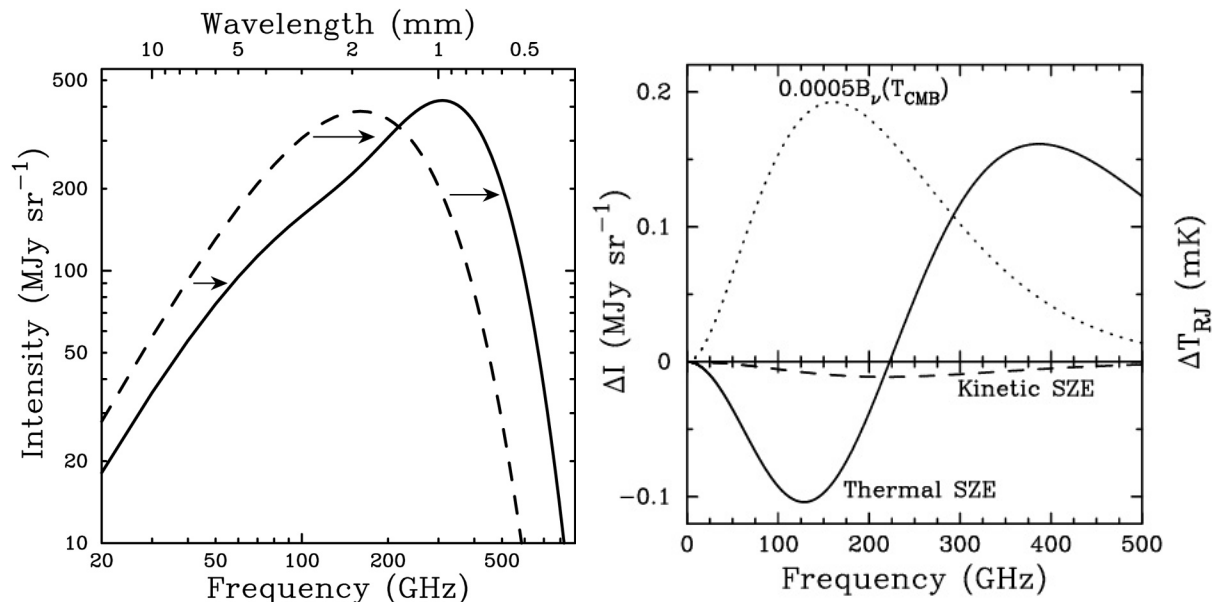


Figure 1.5: Illustration of the Sunyaev-Zel'dovich effect. Scattering of the CMB photons off the hot ICM distorts the spectrum of the CMB (left panel). This leads to a decrease of photons below 218 GHz and an increase of photons above 218 GHz when investigating the difference between the original CMB signal and the signal observed through a galaxy cluster (right panel) (Carlstrom et al., 2002).

baryonic matter. The mass inferred from the motion of the cluster galaxies with the cluster gravitational potential exceeds by far the mass that is obtained from summing up all the visible matter in the cluster (e.g. Zwicky, 1933). Due to the large amount of dark matter, galaxy clusters are so massive that they curve space-time in such a way that they are capable of bending the light path of background objects. This is known as the gravitational lensing effect and has first been predicted by Einstein (1936) (see also Fig. 1.6). This lensing effect can magnify and distort the shapes of the background galaxies or create multiple images of the same source (see Fig. 1.2). Since this distortion is dependent on the mass of the cluster, measuring the strength of the gravitational lensing effect, is another way of independently determine the total cluster mass.

1.2.3 Galaxy Clusters as Cosmological Probes

All of the properties described above make galaxy clusters important crossroads of astrophysics and cosmology. Various methods of observing galaxy clusters can help to constrain important cosmological parameters. In the following the most common ones are briefly described.

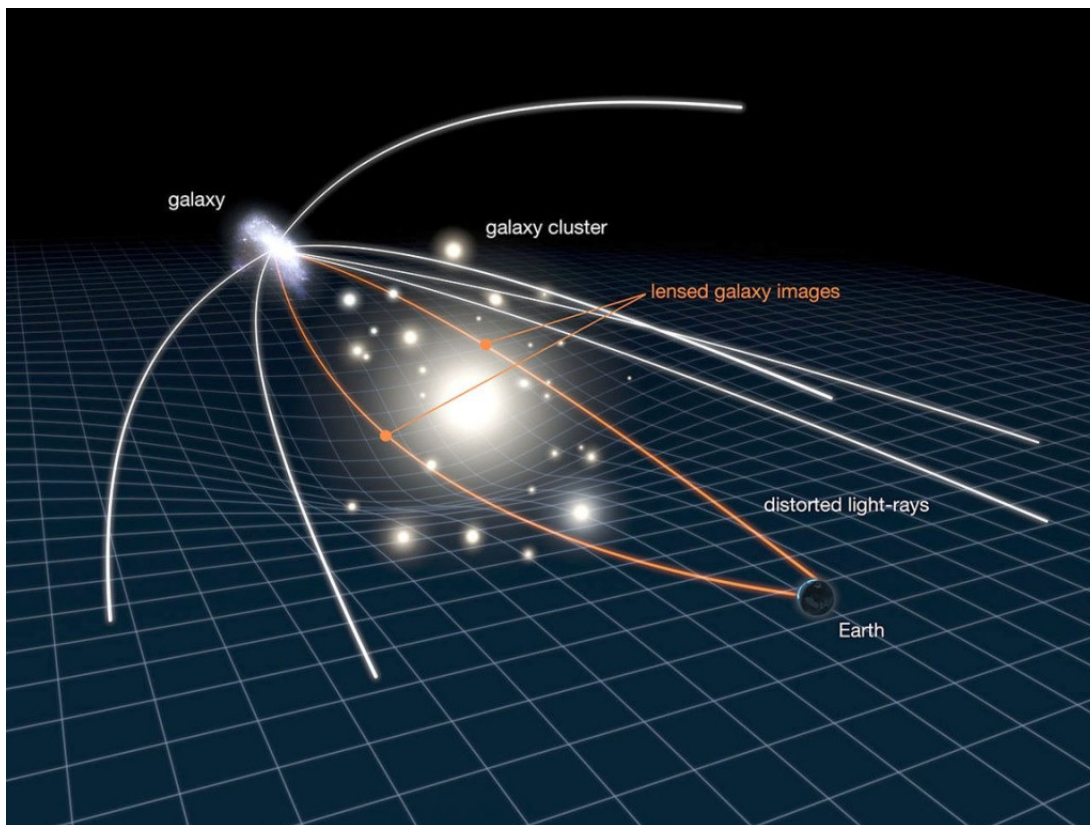


Figure 1.6: Illustration of the gravitational lensing effect. Massive objects like galaxy clusters curve space-time in a way that it distorts the light path of background objects. This leads to observations of multiple images, distorted images and arcs. Credit: NASA/ESA

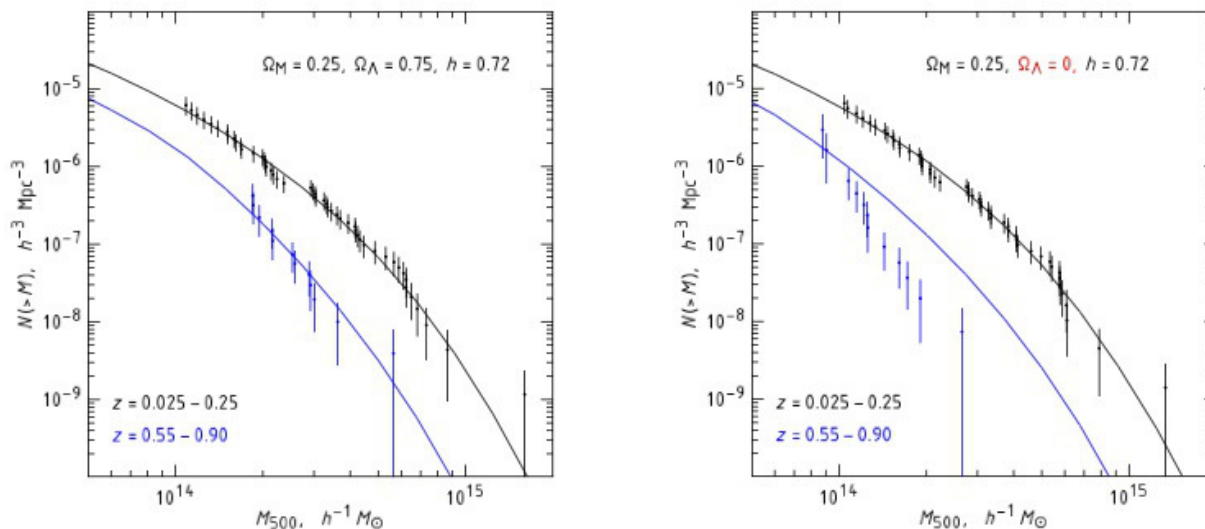


Figure 1.7: Measured mass function in different redshift regimes compared to model predictions. The model without dark energy clearly over-predicts the number of clusters at higher redshift (Vikhlinin et al., 2009)

Cluster Counts

The mass function and expansion history that are dependent on the cosmological model allow to predict the number of clusters as a function of mass and redshift. Therefore mass and redshift limited samples of galaxy clusters can be compared to predictions from different models. Figure 1.7 shows the measured mass functions of low and high-redshift cluster data compared to a Λ CDM model¹⁰ and a model without dark energy. The model without dark energy clearly over-predicts the number of clusters at higher redshift (Vikhlinin et al., 2009). To meaningfully draw conclusions about cosmological parameters from such measurements, the probability of each cluster being detected and included in the sample and the probability of particular measured values given true cluster properties have to be assessed.

Most Massive Cluster Test

The detection of a single, high-redshift, massive cluster could in principle challenge the currently widely accepted Λ CDM model. Such a measurement provides a simple cosmological test as it 'only' requires the measurement of a few massive clusters. The Massive Distant Clusters of WISE survey (MaDCoWS, Gettings et al., 2012, Stanford et al. submit-

¹⁰The Λ CDM model is the current standard model of Big Bang cosmology. The Λ stands for the cosmological constant and denotes that the Universe contains dark energy. CDM stands for Cold Dark Matter that is only weakly interacting with baryonic matter.

ted, Brodwin et al. in prep.) focuses on this technique and aims to find the most massive clusters making use of the all-sky WISE survey. This method still requires a detailed understanding of observing biases and scatter in the mass-observable relations.

Baryon Fractions

Gas mass fractions f_{gas} of clusters measured in a given aperture depend on cosmology and can be measured relatively straightforwardly through X-Ray or SZ observations. Several groups are exploiting this type of test using data from e.g. the *Chandra X-Ray Observatory* (Allen et al., 2008). Current results are consistent with a Λ CDM model and provide powerful constraints on dark energy. These measurements, however, are still limited by a small fraction of massive, relaxed clusters at high redshift.

There are several other measurements that allow to test cosmological models such as measuring the clustering properties of clusters that provide information about the shape and amplitude of the underlying dark matter distribution or measuring the number of arcs in the vicinity of clusters that act as gravitational lenses (the number of arcs is dependent on the cosmology). Reviewing all cosmological tests in detail is beyond the scope of this thesis but this section underlines the importance of cluster physics with respect to testing various models of structure formation.

1.3 Radio-loud active galactic nuclei

1.3.1 Radio Galaxies

High-redshift radio galaxies (HzRGs) belong to the largest and most massive galaxies in the distant Universe ($z > 1$) and have enormous radio luminosities ($L_{500\text{MHz}} > 10^{27}\text{WHz}^{-1}$, Miley & De Breuck, 2008). They are believed to host an accreting supermassive black hole in their centre that powers the radio emission. Clumpy morphologies and close-by companions suggest that they have formed and built-up their mass through subsequent mergers (Ivison et al., 2012). They are extremely rare objects, with number densities $\sim 10^{-8}\text{Mpc}^{-3}$ in the redshift range $2 < z < 5$ (Dunlop & Peacock, 1990; Willott et al., 2001) but some of their unique properties make them important probes of the distant Universe.

Unlike quasars, radio galaxies are spatially resolvable. The central black hole in radio galaxies is obscured by a thick dust torus and does not outshine the host galaxy. Therefore, investigating the spectral energy distribution (SED) of radio galaxies enables to study their host galaxy's stellar, dust and active galactic nuclei (AGN) components. In particular, studies of the stellar and dust components have shown that HzRGs are hosted by massive

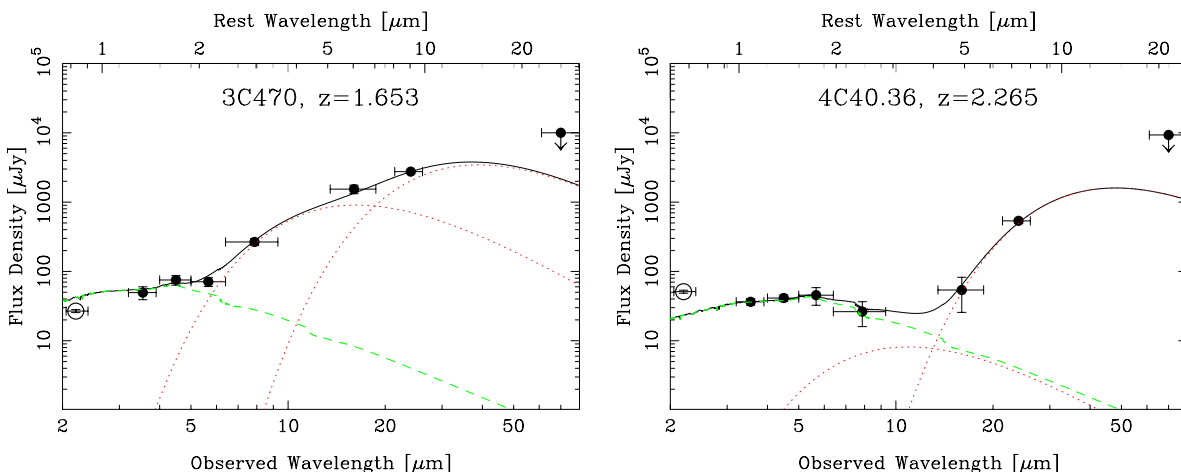


Figure 1.8: Near- to far-IR spectral energy distribution of two radio galaxies. *Left*: The rest-frame 2-5 μm emission is dominated by the AGN and it is very difficult to disentangle the AGN contribution from the far-IR emission due to dust re-heating through young stars. *Right*: The AGN contribution in this galaxy is relatively low and the old stellar bump at 1.6 μm is clearly separated from the far-IR bump. From De Breuck et al. (2010)

elliptical galaxies and seem to be a stage during the evolution of massive galaxies and are observed during a peak of their activity. This particular phase allows to study different models of galaxy formation and the interaction of the AGN, i.e. the supermassive black hole, and the host galaxy.

Old Stellar Population

Old stars are the best tracers of stellar mass in galaxies. The SED of old stellar populations peaks at near-infrared wavelengths (see Fig. 1.8). Its most prominent feature is a bump at 1.6 μm restframe-wavelength that shifts to the mid-infrared regime for high-redshift objects. This feature is independent of the evolutionary type and star-formation history of the galaxy and can therefore be used as a redshift indicator for any type of galaxy (not just radio galaxies, Papovich, 2008). This feature is very important for the work in this thesis and is described in more detail in Section 2.4.1.

Since the near-infrared wavelength regime is dominated by the emission of old stars, the brightness of radio galaxies in the K wavelength-band (2.2 μm), and for higher redshift ($z > 2$) at longer wavelengths (e.g. with *Spitzer* at 3.6 μm) allows to draw conclusions about the mass of the host galaxy. However, caution has to be used when converting simple K -band magnitudes to stellar mass as the near-infrared observations could already be contaminated by hot dust emission from the AGN (but partly also by direct AGN continuum

emission or by contributions of the young stellar population, see Fig. 1.8). Combining observations in the near- and mid-infrared from the *Spitzer Space Telescope* for a large sample of 70 radio galaxies at $1 < z < 5$ and performing a full AGN-stellar decomposition confirmed that radio galaxies are indeed massive, with stellar masses in the range $10 < \log(M)/\log(M_{\odot}) < 12$ (Seymour et al., 2007).

Star Formation

Young and forming stars heat the dust in galaxies that re-emits thermal emission at far-infrared and sub-millimetre wavelengths. The far-infrared luminosity can therefore be used as an indicator for the star-formation rate by e.g. using the simple relation found by Kennicutt (1998):

$$SFR [M_{\odot}] = L_{FIR}/5.8 \times 10^9 L_{\odot} \quad (1.2)$$

where SFR is the star formation rate in units of solar masses, L_{FIR} the far-infrared luminosity of the galaxy and L_{\odot} the solar luminosity.

Radio galaxies are very luminous in this wavelength regime which hints to very high star-formation rates. Observations show that star-formation rates in radio galaxies can be even as high as several thousands M_{\odot}/yr (Archibald et al., 2001; Drouart et al., 2014). Their sub-millimeter luminosity has been found to increase with redshift implying that star-formation rates were higher at early times ($z > 3$, Miley & De Breuck, 2008). However, disentangling if the dust is heated by the powerful AGN or by stars is difficult and requires detailed modelling and SED fitting of each component. For this exercise, the Rayleigh-Jeans tail of the sub-millimeter SED is crucial as it constrains the slope of the dust emission heated by stars (Drouart et al., 2014). This tail is also important for deriving far-infrared photometric redshifts (Wylezalek et al., 2013b), as shown in Section 5.4.1.

Supermassive Black Hole

Radio galaxies are believed to be powered by accretion of matter onto a supermassive black hole that is obscured by a lot of dust and there is convincing evidence for such hidden active black holes. If there is a hidden AGN in the centre, its emission will scatter off the dust that is located around the AGN. No emission from the AGN will be detected with normal flux measurements. This scattering process, however, polarises the light and signatures of the black hole can be detected with polarimetric measurements. Indeed, broad emission and recombination lines similar to those seen in quasars have been detected in polarised light (Vernet et al., 2001). It is, however, very challenging to directly infer black hole masses from line width diagnostics as it is done for unobscured AGN. Indirectly, black hole masses can be inferred through the well established empirical relation between the black

hole mass and the mass of the galaxy bulge (Håring & Rix, 2004). This relation predicts black hole masses of $\sim 10^9 M_{\odot}$ for a radio galaxy with a stellar mass of $\sim 10^{12} M_{\odot}$, indeed a super-massive black hole (Nesvadba et al., 2011; Drouart et al., 2014).

The nature of radio galaxies with their large masses, massive black holes and observations up to very high redshifts make them important laboratories for studying massive galaxy formation. Observations imply that star formation in massive galaxies happens earlier than in lower mass galaxies, in contrast to some hierarchical galaxy evolution scenarios. This ‘galaxy downsizing’ is mostly explained today through AGN ‘feedback’, a scenario in which radiative and mechanical processes and winds due to the AGN slow down star formation. A lot of the details of feedback, however, are poorly understood and radio galaxies are ideal for studying these interactions.

1.3.2 Radio-loud Quasars

Quasars are distant galaxies with the most active and most massive black holes in their centre, i.e. the most active galactic nuclei. Radio-loud quasars are, similarly to radio galaxies, very luminous at radio wavelengths where the radio emission is powered by their supermassive black hole. There is strong evidence that radio galaxies and radio-loud quasars both belong to the same parent population and are linked by a unified model of AGN (see Fig. 1.9, Urry & Padovani, 1995).

In this model the AGN is a compact region in the centre of a galaxy hosting a super-massive black hole. The black hole is powered by infalling material, a process that results in a very efficient conversion from kinetic energy to radiation. Cold material close to the black hole forms an accretion disk and a thick torus of dust is surrounding the whole system. Some accretion disk may produce jets, highly collimated, energetic outflows, that are perpendicular to the disk and emerge in opposite directions.

The difference in the observed properties of radio-loud quasars (e.g. point-like, very bright objects) and radio galaxies (e.g. elliptical galaxies) are, according to the unified model, only due to different orientations of the radio source axis relative to us. In radio galaxies, the dust torus is observed edge-on, obscuring the luminous centre of the AGN and allowing to observe the different components of the host galaxy. Observations of quasars allow to observe the unhidden quasar and luminous jets on the side of the source that is nearest to us. The detection of a hidden AGN in radio galaxies through polarisation measurements is the strongest, but not only, evidence for this unification scheme.

Recently, an alternative paradigm has been gaining attention in which obscured AGN (e.g. radio galaxies) evolve into quasar-type AGN as their merger-triggered, dust-obscured AGN become more powerful and clear out the environment (e.g. Hopkins et al., 2006).

In this dynamical model radio galaxies and radio-loud quasars trace different phases in the evolution of powerful AGN and are potentially associated with different environments.

According to the orientation-driven unification model, however, radio galaxies and radio-loud quasars are the same type of galaxies belonging to the population of galaxies called radio-loud AGN and statistically are similarly massive, host similarly massive black holes and reside in similarly massive dark matter halos. A clear prediction, that is also successfully tested in this thesis, is that they reside in the same type of large-scale environments (see Section 2.4.4 and 2.5).

1.3.3 Large-scale environments

Radio-loud AGN belong to the most massive galaxies in the Universe and according to predictions from the Λ CDM model, they are expected to reside in peaks of dark matter overdensities and to be good tracers for galaxy overdensities. Observations have indeed shown that radio-loud AGN preferentially reside in overdense environments (e.g. Stevens et al., 2003; Venemans et al., 2007; Falder et al., 2010; Stevens et al., 2010; Galametz et al., 2010b, 2012; Mayo et al., 2012). Targeted searches for high-redshift clusters and proto-clusters around powerful high-redshift radio galaxies have proven very successful and have a rich literature (e.g., Pentericci et al., 2000; Stern et al., 2003; Kurk et al., 2004; Venemans et al., 2007; Doherty et al., 2010; Galametz et al., 2009, 2010b; Hatch et al., 2009; Matsuda et al., 2011; Mayo et al., 2012). As HzRGs are found up to very high redshifts, they serve as efficient beacons for identifying very high redshift galaxy clusters. The fields of radio-loud AGN are therefore unique laboratories to study the formation and evolution of the first galaxies and galaxy structures.

For a more complete summary of large-scale environments of radio-loud AGN we refer the reader to Sections 2.1, 3.1, 4.1 and 5.1.

1.4 High-redshift galaxy clusters

Emerging from the cosmic web, galaxy clusters are the most massive gravitationally bound structures in the Universe. Thought to have begun their assembly at $2 < z < 3$, clusters provide insights into the growth of large-scale structure as well as the physics that drives galaxy evolution. How and when did the most massive galaxies assemble their stellar mass? When did they stop forming stars? How did they acquire their observed morphologies that we observe today? These remain outstanding questions that can only be tackled by studying large samples of high-redshift clusters.

The redshift range $1.4 < z < 3$ is a key epoch in the evolution of galaxy clusters (e.g. van Dokkum & Stanford, 2003). Elliptical galaxies start to become the dominant population in

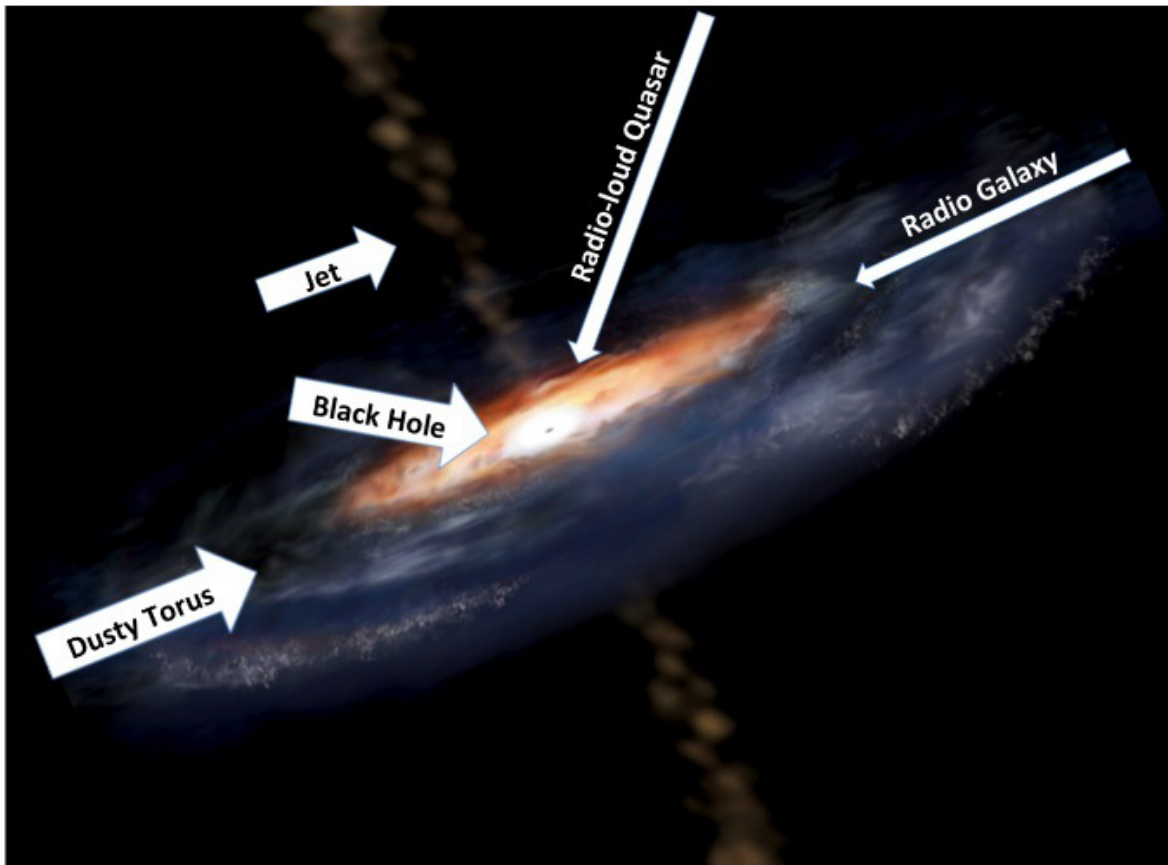


Figure 1.9: An artists impression of a luminous AGN. Surrounding the central black hole is a luminous accretion disk. A thick, dusty torus obscures the central black hole from transverse lines of sight. Radio jets emanate from the region near the black hole, initially at relativistic speeds. The difference between radio galaxies and radio-loud AGN is due to the observing angle. Credit: Aurore Simonnet (Sonoma State University)

cluster cores, and star formation in spiral galaxies is being quenched (e.g. Stanford et al., 2012; Snyder et al., 2012; Zeimann et al., 2012). There is also observational evidence for a progressive increase in the amount of star formation that occurs in galaxy cluster cores at $z > 1.4$ (e.g. Brodwin et al., 2013). This suggests that the majority of star formation is actually occurring in high-density environments at early epochs.

Other studies have shown that the bulk of the stellar mass is already in place by $z \sim 1.3$ (e.g. Lin et al., 2006; Muzzin et al., 2008; Mancone et al., 2010). It seems that processes that might lead to a substantial increase in mass such as mergers and star formation, and processes that would strip mass away from the cluster like galaxy-galaxy interactions, or galaxy harassment do not to play an important role in the overall evolution at $z < 1.3$.

Therefore increasing evidence points to clusters at $1.4 < z < 3$ as being the ideal laboratories to catch in the act transformations in their galaxy stellar population content.

Until recently, this redshift range was unreachable with available instrumentation, and called a 'desert' as at $z \geq 1.4$, features such as [OII] $\lambda\lambda 3726 - 3729 \text{ \AA}$ and D4000¹¹ shift to near-infrared wavelengths, making optical spectroscopic follow-up exceedingly challenging. *Spitzer*, on the other hand, is an incredibly sensitive tool for finding massive galaxies at high redshift. For stellar populations formed at high redshift, negative k -corrections provide a nearly constant $4.5\mu\text{m}$ flux density over a wide redshift range, while red [3.6]-[4.5] colors provide an effective means of isolating galaxies at $z > 1.3$. Several projects are now attempting to exploit this capability to search for high-redshift galaxy clusters (e.g. Eisenhardt et al., 2008; Papovich et al., 2010; Galametz et al., 2012). However, much of this previous work relies on field surveys, which provide both a strength and a weakness: uniformly selected galaxy cluster samples have the power to probe basic cosmological parameters by measuring the growth of structure. However, field surveys - both in the mid-IR and at other wavelengths, such as Sunyaev-Zel'dovich surveys find - due to limited search areas - few clusters at the highest redshifts, $z > 1.5$. Many key galaxy cluster studies do not require knowledge of the cluster space density (e.g. Galametz et al., 2009; Stern et al., 2010), and therefore targeted searches for high-redshift galaxy clusters have many advantages.

As outlined above, targeted searches for clusters and proto-clusters around high-redshift radio-loud AGN, in particular HzRGs, have proven quite successful. Until now, however, there have been no systematic studies of a uniformly selected sample of high-redshift radio-loud AGN that allowed for conclusions about the statistical properties of a large sample of galaxy (proto-)clusters. The project and the work this thesis is based on, is making a first and successful attempt to do so and has already made a significant contribution to this field.

¹¹The 4000 Angström break (D4000) is a clear drop off in intensity of galaxy spectra at 4000 \AA and important feature in galaxy SEDs. It arises because of an accumulation of absorption lines of metals. The 4000 \AA break gets larger with older ages, and it is largest for old and metal-rich stellar populations.

1.5 This Thesis

This work aims at identifying a large sample of high redshift galaxy clusters and at studying various cluster properties with cosmic time. To that purpose, our large project CARLA (Clusters Around Radio-Loud AGN) has targeted 420 radio-loud AGN at $1.3 < z < 3.2$ for a total of more than 400 hours of *Spitzer*/IRAC time. CARLA allows for the first time to systematically study the fields of a large sample of powerful RLAGN over a wide redshift range. We systematically analysed the fields, identified promising cluster candidates and, by using luminosity functions, studied the evolution of their stellar mass in high-redshift clusters over almost 3 Gyrs of cosmic time.

A complementary project, HeRGE (*Herschel* Radio Galaxy Evolution Project) observed a sample of 71 radio galaxies at $1 < z < 5$ at far-IR wavelengths with the *Herschel Space Observatory*. Supporting data in the mid-IR (from *Spitzer*), near-IR and sub-mm allow to study single protocluster fields in more detail and to constrain the star-formation properties of cluster members.

This thesis is organised as follows:

Chapter 2

This chapter summarises the CARLA sample, the data reduction and first analysis. We first isolate high redshift galaxies using IRAC colors, and then search for potential overdensities of the IRAC-selected sources around the targeted AGN. The analysis shows that ~ 200 CARLA fields are rich and compact structures with overdensities established within cells of 0.5 Mpc. The surface density profile proves that indeed most of the excess sources are associated with the targeted RLAGN. We find no difference between the environments of radio galaxies and radio-loud quasars, in agreement with the unification model described earlier.

Chapter 3

This large CARLA (proto-)cluster sample also allows us, for the first time at these redshifts, to systematically measure the luminosity function of clusters around RLAGN. Our results show that the protocluster environment forms very early ($z_f \sim 3$) and evolves almost passively thereafter. This means that the rate at which the young galaxy population grows through star formation, gets quenched and is replenished by in-falling field galaxies does not have a major net effect on the shape of the luminosity function. Comparing these results to field cluster studies suggests that the AGN environments are older and more evolved systems than the general protocluster population. Given that RLAGN reside in the most

massive dark matter halos, this is another example for cosmic downsizing¹².

Chapter 4

With the project described in this chapter our team is aiming at constraining why radio-loud AGN are located in dense environments. Is this just because they are massive? Or is there another intrinsic property of this special kind of galaxies that places them in some of the densest environments we know? To approach this question we select a sample of massive galaxies, that are not radio-loud AGN, but have a similar mass and redshift distribution as our CARLA sample. The analysis shows that radio-loud AGN reside in denser environments than similarly massive galaxies. We detect a weak positive correlation between the black-hole mass and the environmental density on Mpc-scales, suggesting that even at high redshift the growth of the black hole is also linked to collapse of the surrounding cluster.

Chapter 5

As a pilot project for a systematic, multi-wavelength analysis of the HeRGE fields, the field around the radio galaxy 4C41.17 at $z = 3.8$ was analysed in more detail. It was previously found to be a candidate cluster field because of its high density of star-forming galaxies. With the additional data at hand from the HeRGE sample, I was able to derive photometric redshifts, estimate infrared luminosities and star-formation rates for the galaxies in the field of the radio galaxy. The radio galaxy has a close-by companion that is likely merging with the radio galaxy but most of the other objects in the field are not associated with the merging system. This work shows that not every overdense field is necessarily a real (proto-)cluster and that supporting data is needed to study and follow-up cluster candidates to reliably draw conclusions about (proto-)cluster properties at high redshift.

The work on CARLA and HeRGE laid the foundation for systematic studies of high redshift galaxy clusters and **Chapter 6** describes future projects and prospects of the field.

¹²The term downsizing has been used to describe several observational trends that suggest older ages or earlier star formation for more massive galaxies compared to lower mass galaxies. It is not clear yet if and to which extent these observations are in conflict with predictions from Λ CDM cosmology.

High-redshift galaxy clusters around radio-loud AGN

Dominika Wylezalek, Audrey Galametz, Daniel Stern, Joël Vernet, Carlos De Breuck, Nick Seymour, Mark Brodwin, Peter R. M. Eisenhardt, Anthony H. Gonzalez, Nina Hatch, Matt Jarvis, Alessandro Rettura, Spencer A. Stanford, Jason A. Stevens
The Astrophysical Journal, Volume 769, Issue 1, article id. 79, 10 pp. (2013)

Abstract We report the first results from the Clusters Around Radio-Loud AGN (CARLA) program, a Cycle 7 and 8 *Spitzer Space Telescope* snapshot program to investigate the environments of a large sample of obscured and unobscured luminous radio-loud AGN at $1.2 < z < 3.2$. These data, obtained for 387 fields, reach 3.6 and 4.5 μm depths of $[3.6]_{\text{AB}} = 22.6$ and $[4.5]_{\text{AB}} = 22.9$ at the 95% completeness level, which is two to three times fainter than L^* in this redshift range. By using the color cut $[3.6]-[4.5] > -0.1$ (AB), which efficiently selects high-redshift ($z > 1.3$) galaxies of all types, we identify galaxy cluster member candidates in the fields of the radio-loud AGN. The local density of these IRAC-selected sources is compared to the density of similarly selected sources in blank fields. We find that 92% of the radio-loud AGN reside in environments richer than average. The majority (55%) of the radio-loud AGN fields are found to be overdense at a $\geq 2 \sigma$ level; 10% are overdense at a $\geq 5 \sigma$ level. A clear rise in surface density of IRAC-selected sources towards the position of the radio-loud AGN strongly supports an association of the majority of the IRAC-selected sources with the radio-loud AGN. Our results provide solid statistical evidence that radio-loud AGN are likely beacons for finding high-redshift galaxy (proto-) clusters. We investigate how environment depends on AGN type (unobscured radio-loud quasars vs. obscured radio galaxies), radio luminosity and redshift, finding no correlation with either AGN type or radio luminosity. We find a decrease in density with redshift, consistent with galaxy evolution for this uniform, flux-limited survey. These results

are consistent with expectations from the orientation-driven AGN unification model, at least for the high radio luminosity regimes considered in this sample.

2.1 Introduction

The Infrared Array Camera (IRAC; Fazio et al., 2004) of the *Spitzer Space Telescope* is an incredibly sensitive tool for finding and studying massive galaxies at high redshift. For stellar populations formed at high redshift, negative k -corrections provide a nearly constant $4.5\mu\text{m}$ flux density over a wide redshift range — e.g., an L^* galaxy formed at $z_f = 3$ will have $[4.5] \sim 17$ at $0.7 \leq z \leq 2.5$, which is sufficiently bright that it is robustly seen in even 90 sec integrations with *Spitzer*. Several teams have been exploiting this capability to identify large samples of galaxy clusters at $z \geq 1$ (e.g., Eisenhardt et al., 2008; Wilson et al., 2009; Papovich et al., 2010; Galametz et al., 2010a; Muzzin et al., 2013). The *Spitzer* mid-infrared selection is capable of finding both the very rare, massive evolved clusters at $z \geq 1.75$ (e.g., Stanford et al., 2012), as well as the more numerous groups or forming clusters at similarly high redshifts (e.g., Zeimann et al., 2012; Gobat et al., 2011). Teams are now using mid-IR-selected clusters for a range of important studies such as using the colors, sizes, and mid-IR cluster galaxy luminosity function to probe the formation epoch of massive cluster galaxies (e.g. Mancone et al., 2010, 2012; Rettura et al., 2011; Lidman et al., 2012; Mei et al., 2012; Snyder et al., 2012), measuring the galaxy cluster correlation function out to $z \sim 1.5$ (Brodwin et al., 2007), probing evolution in the $\sigma - T_x$ correlation (Brodwin et al., 2011), and targeted cosmological studies of $z > 1$ Type Ia SNe in dust-free cluster environments (Dawson et al., 2009; Suzuki et al., 2012).

Much of the work to date on high-redshift galaxy clusters comes from field surveys, which provide both a strength and a weakness. Uniformly selected galaxy cluster samples have the power to probe basic cosmological parameters by measuring the growth of structure. However, field surveys — both in the mid-IR (e.g., Gettings et al., 2012) and at other wavelengths (e.g., Sunyaev-Zeldovich and X-ray surveys; Vanderlinde et al., 2010; Fassbender et al., 2011; Reichardt et al., 2012) — find few clusters at the highest redshifts, $z \geq 1.5$. While measuring the cluster space density is required to use these systems as cosmological probes, many key galaxy cluster studies do not require such knowledge (e.g., Krick et al., 2008; Galametz et al., 2009; Suzuki et al., 2012; Martini et al., 2013).

In order to efficiently identify the richest environments at yet higher redshifts, targeted searches for high-redshift galaxy clusters have many advantages. Towards that goal, literature that stretches back nearly 50 years shows that powerful radio-selected AGN preferentially reside in luminous red sequence galaxies (e.g., Matthews, 1965; Best et al., 1998; Venemans et al., 2002; Hickox et al., 2009; Griffith & Stern, 2010). Indeed, targeted searches for high-redshift clusters and proto-clusters around powerful high-redshift radio

galaxies (HzRGs) have proven very successful and have a rich literature (e.g., Pentericci et al., 2000; Stern et al., 2003; Kurk et al., 2004; Venemans et al., 2007; Doherty et al., 2010; Galametz et al., 2009, 2010b; Hatch et al., 2009; Matsuda et al., 2011; Mayo et al., 2012).

In a pilot study by our team, Galametz et al. (2012) used a counts-in-cell analysis to identify overdensities of IRAC-selected high-redshift galaxy candidates in the fields of 72 HzRGs from the *Spitzer* High-Redshift Radio Galaxy program (SHzRG; Seymour et al., 2007; De Breuck et al., 2010). The HzRGs in that study spanned a range of $1.2 < z < 3$. Using relatively shallow, ~ 120 s IRAC data, Galametz et al. (2012) showed that radio galaxies preferentially reside in medium to dense regions, with 73% of the targeted fields denser than average. Apart from six newly discovered cluster candidates, several known (proto-)clusters were recovered as overdense fields in that analysis, and we have recently spectroscopically confirmed one of the more promising candidate fields as a new high-redshift cluster at $z = 2.02$ (Galametz et al., 2013).

In this paper, we describe the first results from our ~ 400 hr *Warm Spitzer* snapshot program called Clusters Around Radio-Loud AGN, or CARLA¹, a Cycle 7 and Cycle 8 program which takes advantage of *Spitzer's* impressive sensitivity to identify massive galaxies at high redshift. To date, CARLA has targeted nearly 400 radio-loud AGN, including 187 radio-loud quasars (RLQs) and 200 HzRGs. Targets were uniformly selected in radio luminosity over the redshift range $1.3 < z < 3.2$. Similar to the successful pilot study by Galametz et al. (2012), CARLA allows, for the first time, a sensitive, systematic study of the environments of a large sample of powerful radio-loud sources over a wide redshift range. We isolate high-redshift galaxy candidates using IRAC colors and quantify the environments of the targeted AGN as compared to similar-depth blank-field surveys. CARLA also allows us to investigate how environment depends on radio-loud AGN properties such as redshift, radio luminosity and AGN class (e.g., type-1, or unobscured RLQs vs. type-2, or obscured HzRGs). A companion paper, Wylezalek et al. (2014), investigates the luminosity function of CARLA-selected candidate galaxy cluster members.

The paper is organized as follows: § 2.2 describes how the sample of HzRGs and RLQs was selected and § 2.3 gives details on the observations, data reduction, catalog generation and the completeness limit of the survey. We describe the analysis of the environments of the CARLA targets with respect to galaxy type, redshift and radio luminosity in § 2.4 and draw conclusions from the results in § 2.5. Section 2.6 summarizes our results. Throughout the paper we assume $H_0 = 70 \text{ km s}^{-1} \text{ Mpc}^{-1}$, $\Omega_m = 0.3$, $\Omega_\Lambda = 0.7$. All magnitudes and colors are expressed in the AB photometric system unless stated otherwise.

¹As of March 2013, CARLA targets are still being scheduled; this manuscript/chapter details all observations obtained through February 2013.

2.2 The CARLA Sample

A key goal of the CARLA survey is to investigate how environment depends on AGN classification, and we therefore have targeted a matched sample of unobscured (e.g., type-1) and obscured (e.g., type-2) radio-loud AGN. Type-1 AGN, specifically broad-lined quasars or RLQs for the high-luminosity, radio-loud sources targeted here, show signatures of radiation originating from very close to the central black hole. In contrast, the central black hole is obscured by dense absorbing material in type-2 AGN, or HzRGs for the high-luminosity, high-redshift, radio-loud sample observed here. In the standard AGN unification model (Urry & Padovani, 1995) this obscuration is produced by an optically thick circumnuclear torus and differences in optical appearance only depend on the orientation angle at which the AGN is observed, not due to intrinsic differences between the two AGN types. A clear prediction is that both AGN types should reside in identical environments. Recently, an alternative paradigm has been gaining attention in which type-2 AGN evolve into type-1 AGN as their merger-triggered, dust-obscured AGN become more powerful and clear out the environment (e.g. Hopkins et al., 2006, and references therein). This dynamical model would mean that type-1 and type-2 AGN trace different phases in the evolution of powerful AGN, potentially associated with different environments. On the other hand, if the timescale associated with the AGN breaking out of its obscuring cocoon is much shorter than the timescale on which the environment develops, then no dependence of environment on AGN type would be expected in the dynamical model.

The CARLA sample consists of 387 radio-loud AGN, including 187 RLQs and 200 HzRGs (sample size as of 2013 February 20). The matched RLQ and HzRG samples have been deliberately designed to be of similar size with similar redshift and radio luminosity ranges. HzRGs are defined as powerful, high-redshift radio sources with rest-frame 500 MHz radio luminosities $L_{500\text{MHz}} \geq 10^{27.5} \text{ W Hz}^{-1}$ and have optical spectra free of broad emission lines. This classification as narrow-line, i.e. type-2 AGN is based on the optical spectroscopy used to determine their redshifts. The HzRGs were selected from the updated compendium of Miley & De Breuck (2008) extended down to $z = 1.3$ using both flux-limited radio surveys (e.g. MRC, 3C, 6C, 7C) and ultra-steep spectrum surveys (e.g. Röttgering et al., 1997; De Breuck et al., 2001). The sample contains all 146 powerful HzRGs known as of 2010 at $2 < z < 3.2$.

To calculate $L_{500\text{MHz}}$, we used the procedure described by Miley & De Breuck (2008). In short, we cross-correlated the HzRGs with the 1.4 GHz NRAO VLA Sky Survey (NVSS; Condon et al., 1998) and the 74 MHz VLA Low-Frequency Sky Survey (VLSS; Cohen et al., 2007), using a 30 arcsec search radius. These two radio surveys cover a very large part of the extragalactic sky, and have well-matched spatial resolution, thereby avoiding concerns with missing flux. The rest-frame 500 MHz frequency was deliberately chosen to ensure

that the fluxes were interpolated rather than extrapolated between the two radio surveys. If no VLSS detection was available, we assumed a spectral index $\alpha = -1.1$ ($S_\nu \propto \nu^\alpha$, Miley & De Breuck, 2008).

To create the RLQ sample, we selected all optically bright ($M_B < -26.5$) quasars in the Sloan Digitized Sky Survey (SDSS; Schneider et al., 2010) and the 2dF QSO Redshift Survey (2dFQZ; Croom et al., 2004), where the spectroscopy-based classifications were taken from the original catalogues. For the SDSS quasars the M_B were taken from the original catalogue, and for the 2df quasars we calculated M_B from the original catalogs assuming a quasar SED represented by a power law ($f_\nu \propto \nu^{\alpha_{RLQ}}$, $\alpha_{RLQ} = 0.5$ – as used for the SDSS quasars) and we corrected for Galactic dust extinction.

To identify RLQs, we then correlated this sample with the NVSS using a 10 arcsec search radius. As only $\sim 20\%$ of the RLQs are detected in the VLSS, we could not calculate the radio spectral indices in a systematic way. Moreover, RLQs may contain time-variable, Doppler beamed emission, which would render the spectral indices from surveys observed several years apart unreliable. We therefore assumed a fixed $\alpha = -0.7$ for all RLQs to calculate their $L_{500\text{MHz}}$. We tested and justified this choice by computing the mean and median value for the 133 out of 717 RLQs where the VLSS-NVSS spectral indices could be derived, and find -0.65 and -0.74 , respectively. On average, the radio luminosities calculated with a fixed α only differ from the precise radio luminosities by 3% and this scatter will not have any influence on our results and conclusions.

The final RLQ sample was obtained by considering only sources in regions with low Galactic extinction ($E(B - V) \leq 0.1$) and by matching to the redshift and radio power distribution of the HzRG sample. The top panel in Fig. 2.1 shows rest-frame $L_{500\text{MHz}}$ vs. redshift while the bottom panel shows the distribution of our targets across the sky. This sample selection allows us to study evolutionary trends as well as trends with radio luminosity for both types of AGN without any biases beyond the selection being restricted to the most radio powerful sources.

2.3 Data

2.3.1 Observations

CARLA observed the lower redshift ($1.3 < z < 2$) sources with the *Spitzer* IRAC camera at 3.6 and 4.5 μm (referred to as IRAC1 and IRAC2) during Cycle 7 with total exposure times of 800s in IRAC1 and 2000s in IRAC2. Slightly deeper observations were obtained for the higher redshift ($2 < z < 3.2$) portion of the sample during Cycle 8 with total exposure times of 1000s in IRAC1 and 2100s in IRAC2. IRAC employs 256×256 InSb detector arrays with $1.22''$ pixels to map out a $5.2 \text{ arcmin} \times 5.2 \text{ arcmin}$ field. The IRAC1 and IRAC2 data were

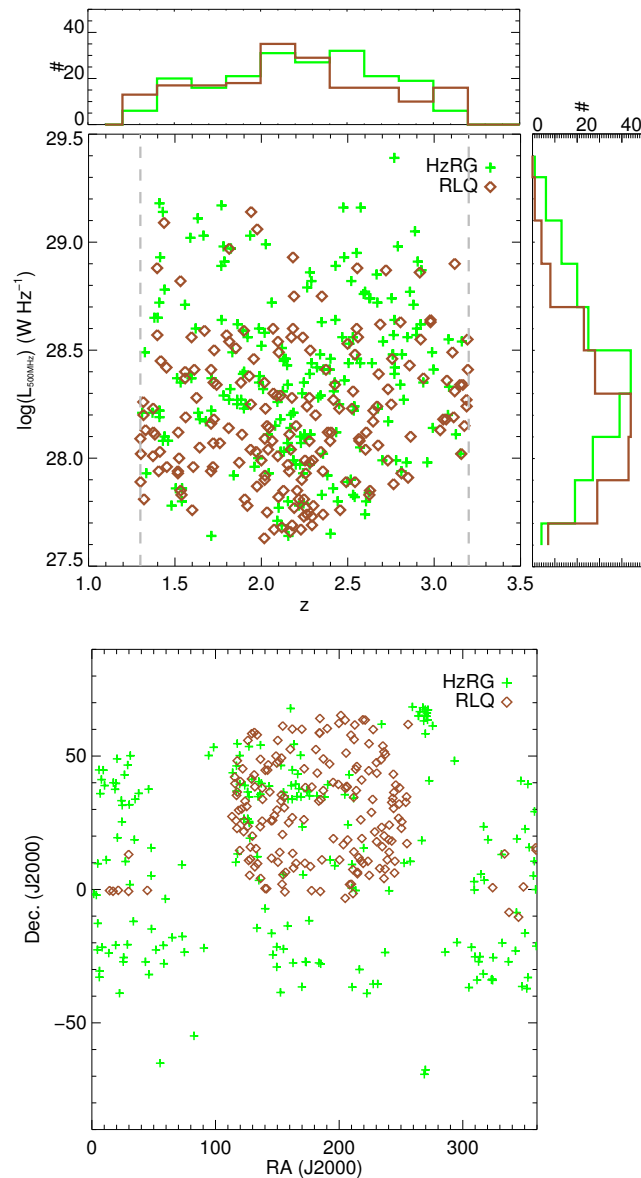


Figure 2.1: *Top panel:* Rest-frame 500 MHz luminosity vs. redshift. As shown by their distributions, both subsamples (HzRGs and RLQs) sample the targeted $L_{500\text{MHz}} - z$ plane in a relatively uniform manner. *Bottom panel:* Distribution of the CARLA radio-loud AGN across the sky. Most of the RLQs are chosen from the SDSS and are thus mainly located in the Northern hemisphere, while the HzRGs cover the full extragalactic sky. In both panels, green crosses show the HzRGs in our sample, while orange diamonds show the RLQs.

obtained simultaneously over slightly offset fields, allowing CARLA to tailor the exposure times in each band for our intended science. Observations were all obtained with dithered

100 s observations. In order to save the ~ 5 min overhead per target had the differing integration times for IRAC1 and IRAC2 been split across two Astronomical Observation Requests (AORs), we instead implemented this observing strategy in a single AOR using the the “Fixed Cluster Offset” mode in array coordinates. In AB magnitudes, the total exposure times give similar depths for both channels (see section 2.3.4) with the IRAC2 observations being slightly deeper. The total exposure times, which are slightly longer for the high-redshift portion of the sample (observed during Cycle 8), reach depths two magnitudes below m^* over the whole redshift range (see Section 2.3.4). This allows us to robustly measure the faint-end slope of the cluster luminosity function out to high redshift, which is the focus of our second CARLA paper (Wylezalek et al., 2014).

2.3.2 Data Reduction

The basic calibrated data were reduced and mosaicked using the MOPEX package (Makovoz & Khan, 2005) and resampled to a pixel scale of $0.61''$. The MOPEX outlier (e.g., cosmic ray, bad pixel) rejection was optimized for the regions of deepest coverage in the center of the maps, corresponding to the location of the targeted AGNs. Due to artifacts and bright foreground stars, the maximum coverage is not reached in every part of the field. Regions with $\leq 85\%$ of the maximum coverage were ignored for source extraction and further analysis.

2.3.3 Source Extraction

Source extraction was performed using SExtractor (Bertin & Arnouts, 1996) in dual image mode using the $4.5 \mu\text{m}$ frame as the detection image. We used the IRAC-optimized SExtractor parameters from Lacy et al. (2005). We measured flux densities in $4''$ diameter apertures, converting from the native MJy ster^{-1} units of the images to $\mu\text{Jy pixel}^{-1}$ by multiplying with the conversion factor of $8.4615 \mu\text{Jy pixel}^{-1} / (\text{MJy ster}^{-1})$ for our $0.61''$ pixel scale. We derived empirical aperture corrections from the curve of growth of bright, isolated stars in the CARLA survey. These multiplication factors, 1.42 for IRAC1 and 1.45 for IRAC2, correct the photometry to $24''$ -radius apertures. These values are systematically $\sim 17\%$ larger than the aperture corrections listed in the *Spitzer* Instrument Handbook but are consistent with the aperture corrections found by Ashby et al. (2009) for the *Spitzer* Deep, Wide-Field Survey. The discrepancy with the Instrument Handbook is most likely due to differences in the background determination and slight differences in aperture radii (Ashby et al., 2009).

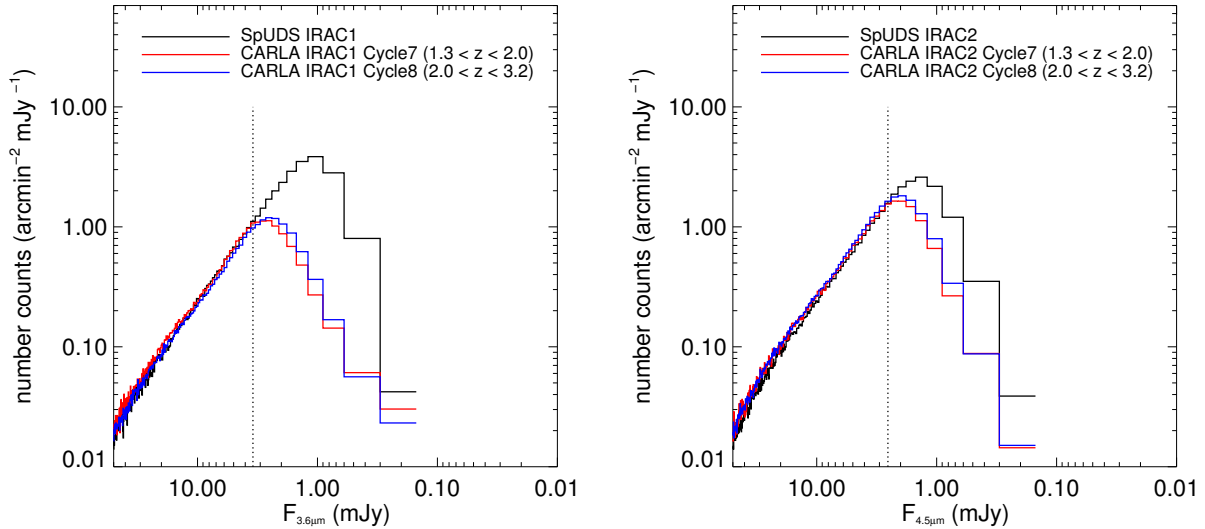


Figure 2.2: Number counts for the SpUDS and CARLA surveys for sources detected at $3.6 \mu\text{m}$ (*left*) and $4.5 \mu\text{m}$ (*right*). These analyses rely on catalogs independently built for detecting sources in each band. The 95% completeness limit in each band is derived by comparing the CARLA number counts to those from the SpUDS survey, which gives completeness limits of $3.45 \mu\text{Jy}$ for IRAC1 and $2.55 \mu\text{Jy}$ for IRAC2, as shown by the vertical dotted lines.

2.3.4 Completeness Limit

We determined the 95% completeness level by comparing the CARLA number counts to number counts from the *Spitzer* UKIDSS Ultra Deep Survey (SpUDS, PI: J. Dunlop), a deep Cycle 4 *Spitzer* Legacy program covering 1 deg^2 in the UKIDSS UDS field with IRAC and the Multiband Imaging Spectrometer aboard *Spitzer* (MIPS; Rieke et al., 2004). SpUDS reaches greater sensitivities than CARLA, with IRAC1 and IRAC2 3σ depths of $\sim 1 \mu\text{Jy}$ ($\text{mag}_{\text{AB}} \simeq 24$). Although SpUDS catalogs are publicly available, we performed source extraction on the final mosaics in the same way as for CARLA to ensure uniformity in our analyses. In particular, the public catalogs are cut at a depth of 8σ , i.e. shallower than CARLA, and thus would not allow us to accurately measure the completeness of the CARLA catalogs. The aperture corrections we derive for bright, isolated sources in SpUDS are consistent with the ones derived for the CARLA survey. We created IRAC1 and IRAC2 SExtractor catalogs using single image mode. The differential number counts are shown in Fig. 2.2. As planned, the IRAC1 and IRAC2 observations match very well in depth. We determine a 95% completeness limit of 3.45 and $2.55 \mu\text{Jy}$ relative to the SpUDS survey, corresponding to limiting magnitudes of $[3.6] = 22.6$ and $[4.5] = 22.9$ for the observations. These values are adopted as flux density cuts for all subsequent analyses.

Table 2.1: The CARLA sample (in R.A. order).

Name	R.A. (J2000)	Dec. (J2000)	z	$\log(L_{500\text{MHz}})$ (W Hz ⁻¹)	Σ (arcmin ⁻²)	AGN Type
USS0003-019	00:06:11.00	-01:41:50.2	1.54	27.86	10.5	HzRG
PKS_0011-023	00:14:25.00	-02:05:56.0	2.08	28.15	10.2	HzRG
MRC_0015-229	00:17:58.20	-22:38:03.8	2.01	28.32	15.6	HzRG
BRL0016-129	00:18:51.40	-12:42:34.6	1.59	29.02	15.3	HzRG
MG0018+0940	00:18:55.20	+09:40:06.9	1.59	28.39	13.4	HzRG
			⋮			

This table is published in its entirety in the electronic edition of ApJ; a portion is shown here for guidance regarding its form and content. A full version of the table, including the full CARLA data set is also given in Appendix A of this thesis.

2.4 The Environments of Radio-Loud AGN

2.4.1 IRAC-Selected Sources

We use a counts-in-cell analysis of color-selected IRAC sources to identify high-redshift overdense fields. Papovich (2008) showed that an IRAC color cut of $[3.6] - [4.5] > -0.1$ efficiently isolates galaxies regardless of age and galaxy type at $z > 1.3$. This criterion makes use of the 1.6 μm bump, a prominent spectral feature in the spectral energy distributions of galaxies that does not depend on the evolutionary stage of the galaxy. The bump is caused by a minimum in the opacity of the H^- ion which is present in the atmospheres of cool stars (John, 1988) and is a commonly used indicator of redshift (e.g., Simpson & Eisenhardt, 1999; Sorba & Sawicki, 2010). The 1.6 μm bump enters the IRAC bands at $z \sim 1$ and provides a redder $[3.6] - [4.5]$ color for high-redshift galaxies as compared to low-redshift ($z < 1$) galaxies (see Fig. 2.3). Contamination can come from strongly star-forming galaxies at $0.2 < z < 0.5$ (Papovich, 2008), cool brown dwarfs (Stern et al., 2007) and powerful AGN at all redshifts (Stern et al., 2005). However, these contaminations are not expected to be significant (for a detailed discussion see Galametz et al., 2012). More than 90% of objects satisfying this simple color criterion will be at $z > 1.3$ (Papovich, 2008). In the following we refer to these high-redshift, mid-IR color-selected sources simply as ‘IRAC-selected sources’.

2.4.2 Comparison to Blank Fields

We use the SpUDS survey to derive a mean blank field density of IRAC-selected sources. The catalogs have been cut at the CARLA depth, i.e. all sources fainter than the CARLA

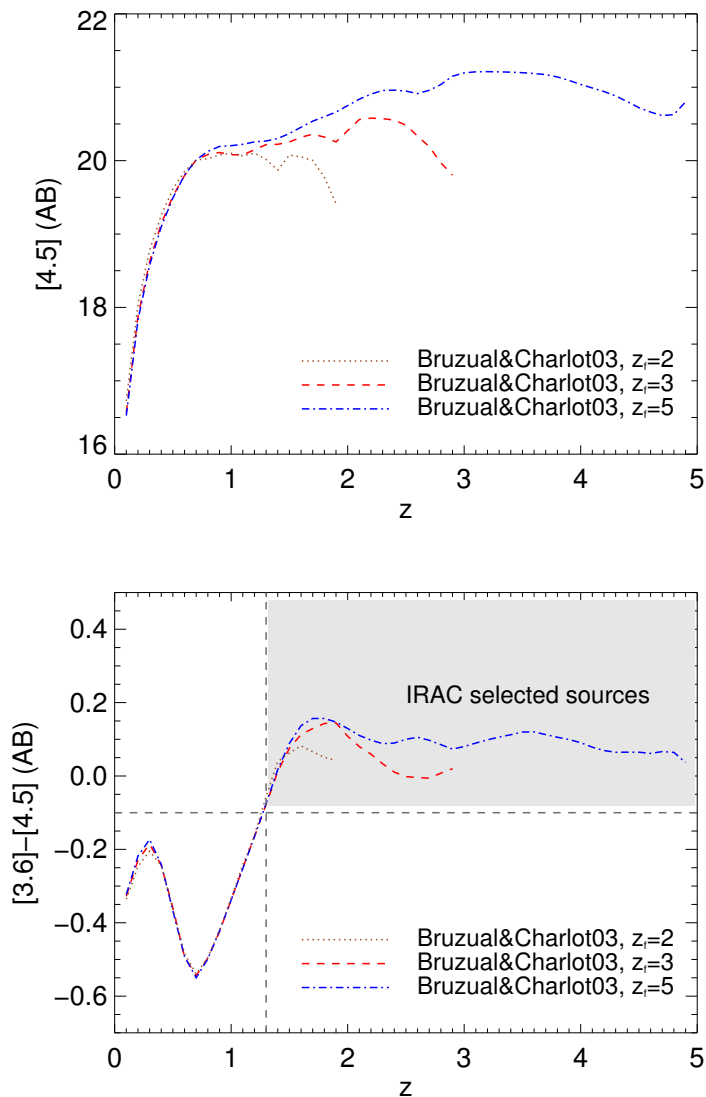


Figure 2.3: Illustration of the IRAC color criterion. *Top panel:* Predicted evolution of IRAC2 magnitude as a function of redshift. We plot the Bruzual & Charlot (2003) models for different formation redshifts z_f assuming a Salpeter initial mass function and a single exponentially decaying burst of star formation with $\tau = 0.1$ Gyr, normalized to the observed m^* for galaxy clusters at $z = 0.7$, $[4.5] = 16.75$ (Vega; Mancone et al., 2010). The models were generated with the model calculator EzGal (Mancone & Gonzalez, 2012). A negative k -correction leads to an almost flat evolution of the IRAC2 magnitude at $z \geq 0.7$. *Bottom panel:* The shift of the $1.6 \mu\text{m}$ bump across the IRAC bands leads to a red IRAC color for galaxies at $z > 1.3$.

95% completeness limit are neglected. We then placed 436 non-overlapping circular cells of $1'$ radius onto the field and measured the density of IRAC-selected sources in these cells. None of the CARLA targets lie in the SpUDS survey.

We then measured the number of IRAC-selected sources in an aperture of $1'$ radius centered on the radio-loud AGN. At $1 < z < 3$, $1'$ corresponds to ~ 500 kpc, matching typical cluster sizes for $z > 1.3$ mid-IR selected clusters with $\log(M_{200}/M_{\odot}) \sim 14.2$ (e.g. Brodwin et al., 2011). The surface density of IRAC-selected sources in the CARLA fields takes into account the low coverage areas (see Section 2.3.2). Table 2.1 lists the names, positions, redshifts, radio luminosities and surface density of IRAC-selected sources in the CARLA fields sorted by right ascension. The full table is available online. The upper panel in Fig. 2.4 shows the distribution of surface densities for IRAC-selected sources in the SpUDS and CARLA fields. A perfect, structure-free blank field would show a Gaussian distribution of densities peaking at the mean blank field density. As expected, both the SpUDS and CARLA distributions are asymmetric with a high-density tail since even the $\sim 1 \text{ deg}^2$ SpUDS field contains large scale structure. For example, a high-density tail of IRAC-selected sources is also seen in the Lockman Hole field (Papovich, 2008). Following the methodology of Papovich (2008), Galametz et al. (2012) and Mayo et al. (2012), we fit a Gaussian to the low-density half of the distribution (i.e. the distribution of the lower density regions determined with respect to the maximum of the distribution) to determine the peak density $\Sigma_{\text{SpUDS}} = 8.3 \text{ arcmin}^{-2}$ and the standard deviation of the low-density half, $\sigma_{\text{SpUDS}} = 1.6 \text{ arcmin}^{-2}$. We find that 92.0% of the CARLA fields are denser than the SpUDS peak density, 55.3% are $\geq 2 \sigma$ overdense and 37.0% are $\geq 3 \sigma$ overdense. At the 5σ level, 9.6% of the CARLA fields are still overdense. The corresponding values for the SpUDS field are significantly lower, with 18.7%, 8.6%, and 0.7% of the fields being denser than $\Sigma_{\text{SpUDS}} + 2\sigma_{\text{SpUDS}}$, $\Sigma_{\text{SpUDS}} + 3\sigma_{\text{SpUDS}}$, $\Sigma_{\text{SpUDS}} + 5\sigma_{\text{SpUDS}}$, respectively (see Fig. 2.4). The densest CARLA field, a HzRG at $z = 2.00$, shows a density of almost $\Sigma_{\text{SpUDS}} + 10\sigma$. A two-sided Kolmogorov-Smirnov (K-S) test gives a $< 10^{-36}$ probability that the CARLA and SpUDS surface density distributions are drawn from the same underlying distribution. In addition, a Mann-Whitney U test rules out that the two distributions have the same mean.

As the CARLA fields are distributed over the whole sky, we compute the Spearman rank correlation coefficient ρ to test the dependence of density on Galactic latitude to rule out any bias due to stellar contamination. We find $\rho = 0.01$, implying a 21% probability of a correlation. According to standard interpretations of the Spearman rank correlation test, this is considered as evidence for the lack of a correlation.

Galametz et al. (2012) also used a counts-in-cell analysis to identify overdensities of IRAC-selected sources among 72 HzRGs in a redshift range of $1.2 < z < 3$, albeit with observations two magnitudes shallower than CARLA. They found that $73 \pm 12\%$ of the fields were denser than the mean blank-field density, derived from the SWIRE survey. They

also found that $23 \pm 7\%$ of the fields were $\geq 2\sigma$ overdense. We cut the CARLA survey at the depth of the Galametz et al. (2012) study to check for consistency with this previous work. The SpUDS mean blank-field density, derived from a Gaussian fit to the low density half of the distribution, gives 2.1 ± 0.7 IRAC-selected sources per arcmin², in good agreement with the blank field mean density derived by Galametz et al. (2012), $\Sigma_{\text{SWIRE}} = 2.8 \pm 1.0$ arcmin⁻². Most of the CARLA fields are denser than the blank field, with $79 \pm 9\%$ denser than the SWIRE surface density, consistent with Galametz et al. (2012). At the high end of the density distribution we find more fields, with $51 \pm 7\%$ being $\geq 2\sigma$ overdense. This may, however, be due to small number statistics in Galametz et al. (2012)

In Fig. 2.4 we show the position of a known cluster, CIG 0218.3-0510 at $z = 1.62$ (Papovich et al., 2010), in the density distribution. This cluster lies in the SpUDS survey and is centered on one of our random apertures placed onto the survey. The aperture covering this cluster is the densest one in the SpUDS survey. In Galametz et al. (2012), the IRAC color criterion has been successfully tested by recovering known high-redshift (proto-) clusters such as PKS1138-262 ($z = 2.16$, the Spiderweb galaxy). In addition, we recently confirmed a cluster in the field of MRC0156-252, a radio galaxy at $z = 2.02$, which is 2σ overdense in the CARLA data (Galametz et al., 2013).

These results confirm that the color criterion is very effective at identifying high-redshift clusters and that the densities found in this work are sufficient to qualify many of the fields as promising (proto-)cluster candidates. To demonstrate the quality of our data, Fig. 2.5 shows the IRAC2 images of two CARLA sources, the quasar J105231.82+08060 ($z = 1.64$; 6.8σ overdense) and the radio galaxy MRC1217-276 ($z = 1.90$; 5.3σ overdense). IRAC-selected sources within 1 arcmin of the radio-loud AGN are indicated, illustrating the diversity of environments. While the former shows a central concentration of IRAC-selected sources close to the radio-loud AGN, the latter shows a more diffuse overdensity, perhaps suggestive of an earlier stage in the cluster formation.

2.4.3 Radial Distribution of IRAC-Selected Sources

We investigate how the surface density of the IRAC-selected sources depends on the distance to the radio-loud AGN. In Fig. 2.6 we show a stack of the surface density of IRAC-selected sources in annuli around the radio-loud AGN for both the CARLA and the SpUDS survey. As expected, the radial distribution of IRAC-selected sources in the SpUDS survey is homogenous and is equivalent to a median blank field surface density. It should be noted that this median is dependent on large-scale structure and existing clusters in SpUDS and is therefore slightly higher than the typical blank field density derived from the Gaussian fitting to the lower part of the density distribution (see Fig. 2.4). For the dense CARLA fields, the surface density peaks towards the position of the radio-loud AGN in the center

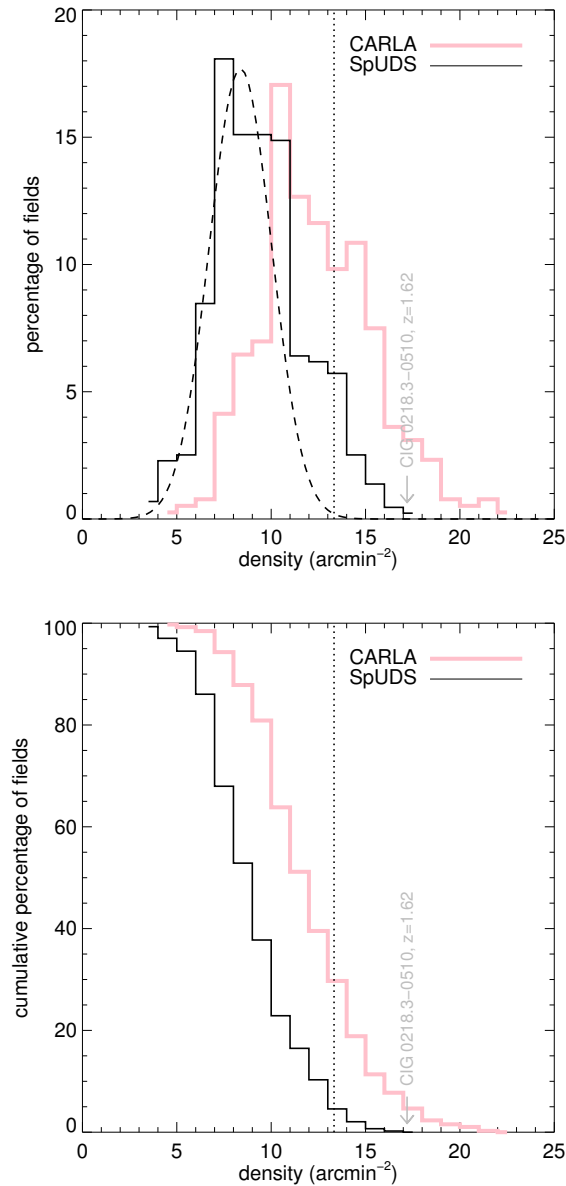


Figure 2.4: *Upper panel:* Histogram of the densities of IRAC-selected sources in the CARLA fields and the SpUDS survey. The Gaussian fit to the low-density half of the SpUDS density distribution is shown by the dashed black curve, giving $\Sigma_{\text{SpUDS}} = 8.3 \pm 1.6 \text{ arcmin}^{-2}$. The vertical dotted line corresponds to $\Sigma_{\text{SpUDS}} + 3\sigma$ density. We find that 37.0% of the CARLA fields are overdense compared to this surface density while only 8.6% of the SpUDS fields have surface densities of IRAC-selected sources above that value. *Lower panel:* Cumulative density distribution of the CARLA and SpUDS fields. Only 18.7% of the SpUDS fields are denser than $\Sigma_{\text{SpUDS}} + 2\sigma_{\text{SpUDS}}$ in contrast to 55.3% for the CARLA fields. Only 0.7% of the SpUDS fields are denser than $\Sigma_{\text{SpUDS}} + 5\sigma_{\text{SpUDS}}$ while 9.6% of the CARLA fields are denser than this cut.

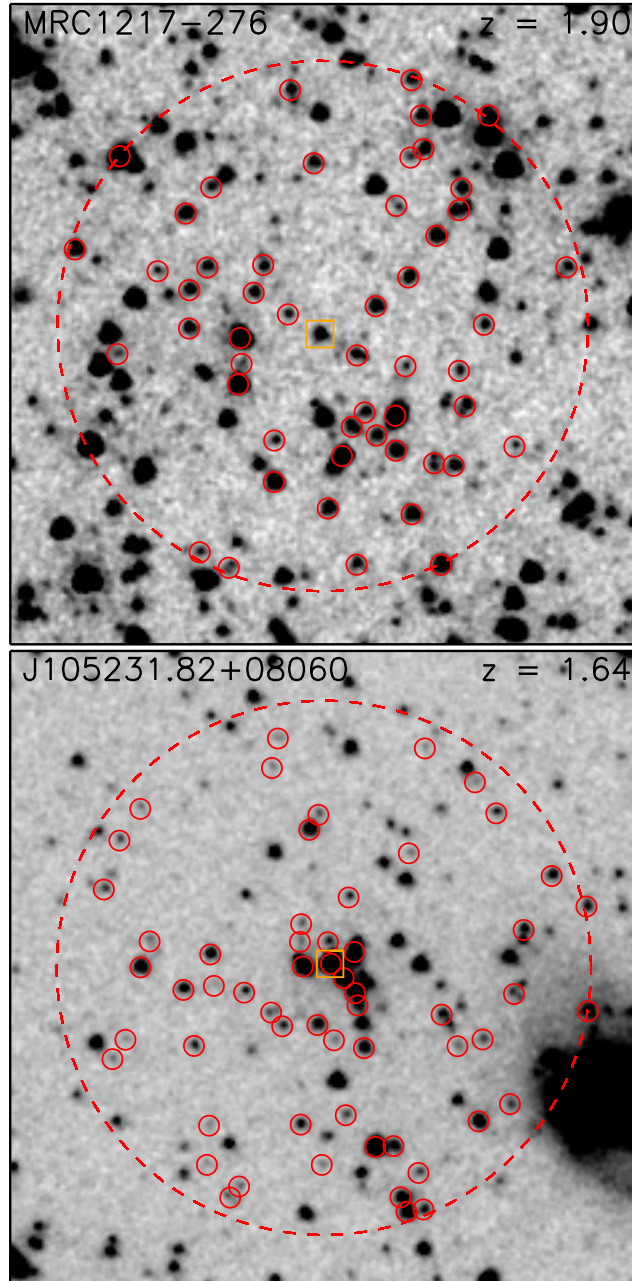


Figure 2.5: Postage stamps of the fields of MRC1217-276 and J105231.82+08060, a radio galaxy and a radio-loud quasar at $z = 1.90$ and $z = 1.64$, respectively. The IRAC color-selected sources within a 1 arcmin radius, shown with the large dashed circle, are marked with small solid red circles. The radio-loud AGN are marked by the orange squares.

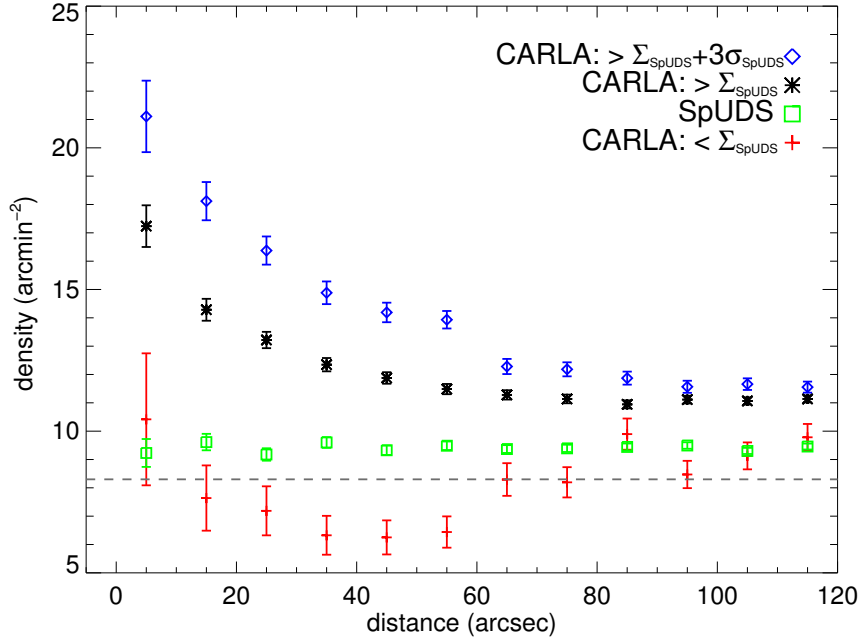


Figure 2.6: Surface density of the IRAC-selected sources as a function of distance to the radio-loud AGN for the CARLA survey. We show a stack of all CARLA fields that are denser and less dense than Σ_{SpUDS} (black asterisks and red crosses, respectively) and a stack of fields denser than $\Sigma_{\text{SpUDS}} + 3\sigma_{\text{SpUDS}}$ (blue diamonds). The radial distribution depends on the overall density of the CARLA fields with a sharp rise towards the center for the densest CARLA fields and an almost homogenous distribution for the lowest density fields. The grey dashed line corresponds to the SpUDS peak density and is slightly lower than the SpUDS radial distribution which is computed from a stack of all SpUDS fields, including both the low- and the high-density fields.

of the image. This rise is even more prominent for the CARLA fields overdense at the 3σ ($\Sigma = \Sigma_{\text{SpUDS}} + 3\sigma_{\text{SpUDS}}$) level than for the CARLA fields that are simply denser than the peak SpUDS density. This means that, on average, the denser a field the more IRAC-selected sources are found very close to the radio-loud AGN. This result clearly shows that for the dense CARLA fields, the radio-loud AGN is a good beacon for the center of the overdensity of IRAC-selected sources.

We also test that this behavior is not simply due to the CARLA sample centering apertures on known massive, high-redshift galaxies while the SpUDS comparison sample targeted random positions in that field. We identify a subsample of SpUDS sources with similar mid-infrared colors and magnitude distributions to the HzRGs in CARLA; the CARLA RLQs are too dominated by their AGN in the mid-infrared to use for this comparison analysis. We find that the density of IRAC-selected sources for this matched sample does not show

a prominent peak towards the center, and is consistent with the SpUDS blank field density at all radii, thus further supporting our primary result that powerful radio-loud AGN are efficient beacons for high-redshift structure.

Finally, we also investigate the radial density distribution for all CARLA fields that are less dense than the SpUDS peak density to rule out systematics in our analysis. The rise towards the center fully disappears and is consistent with the SpUDS peak density shown by the grey dashed line. It is important to note that even at largest radii probed, the CARLA fields show an excess of IRAC-selected sources suggesting that the extent of the overdensity is larger than the area covered in our images. Venemans et al. (2007) measures the size of (proto-)clusters by analyzing the radial extent of Ly α emitters in the fields of radio galaxies at $z \sim 3$. This work showed that only at a ~ 1.75 Mpc (~ 3.8 arcmin) distance from the radio galaxy does the density of Ly α emitters in the field become consistent with the field density. They conclude that the sizes of (proto-)clusters as inferred from the distribution of Ly α emitters at $z \sim 3$ is roughly 2 Mpc. Due to the limited size of the CARLA fields we cannot measure the overall extent of the overdensity but we show that it extends beyond 2 arcmin (~ 1 Mpc for the redshifts probed). The clear rise towards the center at distances < 60 arcsec, however, justifies our choice of 1 arcmin apertures for the counts-in-cell analysis.

2.4.4 Dependence on AGN Type

We compare the fields around the HzRGs and the RLQs separately to investigate any difference in their environments. Fig. 2.7 shows the density distributions for the HzRGs and the RLQs in our sample. We proceed in the same way as earlier and fit a Gaussian to the low density part of the histograms to find the mean and the standard deviation of the distributions. The best fit is found for a mean surface density of IRAC-selected sources of 11.6 ± 2.2 arcmin $^{-2}$ for the HzRGs and 10.8 ± 1.7 arcmin $^{-2}$ for the RLQs. The fitted means agree within the uncertainties. A two-sided K-S test shows the two distributions to be statistically similar, with only a 38% chance of the two distributions being different. The Mann-Whitney U test only gives a 23% chance of the two means of the distributions being different. We repeat the analysis for various redshift bins to test if this result is only true for specific redshifts, finding similar results for all tested redshift bins. We discuss the implications of environment not correlating with AGN obscuration in Section 2.5.

2.4.5 Dependence on Redshift

Figure 2.8 shows the environments of radio-loud AGN as a function of redshift. Spearman rank correlation coefficients suggest a dependence on redshift with a probability of 99.99%. This correlation is mainly driven by fewer data points at $z < 2.0$ and $\Sigma < 10$ arcmin $^{-2}$ and at $z > 2.5$ and $\Sigma > 12$ arcmin $^{-2}$. We therefore also test for a correlation in these two redshift

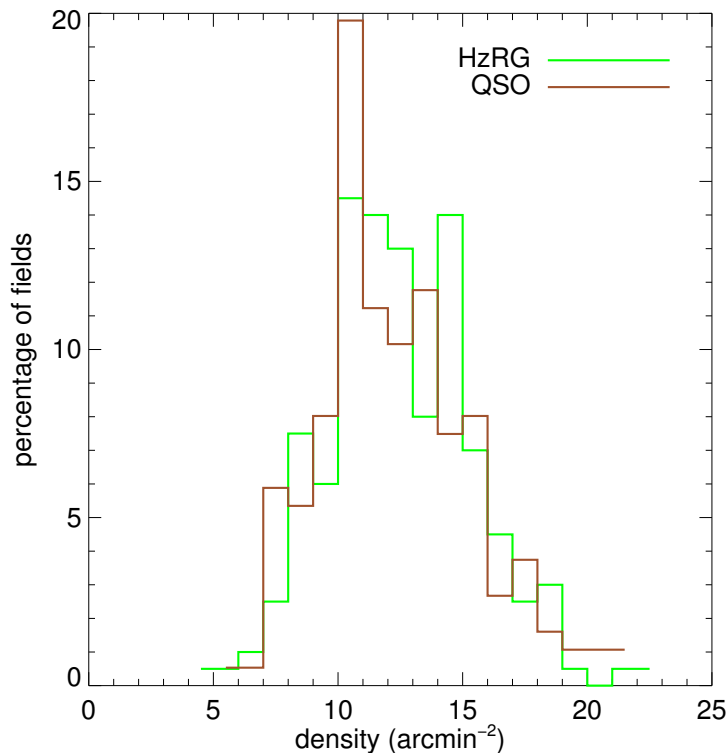


Figure 2.7: Distribution of the densities of IRAC-selected sources for the HzRG and RLQ fields in the CARLA sample. A two sided K-S test shows no significant difference between the two distributions, implying that the environments of the two AGN types are similar.

bins ($1.3 < z < 2.5$ and $2.5 < z < 3.2$); the Spearman rank correlation coefficients suggest a correlation with a probability of 99% and 82%, respectively and confirm that the dependence of density with redshift is true for all redshifts probed here. The density of the environments around the RLQs seems to be more dependent on redshift than those of the HzRGs with probabilities of 99.0% and 83.0% of a correlation, respectively. However, this could be due to slightly different sampling at intermediate redshifts. If galaxy (proto-)clusters have the same number of members at all redshifts, a dependence with redshift would be expected as we observe galaxies that are about 3 magnitudes fainter than L^* at $z \sim 1.3$ but only galaxies that are ~ 2 magnitudes fainter than L^* at $z \sim 3.2$. Wylezalek et al. (2014) uses the CARLA sample to quantitatively examine the redshift evolution of the cluster luminosity function. The fact that we observe a dependence with redshift demonstrates that a non-negligible fraction of the IRAC-selected objects in the vicinity of the radio-loud AGN are associated with the AGN. If the IRAC-selected sources were not associated with the radio-loud AGN then their density would likely be independent of the AGN redshifts.

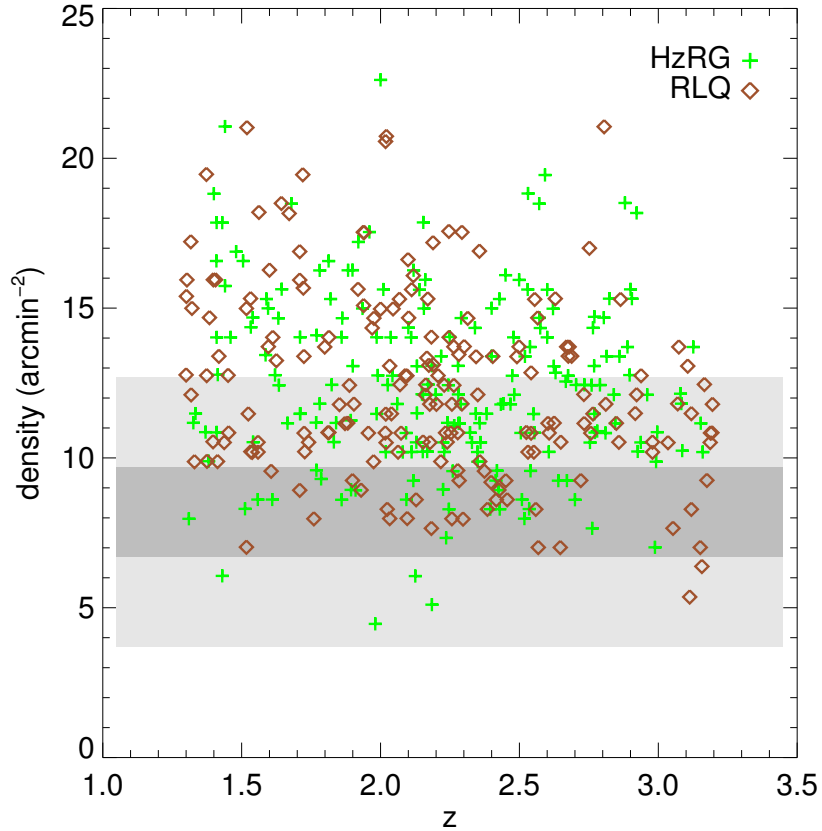


Figure 2.8: Surface density of IRAC-selected sources in the HzRG (green crosses) and RLQ (orange diamonds) fields as a function of redshift. The dark and light grey shaded areas show $\Sigma_{\text{SpUDS}} \pm 1\sigma$ and $\Sigma_{\text{SpUDS}} \pm 3\sigma$ density, respectively. A Spearman rank correlation analysis shows a dependence of surface density with redshift.

2.4.6 Dependence on Radio Luminosity

Figure 2.9 shows how the density of the CARLA fields depends on the radio luminosity of the targeted radio-loud AGN. Spearman rank correlation coefficients do not show a significant dependence of the CARLA field densities on $L_{500\text{MHz}}$. This is in agreement with previous studies at these high radio luminosities (Donoso et al., 2010) and is consistent with expectations from the unified model for AGN (Urry & Padovani, 1995). We discuss this result in the context of other studies at lower redshifts in Section 2.5.

We also test the difference of the density distributions between the HzRG and RLQ fields as a function of radio luminosity. We fit a Gaussian to the density distribution in four radio luminosity bins ($10^{27} - 10^{28} \text{ W Hz}^{-1}$, $10^{28} - 10^{28.25} \text{ W Hz}^{-1}$, $10^{28.25} - 10^{28.5} \text{ W Hz}^{-1}$, $10^{28.5} - 10^{29} \text{ W Hz}^{-1}$, chosen to provide similarly sized samples) to determine the mean

Table 2.2: Comparison to previous work on type-1 and type-2 AGN environments.

Reference	Sample Size	z	$L_{500\text{MHz}, \text{min}}$ (W Hz^{-1})	type-1 vs. type-2 environment
Yates et al. (1989)	25 RGs	$0.15 < z < 0.82$	$1 \cdot 10^{25}$	No difference
Smith & Heckman (1990)	35 RGs, 31 RLQs	< 0.3	$5 \cdot 10^{24}$	No difference
Falder et al. (2010)	75 RLQs, 27 RGs	$z \sim 1$	$2 \cdot 10^{24}$	Slightly denser type-2 environments
Donoso et al. (2010)	307 RLQ, ~ 1400 RGs	$0.4 < z < 0.8$	$2 \cdot 10^{25}$	type-2 more clustered for $10^{25} < L_{500\text{MHz}} < 10^{26}$, similar clustering for $L_{500\text{MHz}} > 10^{26}$
This work	166 RGs, 180 RLQs	$1.3 < z < 3.2$	$3 \cdot 10^{27}$	No difference

and sigma of the histograms. Two-sided K-S tests do not show a significant probability for the distributions to be different. Spearman rank correlation coefficients do not imply a dependence of the density on radio luminosity for either of the two types of AGN.

2.5 The environments of HzRGs and RLQs

It has long been debated whether the environments of radio-quiet AGN are any different from their radio-loud analogs. Many studies show that radio-quiet AGN, which are usually associated with less massive spiral galaxies, are less clustered than radio-loud AGN (e.g., Hutchings et al., 1999; Kauffmann et al., 2008; Hickox et al., 2009; Falder et al., 2010). Several theories have been proposed to explain this difference between the environments of radio-loud and radio-quiet AGN. One theory, known as jet confinement, posits that the higher IGM densities in regions of higher galaxy densities enhance synchrotron losses from radio jets, thereby making them brighter (Barthel & Arnaud, 1996). An alternative theory suggests that mergers in regions of higher galaxy density will produce more rapidly spinning supermassive black holes, which will then be more capable of powering a radio jet (e.g., Wilson & Colbert, 1995; Sikora et al., 2007). Regardless, observational results suggest that radio-quiet AGN reside in less dense environments while the difference between RLQ and RG environments still remains an open issue and observations show inconclusive results.

From a study of ~ 30 radio-selected AGN at $z < 0.3$, Smith & Heckman (1990) finds that RLQs and RGs at $z < 0.3$ were similarly clustered, consistent with the results of Yates et al. (1989) based on a comparably sized sample at similar redshift (see Tab. 2.2). Falder et al. (2010) studies the environments of 75 RLQs and 27 RGs at $z \sim 1$, and finds a small, but notable trend of density with AGN type, with the RG environments being slightly denser than the RLQ environments. He suggests, however, that this might be due to the different sample sizes. Donoso et al. (2010) computes the cross-correlation signal between a sample

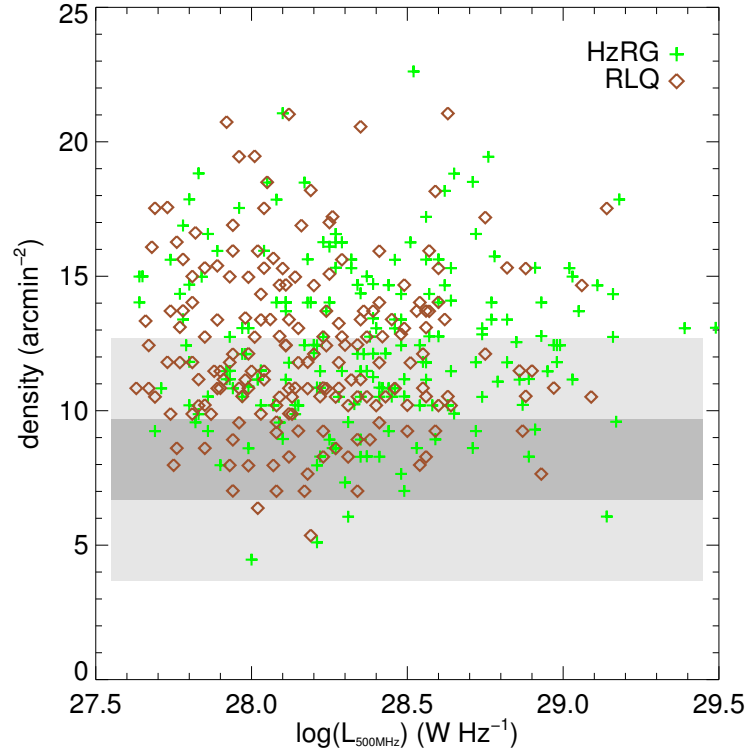


Figure 2.9: Surface density of IRAC-selected sources in the HzRG and RLQ fields as a function of radio luminosity. The dark and light grey shaded areas show $\Sigma_{\text{SpUDS}} \pm 1\sigma$ and $\Sigma_{\text{SpUDS}} \pm 3\sigma$ density, respectively. A Spearman rank correlation analysis shows no significant dependence of surface density with radio luminosity.

of $\sim 14,000$ radio-detected AGN and a sample of 1.2 million luminous red galaxies in the SDSS. They also study a sample of ~ 300 RLQs cross-correlated with the same sample of luminous red galaxies. When comparing the two clustering signals, Donoso et al. (2010) finds the RGs are more clustered than the RLQs for $10^{25} < L_{1.4\text{GHz}} < 10^{26} \text{ W Hz}^{-1}$, but clustered in a similar way for $L_{1.4\text{GHz}} > 10^{26} \text{ W Hz}^{-1}$.

We caution the reader that in each study different lower limits and definitions of radio-loudness are being used. In Tab. 2.2 we summarize the results of these works and list the redshift ranges and the lower limit on radio luminosity used to define a radio-loud object. The radio luminosities have been converted to $L_{500\text{MHz}}$ assuming a radio spectral index of $\alpha = -0.7$ (Miley & De Breuck, 2008). At lower radio luminosity, $L_{500\text{MHz}} < 10^{25} \text{ W Hz}^{-1}$, the studies show somewhat conflicting results. A concerning problem is the small sample sizes providing poor statistics and with imperfectly matched samples. In Falder et al. (2010), for example, the RGs were slightly more radio luminous than the RLQs.

At low radio luminosities, our understanding of the environments of RLQs and RGs is

not yet clear. At higher radio luminosities, $L_{500\text{MHz}} > 10^{25} \text{ W Hz}^{-1}$, previous studies and our analysis agree that there are no significant differences between the environments of type-1 and type-2 AGN. These results are consistent with the popular orientation-driven (e.g., obscuring torus) AGN unification scenario for the most powerful type-1 and type-2 radio-loud AGN. However, at lower radio luminosities, other factors, such as AGN feeding mechanisms, appear to come into play causing less powerful radio-loud type-1 and type-2 AGN to, on average, reside in different environments.

2.6 Summary

We have studied the environments of 387 radio-loud quasars and radio galaxies at $1.3 < z < 3.2$ that have been observed at $3.6\mu\text{m}$ and $4.5\mu\text{m}$ with the *Spitzer Space Telescope*. Our study clearly confirms that radio-loud AGN reside in rich environments. By applying a color cut, we identified likely high-redshift galaxies, which we refer to as 'IRAC-selected sources', and computed their surface density in a $1'$ radius around the radio-loud AGN. More than half of the fields, 55.3%, are overdense at the 2σ level when compared to the blank field density of IRAC-selected sources derived from the SpUDS survey. If we instead consider a 5σ overdensity, 9.6% of the fields are overdense. We detect a significant rise in surface density of IRAC-selected sources towards the position of the radio-loud AGN in contrast to a homogeneous radial surface density distribution for the SpUDS apertures. This reassures us of an association of the majority of the IRAC-selected sources with the radio-loud AGN. These CARLA results provide a promising list of high-redshift galaxy (proto-)cluster candidates for further study.

We also study the dependence of environment on radio luminosity. No statistically significant correlation is observed. We do, however, find a significant dependence on redshift, with higher redshift fields being slightly less dense. This result is consistent with galaxy cluster evolution and reassures us that most of the IRAC-selected sources are indeed associated with the targeted radio-loud AGN as otherwise we would have been unlikely to have observed a redshift dependence. In Wylezalek et al. (in prep.) we discuss how this trend can be explained in the context of the evolution of the luminosity/mass function of galaxy clusters.

We do not find a significant difference between the RLQ and HzRG fields, neither in their overall distribution nor in their dependence with redshift or radio luminosity. We conclude that for high radio luminosities, $L_{500\text{MHz}} > 10^{27.5} \text{ W Hz}^{-1}$, orientation-driven unification models appear valid.

Acknowledgments: We gratefully acknowledge James Falder and Conor Mancone who were involved in the initial CARLA proposals. NS is the recipient of an ARC Future Fel-

lowship. This work is based on observations made with the *Spitzer Space Telescope*, which is operated by the Jet Propulsion Laboratory, California Institute of Technology under a contract with NASA.

The Galaxy Cluster Mid-Infrared Luminosity Function at $1.3 < z < 3.2$

Dominika Wylezalek, Joël Vernet, Carlos De Breuck, Daniel Stern, Mark Brodwin, Audrey Galametz, Anthony H. Gonzalez, Matt Jarvis, Nina Hatch,
Nick Seymour, Spencer A. Stanford

The Astrophysical Journal, Volume 786, Issue 1, article id. 17, 15 pp. (2014)

Abstract We present $4.5 \mu\text{m}$ luminosity functions for galaxies identified in 178 candidate galaxy clusters at $1.3 < z < 3.2$. The clusters were identified as *Spitzer*/IRAC color-selected overdensities in the Clusters Around Radio-Loud AGN (CARLA) project, which imaged 420 powerful radio-loud AGN at $z > 1.3$. The luminosity functions are derived for different redshift and richness bins, and the IRAC imaging reaches depths of $m^* + 2$, allowing us to measure the faint end slopes of the luminosity functions. We find that $\alpha = -1$ describes the luminosity function very well in all redshifts bins and does not evolve significantly. This provides evidence that the rate at which the low mass galaxy population grows through star formation, gets quenched and is replenished by in-falling field galaxies does not have a major net effect on the shape of the luminosity function. Our measurements for m^* are consistent with passive evolution models and high formation redshifts ($z_f \sim 3$). We find a slight trend towards fainter m^* for the richest clusters, implying that the most massive clusters in our sample could contain older stellar populations, yet another example of cosmic downsizing. Modelling shows that a contribution of a star-forming population of up to 40 % cannot be ruled out. This value, found from our targeted survey, is significantly lower than the values found for slightly lower redshift, $z \sim 1$, clusters found in wide-field surveys. The results are consistent with cosmic downsizing, as the clusters studied here were all found in the vicinity of radio-loud AGNs – which have proven to be preferentially located in massive dark matter halos in the richest environments at high redshift – they may therefore be older and more

evolved systems than the general protocluster population.

3.1 Introduction

Many attempts have been made to measure the formation epoch of galaxy clusters, generally finding high formation redshifts, $z_f \sim 2 - 4$. Studies focusing on galaxy colors provide insight into when stellar populations formed (e.g., Stanford et al., 1998; Holden et al., 2004; Eisenhardt et al., 2008), while the assembly of galaxies and their evolution can be measured by analysing the fundamental plane or galaxy luminosity functions (e.g., van Dokkum & Stanford, 2003; Mancone et al., 2010).

As a few examples, Eisenhardt et al. (2008) infer stellar formation redshifts of $z_f > 4$ for cluster galaxies by comparing their $I - [3.6]$ colors to passive galaxy evolution models. Studying the color and the scatter of the main sequence, Mei et al. (2006) infer a mean luminosity-weighted formation redshift of $z_f > 2.8$ for cluster ellipticals in two high-redshift clusters in the Lynx supercluster. Earlier formation epochs are inferred for galaxies closer to the cores, with early-type galaxies within 1 arcmin of the cluster centers having $z_f > 3.7$. Kurk et al. (2009), who also look at the position of the red sequence in color-magnitude diagrams and compare them to theoretical predictions, infer $z_f \sim 3$ for a protocluster at $z = 1.6$. By comparing the fundamental plane of a Lynx cluster at $z = 1.27$ to the fundamental plane of the nearby Coma cluster, van Dokkum & Stanford (2003) infer a stellar formation redshift of $z_f = 2.6$ for the distant cluster, with passive evolution thereafter.

Studying the mid-infrared (mid-IR) luminosity function at high redshifts ($1 < z < 3$) probes rest-frame near-infrared (near-IR) emission (J, H, K), which is a good proxy for stellar mass for all but the youngest starbursting galaxies (Muzzin et al., 2008; Ilbert et al., 2010). Such studies have shown that the bulk of the stellar mass in clusters is already in place by $z \sim 1.3$ (e.g., Lin et al., 2006; Muzzin et al., 2008; Mancone et al., 2010) and that α , the faint end slope of the galaxy luminosity function, does not evolve significantly with redshift (e.g., de Propris et al., 1998; Muzzin et al., 2007; Strazzullo et al., 2010; Mancone et al., 2012). It seems that processes that might lead to a substantial increase in mass such as mergers and star formation, and processes that would strip mass away from the cluster such as galaxy-galaxy interactions, or galaxy harassment, either balance each other or do not to play an important role in cluster evolution.

On the other hand, there is evidence for considerable stochastic star formation in clusters at $z > 1.3$. For a sample of 16 spectroscopically confirmed galaxy clusters at $1 < z < 1.5$ selected from the IRAC Shallow Cluster Survey (ISCS; Eisenhardt et al., 2008), Brodwin et al. (2013) show that star formation is occurring at all radii and increases towards the core of the cluster for clusters at $z > 1.4$. These clusters were identified as 3-D overdensities in the Boötes Survey (Stanford et al., 2005; Elston et al., 2006; Eisenhardt et al., 2008)

using a photometric redshift probability distribution and wavelet analysis (Brodwin et al., 2006). Brodwin et al. (2013) observe a rapid truncation of star formation between $z \sim 1.5$ and $z \sim 1$, by which time the cores of the clusters become mostly quiescent. Investigating the color and scatter of the red sequence galaxies, Snyder et al. (2012) conclude that at $z \sim 1.5$ significant star formation is occurring and that at this redshift the red sequence in the centers of clusters was rapidly growing.

In a related analysis also using the Boötes cluster sample, Mancone et al. (2010) measured the evolution of the mid-IR luminosity function for a sample of galaxy clusters spanning $0.3 < z < 2$. By measuring the luminosity function and the evolution of m^* compared to theoretical passive evolution models, Mancone et al. (2010) found $z_f \sim 2.4$ for the low redshift ($z < 1.3$) portion of their cluster sample. At higher redshift ($1.3 < z < 1.8$) a significant deviation from the passive models was measured which could most likely be explained by ongoing mass assembly at those redshifts. However, the highest redshift bins suffered from small sample sizes.

This paper aims to continue and complement these previous results and extend the luminosity function analysis to higher redshift. We study the evolution of the luminosity function of almost 200 galaxy cluster candidates at $1.3 < z < 3.2$ discovered through the Clusters Around Radio Loud AGN, or CARLA, project (Wylezalek et al., 2013a). The clusters were found in the fields of radio-loud active galactic nuclei (RLAGN), including both typical unobscured (e.g., type-1) radio-loud quasars (RLQs), and obscured (e.g., type-2) radio-loud AGN, also referred to as radio galaxies (RGs). Significant research stretching back many decades show that RLAGN belong to the most massive galaxies in the Universe (Lilly & Longair, 1984; Rocca-Volmerange et al., 2004; Seymour et al., 2007; Targett et al., 2012) and are preferentially located in rich environments up to the highest redshifts (e.g., Minkowski, 1960; Stern et al., 2003; Kurk et al., 2004; Galametz et al., 2012; Venemans et al., 2007; Hutchings et al., 2009; Hatch et al., 2011a; Matsuda et al., 2011; Mayo et al., 2012; Husband et al., 2013; Ramos Almeida et al., 2013a; Wylezalek et al., 2013a). As described in Wylezalek et al. (2013a), the selection of candidate cluster members in the vicinity of the CARLA targets is based purely on the mid-IR colors of galaxies around a luminous RLAGN with a spectroscopic redshift. The selection is thus independent of galaxy age, morphology, or the presence of a red sequence; we discuss the selection in more detail in § 3.6. This sample allows us to perform a statistical study of the mid-IR luminosity functions of a large sample of very high-redshift galaxy clusters, achieving statistics never before achieved at these early epochs.

The paper is structured as follows: §3.2 describes the observations and the cluster sample used in this work, §3.3 describes the fitting procedure and estimation of the uncertainties while the results are presented in §3.4. In §3.5 we explain the robustness tests carried out and discuss our measurements in §3.6. Section 3.7 summarises the work. Throughout the

paper we assume $H_0 = 70 \text{ km s}^{-1} \text{ Mpc}^{-1}$, $\Omega_m = 0.3$, $\Omega_\Lambda = 0.7$. All magnitudes and colors are expressed in the AB photometric system unless stated otherwise.

3.2 Data

3.2.1 Observations and Data Reduction

As part of the *Spitzer* snapshot program ‘Clusters Around Radio-loud AGN’ (CARLA), we observed the fields of 209 high-redshift radio galaxies (HzRGs) and 211 RLQs at $1.3 < z < 3.2$. A description of the sample selection, observation strategy, data reduction, source extraction, determination of completeness limits and initial scientific results are given in Wylezalek et al. (2013a).

Briefly, the fields, covering $5.2 \text{ arcmin} \times 5.2 \text{ arcmin}$ each, corresponding to a physical size of $\sim 2.5 \times 2.5 \text{ Mpc}$ for the redshift range of the targeted RLAGN, were mapped with the Infrared Array Camera (IRAC; Fazio et al., 2004) on board the *Spitzer Space Telescope* at 3.6 and 4.5 μm (referred to as IRAC1 and IRAC2). The total exposure times give similar depths for both channels with the IRAC2 observations having been tailored to be slightly deeper for our intended science. The HzRG and RLQ samples have been matched with respect to their redshift and radio-luminosity distributions. The $L_{500\text{MHz}}-z$ plane is covered relatively homogeneously in order to be able to study the environments around the AGN as a function of both redshift and radio luminosity.

The data were reduced using the MOPEX (Makovoz & Khan, 2005) package and source extraction was performed using SExtractor (Bertin & Arnouts, 1996) in dual image mode with the IRAC2 image serving as the detection image. The CARLA completeness was measured by comparing the CARLA number counts with number counts from the *Spitzer* UKIDSS Ultra Deep Survey (SpUDS, PI: J. Dunlop) survey. The SpUDS survey is a *Spitzer* Cycle 4 legacy program that observed $\sim 1 \text{ deg}^2$ in the UKIDSS UDS field with IRAC and the Multiband Imaging Spectrometer (MIPS; Rieke et al., 2004) aboard *Spitzer*. SpUDS reaches 5σ depths of $\sim 1 \mu\text{Jy}$ ($\text{mag} \approx 24$). We determine 95% completeness of CARLA at magnitudes of $[3.6] = 22.6$ ($= 3.45 \mu\text{Jy}$) and $[4.5] = 22.9$ ($= 2.55 \mu\text{Jy}$).

3.2.2 Cluster Sample

The cluster candidates studied in this paper were identified as IRAC color-selected galaxy overdensities in the fields of CARLA RLAGN. In order to isolate galaxy cluster candidates we first identify high-redshift sources ($z > 1.3$) by applying the color cut $[3.6]-[4.5] \geq -0.1$ (e.g. Papovich, 2008). This color selection has proven to be very efficient at identifying high-redshift galaxies independent of their evolutionary stage. A negative k -correction,

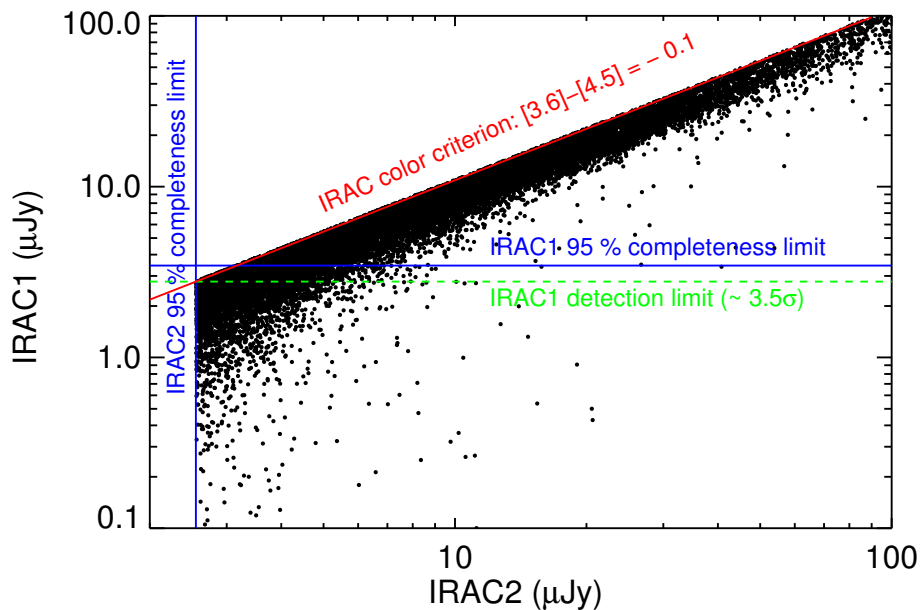


Figure 3.1: IRAC1 flux density versus IRAC2 flux density for all sources in CARLA that pass the color criterion $[3.6]-[4.5] > -0.1$ (red line). The IRAC1 and IRAC2 95% completeness limits are shown by the blue horizontal and vertical lines, respectively. The IRAC1 detection limit used in the color criterion analysis (see Section 3.2.2) is shown by the green dashed line. To build IRAC2 luminosity functions a clear IRAC1 detection is not necessary and we therefore focus on the IRAC2 luminosity function in this paper. The IRAC1 luminosity functions are presented in Appendix B.

caused by the $1.6 \mu\text{m}$ bump that enters the IRAC bands at $z \sim 1$, leads to an almost constant IRAC2 apparent magnitude at $z > 1.3$ and a red $[3.6]-[4.5]$ color (Stern et al., 2005; Eisenhardt et al., 2008; Wylezalek et al., 2013a). We apply a counts-in-cells analysis to such color-selected IRAC sources, which we simply refer to as IRAC-selected sources, to identify overdense fields.

Specifically, we define a source to be an IRAC-selected source if (i) it is detected above the IRAC2 95% completeness limit and above an IRAC1 flux of $2.8 \mu\text{Jy}$ (3.5σ detection limit) and has a color of $[3.6]-[4.5] > -0.1$ or (ii) it is detected above the IRAC2 95% completeness limit and has an IRAC1 flux $< 2.8 \mu\text{Jy}$ but has a color > -0.1 at the 3.5σ detection limit of the IRAC1 observation (e.g. Fig. 3.1). This refined criterion means that all IRAC-selected sources are 95% complete in IRAC2 down to $[4.5] = 22.9$ ($= 2.55 \mu\text{Jy}$) but are not necessarily well-detected in IRAC1.

We measure the density of IRAC-selected sources in a radius of 1 arcmin centered on the RLAGN and compare it to the mean blank-field density. A radius of 1 arcmin

corresponds to ~ 500 kpc over the targeted redshift range and matches typical sizes for $z > 1.3$ mid-IR selected clusters with $\log(M_{200}/M_{\odot}) \sim 14.2$ (e.g., Brodwin et al., 2011). The typical blank-field density of IRAC-selected sources was measured by placing roughly 500 independent apertures of 1 arcmin radius onto the SpUDS field with its catalogs having been cut at the CARLA depth. Since the publication of Wylezalek et al. (2013a), 33 new CARLA fields have been observed and we provide the full table of CARLA fields and their overdensities in the electronic journal version of this paper and in Appendix A of this thesis.

In Wylezalek et al. (2013a), we used the IRAC1 95% completeness limit of $3.45 \mu\text{Jy}$ as the IRAC1 limit in the color selection process, rather than the 3.5σ detection limit of $2.8 \mu\text{Jy}$ used above. As the IRAC1 95% completeness limit is brighter than the IRAC2 95% completeness limit, this IRAC1 limit together with the color criterion introduced an artificially brighter IRAC2 limit ($[4.5] = 22.7, 3.0 \mu\text{Jy}$). In this work we therefore raise the IRAC1 limiting magnitude to $[3.6] = 22.8 (= 2.8 \mu\text{Jy})$, i.e. we lower the flux density cut, to include all IRAC2 sources down to the formal completeness limit of $[4.5] = 22.9$. This new IRAC1 flux density cut still corresponds to a $> 3.5 \sigma$ detection. This is necessary as we are aiming to include as many faint sources as possible in the analysis. We apply this refined color criterion to the CARLA and SpUDS fields and plot the distribution of their densities in Fig. 3.2. Promising galaxy cluster fields are defined as fields that are overdense by at least 2σ ($\Sigma_{\text{CARLA}} > \Sigma_{\text{SpUDS}} + 2\sigma_{\text{SpUDS}}$, Wylezalek et al., 2013a). This criterion is met by 46% of the CARLA fields, 27% are $\geq 3 \sigma$ overdense and 11% are overdense at the 4σ level. Excluding bad fields (e.g. fields that are contaminated by nearby bright stars), this provides us with 178, 101 and 42 high-redshift galaxy cluster fields at the 2σ , 3σ and 4σ level, respectively.

Note that this selection is a measure of the overdensity signal compared to a blank field, i.e. to a distribution of cell densities centred on random positions. Since the sample is selected using specific galaxies, RLAGN, there will always be at least one source in the overdensity. As all galaxies are clustered to some extent (Coil, 2013) the exact measurement of the overdensity signal of RLAGN would be to compare it to a distribution of background cells centred on random galaxies, not random positions.

However, the average number density of IRAC-selected sources in SpUDS is very high, on average 34 sources per aperture with radius $r = 1$ arcmin. This means that if the IRAC-selected sources were extended and filled the aperture maximally, their radius would only be $r_{\text{ext}} = 10.3$ arcsec and the average distance between two sources would be $2 \times r_{\text{ext}} = 20.6$ arcsec. We repeated the blank-field analysis by measuring the densities in roughly 500 apertures centred on random SpUDS IRAC-selected sources. Due to the large aperture radius of $r = 1$ arcmin and small r_{ext} , the difference between the two background measurements is not significant ($\Sigma_{\text{SpUDS}} = 10.3 \pm 2.6 \text{ arcmin}^{-2}$ compared to $\Sigma_{\text{SpUDS}} = 9.6 \pm 2.1 \text{ arcmin}^{-2}$, see Section 3.3.2). As we will work with the blank field background for

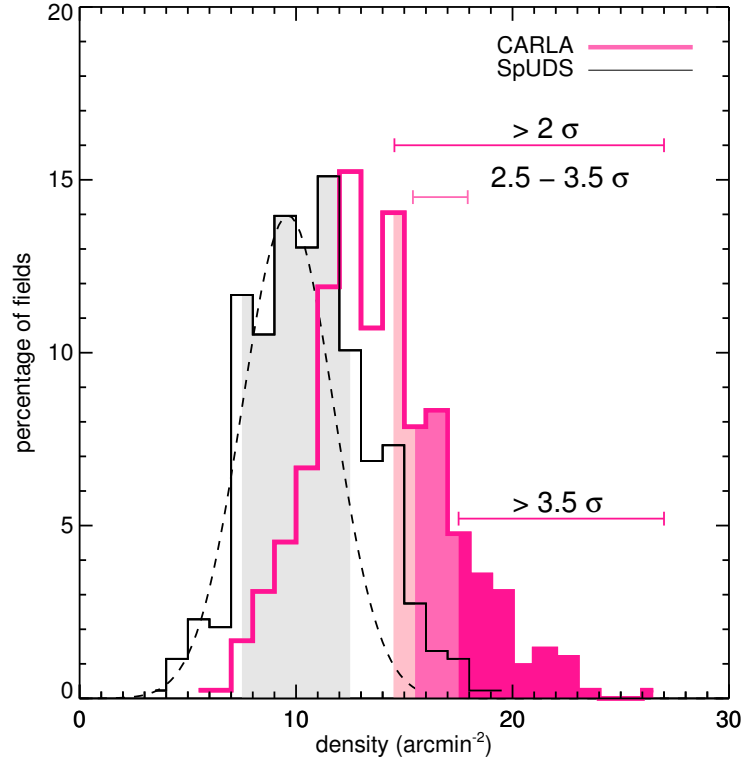


Figure 3.2: Histogram of the surface densities of IRAC-selected sources in the CARLA fields and the SpUDS survey. Surface densities are measured in circular regions of radius $r = 1$ arcmin. The Gaussian fit to the low-density half of the SpUDS density distribution is shown by the dashed black curve, giving $\Sigma_{\text{SpUDS}} = 9.6 \pm 2.1 \text{ arcmin}^{-2}$. The grey shaded area shows all SpUDS cells with a surface density of $\Sigma_{\text{SpUDS}} = 9.6 \pm 2.1 \text{ arcmin}^{-2}$, which are used to derive the blank field luminosity function. CARLA clusters are defined as fields with a surface density of $\Sigma_{\text{CARLA}} > 2\sigma$. In this paper, however, we also study the dependence of the luminosity function on the CARLA overdensity and repeat the analysis for fields with $2.5\sigma < \Sigma_{\text{CARLA}} < 3.5\sigma$ and $\Sigma_{\text{CARLA}} > 3.5\sigma$. The fields that go into those analyses are shown by the pink shaded regions, as indicated.

the LF analysis and to be consistent with Wylezalek et al. (2013a) we show the SpUDS blank field distribution in Fig. 3.2.

Wylezalek et al. (2013a) shows that the radial density distribution of the IRAC-selected sources is centered on the RLAGN, implying that the excess IRAC-selected sources are associated with the RLAGN. For the following analysis we assign the redshift of the targeted RLAGN to the IRAC-selected sources in the cell and study the evolution of these galaxy cluster member candidates as a function of redshift. To exclude problematic cluster candidates, we also checked that the median $[3.6] - [4.5]$ color of the IRAC-selected sources per

field is in agreement with the [3.6]–[4.5] color expected for a source with the redshift of the targeted RLAGN. No obvious problematic fields were found. For the rest of the manuscript we will use the term ‘galaxy clusters’ to refer to these cluster and protocluster candidates.

3.3 The Luminosity Function for Galaxy Clusters at $z > 1.3$

3.3.1 Method

Luminosity functions, $\Phi(L)$, provide a powerful tool to study the distribution of galaxies over cosmological time. They measure the comoving number density of galaxies per luminosity bin, such that

$$dN = \Phi(L)dLdV \quad (3.1)$$

where dN is the number of observed galaxies in volume dV within the luminosity range $[L, L + dL]$.

There are many ways in which $\Phi(L)$ can be estimated and parametrised, but the most common of these models is the Schechter function (Schechter, 1976)

$$\Phi(L)dL = \Phi^* \left(\frac{L}{L^*}\right)^\alpha \exp\left(-\frac{L}{L^*}\right) \frac{dL}{L^*} \quad (3.2)$$

where Φ^* is a normalisation factor defining the overall density of galaxies, usually quoted in units of $h^3\text{Mpc}^{-3}$, and L^* is the characteristic luminosity. The quantity α defines the faint-end slope of the luminosity function and is typically negative, implying large numbers of galaxies with faint luminosities. The luminosity function can be converted from absolute luminosities L to apparent magnitudes m and be written as

$$\Phi(m) = 0.4 \ln(10) \Phi^* \frac{(10^{0.4(m^*-m)})^{(\alpha+1)}}{e^{10^{0.4(m^*-m)}}} \quad (3.3)$$

where m^* is the characteristic magnitude.

In this work we study the evolution of m^* in galaxy clusters as a function of redshift for both α as a free fitting parameter and fixed $\alpha = -1$. We include all CARLA fields that are overdense at the 2σ level or more.

We measure the IRAC2 luminosity function of the galaxy clusters from the CARLA survey as a function of redshift, defined as the redshift of the AGN, and galaxy cluster richness. The CARLA galaxy cluster richness is defined in terms of the significance of the overdensity of IRAC-selected sources within the cell centered on the RLAGN (Fig. 3.2). For the largest sample of CARLA clusters, i.e. those overdense at the $> 2\sigma$ level, we measure the luminosity function in six redshift bins chosen in a way that all redshift bins contain the same number of galaxy clusters. We also consider CARLA clusters overdense

at the $2.5\text{--}3.5\sigma$ and $> 3.5\sigma$ level. For these smaller subsamples we measure the luminosity function in three redshift bins. IRAC1 luminosity functions are presented in Appendix B.

For each CARLA cluster candidate j we compute the k - and evolutionary corrections (k_j and e_j) that are required to shift the galaxy cluster members to the center of the redshift bin and apply them to the apparent magnitudes of the galaxy cluster members. The corrections were computed using the publicly available model calculator EzGal (Mancone & Gonzalez, 2012) using the predictions of passively evolving stellar populations from Bruzual & Charlot (2003) with a single exponentially decaying burst of star formation with $\tau = 0.1$ Gyr and a Salpeter initial mass function. The k_j+e_j corrections are of order 0.04 mag and do not have a significant impact on the LF analysis; they are simply applied for completeness. The typically bright targeted radio-loud AGNs have been removed from the analysis.

For each CARLA cluster candidate j we measure the number of cluster members n_{m_i} (in a cell with radius $r = 1$ arcmin centered on the RLAGN) in the i^{th} magnitude bin with $m_i = [m_i, m_i + \delta m_i]$:

$$\Phi_{i\text{CARLA},j,k_j+e_j} = n_{m_i} \quad (3.4)$$

This number density is a superposition of the cluster luminosity function and the luminosity function of background/foreground galaxies. In the following we describe the statistical background determination and how the true galaxy cluster luminosity function is determined.

3.3.2 Background Subtraction

The CARLA fields cover an area of $\sim 5.2\text{arcmin} \times 5.2\text{arcmin}$, roughly corresponding to a region with a radius of 1–1.5 Mpc for the typical redshift of the RLAGN. This radius is in good agreement with sizes of typical mid-IR selected clusters (e.g. Brodwin et al., 2011). Therefore a local background subtraction in each field is not possible. Instead, we determine a global background in a statistical way using the SpUDS survey.

As described in Section 3.2.2, we placed roughly 500 random, independent (i.e. non-overlapping) apertures with radius $r = 1$ arcmin onto the SpUDS survey to estimate the typical blank field density of IRAC-selected sources. Fitting a Gaussian to the low-density half of the SpUDS density distribution finds a mean surface density of $\Sigma_{\text{SpUDS}} = 9.6 \text{ arcmin}^{-2}$ with a width of $\sigma_{\text{SpUDS}} = 2.1 \text{ arcmin}^{-2}$. The tail at larger densities arises as even a 1 deg^2 survey has large scale structure and contains clusters. To determine the mean background, we consider cells in the SpUDS survey with surface densities of IRAC-selected sources in the range $9.6 \pm 2.1 \text{ arcmin}^{-2}$ (see Fig. 3.2).

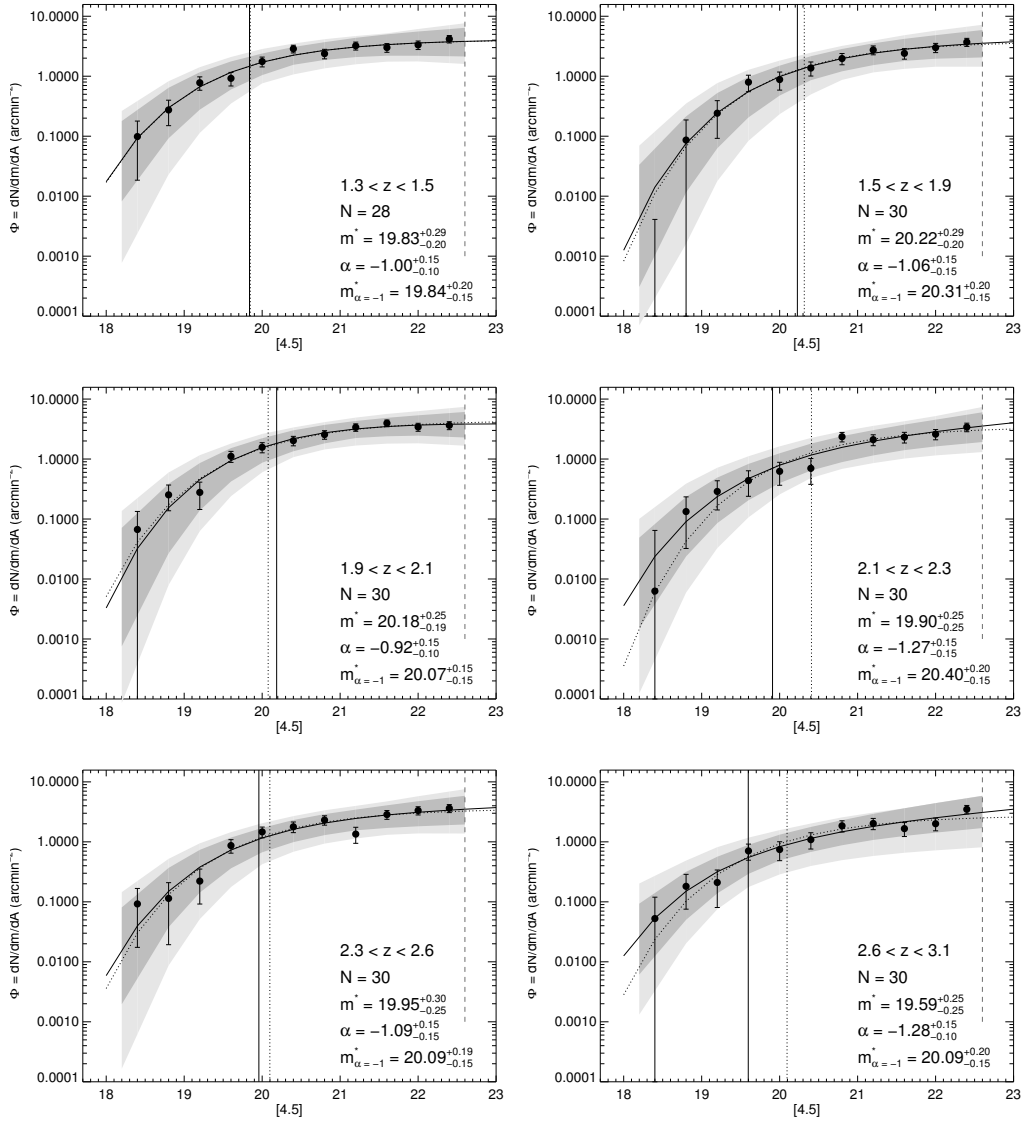


Figure 3.3: Schechter function fits to the $4.5 \mu\text{m}$ cluster luminosity function in each redshift bin for CARLA cluster members with $\Sigma_{\text{CARLA}} > 2\sigma$. The redshift bins were chosen to contain similar numbers of objects, N . The solid circles are the binned differences between the luminosity function for all IRAC-selected sources in the clusters and the background luminosity function derived from the SpUDS survey. The solid curve shows the fit to the data for a free α while the dotted curve shows the fit for $\alpha = -1$. The vertical solid and dotted lines show the fitted values for m^* for free and fixed α , respectively. The dark and light grey shaded regions show the 1σ and 2σ confidence regions for the α -free-fit derived from Markov Chain Monte Carlo simulations. The vertical dashed line shows the apparent magnitude limit. Note that due to binning of the data and the application of k - and e -corrections, that are largest for the low-redshift LFs, we here show the 99% magnitude limit.

The average background luminosity function per cell is given by

$$\Phi_{i_{\text{BG}}} = n_{m_i, \text{BG}} / N_{\text{BG}} \quad (3.5)$$

where $n_{m_i, \text{BG}}$ is the number of galaxies with magnitudes $m_i = [m_i, m_i + \delta m_i]$ in the SpUDS background cells and N_{BG} is the number of SpUDS cells used for the background determination.

We then subtract this average blank field luminosity function from the luminosity function of each CARLA cluster field j after having applied the same k_j - and e_j -correction as for the corresponding CARLA field, such that

$$\Phi_{i,j} = \Phi_{i_{\text{CARLA},j,k_j+e_j}} - \Phi_{i_{\text{BG},k_j+e_j}} \quad (3.6)$$

After this background subtraction the signal of all CARLA cluster fields per redshift bin is stacked to obtain the background-subtracted luminosity function:

$$\Phi_i = (\sum_{j=0}^N \Phi_{i,j}) \times \frac{1}{N} \times \frac{1}{A} \quad (3.7)$$

where N is the number of CARLA clusters in the redshift bin and $A = 1 \text{ arcmin}^2 \times \beta$ is the area of a cell with a radius of 1 arcmin. Figure 3.3 shows the luminosity functions for CARLA fields of richness $\geq 2\sigma$ divided into six redshift bins.

The accurate measurement of the background number counts is essential for measuring the true cluster luminosity function. Because the SpUDS survey, used in this paper, covers only $\sim 1 \text{ deg}^2$, it needs to be confirmed that it represents a typical blank field and is not significantly affected by cosmic variance. At the depth of the CARLA observations, however, it is the largest contiguous survey accessible.

The 18 deg^2 *Spitzer* Extragalactic Representative Volume Survey (SERVS, Mauduit et al., 2012) reaches almost the same depth as CARLA and allows a test of the goodness of SpUDS as a blank field. SERVS maps five well observed astronomical fields (ELAIS-N1, ELAIS-S1, Lockman Hole, *Chandra* Deep Field South and *XMM*-LSS) with IRAC1 and IRAC2. Coverage is not completely uniform across the fields but averages $\sim 1400 \text{ s}$ of exposure time. We extracted sources from the SERVS images (Mark Lacy, priv. communication) in the same way as we did for CARLA and SpUDS to allow for a consistent comparison. In Fig. 3.4 we show the IRAC2 number counts in SpUDS and SERVS observations of the *XMM*-LSS field, illustrating the difference in depths of the two surveys. Comparing the SERVS number counts with the SpUDS number counts gives an IRAC2 95 % completeness limit of $2.85 \mu\text{Jy}$ for the SERVS observations. As we aim to go as deep as possible for the CARLA analysis, the SERVS 95% completeness is slightly shallow compared to the corresponding depth of $2.55 \mu\text{Jy}$ for the CARLA observations. We therefore use the smaller area SpUDS survey for the background determinations.

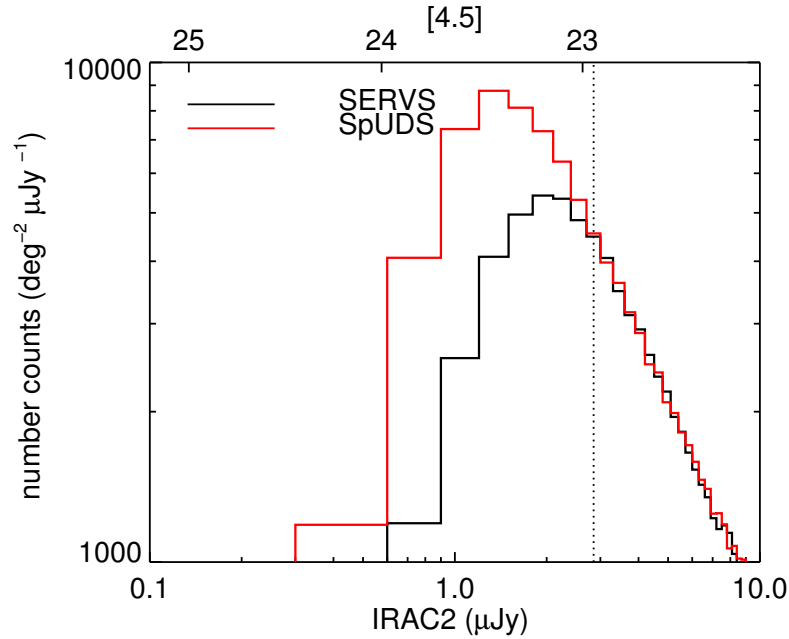


Figure 3.4: Number counts for the SpUDS and SERVS survey for sources detected at $4.5 \mu\text{m}$. The 95 % completeness limit of SERVS is derived by comparing the SERVS number counts to those from the SpUDS survey, which gives a completeness limit of $2.85 \mu\text{Jy}$ for IRAC2, as shown by the vertical dotted line.

To test the validity of our background subtraction we placed 200 random apertures onto the 18 deg^2 SERVS survey and measured the density of IRAC-selected sources in those random cells. There is a chance that a CARLA cluster field and a non-associated large scale structure are found in projection. In this case our background subtraction would underestimate the actual background in that field. By placing 200 random apertures onto the 18 deg^2 SERVS survey we can get a qualitative upper limit of this probability. Figure 3.5 shows the distribution of densities of IRAC-selected sources in those 200 random cells at the magnitude limit of the SERVS survey and compares it to the distribution in SpUDS. SpUDS only covers $\sim 1 \text{ deg}^2$ and is known to be biased to contain clusters and large scale structure. The apertures placed on SpUDS cover almost the full area and will thus pick up any large scale structure or clusters in that field. That is why a prominent high density tail arises. By placing random apertures onto a larger survey that is less biased by large-scale structure the high-density tail becomes less prominent, as expected.

To make sure, however, that we do not underestimate the background luminosity function by not taking enough of the high density tail into account, we test here what impact our choice of background has on the overall results in this work. We repeat the luminosity

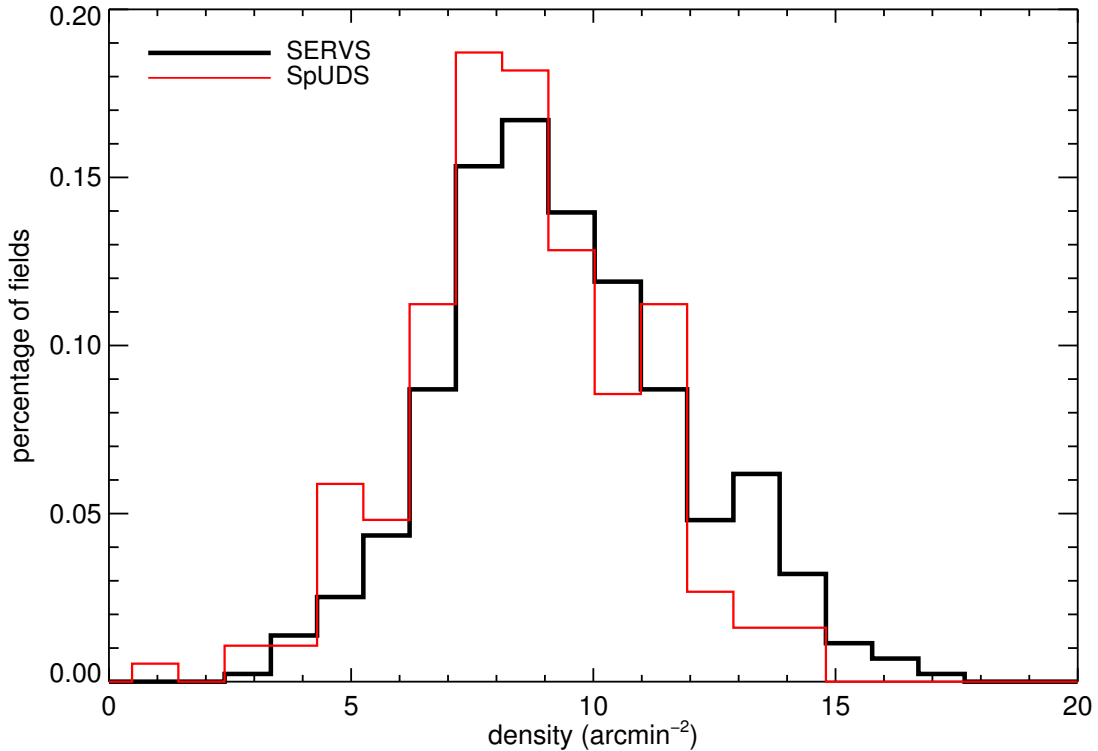


Figure 3.5: Distribution of IRAC-selected sources in the SpUDS and SERVS surveys. The apertures placed on SpUDS cover almost the full area of SpUDS and will pick up any cluster or large scale structure in that field. By placing apertures onto the much wider SERVS survey that is less biased by large-scale structure the high-density tail becomes less prominent, as expected. This motivates using SpUDS cells with $\Sigma_{\text{SpUDS}} \pm \sigma_{\text{SpUDS}}$ as a sensible measure of the blank field density of IRAC-selected sources.

function fitting analysis by choosing different density intervals to estimate the background, namely $\Sigma_{\text{SpUDS}} \pm 0.8 \times \sigma_{\text{SpUDS}}$ and $\Sigma_{\text{SpUDS}} \pm 1.6 \times \sigma_{\text{SpUDS}}$. Taking an even narrower interval than $\Sigma_{\text{SpUDS}} \pm 0.8 \times \sigma_{\text{SpUDS}}$ gives too few apertures and results in a very noisy background luminosity function. In Fig. 3.6 we show the results for the luminosity function fits with fixed α for the original background subtraction (1σ) and for the test background subtractions ($0.8 \sigma, 1.6 \sigma$). The results for the different runs agree remarkably well and no systematic effect is seen. At $\Sigma_{\text{SpUDS}} = \Sigma_{\text{SpUDS}} \pm 1.6 \times \sigma_{\text{SpUDS}}$ we are already sampling part of the high density tail. Table 3.1 shows that this has a minimal impact on the Schechter function fits. The exact choice of the density interval of the background subtraction is not critical and illustrates that choosing SpUDS cells with $\Sigma_{\text{SpUDS}} \pm \sigma_{\text{SpUDS}}$ is a sensible measure for the blank field density of IRAC-selected sources.

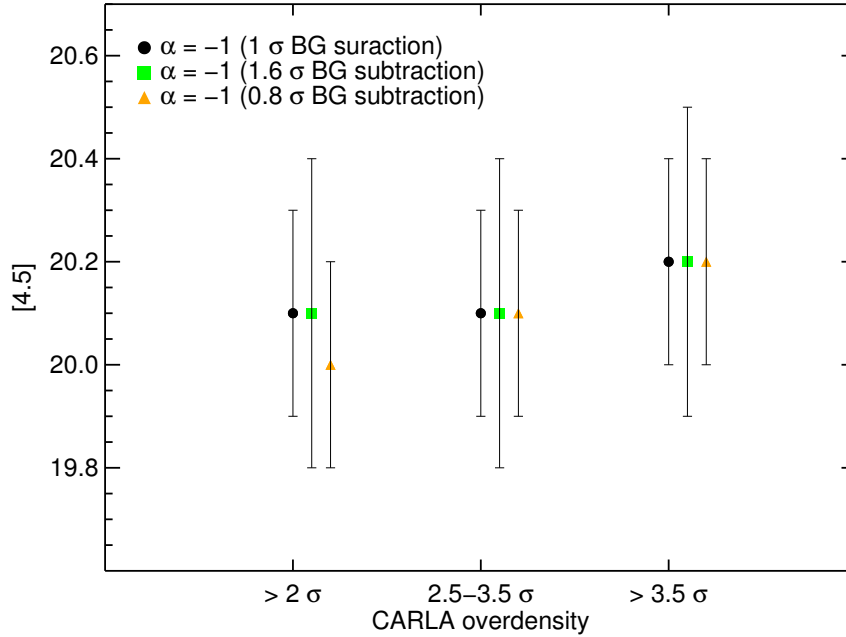


Figure 3.6: Median best-fit $m_{4.5}^*$ with $\alpha = -1$ as a function of galaxy cluster candidate richness for three different background-subtraction intervals. This demonstrates that the exact prescription of the background interval has an insignificant effect on the derived parameters. For clarity, data points for each background interval are shifted slightly along the horizontal axis.

3.3.3 Fitting Details

We make use of the Levenberg-Marquardt technique to solve the least-squares problem and to find the best solution for m^* , α and Φ^* using the parametrization given in equation 3.3. This method is known to be very robust and to converge even when poor initial parameters are given. However, it only finds local minima. In order to find the true global minimum and true best Schechter fit to our data we vary the starting parameters and choose the best fit solution. We show the Schechter fits for the for CARLA fields of richness $\geq 2\sigma$ in Fig. 3.3.

Our data are deep enough to not just fit for m^* and Φ^* and assume a fixed α as had to be done in previous studies but to fit for all three quantities, α , m^* and Φ^* simultaneously. Mancone et al. (2012) shows that $\alpha = -1$ fits well the galaxy cluster luminosity function at $1 < z < 1.5$ and that it stays relatively constant down to $z \sim 0$. We therefore also repeat the Schechter fits with fixed $\alpha = -1$ (Table 3.1).

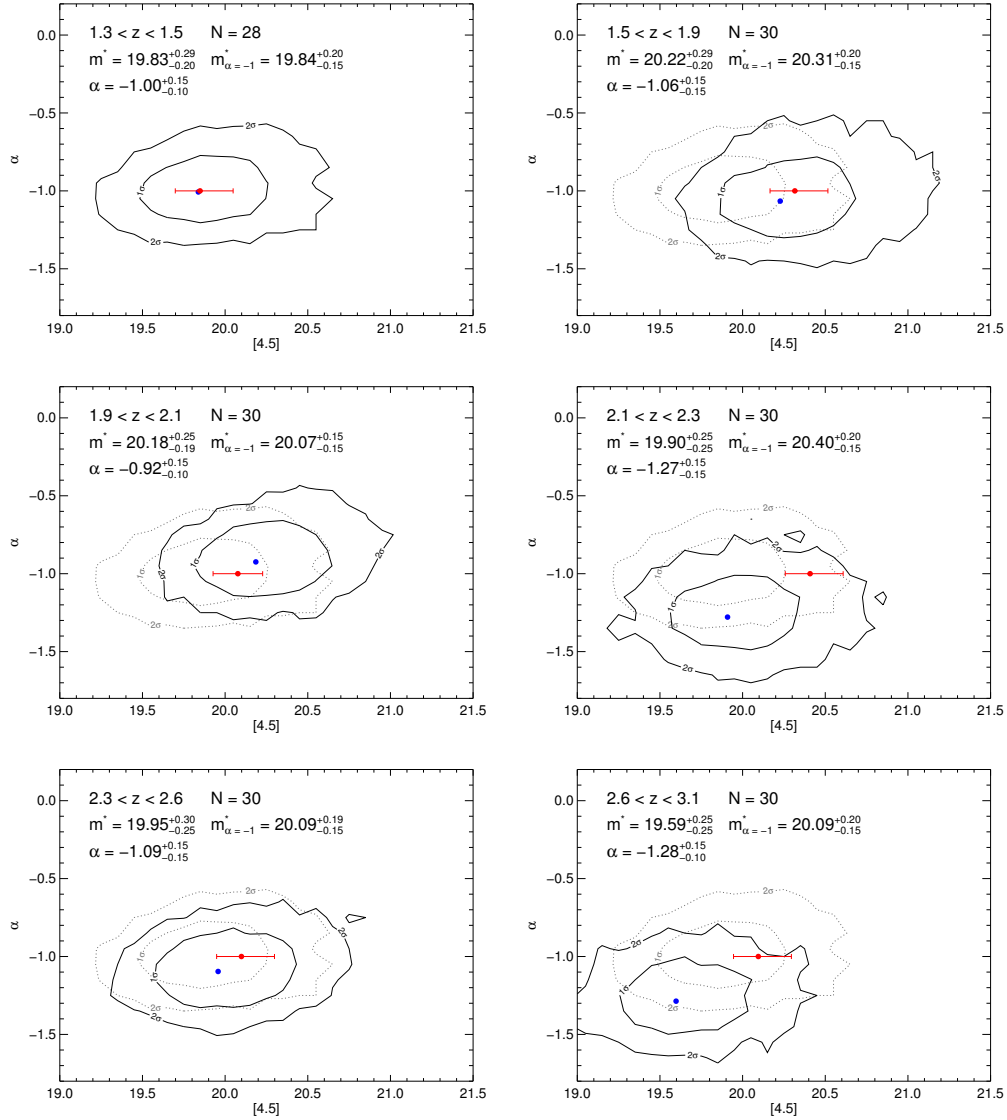


Figure 3.7: Confidence regions for α vs. m^* for Schechter fits with α as a free parameter derived from the Markov Chain Monte Carlo simulations. The contours show the 1 σ and 2 σ contour levels and the blue solid circle shows the result of the best Schechter fit using the Levenberg-Marquart technique. The redshift bins were chosen to contain similar numbers of objects, N . The red solid circle with uncertainty on m^* shows the best Schechter fit for a fixed $\alpha = -1$. In all cases the results from the fixed α fit and the free α fit agree within their confidence regions implying that $\alpha = -1$ describes the luminosity function well over the whole redshift range probed in this work. For comparison, we show the lowest redshift contours (dotted grey) in the higher redshift panels.

3.3.4 Uncertainty and Confidence Region Computation

We estimate the uncertainties of the fitted parameters and the confidence regions of our fits using a Markov Chain Monte Carlo (MCMC) simulation. Fig. 3.7 shows the 1σ and 2σ contours for α and m^* and the best Schechter fit.

We test our MCMC simulation by choosing a random set of Φ^* , α and m^* and computing Φ_i at m_i following equation (3.3). We then add normally distributed uncertainties $\Delta\Phi_i$ so that $\Phi_{i,err} = \Phi_i + \Delta\Phi_i$ and fit a Schechter function to $\Phi_{i,err}$. The original Schechter function $\Phi(\Phi^*, \alpha, m^*)$, the disturbed data points $\Phi_{i,err}$ and the Schechter fit agree very well with the 1 and 2σ confidence regions derived from the MCMC simulation and prove that the MCMC simulation provides us with a proper description of the uncertainties. Figure 3.3 shows the results of the Schechter fits to the CARLA clusters with $\Sigma_{CARLA} > 2\sigma$ for all redshift bins and the confidence regions derived from MCMC simulations.

3.4 Robustness Tests

3.4.1 Stability of the IRAC Color Criterion with Redshift

The evolution of the $[3.6]-[4.5]$ color is very steep at $1.3 < z < 1.7$; cluster members in our lowest redshift bin are expected to have bluer colors, i.e. closer to -0.1 , than cluster members at higher redshift. Faint sources which have a larger color uncertainty would therefore be expected to pass the criterion in some cases and not pass the criterion in other cases. For the contaminating background/foreground sources, this scattering is expected to be the same at all cluster redshifts. We therefore test if this effect has a statistically significant influence on the faint end of the luminosity function in the lowest redshift bin. Fig. 3.8 shows the normalised number difference between sources where $[3.6]-[4.5] > -0.1$ but $[3.6]-[4.5] - \sigma_{[3.6]-[4.5]} < -0.1$ and sources where $[3.6]-[4.5] < -0.1$ but $[3.6]-[4.5] + \sigma_{[3.6]-[4.5]} > -0.1$. In the following we refer to these sources as ‘scatter-in sources’ and ‘scatter-out sources’, respectively. As the sum of the background and foreground color distribution is not expected to be dependent on cluster redshift and will therefore be the same for all redshift bins, any evolution in the difference between ‘scatter-in’ and ‘scatter-out’ sources will be caused by the cluster members. As Fig. 3.8 shows, the evolution of the difference is consistent with being flat with redshift. The mean of the distribution is $0.06 (N_{\text{fields}})^{-1}$ and a Spearman rank correlation analysis only gives a 33% chance that there is an evolution of the difference with redshift. This test confirms that the color selection is very efficient and stable with redshift and that statistically the same portion of cluster members is selected at all redshifts.

Table 3.1: Schechter fit results for both α free and α fixed to -1 to the $4.5\mu\text{m}$ luminosity function. Below the horizontal line we also show Schechter fit results for the same analysis but taking SpUDS cells $\Sigma_{\text{SpUDS}} = \Sigma_{\text{SpUDS}} \pm 1.6 \times \sigma_{\text{SpUDS}}$ to estimate the background.

Σ_{CARLA}	$\langle z \rangle$	$m_{4.5\mu\text{m}}^*$	α	$m_{4.5\mu\text{m}, \alpha=-1}^*$	N
$> 2 \sigma$	1.45	$19.84^{+0.30}_{-0.20}$	$-1.01^{+0.10}_{-0.10}$	$19.85^{+0.15}_{-0.15}$	28
$> 2 \sigma$	1.77	$20.23^{+0.30}_{-0.20}$	$-1.07^{+0.15}_{-0.15}$	$20.32^{+0.20}_{-0.15}$	30
$> 2 \sigma$	2.05	$20.19^{+0.30}_{-0.20}$	$-0.92^{+0.15}_{-0.15}$	$20.08^{+0.20}_{-0.15}$	30
$> 2 \sigma$	2.26	$19.91^{+0.25}_{-0.25}$	$-1.28^{+0.15}_{-0.15}$	$20.41^{+0.20}_{-0.15}$	30
$> 2 \sigma$	2.51	$19.96^{+0.35}_{-0.20}$	$-1.10^{+0.15}_{-0.15}$	$20.10^{+0.20}_{-0.15}$	30
$> 2 \sigma$	2.92	$19.60^{+0.30}_{-0.20}$	$-1.29^{+0.10}_{-0.15}$	$20.10^{+0.20}_{-0.15}$	30
$2.5 < \sigma < 3.5$	1.65	$20.38^{+0.20}_{-0.20}$	$-0.75^{+0.20}_{-0.10}$	$20.10^{+0.15}_{-0.15}$	25
$2.5 < \sigma < 3.5$	2.23	$19.99^{+0.20}_{-0.20}$	$-1.13^{+0.20}_{-0.15}$	$20.21^{+0.15}_{-0.15}$	27
$2.5 < \sigma < 3.5$	2.81	$19.74^{+0.20}_{-0.20}$	$-1.17^{+0.15}_{-0.15}$	$19.99^{+0.15}_{-0.15}$	27
$> 3.5 \sigma$	1.49	$19.88^{+0.20}_{-0.25}$	$-0.89^{+0.10}_{-0.10}$	$19.72^{+0.15}_{-0.15}$	18
$> 3.5 \sigma$	1.88	$20.18^{+0.30}_{-0.20}$	$-1.01^{+0.20}_{-0.15}$	$20.20^{+0.25}_{-0.15}$	19
$> 3.5 \sigma$	2.49	$20.23^{+0.30}_{-0.20}$	$-0.95^{+0.20}_{-0.15}$	$20.16^{+0.20}_{-0.15}$	20
$> 2 \sigma$	1.45	$19.81^{+0.30}_{-0.20}$	$-1.02^{+0.10}_{-0.15}$	$19.84^{+0.20}_{-0.15}$	28
$> 2 \sigma$	1.77	$20.25^{+0.30}_{-0.20}$	$-1.07^{+0.15}_{-0.15}$	$20.34^{+0.15}_{-0.15}$	30
$> 2 \sigma$	2.05	$20.16^{+0.30}_{-0.20}$	$-0.93^{+0.15}_{-0.15}$	$20.07^{+0.20}_{-0.15}$	30
$> 2 \sigma$	2.26	$19.86^{+0.25}_{-0.25}$	$-1.32^{+0.15}_{-0.10}$	$20.44^{+0.20}_{-0.15}$	30
$> 2 \sigma$	2.51	$19.91^{+0.20}_{-0.30}$	$-1.12^{+0.10}_{-0.15}$	$20.09^{+0.20}_{-0.15}$	30
$> 2 \sigma$	2.92	$19.49^{+0.30}_{-0.25}$	$-1.33^{+0.15}_{-0.10}$	$20.09^{+0.20}_{-0.15}$	30
$2.5 < \sigma < 3.5$	1.65	$20.39^{+0.20}_{-0.20}$	$-0.73^{+0.15}_{-0.15}$	$20.10^{+0.15}_{-0.15}$	25
$2.5 < \sigma < 3.5$	2.23	$19.94^{+0.20}_{-0.20}$	$-1.16^{+0.15}_{-0.15}$	$20.22^{+0.15}_{-0.10}$	27
$2.5 < \sigma < 3.5$	2.81	$19.69^{+0.25}_{-0.15}$	$-1.19^{+0.15}_{-0.10}$	$19.97^{+0.15}_{-0.15}$	27
$> 3.5 \sigma$	1.49	$19.86^{+0.25}_{-0.20}$	$-0.89^{+0.10}_{-0.10}$	$19.71^{+0.15}_{-0.15}$	18
$> 3.5 \sigma$	1.88	$20.19^{+0.20}_{-0.20}$	$-1.01^{+0.10}_{-0.15}$	$20.21^{+0.15}_{-0.15}$	19
$> 3.5 \sigma$	2.49	$20.21^{+0.20}_{-0.20}$	$-0.95^{+0.15}_{-0.10}$	$20.15^{+0.15}_{-0.15}$	20

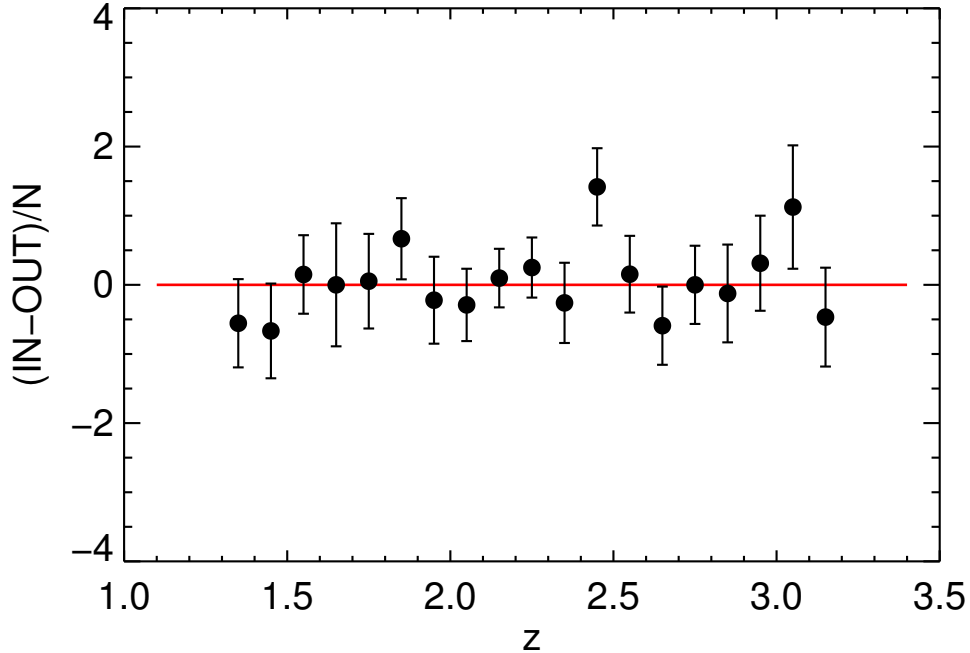


Figure 3.8: Average number of sources that could scatter in or out of the IRAC color selection due to photometric uncertainties as a function of candidate cluster redshift. ‘IN’ are defined as sources currently not selected (e.g., $[3.6] - [4.5] < -0.1$), but which could easily scatter in due to photometric uncertainties, $[3.6] - [4.5] + \sigma[3.6] - [4.5] > -0.1$. ‘OUT’ are defined as currently selected sources (e.g., $[3.6] - [4.5] > -0.1$), but which could easily scatter out due to photometric uncertainties, $[3.6] - [4.5] - \sigma[3.6] - [4.5] < -0.1$. The results are relatively flat and centered at zero, implying that the color criterion used is efficient and stable at all redshifts probed here.

3.4.2 Validation of Luminosity Function Measurement Method Using ISCS Clusters

We use the ISCS (Eisenhardt et al., 2008) to validate the methodology used in this paper and to compare to previously obtained results. Mancone et al. (2010) uses the ISCS to derive luminosity functions, though he restricted the analysis to candidate cluster members based on photometric redshifts, computed as in Brodwin et al. (2006) and with deeper photometry from the *Spitzer* Deep, Wide-Field Survey (SDWFS; Ashby et al., 2009). We measure the luminosity function around ISCS clusters at $1.3 < z < 1.6$ and $1.6 < z < 2$, i.e. overlapping in redshift with the CARLA cluster sample. We again first apply the IRAC

color criterion to the sources in a cell with radius $r = 1$ arcmin around the cluster center to determine cluster member candidates and carry out a background subtraction using SpUDS as described above. We then fit a Schechter function to the resulting data with α fixed to -1 . The SDWFS data is shallower than CARLA and we can therefore only measure the luminosity function down to $[4.5] = 21.4$. The fitted values for m^* at $4.5 \mu\text{m}$ are $20.25^{+0.30}_{-0.30}$ and $20.57^{+0.35}_{-0.35}$ for clusters at $1.3 < z < 1.6$ and $1.6 < z < 2$, respectively. The m^* for the same redshift bins and $\alpha = -1$ found by Mancone et al. (2010) are $20.48^{+0.12}_{-0.09}$ and $20.71^{+0.18}_{-0.12}$. Our results agree very well with these values, though note the larger error bars inherent to our simple color selection compared to the photometric redshift selection of Mancone et al. (2010) which minimizes background contamination by incorporating extensive multi-wavelength supporting data. This test confirms that the method used in this paper, i.e. color-selecting galaxy cluster members and carrying out a statistical background subtraction, provides robust results. With this test we also confirm the trend towards fainter magnitudes for m^* in ISCS clusters in the highest redshift bins reported by Mancone et al. (2010).

3.5 The Redshift Evolution of m^*

3.5.1 Comparison to Galaxy Evolution Models

Figure 3.9 shows the evolution of m^* with redshift in the context of passively evolving stellar population models. We also include results from Mancone et al. (2010). The measured m^* values are compared to previous work and to model predictions of passively evolving stellar populations from Bruzual & Charlot (2003) normalized to match the observed m^* of galaxy clusters at $z \sim 0.82$, $[4.5]^* = 19.82^{+0.08}_{-0.08}$ (AB) for $\alpha = -1$ (Mancone et al., 2012). Note that the results and implications of our work are independent of the model normalisation. Although Mancone et al. (2010) used a normalisation obtained from lower redshift cluster analyses we use a normalisation at relatively high redshift to match the redshift of the CARLA data as best as possible.

Mancone et al. (2010) carried out a similar study and measured the IRAC1 and IRAC2 luminosity function for 296 galaxy clusters from SDWFS over $0.3 < z < 2$. The clusters were identified as peaks in wavelet maps generated in narrow bins of photometric redshift probabilities. At $z < 1.3$, the evolution of m^* agreed well with predictions from passively evolving stellar populations and no mass assembly, with an inferred formation redshift of $z_f = 2.4$. For the two highest redshift bins at $z > 1.3$, the results disagreed significantly from the continuation of the passive evolution model. Mancone et al. (2010) interpreted this deviation as possible ongoing mass assembly at these epochs. The results here for the CARLA clusters do not agree with nor continue the trend Mancone et al. (2010) report at $z > 1.3$. In the redshift bins in which our study and Mancone et al. (2010) overlap, we

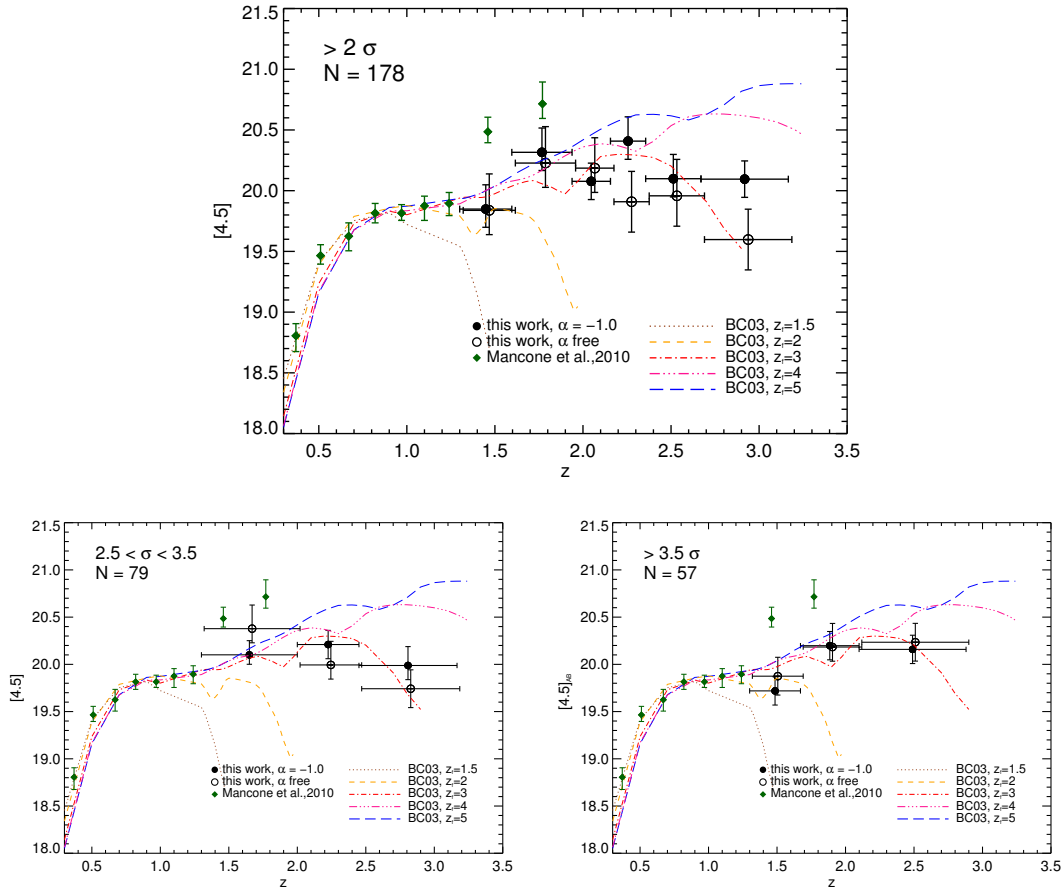


Figure 3.9: Evolution of $m_{4.5\mu m}^*$ with redshift for different CARLA cluster densities compared with results from Mancone et al. (2010) and model predictions for passive stellar population evolution (Bruzual & Charlot, 2003) with different formation redshifts, z_f . The number of CARLA fields going into each analysis is indicated on the plots. In most cases the results for the Schechter fits with fixed α and free α agree well. In cases where they don't this is due to bigger uncertainties at the faint end of the luminosity function in the data. In these cases the fixed α fit is probably the more meaningful result as it has been shown that generally a faint end slope of $\alpha = -1$ describes the data well at all CARLA densities and all redshifts. In general, our results are consistent with the passive evolution models out to $z \sim 3$ with formation redshifts $3 < z_f < 4$. The lower-density CARLA sample, shown in the lower left panel, seems to be consistent with results from Mancone et al. (2012) at $z \leq 1.3$ and suggests that this CARLA subsample is similar to the clusters studied there. The high-density subsample of CARLA clusters, shown in the lower right panel are ~ 0.7 mags fainter in the highest redshift bin compared to the lower richness samples. This might imply that the high richness sample consists of older clusters and therefore could provide a valuable sample of high-richness high-redshift clusters to study the formation of the earliest massive galaxies. For clarity, the results for a fixed α are slightly shifted along the x-axis.

find m^* to be ~ 0.5 mag brighter and to continue the trend found at lower redshifts by Mancone et al. (2010). At lower redshift ($1.3 < z < 1.8$) the models do not differ much and m^* is therefore consistent with a range of formation redshifts. At higher redshift the models diverge and show that clusters may have formed early with formation redshifts in the range $3 < z_f < 4$.

At all redshifts our results are consistent with passive evolution models with $3 < z_f < 4$. As CARLA clusters at $z \sim 3$ will not necessarily be progenitors of CARLA clusters at $z \sim 1.5$, it does not necessarily imply that they will remain passive subsequently. However, even at the highest redshifts probed here ($z \sim 3$) we do not measure a prominent deviation from passive evolution models nor do we see signs of significant mass assembly.

3.5.2 Dependence on Cluster Richness

We also study the evolution of m^* for two CARLA subsamples of different richnesses ($2.5 \sigma < \Sigma_{\text{CARLA}} < 3.5 \sigma$ and $\Sigma_{\text{CARLA}} > 3.5 \sigma$) and plot the results in Fig. 3.9. Although it is not fully known how the richness of IRAC-selected sources scales with mass, we assume here that statistically these two subsamples will represent clusters of increasing mass. For the lower richness sample, the evolution of m^* appears to be similar to the full sample with formation redshifts of $3 < z_f < 4$. Excluding the highest and lowest richness clusters therefore does not seem to have a significant effect on the luminosity functions. At lower redshift (i.e. $1.3 < z < 2.0$) the result for m^* and free α is consistent with results from Mancone et al. (2010) at $z \leq 1.3$ which might suggest that the CARLA lower richness clusters at this redshift are similar to the ISCS clusters studied Mancone et al. (2010).

Only considering the highest richness sample of CARLA clusters results in a monotonically increasing m^* , with $m^* \sim 0.7$ mags fainter in the highest redshift bin compared to the lower richness samples. This might imply that the high richness sample includes slightly older stellar populations. This subsample is thus of particular interest for future follow-up as this population of rich, high-redshift clusters could provide a powerful probe to study the early formation of massive galaxies in the richest environments and — from a cosmological point of view — test the predictions of Λ CDM (Brodwin et al., 2010).

3.5.3 Difference between $\alpha = \text{free}$ and $\alpha = -1$ fits

As can be seen in Fig. 3.7 and Fig. 3.9, the Schechter fit results for α as a free parameter and α fixed to -1 generally agree well within the 1σ uncertainties. For the few exceptions, the fits do agree within the 2σ uncertainties. We conclude that a fixed α of -1 describes the luminosity function functions well at all redshifts and all densities probed in this paper. With deeper IRAC observations (1400 s of exposure time), albeit not as deep as the CARLA observations (2000 s of exposure time) and deep multi-wavelength supporting data, Man-

cone et al. (2012) study a subset of the original Böotes sample and measure the faint end slope α of the mid-IR galaxy cluster luminosity function to be ~ -1 at $1 < z < 1.5$. Similar studies at lower redshift measure similar slopes. This suggests that the shape of the cluster luminosity function is mainly in place at $z = 1.3$.

The luminosity functions measured in this paper are consistent with $\alpha = -1$ at all redshifts and all richnesses probed. Combined with results from Mancone et al. (2010) and Mancone et al. (2012), this result suggests that galaxy clusters studied in this paper have already started to assemble low-mass galaxies at early epochs. Further processes that govern the build up of the cluster and that are discussed in more detail in § 3.6 and § 3.7 then have probably no net effect on the shape of the luminosity function. This is consistent with the results found by Mancone et al. (2010).

3.6 Discussion

3.6.1 Alternatives to pure passive Evolution Models

The above results suggest an early formation epoch for galaxy clusters that are passively evolving and an early build-up of the low-mass galaxy population. These measurements, however, seem to be at odds with results investigating lower redshift clusters. Thomas et al. (2010) shows that the age distribution in high-density environments is bimodal with a strong peak at old ages and a secondary peak comprised of young, ~ 2.5 Gyr old galaxies. This secondary peak contains about $\sim 10\%$ of the objects. Similarly, Nelan et al. (2005) derives a mean age of low-mass objects of low redshift galaxy clusters to be about 4 Gyrs in low-redshift clusters. Although their observation suggests a decline of star-forming galaxies and a trend of downsized galaxy formation, low mass galaxies are still assembling until relatively recent times. Measurements of the star-formation activity for higher redshift cluster galaxies also provide evidence for continuous star-formation activity, albeit evolving more rapidly than the star-formation activity in field galaxies (Alberts et al., 2014, e.g.).

We therefore investigate the extent to which our results can be explained by a sum of various stellar populations to estimate the maximum fraction of a star-forming cluster population that is still consistent with the data. We divide the cluster population into two stellar populations, a simple stellar population (SSP) with a delta-burst of star formation at high redshift and a composite stellar population (CSP) with a continuous, only slowly decaying star-formation rate of the form $\propto \exp(-t/\tau)$ and large τ . The details of the three different model sets we derive are as follows:

- Model 1: Sum of SSP with $z_f = 3$ and CSP with $z_f = 3$ and $\tau = 10$ Gyr with ratios

(SSP:CSP) ranging between 90:10 and 0:100¹ by mass.

- Model 2: Sum of SSP with $z_f = 3$ and CSP with $z_f = 3$ and $\tau = 1$ Gyr with ratios (SSP:CSP) ranging between 90:10 and 0:100 by mass.
- Model 3: Sum of SSP with $z_f = 5$ and CSP with $z_f = 3$ and $\tau = 10$ Gyr with ratios (SSP:CSP) ranging between 90:10 and 0:100 by mass.

A prolonged mass assembly means that at high redshift the observed $4.5 \mu\text{m}$ magnitude of galaxies is fainter because the stellar population is still forming. Therefore, accounting for mass assembly, i.e. allowing for star-forming population to contribute to the observed m^* , causes m^* to become fainter at high redshift depending on the contribution of this star-forming population.

In Figure 3.10 we show these models in the context of our results. They allow us to set an upper limit on the star-forming fraction, P , in our candidate cluster sample. Model 1, which allows for a significant star formation that is only very slowly decaying with cosmic time, shows that at all redshifts the mass fraction of the star-forming population cannot be larger than 40% (with one outlying exception of up to 60% at $z \sim 1.7$). In Model 2 the star formation rate (SFR) of the CSP decays faster and the contribution of the SSP becomes dominant much earlier than in Model 1. It therefore predicts m^* to be brighter at high redshifts and resemble the prediction of the passive evolution model. Consequently, our empirical results are in agreement with large contributions of up to 90% of the CSP in Model 2, with the CSP starting to passively evolve ~ 2.3 Gyrs earlier (at $z \sim 1.7$) than in Model 1 (at $z \sim 0.9$). Model 3 shows the evolution of a mixed population with a delta burst of star formation at $z_f = 5$ (SSP) and a long burst of star formation at $z_f = 3$ (CSP with $\tau = 10$ Gyrs). The SSP with $z_f = 5$ is fainter in IRAC2 at $1.5 < z < 3$ than a SSP with $z_f = 3$, so that an additional starburst at $z = 3$ leads to an even fainter m^* at $1 < z < 3$ for Model 3. Model 3 does not reproduce the results of the LF analysis and therefore this scenario can be ruled out by the data.

This shows that the results for the evolution of m^* obtained in this analysis – although consistent with passive evolution models – also allow for a limited contribution of a star-forming population in galaxy clusters. Our models show that this contribution is small (up to 40 % by mass, but probably on average around ~ 20 %) for a population with a high and slowly decaying star-formation rate, or that this contribution is large (up to 80%) for a population with a fast decaying SFR and an evolution that resembles passive evolution ~ 2.3 Gyrs earlier.

For a sample of 10 rich clusters at $0.86 < z < 1.34$ van der Burg et al. (2013) compares the contributions of quiescent and star-forming populations to the total mass function. We

¹a ratio (SSP:CSP) of (100:0) is equivalent with a passive evolution model and is already discussed above

integrate the published mass functions for the quiescent and star-forming population (van der Burg et al., 2013) over galaxy masses with $10^{10.1} < M_*/M_\odot < 10^{11.5}$. We find a mass fraction of the quiescent population of $\sim 80\%$ compared to the total stellar mass of the clusters. This is also in agreement with the upper limit for the fraction of the star-forming population derived for CARLA clusters in the lowest redshift bin.

As CARLA clusters at $z \sim 3$ will not necessarily be the progenitors of CARLA clusters at $z \sim 1.5$, we unfortunately cannot constrain the evolution of the maximum fraction of a star-forming population and cannot make conclusions about the quenching timescales and processes.

3.6.2 Biases of the CARLA cluster sample

Our analysis shows that the evolution of the CARLA clusters seems to be significantly different from the cluster sample analysed by Mancone et al. (2010). Using *Spitzer* 24 μm imaging for the same cluster sample, Brodwin et al. (2013) analysed the obscured star formation as a function of redshift, stellar mass and clustercentric radius. They find that the transition period between the era where cluster galaxies are significantly quenched relative to the field and the era where the SFR is similar to that of field galaxies occurs at $z \sim 1.4$. Combining these measurements with other independent results on that sample (Snyder et al., 2012; Martini et al., 2013; Alberts et al., 2014), the authors conclude that major mergers contribute significantly to the observed star formation history and that merger-fueled AGN feedback may be responsible for the rapid truncation between $z = 1.5$ and $z = 1$.

While the ISCS clusters studied in Mancone et al. (2010) and Brodwin et al. (2013) were selected from a field survey as 3-D overdensities using a photometric redshift wavelet analysis, the clusters studied here are found in the vicinity of RLAGN. With RLAGN belonging to the most massive galaxies in the Universe ($m \sim 10^{11.5} M_\odot$; Seymour et al., 2007; De Breuck et al., 2010), these clusters could reside in the largest dark matter halos, deepest potential wells and densest environments.

Indeed, Mandelbaum et al. (2009) derives halo masses for 5700 radio-loud AGN from the Data Release 4 of the Sloan Digital Sky Survey and finds the halo masses of these radio-loud AGN to be about twice as massive as those of control galaxies of the same stellar mass. Previous work (e.g. Best et al., 2005) has shown that more massive black holes seem to trigger radio jets more easily, but as this boost in halo mass is independent of radio luminosity, the authors conclude that the larger-scale environment of the RLAGN must play a crucial role for the RLAGN phenomenon. Similarly, albeit at higher redshift, Hatch et al., submitted, finds that the environments of CARLA RLAGN are significantly denser than similarly massive quiescent galaxies. They detect a weak positive correlation

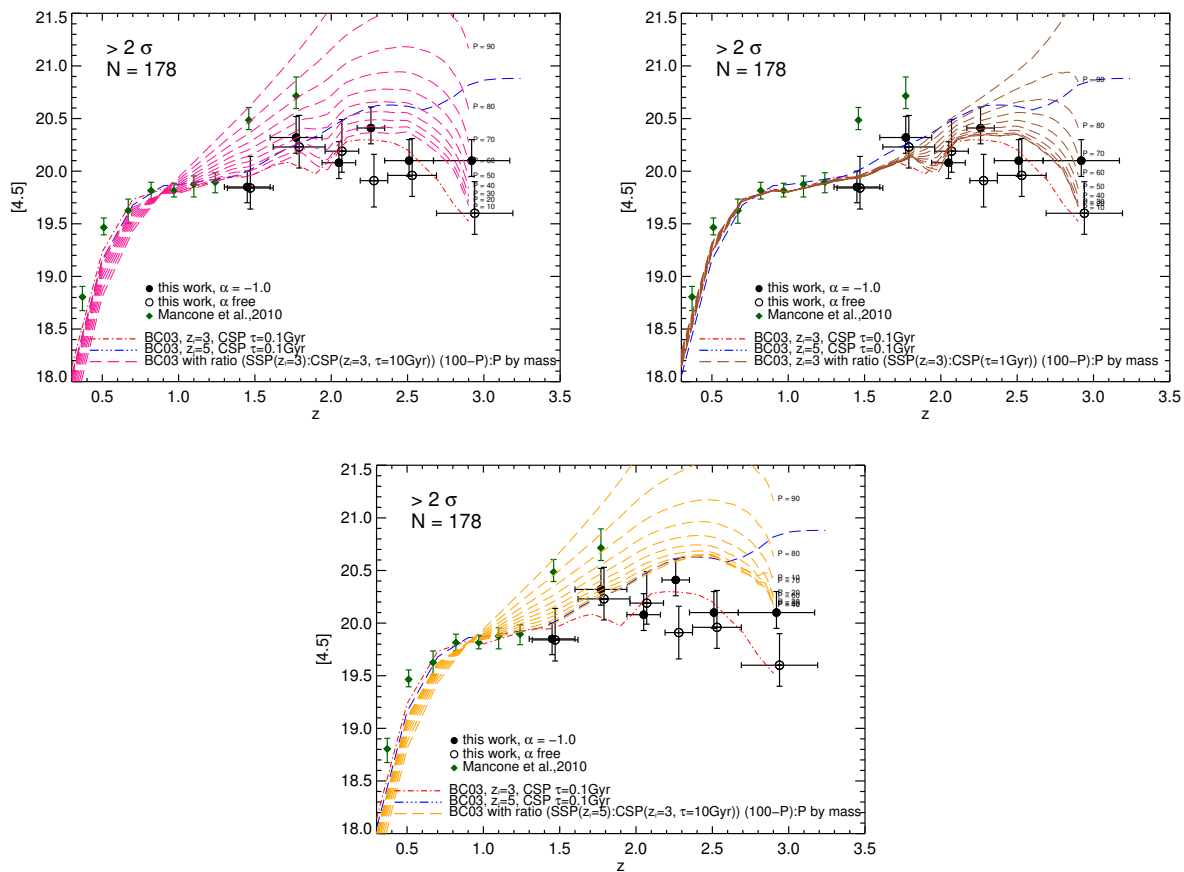


Figure 3.10: Model predictions for the evolution of m^* for a superposition of a passive and star-forming galaxy population. The passive, simple stellar population (SSP) formed stars in a delta burst at z_f and evolved passively thereafter while the star-forming, composite stellar population (CSP) shows an exponentially decaying SFR with an e -folding timescale τ . We show models with differing mass ratios of the SSP and CSP. Comparing the models with our measurements for m^* allows to set an upper limit on the contribution of the CSP. *Top left panel: Model 1: SSP with $z_f = 3$, CSP with $z_f = 3$ and $\tau = 10$ Gyrs* *Top right panel: Model 2: SSP with $z_f = 3$, CSP with $z_f = 3$ and $\tau = 1$ Gyr* *Bottom panel: Model 3: SSP with $z_f = 5$, CSP with $z_f = 3$ and $\tau = 10$ Gyrs*

between the black-hole mass and the environmental density on Mpc-scales, suggesting that even at high redshift the growth of the black hole is also linked to collapse of the surrounding cluster.

This peculiar interplay between radio jet triggering, stellar mass, black hole and halo mass of the RLAGN and the larger-scale environment suggest that (proto-)clusters and the large-scale environments of RLAGN are distinct from clusters found in field surveys.

If mergers are significantly contributing to the transition of clusters from unquenched to quenched systems, as suggested in Brodwin et al. (2013), this transition redshift will be dependent on cluster halo mass. If the environments and dark matter halos around radio-loud AGN are indeed more massive this would explain the conflict of our results with those from Mancone et al. (2010). CARLA clusters have probably undergone this transition period much earlier than the ISCS clusters. At $1.4 < z < 1.8$ where the star-forming fraction of ISCS clusters analysed by Mancone et al. (2010) still seems to be very high ($\sim 80\%$), this contribution is already much smaller in CARLA clusters. As mentioned earlier, our measurements allow us to derive upper limits on the contribution of a star-forming population but do not allow for a definite constraint on the transition redshift.

3.7 Summary

We have shown the evolution of the mid-IR luminosity function for a large sample of galaxy cluster candidates at $1.3 < z < 3.2$ located around RLAGN. All cluster candidates in this work were identified as mid-IR color-selected galaxy overdensities, a selection that is independent of galaxy type and evolutionary stage. Wylezalek et al. (2013a) has shown that indeed these excess color-selected sources are centered on the RLAGN, implying they are associated. There is a steep increase of density toward the RLAGN which would not be seen if there was not a physical link between the galaxies in the field and the AGN. We therefore expect most of these overdensities to be true galaxy (proto)-clusters. Having neither spectroscopic nor photometric redshifts at hand, this study relies on statistics with 10 to 30 clusters per redshift bin.

We have shown that our results are consistent with theoretical passive galaxy evolution models up to $z = 3.2$. Mancone et al. (2010) measured significant deviation from these passive galaxy evolution models in their highest redshift bins ($1.3 < z < 1.8$), which correspond to our lowest redshift bins. They attributed this to possible ongoing mass assembly at these ($1.3 < z < 1.8$) redshifts. The work in this paper fails to confirm this previously observed trend but, on the contrary, finds that the cluster luminosity function agrees well with passive evolution models. To test our analysis, we apply our methodology to the clusters in Mancone et al. (2010) and confirm their results at $1.3 < z < 1.8$. For lower richness CARLA clusters our results in the lowest redshift bins ($1.3 < z < 1.8$, free α) are consistent

with what has been found in Mancone et al. (2010) for their $z < 1.3$ clusters and shows that the lower richness CARLA clusters are probably more similar to the clusters analysed in Mancone et al. (2010).

We construct three different sets of galaxy evolution models to test to which extent our results are consistent with a star-forming population of galaxies contributing to m^* . This allows us to obtain upper limits on the mass fraction of a star-forming population. This modelling shows that at $z < 1.5$ the CARLA clusters are mostly passively evolving with very little contribution of a star-forming population.

At $1.5 < z < 3$ the LF measurements are consistent with a star-forming population contributing to the cluster LF. This contribution is very likely low, i.e. less than 40% by mass, for a star-forming population with large (10 Gyr) e -folding timescale.

For star-forming populations with short (1 Gyr) e -folding timescale the modelling also allows for larger mass fractions. But due to the short e -folding timescales these models are effectively passively evolving.

Because CARLA clusters in the highest redshift bins ($z \sim 3$) are likely not progenitors of those at lower redshift ($z \sim 1.5$) and because uncertainties in m^* are large we cannot constrain the evolution of the mass fraction of the star-forming population. This study shows, however, that the fraction of star-forming galaxies in CARLA clusters must be significantly smaller than in clusters studied in Mancone et al. (2010).

It has been shown that RLAGN seem to reside in dark matter halos twice as massive and denser galaxy environments as quiescent galaxies of similar stellar mass (Mandelbaum et al., 2009). Recent work on the evolution of the star formation in ISCS clusters by Brodwin et al. (2013) also suggests that the epoch of mass assembly should be considerably higher for high-redshift high-mass systems like SPT-CL J0205-5829 at $z = 1.32$ (Stalder et al., 2013) or XMMU J2235.3-2557 at $z = 1.39$ (Mullis et al., 2005). These clusters have very low central star formation rates (e.g. Stalder et al., 2013) and already seem to be largely quenched and passive in their cores. In agreement with this prediction, CARLA clusters appear to have undergone this transition period to largely quiescent systems much earlier than ISCS clusters from Mancone et al. (2010). This can explain the discrepancies in the m^* measurements for ISCS clusters and CARLA clusters at $z \sim 1.5$.

While the lower richness CARLA clusters are probably more similar to clusters found in Mancone et al. (2010), the high-richness CARLA clusters likely represent the high richness portion of the cluster population and therefore could provide a powerful cluster sample to study the formation of high-redshift, rich clusters and test predictions of the standard Λ CDM Universe (e.g., Mortonson et al., 2011).

Another key result of our work is the agreement of the data with of a relatively flat luminosity function ($\alpha = -1$) out to the highest redshifts. Mancone et al. (2012) had already shown that at least up to a redshift of $z = 1.5$ the faint end slope of the luminosity

function seems to be already in place and does not evolve since then. This implies that processes that are responsible for the build-up of the mass of low-mass cluster galaxies do not have any net effect on the overall slope of the luminosity function. Processes that could steepen the slope of the luminosity function are star formation and mergers. Processes that could flatten the slope are galaxy-galaxy interactions, galaxy harassment or the dissolution of cluster galaxies (see Mancone et al., 2012, and references therein for more extensive discussion). In this work, we find that a slope of $\alpha = -1$ describe the luminosity functions very well even to the highest redshifts probed in this work ($z = 3.2$). Processes that could steepen or flatten the faint end slope of the luminosity function seem not to have a significant net effect up to $z \sim 3$. Low mass galaxies seem to grow through star formation, get quenched and are replenished by in-falling field galaxies at a rate that does not have a major effect on the shape of the LF.

This study provides a first statistical approach to measuring the high-redshift cluster LF, albeit biased to cluster candidates found in the fields of RLAGN. We have successfully started the follow-up of our most promising candidates and recently confirmed a structure around the radio galaxy MRC 0156-252 at $z = 2.02$ (Galamez et al., 2013). We also started multi-object near-IR spectroscopic follow-up to confirm additional high-redshift clusters. Obtaining clean samples of spectroscopically confirmed galaxy clusters at high redshift with different techniques with different selection biases is necessary to fully probe the different scenarios and paths that galaxy clusters take in their evolution.

Acknowledgments: We thank the referee for helpful comments that have improved the manuscript. We gratefully thank Mark Lacy for allowing us to access SERVS images and catalogs and Roberto Assef and Conor Mancone for helpful discussions and advice. N. Seymour is the recipient of an ARC Future Fellowship. This work is based on observations made with the *Spitzer Space Telescope*, which is operated by the Jet Propulsion Laboratory, California Institute of Technology under a contract with NASA.

Why $z > 1$ radio-loud galaxies are located in dense environments

N. A. Hatch, D. Wylezalek, J. D. Kurk, D. Stern, C. De Breuck, M. J. Jarvis, A. Galametz,
A. H. Gonzalez, N. Seymour, J. A. Stevens
Monthly Notices of the Royal Astronomical Society, submitted

Abstract We compare the environment of powerful radio-loud active-galactic nuclei (RLAGN) at $1.3 < z < 3.2$ to a sample of radio-quiet galaxies matched in mass and redshift. The environments of RLAGN differ so significantly to the radio-quiet galaxies that not more than 50% of massive galaxies ($\gtrsim 10^{11} M_{\odot}$) in this epoch can experience powerful radio-loud jet feedback. The RLAGN are located in denser and more massive large-scale environments than similarly massive radio-quiet galaxies. This is not an observational selection effect as we find no evidence that radio emission is enhanced in dense environments. We therefore suggest that the jet launching mechanism is triggered by the halo environment in addition to the host galaxy properties. The tendency for powerful RLAGN to reside in dense environments explains why protoclusters are reliably found surrounding radio-galaxies; the number density of potential RLAGN host galaxies is consistent with every $> 10^{14} M_{\odot}$ cluster having experienced at least one powerful radio-mode feedback outburst during $1.3 < z < 3.2$.

4.1 Introduction

Active galactic nuclei (AGN) are accreting supermassive black holes (SMBHs) located in the centres of galaxies. The observed correlation between the SMBH mass and the bulge stellar mass of a galaxy strongly suggest that SMBHs regulate the growth of their host galaxies through feedback (Ferrarese & Merritt, 2000). Powerful FR II (Fanaroff & Riley, 1974) radio-loud active galactic nuclei (RLAGN) are a subset of the AGN population which launch

jets of relativistic particles whose kinematic power are comparable to the photoionizing luminosity of the AGN (Rawlings & Saunders, 1991). These jets can travel hundreds of kpcs away from the host galaxy and deposit a huge amount of energy, more than 10^{60} erg, into the surrounding intergalactic or intracluster medium (Erlund et al., 2008). The mechanical feedback can be as strong as the radiative feedback from these AGN (Mocz et al., 2013), and a single outburst may dramatically affect the surrounding galaxies (Rawlings & Jarvis, 2004).

Extensive studies over several decades have shown that distant RLAGN preferentially reside in overdense environments (e.g. Yates et al., 1989; Hill & Lilly, 1991; Roche et al., 1998; Best et al., 1998; Best, 2000; Donoso et al., 2010; Falder et al., 2010; Ramos Almeida et al., 2013b; Wylezalek et al., 2013a). Thus the mechanical feedback from these RLAGN preferentially occurs in certain environments such as galaxy groups and clusters. What remains unclear is whether this correlation is due to an underlying causal relation between the large-scale environment and the jet-triggering mechanism or the visibility of radio jets.

Standard Λ CDM cosmology predicts that the most massive galaxies emerged from the densest regions in the Universe which grew to become galaxy groups and clusters. The host galaxies of RLAGN are massive, typically $M_* \sim 10^{11.3} M_\odot$ (Seymour et al., 2007), and are amongst the most massive galaxies at all redshifts (Rocca-Volmerange et al., 2004). It is possible that RLAGN are typically found in dense regions simply because they are hosted by massive galaxies, which are preferentially located in rich environments. If this hypothesis holds true then the Mpc-scale environment of RLAGN should be no different than similarly massive galaxies without strong radio emission.

Alternative theories suggest that dense environments can affect whether an AGN launches jets, or enhance the radio luminosity of the jets. Dense gaseous environments can boost radio emission by confining the jets (Barthel & Arnaud, 1996) which would lead to a selection bias within a radio-luminosity limited sample. Best et al. (2005) found that the fraction of galaxies that are radio-loud depends strongly on the black hole mass, so it is possible that black hole growth is enhanced in dense environments.

In this paper we test these hypotheses by comparing the Mpc-scale environments of very powerful RLAGN (with 500 MHz luminosities $\geq 10^{27.5} \text{ W Hz}^{-1}$) at $1.3 < z < 3.2$ from the Clusters Around Radio-Loud AGN (CARLA) survey (Wylezalek et al., 2013a) to those of a mass- and redshift-matched sample of galaxies selected from the UKIDSS Ultra Deep Survey (UDS; Almaini et al., in prep). We also look for correlations between the environments of RLAGN and the properties of the AGN, such as their black hole mass, fraction of bolometric power emitted as radio, and the size and spectral index of the radio source. We use AB magnitudes throughout and a Λ CDM flat cosmology with $\Omega_M = 0.3$, $\Omega_\Lambda = 0.7$, $H_0 = 70 \text{ km s}^{-1} \text{ Mpc}^{-1}$.

4.2 Method

4.2.1 Data

RLAGN sample

CARLA is a 400-hour Warm *Spitzer Space Telescope* programme designed to investigate the environments of powerful RLAGN. The CARLA sample consists of 419 very powerful RLAGN lying at $1.3 < z < 3.2$ and having a 500 MHz luminosity $\geq 10^{27.5} \text{ W Hz}^{-1}$. The sample comprises of 211 radio-loud quasars (RLQs) and 209 radio galaxies (RGs) which were matched in redshift and radio-luminosity space. No information about the RLAGN environments was taken into account for selecting targets so this sample is a good representation of the environments of the entire RLAGN population at these redshifts. Deep *Spitzer* data covering $5.2\text{arcmin} \times 5.2\text{arcmin}$ were obtained on each field with the Infrared Camera Array (IRAC; Fazio et al. 2004) on board the *Spitzer Space Telescope* at 3.6 and $4.5 \mu\text{m}$ (IRAC1 and IRAC2, respectively) during cycles 7 and 8. The CARLA 95% completeness limiting magnitudes are $[3.6] = 22.6$ and $[4.5] = 22.9$ mag. An introduction to the survey and details of the sample selection, observations and data reduction can be found in Wylezalek et al. (2013a). Using the well-tested *Spitzer* IRAC color criterion $[3.6] - [4.5] > -0.1$ to select galaxies at $z > 1.3$, Wylezalek et al. (2013a) showed that 46 per cent of these RLAGN are surrounded by significant excesses of galaxies that are likely associated with the RLAGN.

Control fields: UDS and SpUDS

To obtain a control field sample of radio-quiet galaxies with the same mass and redshift distribution as the RLAGN, we utilise the UDS (Almaini *et al.*, in prep.). The UDS is a deep 0.8 deg^2 near-infrared survey overlapping part of the *Subaru/XMM-Newton* Deep Survey (SXDS; Furusawa 2008). The total co-moving volume between $z = 1.3$ and 3.2 is 0.012 Gpc^{-3} , therefore there are approximately 50 proto-clusters that will collapse to form clusters of $M_{200} \geq 10^{14} M_{\odot}$ located within this survey in this redshift range (assuming local galaxy cluster number counts from Vikhlinin et al. 2009).

A sample of massive galaxies are identified from the UDS using the photometric redshifts and stellar masses derived by Hartley et al. (2013) and Mortlock et al. (2013). These authors combine U -band data from the Canada-France-Hawaii Telescope (Foucaud et al., in preparation) with optical photometry from the SXDS, JHK photometry from the 8th data release (DR8) of the UDS and IRAC1 and IRAC2 photometry from the *Spitzer* Ultra Deep Survey (SpUDS; PI J. Dunlop) to create a matched K -selected $UBVRizJHK[3.6][4.5]$ catalogue.

Photometric redshifts were determined by fitting spectral energy distribution (SED) tem-

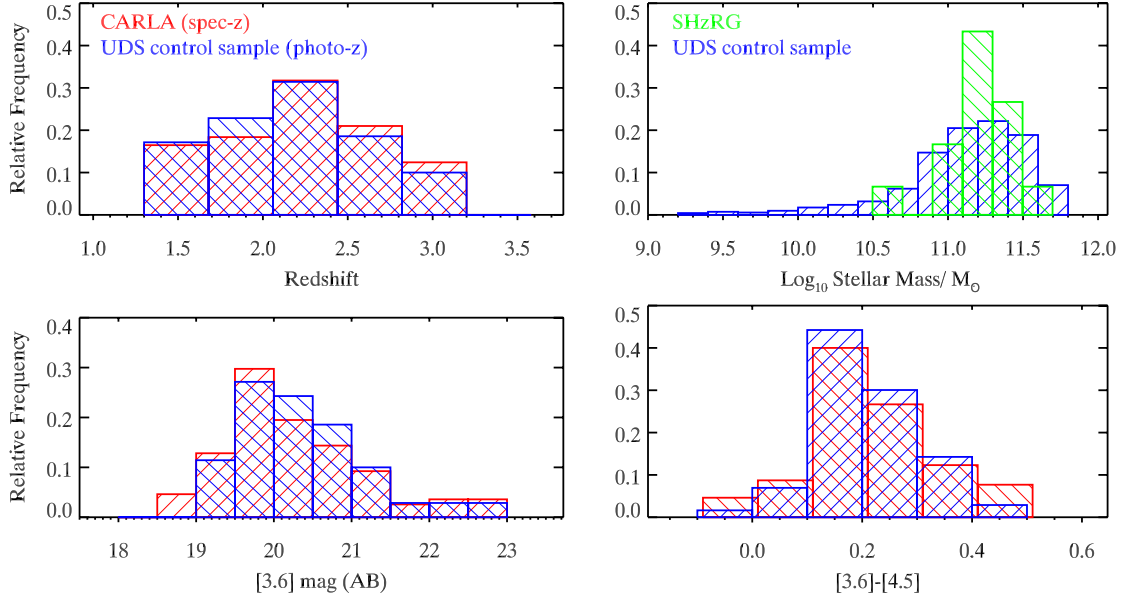


Figure 4.1: The distributions of the redshifts (top left), [3.6] magnitudes (bottom left), [3.6]-[4.5] colors (bottom right) of the CARLA sample and the UDS control sample shown in red and blue, respectively. The top right panel shows the stellar mass distribution of the UDS control sample compared to the stellar masses of the SHzRG radio galaxies with a similar range of redshift and radio-power as the CARLA sample.

plates to the photometric data points; the dispersion of the resulting photometric redshifts is $\Delta z / (1 + z) = 0.031$. For full details regarding the methodology and resulting photometric redshifts of the UDS catalogue, see Hartley et al. (2013).

The stellar masses of the K -selected UDS galaxies were measured by fitting the photometry to a large grid of synthetic SEDs from Bruzual & Charlot (2003) stellar population models (created using a Chabrier initial mass function; Chabrier 2003). Full details of the fitting procedure are given in Mortlock et al. (2013). The catalogue is 95 per cent complete to $\log(M/M_{\odot}) = 10.3$ at the highest redshift of the CARLA sample ($z = 3.2$). We assume the RLAGNs have a mass distribution similar to the De Breuck et al. (2010) sample (see Section 4.2.2) which has a lower mass limit of $\log(M/M_{\odot}) = 10.5$. Thus the UDS catalogue is complete in mass across the redshift range of the CARLA RLAGN, i.e., $1.3 < z < 3.2$. Following Hartley et al. (2013) we remove objects with poorly determined photometric redshifts and stellar masses by removing the objects whose minimum χ^2 is greater than 11.35 the photometric redshift fitting procedure (15 per cent of the sample). Many of the removed objects are blended sources or optically bright AGN, so the UDS sample may be biased against galaxies containing optically bright AGN.

The environment of the UDS massive galaxies are measured using SpUDS: a cycle 4

Spitzer Legacy program which deeply images 1 deg² encompassing the UDS field. We use the SpUDS IRAC1 and IRAC2 catalogues of Wylezalek et al. (2013a), which were extracted from the public final mosaics in the same way as for CARLA data. The catalogues were extracted in dual-image mode with the IRAC2 image used as the detection image. The SpUDS data reach 3σ sensitivities of $[3.6] \sim [4.5] \sim 24$ mag but in all following work the catalogues have been cut to the shallower depth of the CARLA data.

4.2.2 Obtaining a mass- and redshift-matched galaxy control sample

A sample of galaxies that have similar masses and redshifts to the CARLA RLAGN were selected from the UDS catalogues. To form a radio-quiet sample we removed all UDS galaxies from the catalogue that were detected in the $100\mu\text{Jy}$ *Subaru/XMM-Newton* Deep Field radio source sample of Simpson et al. (2006). Although we refer to the remaining galaxy sample as ‘radio-quiet’ we note that the $100\mu\text{Jy}$ flux limit of the Simpson et al. (2006) catalogue means that the sample may still include radio-emitting galaxies with 500 MHz luminosity of $10^{24.4}\text{W Hz}^{-1}$ at $z = 1.3$ and up to $10^{25.2}\text{W Hz}^{-1}$ at $z = 3.2$ (assuming a spectral index $\alpha = -0.9$: see Fig. 4.5c). These radio luminosities are at least two orders of magnitude lower than the radio luminosities of the CARLA RLAGN.

We do not have an estimate of the stellar masses of the CARLA RLAGN, and since half of the sample consists of quasars it is impossible to accurately measure their stellar mass without complex SED fitting that takes into account light from the AGN as well as the stellar population. To do this requires mid-infrared data at wavelengths $> 5\mu\text{m}$. Since these data are not available for the CARLA sample we are unable to perform adequate fits to the RLAGN SEDs to obtain stellar masses.

Spitzer [3.6] and [4.6] bands cover rest-frame $0.8 - 2 \mu\text{m}$ emission from galaxies at $1.3 < z < 3.2$, hence they are relatively good tracers of the stellar mass of the 209 CARLA radio galaxies. UDS galaxies with the same [3.6] magnitudes and [3.6]-[4.5] colors are likely to have similar masses as the radio galaxies of the CARLA sample. We assume that the masses of the CARLA radio galaxies and radio-loud quasars are similar. Wylezalek et al. (2013a) found no difference between the environments of the radio-loud quasars and radio galaxies in the CARLA sample which supports the orientation unification theory of radio sources, so this assumption is likely to be valid for this sample. Therefore a sample of UDS galaxies matched with the [3.6] magnitudes and [3.6]-[4.5] colors of the CARLA radio galaxies is likely to be a good approximation for the entire CARLA RLAGN sample.

The caveat to using the [3.6] magnitudes as a mass proxy is that approximately a third of radio galaxies in this redshift range are dominated at rest-frame $1.6\mu\text{m}$ by AGN-heated hot dust emission rather than stellar emission (De Breuck et al., 2010). Hot dust emission will contaminate both the observed [3.6] and [4.5] fluxes, but will contribute more to the [4.5]

magnitudes than to the [3.6] magnitudes. Therefore the radio galaxies are expected to be slightly brighter in [3.6] and redder in [3.6]-[4.5] color than galaxies of similar mass without AGN. To minimise the number of radio galaxies whose IRAC fluxes are dominated by hot dust emission we removed the 13 radio galaxies that have $[3.6] - [4.5] > 0.5$ colors. Only 1% of $\log(M/M_{\odot}) = 11$ UDS galaxies have such red colors compared to 6% of CARLA radio galaxies, which implies the IRAC fluxes of such red radio galaxies are likely to be strongly contaminated by hot dust emission.

All 419 RLAGN have spectroscopically measured redshifts; the distribution is shown in the top left panel of Fig. 4.1. We divided the sample into 5 redshift bins of width $\Delta z = 0.38$, and measured the [3.6] magnitudes and [3.6]-[4.5] colors of the CARLA radio galaxies in each redshift bin. The UDS galaxies were divided into the same five redshift bins. From each redshift bin we randomly selected UDS galaxies to match the [3.6] magnitudes and [3.6]-[4.5] colors of the CARLA radio galaxies with $[3.6] - [4.5] < 0.5$. The control sample was limited to 70 galaxies and the selection was repeated 100 times; a larger control sample skewed the UDS control sample to lower [3.6] magnitudes than the CARLA radio galaxy sample due to a lack of bright galaxies with $[3.6] < 19.5$ at high redshift. The [3.6] magnitude, [3.6]-[4.5] color, and redshift distributions plotted in Fig. 4.1 compare the average of the 100 selections of the UDS control sample to the CARLA RLAGN. Kolmogorov-Smirnov (KS) tests of the [3.6] magnitudes, [3.6]-[4.5] colors, and redshifts do not find any statistically significant difference between the CARLA and 70 UDS control galaxies so we are confident these samples are closely matched.

To check whether the masses of the UDS control sample are a good representation of the radio galaxy masses we compare them to the mass distribution of the *Spitzer* high-redshift radio galaxy (SHzRG) sample (De Breuck et al., 2010), which are of similar radio luminosities and redshifts as the CARLA RLAGN. Seymour et al. (2007) and De Breuck et al. (2010) combined data from the near to mid-infrared wavelengths to obtain SEDs of the radio galaxies and then fit them with combined AGN and stellar population synthesis templates to derive stellar masses. Thirty radio galaxies lie at $1.3 < z < 3.2$ and exhibited SEDs from which a stellar mass could be measured. The SHzRG galaxy masses are reduced by 13% to account for the differences in assumed initial mass functions in the SED fitting (Kroupa 2001 for SHzRG versus Chabrier 2003 for the UDS). The resulting mass function is shown in the top right panel of Fig. 4.1; the mass distribution of the UDS control sample is similar to the SHzRG masses.

The fraction of control galaxies that host a radio-quiet AGN was measured using deep *XMM-Newton* data (Ueda et al., 2008). The closest K-band selected galaxy within 5 arcsec of the X-ray point source was assumed to be the galaxy counterpart, which resulted in 191 X-ray point sources in the redshift range $1.3 < z < 3.2$. Approximately 8% of the control galaxies have X-ray detections indicating they host radio-quiet AGN.

4.2.3 Measuring environment

The environments of the CARLA RLAGN and the matched UDS galaxy sample are measured by counting the number of *Spitzer* IRAC color-selected galaxies within 1arcmin radius circles centred on each galaxy in the samples. This radius corresponds to an angular diameter distance of ~ 0.5 Mpc at $1.3 < z < 3.2$. The well-tested $[3.6] - [4.5] > -0.1$ color-cut was used to remove galaxies with $z < 1.3$ (Papovich, 2008). Using this criterion we expect to obtain a $z > 1.3$ galaxy sample with only 10 – 20% contamination by low-redshift interlopers (Muzzin et al., 2013). This color selection criterion identifies a homogenous sample of galaxies out to $z \sim 3.2$ because $[4.5]$ is almost constant for galaxies at $z > 0.7$ due to a negative k -correction and these wavelengths cover the $1.6\mu\text{m}$ stellar bump for galaxies at $1.3 < z < 3.2$. This stellar bump is a prominent feature regardless of a galaxy's star formation history. For the rest of this work we refer to the objects matching the $[3.6] - [4.5] > -0.1$ color selection as 'IRAC-selected sources'.

An object is defined as an IRAC-selected source if it is detected above the IRAC2 95% completeness limit of the CARLA data ($[4.5]=22.9$ mag) and has a color of $[3.6] - [4.5] > -0.1$. If the source is not detected in IRAC1 an upper limit of the $[3.6]-[4.5]$ color is determined using the 3.5σ detection limit of the IRAC1 CARLA data ($[3.6]=22.8$ mag). The SpUDS data are significantly deeper than the CARLA data. This is the same criteria used as in (Wylezalek et al., 2014), although differs from that used in Wylezalek et al. (2013a) in terms of the IRAC1 depth.

4.2.4 Properties of CARLA RLAGN

Black hole masses and bolometric quasar luminosity

The SMBH masses and the bolometric luminosities of the 211 radio-loud quasars in the CARLA sample were obtained from the Sloan Digital Sky Survey (SDSS); Shen et al. (2011). The SMBH masses are virial masses, i.e. it is assumed that the broad-line emission region is virialised and the continuum luminosity and broad emission line width are good proxies for the broad-line region radius and velocity, respectively. Due to the spectral coverage of the SDSS data the Mgii line is used to calculate the virial mass of the SMBH for RLAGN at $z < 1.9$, whilst for all higher redshift RLAGN the Civ line is used. We note that there are large uncertainties and significant systematic biases associated with these SMBH mass estimates which are described in detail in Shen et al. (2011).

Extent of the radio emission

The sizes of the radio emission of CARLA sources were measured from the Very Large Array (VLA) Faint Images of the Radio Sky at Twenty-cm (FIRST) survey (White et al., 1997)

at ~ 1.4 GHz which has a resolution of 5arcsec. We matched the 2013 June 05 version of the FIRST catalogue with the CARLA sources and identified 284 sources covered by FIRST. All sources in the catalogue that have a probability $P > 0.05$ of being a spurious source were removed; the RLAGN are very bright so it is common that nearby sources are sidelobes.

We identified RLAGN which had multiple radio components within 60arcsec. We define the size as the largest distance between the radio sources detected within 1arcmin of the CARLA RLAGN. For AGN with only single radio components we identified the closest radio counterpart within 5arcsec and the size was defined as the full-width-at-half-maximum (FWHM) of the major axis, which had been deconvolved to remove blurring by the elliptical Gaussian point-spread function, down to a major axis FWHM < 2 arcsec. Sources with major axis FWHM < 2 arcsec were classified as unresolved. Of the 284 CARLA RLAGN with FIRST coverage 131 are extended sources (84 with multiple radio components) and 153 are unresolved sources.

Spectral indices

The spectral index, α (where $S_\nu \propto \nu^\alpha$), of the radio emission was measured by cross-correlating two radio surveys with similar spatial resolution: the 1.4 GHz NRAO VLA Sky Survey (Condon et al., 1998) and the 74 MHz VLA Low-Frequency Sky Survey (Cohen et al., 2007). Radio-loud quasars may emit time-variable Doppler beamed emission so it is not reliable to measure their spectral indices from surveys taken several years apart. Thus we only measure the spectral indices for the 158 radio-loud galaxies in the CARLA sample that are covered by both radio surveys.

4.3 Results

4.3.1 Are RLAGN in dense environments because they are massive galaxies?

In the model of hierarchical structure formation distant massive galaxies are formed in the highest density peaks that evolve to become the most massive dark matter halos. These high density peaks contain a larger number of galaxies than average, hence they can be observed as overdense environments. If RLAGN reside in dense environments simply because they are hosted by massive galaxies then we expect massive radio-quiet galaxies to occupy similarly dense environments as the RLAGN.

In Fig. 4.2 we compare the environments of the 419 RLAGN in the CARLA sample to the control sample selected from UDS with the same redshifts, $[3.6]$ magnitudes and

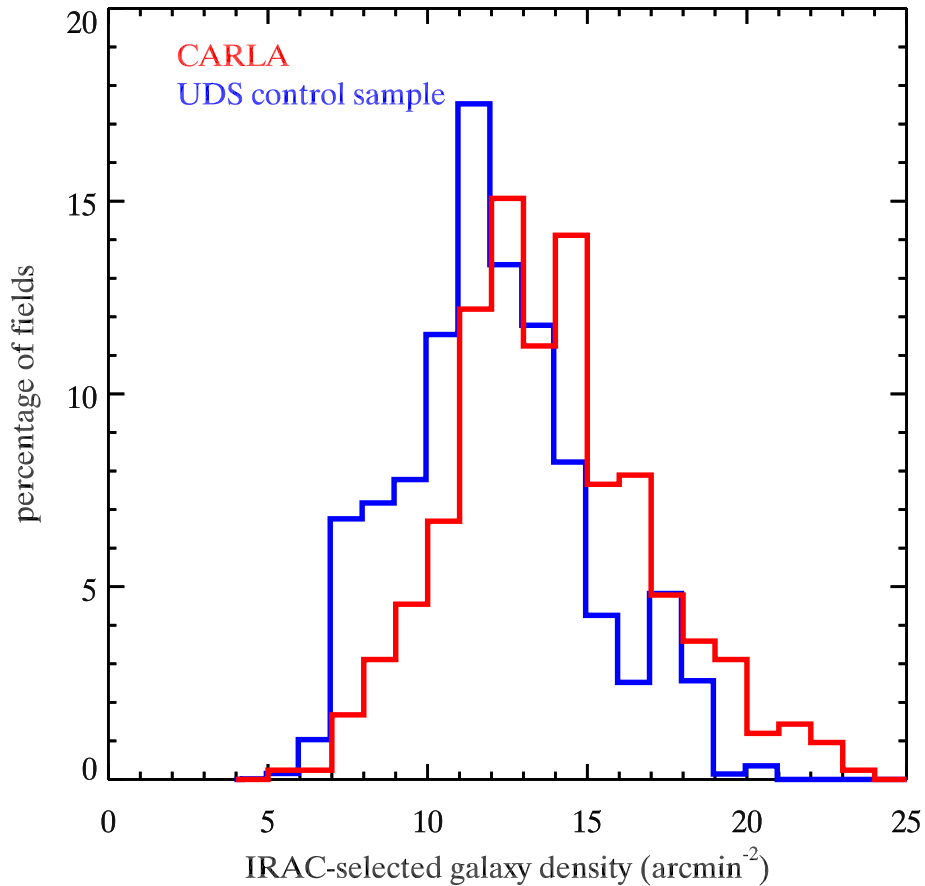


Figure 4.2: A comparison of the environment surrounding the CARLA RLAGN (red) and the UDS control sample (blue) that was matched in redshift, $[3.6]$ magnitude and $[3.6]$ - $[4.5]$ color. The environment is assessed using the IRAC-selected sources galaxy density within an arcmin of the targeted UDS galaxies and RLAGN.

$[3.6]$ - $[4.5]$ colors as the RLAGN. The environments of the control galaxies are on average less dense than the surroundings of the RLAGN in the CARLA sample. A Kolmogorov-Smirnov test results in a probability of $< 10^{-4}$ that these two galaxy populations lie in similar environments. This implies that the high masses of the RLAGN host galaxies is not the only reason why RLAGN occupy denser than average environments.

In Fig. 4.3 we split the CARLA sample into two redshift bins separating the sample at $z = 2.2$ and compare the environments of these samples with UDS galaxies in 2 mass bins: $11 < \log M/M_{\odot} < 11.5$ and $\log M > 11.5 M_{\odot}$.¹ The UDS galaxies are selected to have the same redshift distribution as the CARLA galaxies.

¹For this analysis UDS galaxies whose minimum χ^2 is greater than 11.35 in the stellar mass fitting procedures were removed.

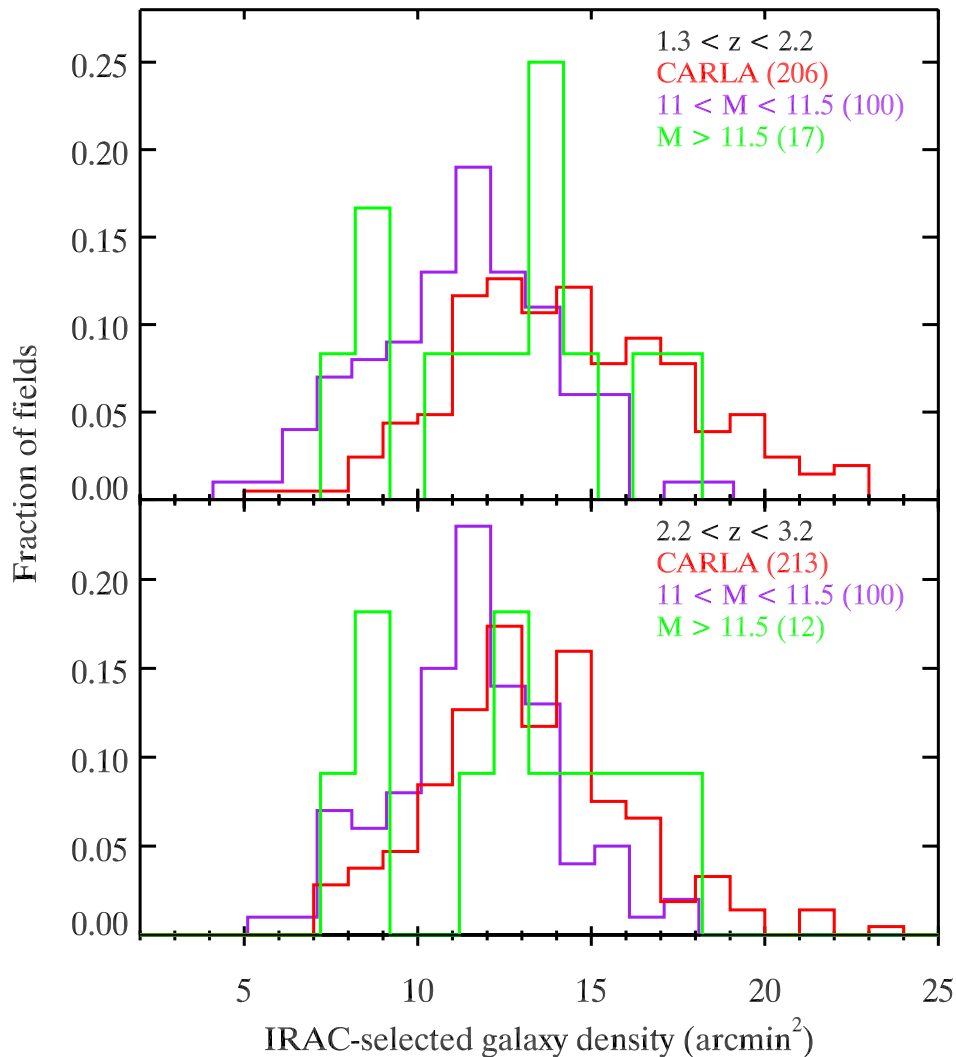


Figure 4.3: A comparison of the environment surrounding radio-quiet UDS galaxies with stellar masses of $11 < \log(M/M_{\odot}) < 11.5$ (which are similar to masses of CARLA host galaxies) and $\log M > 11.5 M_{\odot}$ to the CARLA RLAGN. The top panel displays galaxies at $1.3 < z < 2.2$, the bottom panel displays galaxies at $2.2 < z < 3.2$. The environment is assessed using the IRAC-selected galaxy density within an arcmin of the targeted UDS galaxies and RLAGN. The number of galaxies in each group is shown in brackets in the legend.

	Spearman-rank coefficient	P
Extent of radio emission	0.00	0.99
$L_{\text{Radio}}/L_{\text{Bolometric}}$	-0.05	0.40
Spectral index	0.08	0.29
SMBH mass	0.16	0.02

Table 4.1: Results from Spearman rank correlation test between the listed parameters and the surrounding galaxy density of RLAGN. P is the probability of obtaining the rank coefficient by chance; P values greater than 0.05 mean the correlation is not significant. The only significant correlation is between IRAC-selected galaxy density and SMBH mass of the RLAGN.

The $11 < \log(M/M_{\odot}) < 11.5$ galaxies typically occupy lower density environments than the CARLA galaxies at all redshifts, whereas the $\log(M/M_{\odot}) > 11.5$ galaxies occupy slightly lower density environments at $z < 2.2$ (KS $p=0.04$), but similar environments at higher redshifts. The numbers in the brackets indicate how many galaxies are in each distribution; the number of $\log M > 11.5 M_{\odot}$ UDS galaxies at these redshifts is very limited.

We expect that the CARLA host galaxies have masses of $11 < \log(M/M_{\odot}) < 11.5$ for two reasons: (i) the majority of the UDS galaxies with similar [3.6] magnitudes and [3.6]-[4.5] colors typically have masses in this range, and (ii) the SHzRG masses are mostly in this range. Thus these results show that the environments of CARLA RLAGN are typically denser than the radio-quiet galaxies of similar mass.

In Fig. 4.4 we compare the average radial density profile around the CARLA and control galaxies which are surrounded by between 14 and 18 IRAC-selected galaxies per arcmin² within a 1 arcmin radius (regions with $2 - 4\sigma$ galaxy overdensities). The central densities are similarly overdense (by construction), but beyond 1 arcmin (~ 0.5 Mpc) the profiles diverge: the regions around RLAGN are denser than the control galaxies. This implies that the structures surrounding the RLAGN are more extended and therefore more massive than those around the radio-quiet control galaxies. RLAGN are more likely to reside in high-mass groups and clusters than the average radio-quiet massive galaxy.

This results mean the RLAGN are not simply analogues of the radio-quiet sample that are observed in an active phase. The RLAGN are a subset of the general massive galaxy population that are located in denser environments. This suggests an intimate link between the jet-launching probability of the central supermassive black hole and the host galaxy's environment on scales of ≥ 0.5 Mpc.

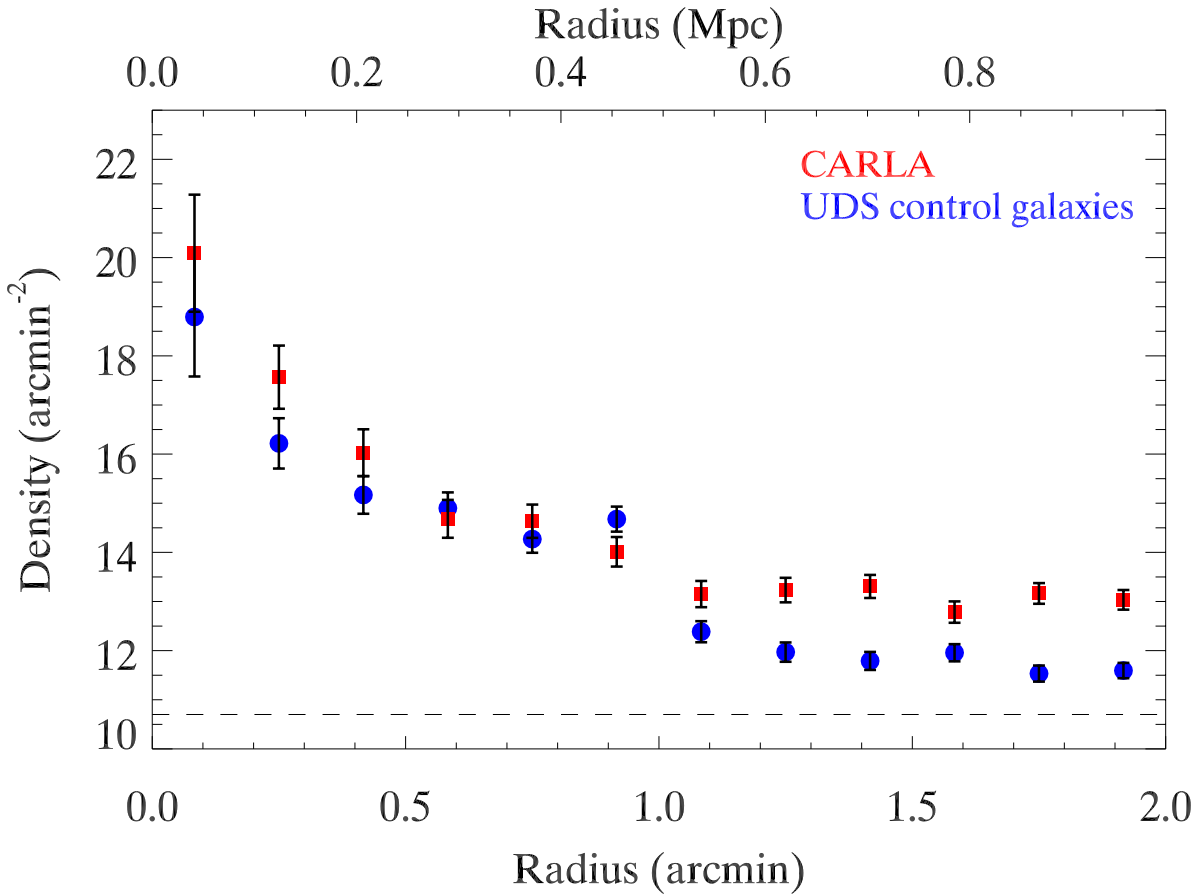


Figure 4.4: The radial profile of the IRAC-selected sources galaxy density surrounding CARLA RLAGN and UDS control galaxies which have environmental densities between 14 and 18 galaxies per arcmin⁻². The profile of the central 1 arcmin are similar (by construction), but the overdensities around the CARLA galaxies extend further out indicating that larger and more massive structures surround the RLAGN. The radius is shown both in arcmin, and proper angular distance for galaxies at $z = 2.2$.

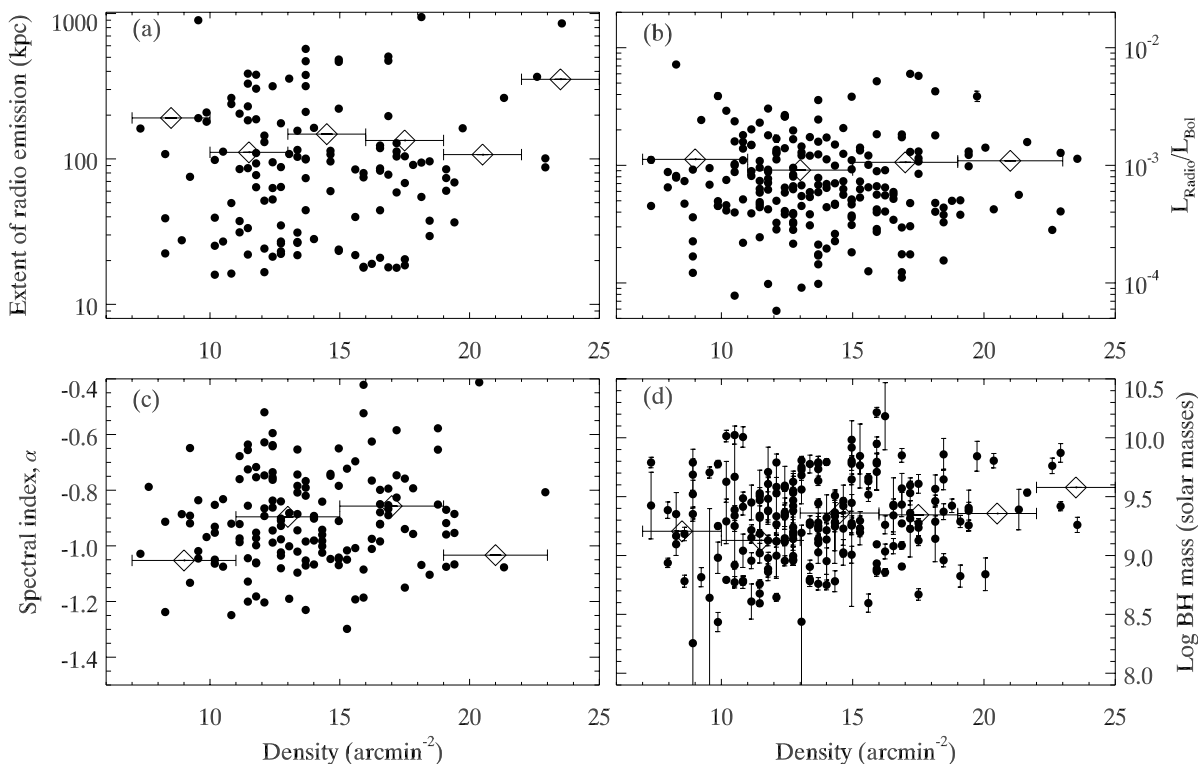


Figure 4.5: Examining relationships between the large-scale density of the CARLA RLAGN and properties of the radio emission and SMBH. From the top to bottom: (a) the extent of the radio emission for 131 resolved CARLA sources covered by the FIRST survey. Open diamonds are the mean radio extent of RLAGN in each density bin. (b) Ratio of radio to bolometric AGN power. (c) Spectral index α (where $S_\nu \propto \nu^\alpha$); and (d) SMBH mass for the 211 CARLA AGN matched with the Shen et al. (2011) SDSS catalogue

4.3.2 Environmental selection bias due to radio properties

The radio properties of a source may be affected by its environment. Radio luminosities may be enhanced in rich environments if the relativistic plasma is confined by dense intergalactic/intracluster medium (Barthel & Arnaud, 1996), or the environment could influence the supermassive black hole (SMBH) accretion mode or the properties of the SMBHs themselves (e.g. mass or spin) increasing the likelihood of powerful radio emission (Fanidakis et al., 2011). In a luminosity-limited sample of radio-loud galaxies such as the CARLA sample these effects may create a selection bias.

We examine these ideas by comparing the environments of the CARLA galaxies with the extent and spectral index of their radio emission, their SMBH mass, and the ratio of their radio to bolometric luminosity (for the quasars) in Fig. 4.5. Our measure of environment is not robust for individual objects as it is strongly influenced by cosmic variance along the

line of sight. Nevertheless, our large sample means this large-scale structure should balance out and we are able to measure statistical properties. This means that whilst we cannot be certain that any particular source is in a cluster or dense environment, we can be confident that correlations of environmental galaxy density with other properties will be apparent if they exist.

If radio jets are confined by surrounding gas in dense environments causing the emission to be enhanced we expect the RLAGN in dense environments to have smaller radio sizes, a higher spectral index and emit more radio power for a given bolometric luminosity than those in less dense environments. Figs. 4.5a, b and c show no significant correlation with these properties: the mean radio extent of resolved sources is ~ 140 kpc (median ~ 90 kpc) and is approximately constant with density (the Spearman correlation coefficient is 0.0, $P = 0.99$); and a Spearman rank correlation test shows that neither the ratio of radio to bolometric luminosity nor the spectral index is correlated with the surrounding galaxy density. There is also no significant difference between the environments of radio sources that are resolved in the FIRST survey and those that are not (KS $p=0.13$) confirming that the size of the radio emission is not affected by the Mpc-scale environment of the AGN host galaxy.

There is no evidence that the size, spectral index or radio luminosity of the AGN are affected by their environment, but since the radio extent and luminosity of a RLAGN depends on orientation and redshift we are unable to draw strong conclusions from these null results alone. However the literature also suggests that powerful radio emission is not enhanced in dense environments, nor is a dense environment a prerequisite for visible radio emission. Wylezalek et al. (2013a) found no correlation between the radio power of the CARLA AGN and their environment over 2 orders of magnitude in radio power, from $10^{27.5-29.5} \text{W Hz}^{-1}$ (although this result may be radio-luminosity or redshift dependant since Donoso et al. 2010 found a negative trend between radio power and galaxy clustering at lower radio luminosities and redshifts).

Powerful radio jets can also be observed outside dense environments: Venemans et al. (2007) searched for proto-clusters around 8 RLAGN and found that 2 were not in dense environments. Hatch et al. (2011b) and Galametz et al. (2010b) also found approximately half of their sample of 8 RLAGN did not reside in dense environments. Additionally, almost a quarter (24%) of CARLA RLAGN reside in average environments: the IRAC-selected galaxy densities within 1arcmin of these sources are less than 1σ above the typical galaxy density of the control field. This suggests that a surrounding dense intracluster environment is not a prerequisite for the formation of radio-loud jets, although it is clear that there is a strong bias.

If the environment influences the properties of the SMBH directly we may expect a correlation between the SMBH mass and its environment. Although there is a great deal of scatter in Fig. 4.5d there is a statistically significant, but small tendency for more massive

SMBHs to lie in denser environments; the Spearman correlation coefficient is 0.16 at 98% confidence.

4.4 Implications of results

4.4.1 Maximum fraction of massive galaxies that become RLAGN

The environments of radio-quiet massive galaxies differs from that of RLAGN significantly, therefore not all massive galaxies undergo powerful radio-loud feedback during $1.3 < z < 3.2$. The massive galaxy population, whose environments are shown in the blue histogram of Fig. 4.2, must consist of a population of massive galaxies that might become radio-loud at some point (which reside in the range of environments shown by the red histogram), and a population of massive galaxies that will never be host to a RLAGN.

We estimate the maximum fraction of massive galaxies that can host a RLAGN by scaling the CARLA distribution to match the dense tail of the UDS environment distribution. We use a least squares fitting algorithm to match the distributions in galaxy density bins from 15 galaxies per arcmin⁻² to the maximum density surrounding the control sample². We find that less than 50% of the control galaxies can ever go through a powerful RLAGN phase.

This fraction is likely to be significantly less. Comparing the radial profile of control and CARLA galaxies with the same central density in Fig. 4.4 showed that the CARLA overdensities are larger than those around the control galaxies. Thus only a fraction of the control galaxies situated in dense environments may have a powerful RLAGN phase.

The number density of powerful radio galaxies changes dramatically over the full redshift range of the CARLA survey, with powerful FR II RLAGN being much more numerous at $z \gtrsim 2$ than at $z \sim 1$ (Willott et al., 2001). We therefore divided the CARLA sample into two redshift bins, $1.3 < z < 2.2$ and $2.2 < z < 3.2$. To match the mass distribution in each redshift bin we were limited to 51 UDS control galaxies at $1.3 < z < 2.2$ and 31 control galaxies at $2.2 < z < 3.2$ ³. The selection was repeated 100 times and the averaged distributions are shown in Fig. 4.6. Each subset shows the same trend as the entire ensemble: RLAGN at all redshifts typically occupy denser environments than radio-quiet galaxies, however there is a larger discrepancy at lower redshift. Up to $z = 2.2$, less than 30% of massive galaxies can ever go through a powerful RLAGN phase, whilst up to 59% of massive galaxies at $2.2 < z < 3.2$ have a powerful RLAGN phase. Hence we find some evidence for a decrease with time in the fraction of massive galaxies that undergo

²The result is not sensitive to this lower limit. We obtain similar results when we run the algorithm using lower limits of 14-16 galaxies per arcmin⁻²

³However even in this limited control sample we are unable to match the [3.6] magnitudes exactly: 13% of the CARLA galaxies have $[3.6] < 19.5\text{mag}$ whereas 4% of the control galaxies have such bright magnitudes.

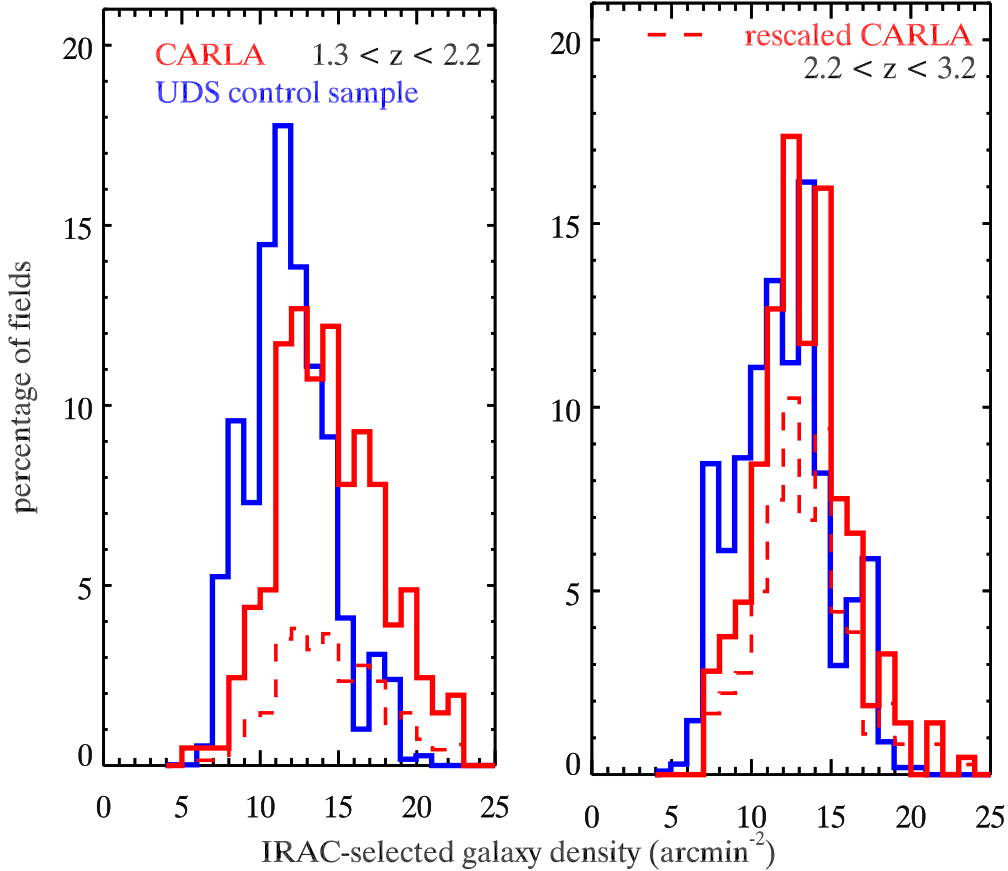


Figure 4.6: A comparison of the environment surrounding the CARLA RLAGN (red solid line) and UDS control galaxies (blue) in two redshift bins, $1.3 < z < 2.2$ (left) and $2.2 < z < 3.2$ (right). The maximum fraction of massive galaxies that can host a RLAGN is determined by scaling the CARLA distribution to match the dense tail of the control sample. These are shown as the dashed red histograms. Not more than 59% of the massive galaxy population at $2.2 < z < 3.2$ can host a RLAGN. This fraction decreases to less than 30% at $1.3 < z < 2.2$.

powerful radio-feedback.

4.4.2 Total lifetime of the radio emitting phase

Only ~ 70 UDS galaxies at $1.3 < z < 3.2$ can be selected to match the $[3.6]$ magnitudes and $[3.6]$ - $[4.5]$ colors of the CARLA radio galaxy sample so the number density of massive galaxies with the same mass distribution as the RLAGN host galaxies is $n(\text{massive galaxies}) \sim 7 \times 10^{-6} \text{ Mpc}^{-3}$ comoving.

The fraction of time a RLAGN is observable as radio-loud can be estimated through the

ratio of the density of active RLAGN to the density of galaxies that will host a RLAGN:

$$f = \frac{n(RLAGN)}{n(\text{massive galaxies}) \times f_{RL}} \quad (4.1)$$

where f_{RL} is the fraction of galaxies that can become radio-loud, $n(RLAGN)$ is the number density of RLAGN with $L_{500\text{MHz}} > 10^{27.5} \text{ W Hz}^{-1}$, which is $5 - 10 \times 10^{-8} \text{ Mpc}^{-3}$ comoving at $1.3 < z < 3.2$ (Rigby et al., 2011). Under these assumptions a RLAGN is radio-bright for at least 2 per cent of the time between $z = 3.2$ and $z = 1.3$, i.e. $\gtrsim 60 \text{ Myr}$. We obtain similar time periods of radio-bright AGN activity if the sample is divided into 2 redshift bins.

The radio-bright lifetime of RLAGN is limited to a few $\times 10 \text{ Myr}$ (Blundell & Rawlings, 1999) so this result is consistent with galaxies undergoing a single powerful RLAGN during this period. However, since we derive lower limits of the total radio-emitting lifetime we cannot rule out that powerful radio-loud AGN feedback is a reoccurring phenomenon with each RLAGN host galaxy undergoing multiple powerful radio-loud episodes between $z = 3.2$ and $z = 1.3$.

4.4.3 Heating the intracluster medium

The maximum number density of galaxies that become radio-loud is $\sim 7 \times 10^{-6} \text{ Mpc}^{-3}$ and is therefore similar to that of $> 10^{14} M_{\odot}$ galaxy clusters in the present day. It is therefore possible that every galaxy cluster hosted a powerful RLAGN at some point between $1.3 < z < 3.2$.

The minimum radio-loud lifetime allows us to estimate the total energy deposited into the forming intracluster medium (ICM). The energy output by powerful RLAGN at $z \geq 2$ is a few $\times 10^{59} \text{ erg}$ in 30 Myr considering only the electron population, and up to 10^{62} erg when including the protons in the jets (Erlund et al., 2006; Johnson et al., 2007; Erlund et al., 2008). Across the entire radio-loud lifetime of these jets a total of a $2 \times 10^{62} \text{ erg}$ may be pumped into the surrounding intergalactic medium.

It is well known that extra heating of the ICM on top of gravitational heating of about 1 keV per particle is required to reproduce the observed excess of ICM entropy (Borgani et al., 2001). In a cluster of gas mass $1 \times 10^{14} M_{\odot}$ this would require $2 \times 10^{62} \text{ erg}$, so the energy deposited by the RLAGN across their active lifetime is sufficient to provide this energy to the ICM provided the jets contain protons as well as electrons and positrons.

4.5 Conclusions

We have shown that the environments of RLAGN and similarly massive radio-quiet galaxies differ so significantly that only a subset ($< 50\%$) of massive galaxies at $1.3 < z < 3.2$ may

host a powerful RLAGN. Even when we compare the subset of RLAGN and control galaxies that have the same local density we find that the RLAGN reside in larger and more massive groups/clusters. Thus having a high stellar mass does not ensure that a galaxy will host a RLAGN and we conclude that the presence of a radio-loud jet must be influenced by the large-scale environment of the host galaxy.

The correlation between radio-loud AGN activity and high density environments is not the result of an observational selection bias. We examined whether dense environments enhanced radio emission from a RLAGN by confining the radio emitting plasma or transforming AGN power into radio power. We found no correlation between the environment and the radio size, spectral index or fraction of AGN power emitted at radio frequencies. In addition, approximately a quarter of RLAGN appear to reside in average environments. We therefore conclude that dense environments do not greatly enhance the radio emission from a RLAGN at this redshift.

We estimate the maximum space density of galaxies that experience a radio-loud episode in the epoch at $1.3 < z < 3.2$ to be $\sim 7 \times 10^{-6} \text{ Mpc}^{-3}$ which is similar to the space density of proto-clusters: objects that can collapse to form a $> 10^{14} M_{\odot}$ galaxy cluster by the present day. Distant clusters and proto-clusters are reliably found near powerful radio-loud AGN (Venemans et al., 2007; Galametz et al., 2010a, 2013; Hatch et al., 2011b,a; Wylezalek et al., 2013a) so it is possible that every cluster progenitor experienced a powerful feedback episode during $1.3 < z < 3.2$. We estimate that each powerful radio-loud galaxy is active for at least 60 Myr and produces jets that can extend for several hundred kpc. If the jets contain protons then this feedback could provide enough energy per gas particle to pre-heat the forming ICM which can have a dramatic effect on the surrounding proto-cluster galaxies by cutting off the gas supply to limit further stellar and SMBH growth.

Acknowledgments: We thank Will Hartley, Alice Mortlock and Omar Almaini for providing us with their DR8 UDS catalogues including the derived photometric redshifts and stellar masses. NAH acknowledges support from STFC through an Ernest Rutherford Fellowship.

The *Herschel* view of the environment of the radio galaxy 4C+41.17 at $z = 3.8$

Dominika Wylezalek, Joël Vernet, Carlos De Breuck, Daniel Stern, Audrey Galametz, Nick Seymour, Matt Jarvis, Peter Barthel, Guillaume Drouart, Thomas R. Greve, Martin Haas, Nina Hatch, Rob Ivison, Mathew Lehnert, Klaus Meisenheimer, George Miley, Nicole Nesvadba, Huub J.A. Röttgering, Jason A. Stevens

Monthly Notices of the Royal Astronomical Society, Volume 428, Issue 4, p.3206-3219

Abstract We present *Herschel* observations at 70, 160, 250, 350 and 500 μm of the environment of the radio galaxy 4C+41.17 at $z = 3.792$. About 65% of the extracted sources are securely identified with mid-IR sources observed with the *Spitzer Space Telescope* at 3.6, 4.5, 5.8, 8 and 24 μm . We derive simple photometric redshifts, also including existing 850 μm and 1200 μm data, using templates of AGN, starburst-dominated systems and evolved stellar populations. We find that most of the *Herschel* sources are foreground to the radio galaxy and therefore do not belong to a structure associated with 4C+41.17. We do, however, find that the SED of the closest ($\sim 25''$ offset) source to the radio galaxy is fully consistent with being at the same redshift as 4C+41.17. We show that finding such a bright source that close to the radio galaxy at the same redshift is a very unlikely event, making the environment of 4C+41.17 a special case. We demonstrate that multi-wavelength data, in particular on the Rayleigh-Jeans side of the spectral energy distribution, allow us to confirm or rule out the presence of protocluster candidates that were previously selected by single wavelength data sets.

5.1 Introduction

5.1.1 High-Redshift Radio Galaxies as Tracers of Protoclusters

High-redshift radio galaxies (HzRGs) are galaxies in the distant Universe ($z > 1$) showing enormous radio luminosities ($L_{500\text{MHz}} > 10^{27}\text{WHz}^{-1}$, Miley & De Breuck, 2008). They are extremely rare objects, with number densities $\sim 10^{-8}\text{Mpc}^{-3}$ in the redshift range $2 < z < 5$ (Dunlop & Peacock, 1990; Willott et al., 2001; Venemans et al., 2007). Investigating their spectral energy distribution (SED) reveals features of their stellar, dust and AGN components. In particular, studies of the stellar and dust component have shown that HzRGs are amongst the most massive galaxies in the early Universe (e.g., Seymour et al., 2007; Bryant et al., 2009; De Breuck et al., 2010). According to the hierarchical model of galaxy assembly (White & Rees, 1978), this implies that they reside in peaks of dark matter overdensities. As galaxy clusters represent the most massive structures in the Universe, HzRGs are expected to preferentially reside in sites of galaxy cluster formation. At $z = 2$ the Universe is only ~ 3.2 Gyr old and galaxy clusters are likely still forming but have not had time to virialize. For this reason we refer to these matter overdensities as protoclusters. Observations have indeed shown that HzRGs preferentially reside in overdense environments (e.g. Stevens et al., 2003; Falder et al., 2010; Stevens et al., 2010; Galametz et al., 2010b, 2012; Mayo et al., 2012) and protoclusters are very likely to be found in the vicinity of these objects. As HzRGs are found up to very high redshift, they serve as efficient beacons for identifying very high redshift galaxy clusters. The fields of HzRGs are therefore unique laboratories to study the formation and evolution of the first galaxies and galaxy structures.

5.1.2 The HeRGÉ Project

With the launch of the *Herschel* satellite (Pilbratt et al., 2010), it is possible for the first time to obtain full coverage of the far-IR SED for a large sample of HzRGs. The *Herschel* Radio Galaxy Evolution project (HeRGÉ) makes use of the two imaging instruments on board *Herschel*: PACS, the Photodetecting Array Camera (Poglitsch et al., 2010) and SPIRE, the Spectral and Photometric Imaging Receiver (Griffin et al., 2010). These instruments cover a wavelength range of $70 - 500\mu\text{m}$ and thus constrain the far-IR dust peak very well for a range of redshifts. The project was granted $\sim 27\text{h}$ of OT1 observing time (PI: N. Seymour) allowing 71 HzRGs to be observed in five bands in PACS and SPIRE (PACS: $70/100\mu\text{m}$, $160\mu\text{m}$; SPIRE: $250\mu\text{m}$, $350\mu\text{m}$, $500\mu\text{m}$). In addition to studying the radio galaxies themselves in more detail (Ivison et al., 2012; Rocca-Volmerange et al., 2013; Seymour et al., 2012) project HeRGÉ allows us, for the first time, to systematically study the environments of the radio galaxies at these wavelengths, reaching out $1-3'$ from the HzRGs. This complements our statistical studies of the HzRG environments in the mid-IR

(Galametz et al., 2012; Mayo et al., 2012). Reaching out to longer wavelengths allows us to constrain the dust peak of the SEDs and derive photometric redshift estimates to confirm or rule out overdensities associated with the HzRG.

This work reports our pilot study of the well known HzRG 4C+41.17. This analysis will be expanded systematically to the whole data set in future work.

5.1.3 4C+41.17

4C+41.17 at $z = 3.792$ is one of the best studied HzRGs. It was discovered by Chambers, Miley, & van Breugel (1990). The steep radio spectrum ($\alpha \sim -1.3$) together with extended optical continuum emission and the large rest frame Ly α equivalent width ($\sim 270 \text{ \AA}$) identified 4C+41.17 as a HzRG. Its high far-infrared luminosity, $L_{\text{FIR}} \sim 10^{13} L_{\odot}$ (Benford et al., 1999; Humphrey et al., 2011), large dust mass (Dunlop et al., 1994) and molecular gas reservoir (De Breuck et al., 2005) make this radio galaxy a very likely site of an enormous starburst at high redshift. Similar far-infrared luminosities have also been found for other high redshift radio galaxies (Barthel et al., 2012; Seymour et al., 2012) accumulating the evidence for massive starburst in these galaxies. Deep observations at $450 \mu\text{m}$ and $850 \mu\text{m}$ carried out with SCUBA (Submillimeter Common-User Bolometer Array, Holland et al., 1999) by Ivison et al. (2000) in the field centered on 4C+41.17 show an order-of-magnitude overdensity of luminous sub-mm galaxies within a 2.5 arcmin diameter region centered on the radio galaxy. From tentative redshift constraints based on the 450 to $850 \mu\text{m}$ and the $850 \mu\text{m}$ to 1.4 GHz flux density ratios of sources then available, Ivison et al. (2000) conclude that the overdensity is consistent with lying at the same redshift as the radio source, 4C+41.17, and therefore suggests a likely protocluster. However, photometric redshifts estimated from the $1.6 \mu\text{m}$ stellar bump by Greve et al. (2007) place at least two out of the five sub-mm sources reported by Ivison et al. (2000) at redshifts lower than 1.3. Greve et al. (2007) also present deep SHARC-II (Dowell et al., 2003) $350 \mu\text{m}$ and MAMBO (Max-Planck Millimeter Bolometer Array, Kreysa et al., 1998) $1200 \mu\text{m}$ imaging of the field around 4C+41.17 and combine them with multi-wavelength data at 3.6, 4.5, 5.8, $8 \mu\text{m}$ from *Spitzer* IRAC (Infrared Array Camera, Fazio et al., 2004), 24 and $70 \mu\text{m}$ data from *Spitzer* MIPS (Multiband Imaging Photometer, Rieke et al., 2004) and $850 \mu\text{m}$ observations from SCUBA. They find a surface density of ~ 0.24 $1200 \mu\text{m}$ sources per arcmin^{-2} to a depth of ~ 2 mJy, consistent with the blank field source density at this wavelength. From cross-correlation analysis and estimation of photometric redshifts, Greve et al. (2007) conclude that at least half of the sub-mm galaxies are foreground sources and are not, in fact, associated with 4C+41.17.

In this paper, we present a multi-wavelength study of the environment of the HzRG 4C+41.17, recently observed within the HeRGÉ project in five PACS and SPIRE bands. Rocca-

Volmerange et al. (2013) present a full, in-depth study of the SED of the radio galaxy itself. We make use of the data at hand to derive photometric redshifts and to confirm or rule out the companionship of the galaxies in the field with the HzRG. Section 5.2 describes the observations and reduction of the multi wavelength data. Section 5.3 gives details of the source extraction and cross-correlation. In section 5.4 we present our analysis and draw conclusions in §5.5. Throughout the paper we assume $H_0 = 70 \text{ km s}^{-1} \text{ Mpc}^{-1}$, $\Omega_{\text{matter}} = 0.3$, $\Omega_{\Lambda} = 0.7$.

5.2 Observations and Data Reduction

5.2.1 Far-Infrared Observations

Observations at 70 and 160 μm were obtained with the Herschel/PACS instrument on UT 2010 October 12. The image covers $\sim 20 \text{ arcmin}^2$. We retrieved the Level 0 data from the *Herschel* Science Archive and processed it using version 7.3.0 of the *Herschel* Interactive Processing Environment, HIPE (Ott, 2010). The data were taken to Level 1 following the standard pipelines provided in HIPE. To create Level 2 products, we slightly adapted the standard pipeline to correct for the slew to target data and to improve the point source sensitivity by decreasing the high pass filter radius¹.

The *Herschel*/SPIRE instrument observed a region covering $\sim 80 \text{ arcmin}^2$ around 4C+41.17 on UT 2010 September 21 with all three bands, at 250 μm , 350 μm and 500 μm . The exposure times for the PACS/SPIRE observations were $2 \times 1404 \text{ s}$ and 721s, respectively, reaching an average 1σ depth of 6.0, 6.4, 10.2, 9.6, 11.2 mJy at 70, 160, 250, 350 and 500 μm , respectively. Both the SPIRE and PACS observations are part of the guaranteed time key program *The Dusty Young Universe: Photometry and Spectroscopy of Quasars at $z > 2$* (Observation ID: 1342206336/7 and 1342204958, PI: Meisenheimer).

5.2.2 Mid-Infrared Data

In addition, we include *Spitzer* IRAC and MIPS observations in the analysis from Seymour et al. (2007). The field was deeply mapped using all four IRAC bands (3.6, 4.5, 5.8, 8 μm - referred to as channels 1, 2, 3 and 4), covering an area of $5.3 \times 5.3 \text{ arcmin}^2$, and all three MIPS bands (24, 70 and 160 μm), covering an area of $\sim 8.0 \times 7.4 \text{ arcmin}^2$. The exposure times were 5000s for the IRAC observations and 267 s, 67 s and 2643 s for the three MIPS bands, in order of increasing wavelength. The data were reduced using the *Spitzer* reduction package, MOPEX. In this work, we only use the 24 μm images given the deeper PACS observations at longer wavelengths. The 3σ depths reached were 0.8, 1.1,

¹<http://herschel.esac.esa.int/twiki/pub/Public/PacsCalibrationWeb/bolopsfv1.01.pdf>

3.2 and 4.3 μJy for the IRAC channels 1, 2, 3 and 4, respectively and 30 μJy for the MIPS 24 μm image (Greve et al., 2007).

5.2.3 (Sub)millimetre Data

A field covering $\sim 58 \text{ arcmin}^2$ around 4C+41.17 was imaged at 1200 μm with MAMBO. Details of the observations, data reduction and analysis are reported by Greve et al. (2007). Positions and flux densities of the extracted sources are taken from there.

4C+41.17 was also observed at 850 μm with SCUBA (covering an area $\sim 2.5 \text{ arcmin}$ in diameter, Ivison et al., 2000; Stevens et al., 2003). The data were initially published by Ivison et al. (2000) and details can be found there.

5.3 Source Extraction and Cross-correlation Analysis

5.3.1 Source Extraction

PACS/SPIRE Source Extraction

Source extraction in the PACS and SPIRE images is performed using the tool `sourceExtractorDaophot` that is included in HIPE. The FWHM of the different bands are taken from the *PACS Observer's Manual*² and are 5.2, 12, 18.1, 25.2 and 36.3'' for 70, 160, 250, 350 and 500 μm , respectively. The parameters for the source extraction, such as shape parameters roundness and sharpness, are tuned such that false detection rates and source blending is minimized (Table 5.1). We extract sources at a significance $\geq 2.5\sigma$ within a circle of 3.3' (corresponding to 34.2 arcmin^2) radius around the radio galaxy. Due to the scanning mode the coverage is inhomogeneous further away from the image center. We extract two sources from the PACS 70 μm image, 8 sources from the PACS 160 μm image, 27 sources from the SPIRE 250 μm image, 16 sources from the SPIRE 350 μm image and 8 sources from the SPIRE 500 μm image. The extracted source positions and given names are listed in Table 5.3 in order of increasing RA. We derive aperture photometry for the extracted sources applying an aperture correction of 1.45 and 1.44 to the blue and red PACS flux densities, respectively³. Due to the inhomogeneous coverage in the *Herschel* images the uncertainty on the flux densities is derived from sky annuli (see Table 5.1) around each source.

Aperture photometry is, however, not applicable in the case of source 16 and 4C+41.17, which are blended. We therefore apply PSF photometry to those sources using `StarFinder` (Diolaiti et al., 2000), a code designed to analyze images in very crowded fields. The deblending strategy in `StarFinder` consists of an iterative search for residuals around the object

²http://www.iac.es/proyecto/herschel/pacs/pacs_om.pdf, p. 13

³http://herschel.esac.esa.int/Docs/PACS/html/pacs_om.html

96 5. A Herschel view of the environment of the radio galaxy 4C+41.17 at $z = 3.8$

Table 5.1: HIPE parameters used to extract sources with sourceExtractorDaophot and details of the observations in different *Herschel* bands. Roundness and sharpness parameters between -2 to 2 and -1.5 to 2 were used for the extraction in all bands.

Band	FWHM [arcsec]	beam area [arcsec ²]	aperture radius [arcsec]	sky annulus [arcsec]	exposure time	average 1σ depth [mJy]
PACS 70 μm	5.2	30.6	6	6-10	$2 \times 1404\text{s}$	6.0
PACS 160 μm	12	163.2	10	10-15	$2 \times 1404\text{s}$	6.4
SPIRE 250 μm	18.1	373.3	22	22-32	721s	10.2
SPIRE 350 μm	25.2	716.7	30	30-40	721s	9.6
SPIRE 500 μm	36.3	1493.1	42	42-52	721s	11.2

and subsequent fitting. We assumed the PSF to be Gaussian with a FWHM corresponding to the beam size. The positions of the two sources were determined independently in each *Herschel* image as different material is probed at different wavelengths. The flux density measurements with StarFinder are consistent with the ones obtained with HIPE for unblended sources. Postage stamps of the image, synthetic image and residual image after deblending is shown in Figure 5.1. No other sources in the field are blended and the fluxes densities and uncertainties (including the 15% and 7% flux calibration uncertainties added in quadrature to the statistical uncertainties for PACS and SPIRE flux densities, respectively, Seymour et al., 2012) are given in Table 5.2.

IRAC/MIPS Source Extraction

Source extraction is performed using SExtractor (Bertin & Arnouts, 1996) in dual image mode using the 4.5 μm image for detection. We only report sources detected with a significance $\geq 3\sigma$. Unlike Greve et al. (2007), we use a smaller, 4" diameter aperture for the IRAC images because of the close proximity of other sources in that crowded field. Tests with an aperture of 9.26" diameter show that flux from neighbouring sources results in overestimated flux densities (e.g. for 4C+41.17 itself). We apply aperture corrections of 1.205, 1.221, 1.363, 1.571 to IRAC channels 1, 2, 3 and 4, respectively. MIPS 24 μm flux densities are measured in 5.25" aperture radii. The aperture correction applied, 1.78, is calculated as described by the MIPS instrument handbook⁴. The uncertainties reported in Table 5.2 include the 10% and 4.5% systematic uncertainties for the IRAC and MIPS flux densities, respectively, that were added in quadrature to the statistical uncertainties to account for the absolute flux calibration and color correction uncertainties (Seymour et al., 2007).

⁴<http://irsa.ipac.caltech.edu/data/SPITZER/docs/mips/mipsinstrumenthandbook/50/>

Table 5.2: Flux densities and 1σ uncertainties of sources with at least two *Herschel* detections

Source	$S_{3.6\mu m}$ [μ Jy]	$S_{4.5\mu m}$ [μ Jy]	$S_{5.8\mu m}$ [μ Jy]	$S_{8\mu m}$ [μ Jy]	$S_{24\mu m}$ [mJy]	$S_{70\mu m}$ [mJy]	$S_{160\mu m}$ [mJy]	$S_{250\mu m}$ [mJy]	$S_{350\mu m}$ [mJy]	$S_{500\mu m}$ [mJy]	$S_{850\mu m}$ [mJy]	$S_{1200\mu m}$ [mJy]
1	-	-	-	-	-	-	-	54 ± 15	61 ± 13	42 ± 11	-	-
2	41 ± 4	46 ± 5	44 ± 5	51 ± 5	0.37 ± 0.03	-	-	47 ± 11	38 ± 11	36 ± 16	-	3.0 ± 0.6
4	-	-	-	-	0.48 ± 0.03	-	-	42 ± 13	22 ± 7	-	-	-
5	16 ± 2	20 ± 2	26 ± 3	13 ± 2	0.31 ± 0.02	-	-	19 ± 3	26 ± 8	10 ± 3	-	7.5 ± 0.6
7	130 ± 13	104 ± 10	72 ± 8	193 ± 20	0.39 ± 0.03	-	-	31 ± 13	24 ± 11	19 ± 9	-	-
9	99 ± 10	73 ± 7	79 ± 9	97 ± 10	0.98 ± 0.05	19 ± 5	67 ± 6	64 ± 11	31 ± 6	-	-	-
11	29 ± 3	29 ± 3	24 ± 3	26 ± 3	0.35 ± 0.03	-	24 ± 7	44 ± 10	39 ± 8	33 ± 9	9 ± 1	4.6 ± 0.4
12	-	-	-	-	-	-	19 ± 7	27 ± 9	17 ± 4	-	-	3.0 ± 0.6
13	-	27 ± 3	-	45 ± 5	0.32 ± 0.02	-	-	15 ± 6	30 ± 14	-	-	-
16	11 ± 1	14 ± 2	24 ± 3	45 ± 5	0.47 ± 0.03	-	15 ± 6	42 ± 5	48 ± 4	39 ± 4	12 ± 1	3.8 ± 0.4
4C+41.17	17 ± 2	20 ± 2	27 ± 3	31 ± 4	0.36 ± 0.03	-	16 ± 7	36 ± 4	43 ± 4	38 ± 5	12 ± 1	4.4 ± 0.4
18	-	-	-	-	-	-	27 ± 6	33 ± 8	21 ± 6	-	-	-
19	128 ± 13	106 ± 11	98 ± 11	131 ± 13	0.62 ± 0.03	8 ± 3	23 ± 7	29 ± 11	-	-	-	-
21	21 ± 2	26 ± 3	28 ± 3	22 ± 2	-	-	-	15 ± 3	36 ± 15	21 ± 9	-	2.6 ± 0.6
24	38 ± 4	-	51 ± 5	-	-	-	-	10 ± 4	11 ± 5	-	-	3.6 ± 0.6
28	-	-	-	-	0.35 ± 0.03	-	-	37 ± 4	22 ± 8	-	-	-
29	130 ± 13	137 ± 14	117 ± 12	368 ± 37	1.41 ± 0.07	-	-	13 ± 4	17 ± 5	-	-	-

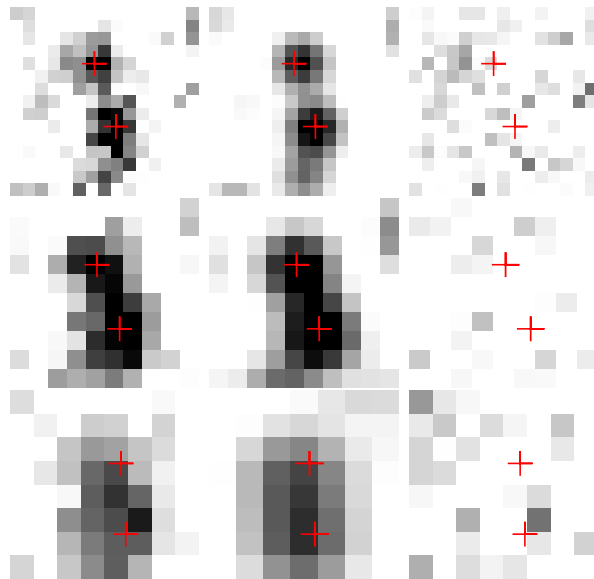


Figure 5.1: $0.6' \times 0.6'$ postage stamps of the data (left), synthetic image derived by StarFinder (center) and residuals (right) for source 16 and 4C+41.17. From top to bottom the images at 250, 350 and 500 μm are shown. The sources are blended in all three images but the homogeneous residual image shows the good deblending with StarFinder. Red crosses indicate the positions of 4C+41.17 (upper source) and source 16 (lower source).

5.3.2 Cross-Correlation Between Bands

After extracting sources in the different images with very different spatial resolutions we cross-correlate the sources in order to derive a clean, multi-wavelength source catalog. We only consider the 17 sources that have at least two detections in the *Herschel* bands in order to minimize false detections. For the cross-correlation, we choose the SPIRE 250 μm whose 1σ positional accuracy ($\sim 0.6 \times \frac{\text{FWHM}}{\text{SN}}$)⁵ outperforms the other bands. Although the PACS images have an even better spatial resolution, they cannot be used systematically as reference images due to their shallowness and small field of view (see Figure 5.2). We then cross-correlate the cleaned source list with the sources detected at shorter and longer wavelengths.

We look for MIPS counterparts within $10''$ of the 250 μm sources which corresponds to about the half-width at half maximum for the 250 μm observations and which also corresponds to their 3σ positional error assuming the bulk of the 250 μm detections has a signal to noise ratio (SN) of ~ 3 (Magnelli et al., 2012). Following Sutherland & Saunders (1992), we calculate the reliability $R = \exp(-\pi r^2 \sigma_1 \sigma_2 N)$ of finding no random source

⁵http://herschel.esac.esa.int/hcss-doc-8.0/load/hcss_urm/html/herschel.ia.toolbox.srcext.SourceExtractorDaophotTask.html

Table 5.3: Astrometry of the *Herschel* sources in the 4C+41.17 field, listed in order of increasing RA. Positions are in the J2000 system.

Source	RA _{70μm}	Dec. _{70μm}	RA _{160μm}	Dec. _{160μm}	RA _{250μm}	Dec. _{250μm}	RA _{350μm}	Dec. _{350μm}	RA _{500μm}	Dec. _{500μm}
1					6:50:37.0	41:28:54	6:50:36.9	41:28:53	6:50:36.6	41:28:44
2					6:50:40.5	41:30:03	6:50:40.7	41:30:05	6:50:40.7	41:30:05
3					6:50:40.9	41:32:35				
4					6:50:42.6	41:28:27	6:50:42.8	41:28:25		
5					6:50:43.1	41:29:21	6:50:43.7	41:29:16	6:50:43.2	41:29:17
6					6:50:44.0	41:27:43				
7					6:50:45.6	41:32:40	6:50:44.9	41:32:37	6:50:46.4	41:32:52
8					6:50:47.1	41:27:37				
9	6:50:47.4	41:30:46	6:50:51.1	41:30:06	6:50:47.2	41:30:44	6:50:47.3	41:30:46		
10					6:50:47.4	41:28:11				
11			6:50:48.9	41:31:27	6:50:48.8	41:31:26	6:50:49.1	41:31:28	6:50:49.0	41:31:22
12			6:50:50.1	41:28:21	6:50:50.1	41:28:19	6:50:50.0	41:28:21		
13					6:50:50.3	41:33:01	6:50:50.5	41:32:58		
14					6:50:50.3	41:27:37				
15					6:50:51.2	41:29:48				
16			6:50:51.2	41:30:06	6:50:51.4	41:30:07	6:50:50.9	41:30:04	6:50:51.1	41:30:06
4C+41.17			6:50:51.9	41:30:32	6:50:51.7	41:30:32	6:50:52.1	41:30:31		
18			6:50:52.4	41:28:53	6:50:52.2	41:28:51	6:50:52.4	41:28:55		
19	6:50:54.4	41:29:33	6:50:54.4	41:29:33	6:50:54.2	41:29:34				
20			6:50:54.6	41:30:47						
21					6:50:54.8	41:32:36	6:50:54.8	41:32:29	6:50:53.8	41:32:42
22									6:50:56.1	41:33:35
23					6:50:56.4	41:34:57				
24					6:50:60.0	41:27:58	6:50:59.6	41:27:58		
25					6:51:00.6	41:29:07				
26					6:51:00.8	41:31:16				
27					6:51:01.8	41:33:03				
28					6:51:02.1	41:31:59	6:51:01.7	41:31:57		
29					6:51:04.5	41:29:44	6:51:03.9	41:29:49		

closer than the nearest candidate where N is the number density of background objects, $r = \sqrt{(d_1/\sigma_1)^2 + (d_2/\sigma_2)^2}$ is the normalized distance, d_1 and d_2 are the positional differences in each axis between the sources, and σ_1 and σ_2 are the standard deviations of the error ellipse. Since $\sigma_1 = \sigma_2$ for our case, R simplifies to $R = \exp(-\pi(d_1^2 + d_2^2)N)$. Mayo et al. (2012) find a surface density $0.549 \text{ arcmin}^{-2}$ at the depth of the MIPS image. This is in agreement with the density found by Papovich et al. (2004) for the $23.1 \mu\text{Jy}$ depth of the MIPS image of 4C+41.17. We adopt this value for calculating the reliability of MIPS-250 μm sources counterparts. Candidates with reliabilities $R \geq 90\%$ are counted as correct identifications. We then cross-correlate the MIPS identifications with the IRAC catalogs and compute the reliability in the same way using a surface density of 2.80 arcmin^{-2} from Galametz et al. (2012). For sources with no MIPS identification, we cross-correlated the 250 μm sources directly with the IRAC catalogs. Again, candidates with reliabilities $\geq 90\%$ are counted as correct identifications. Although we require $R \geq 90\%$, the reliabilities for MIPS identifications are all above 96% and for IRAC identifications above 98%. Table 5.4 lists the separations between the MIPS and 250 μm counterparts and the IRAC and MIPS counterparts together with the corresponding reliabilities of them to be the correct identifications. Following this methodology, out of the 17 *Herschel* 250 μm sources, we identified MIPS counterparts for 11 sources (65%), and IRAC counterparts for an overlapping, but not identical set of 11 far-IR sources (65%). We checked the identifications where better

resolved PACS, intermediate wavelength data were available and confirmed our identified sources.

In Appendix C we show postage stamps of all sources with SPIRE 250 μm sources that have high probability ($R > 90\%$) counterparts in at least two IRAC bands and are detected in at least two *Herschel* bands. We also overplot the sub-mm position from Greve et al. (2007) where available. Except for sources 19 and 24, the Greve et al. (2007) astrometry is in very good agreement with our mid-IR identifications.

5.4 Analysis

5.4.1 Photometric Redshifts

We now derive photometric redshifts in order to investigate a physical connection between the radio galaxy and the objects in its vicinity. The following issues must be kept in mind when deriving photometric redshifts from combined sub-mm, far-IR and near-IR observations:

- (1). As the far-IR emission is of thermal origin, changing the dust temperature has the same effect on the sub-mm/mm colors as shifting the spectrum in redshift (Blain et al., 2002). It is thus impossible to estimate the redshift from far-IR data alone; supporting observations are necessary to constrain a redshift.
- (2). The dust (at far-IR, sub-mm wavelengths) to stellar flux density (at near-IR wavelengths) ratio has a range of about 3 decades and varies with morphology, total IR luminosity and gas-phase metallicity (Skibba et al., 2011). This is not always well represented in the available template libraries. When deriving our own empirical templates, we therefore create templates with a wide range of dust to stellar ratios, ranging from 100 to 5000.
- (3). Differing error bars for near-IR and far-IR observations will introduce a bias in the photometric redshift fitting procedure, giving the high signal-to-noise ratio of the IRAC data more weight.

For all 11 sources with detections in more than five wavelength bands we calculate photometric redshifts using the code `hyperz` (Bolzonella, Miralles, & Pelló, 2000) which minimizes the reduced χ^2 to find the best photometric redshift solution. We use both synthetic and empirical AGN and starburst templates from the SWIRE template library (Polletta et al., 2007) complemented with our own newly derived templates. The latter are obtained by combining a 1 Gyr old stellar population template from the Pégase.2 spectral evolution model (Fioc & Rocca-Volmerange, 1999) dominating the near-IR emission and

Table 5.4: Separation between MIPS and 250 μm sources, between IRAC and MIPS sources, and calculated reliabilities for the nearest source to be the correct identification. Where no value is given, the IRAC and/or MIPS source is either outside the field of view or there are no detections within a 10'' radius. Italized numbers indicate that there are only IRAC2 and 4 or IRAC1 and 3 detections for the 250 μm source as the other bands are outside the field of view. In case of source 21 the IRAC-250 μm position and corresponding probability is listed.

Source	MIPS–250 μm separation [']	$R_{24\mu\text{m}}$	IRAC–MIPS separation [']	R_{IRAC}
1	–	–	–	–
2	9.18	0.96	2.81	0.98
5	4.37	0.99	0.58	0.99
7	3.70	0.99	0.89	0.99
9	4.99	0.99	0.62	0.99
11	5.01	0.99	2.46	0.99
12	–	–	–	–
13	2.54	0.99	<i>0.51</i>	<i>0.99</i>
16	0.60	0.99	0.59	0.99
4C+41.17	6.46	0.98	0.96	0.99
19	4.86	0.99	0.71	0.99
21	–	–	2.47	0.99
28	4.87	0.99	–	–
29	5.26	0.99	0.40	0.99

empirical dust templates dominating the far-IR/sub-mm emission. Three dust templates are derived by (1) fitting the dust peak of 4C+41.17, a typical AGN dominated galaxy at high redshift; (2) the dust peak of the lensed “eyelash” galaxy at $z = 2.3$ (SMM J2135-0102, Ivison et al., 2010; Swinbank et al., 2010), a typical starburst galaxy at high redshift; and (3) source 11, which is very well sampled at far-IR/sub-mm wavelengths and for which the spectroscopic redshift is known ($z_{\text{spec}} = 1.18$, Greve et al., 2007). In this way, not only templates derived from lower redshift galaxies, such as the SWIRE templates, are available to us but also templates derived from higher redshift galaxies. For each of the three dust templates we create 15 composite templates with different ratios between the stellar emission in the near-IR and the dust emission in the far-IR. In order to get a matching wavelength coverage of the self-derived templates and the SWIRE templates we extend our templates by using greybody fitting results (see Section 5.4.2) for $\lambda > 1200 \mu\text{m}$. We

102 5. A Herschel view of the environment of the radio galaxy 4C+41.17 at $z = 3.8$

then extract the best-fitting templates from our 45 self-derived templates and the SWIRE library templates. Ultimately, a set of 9 different templates (see Table 5.5) are used for the 11 sources for which we derive photometric redshifts. Templates 1 (Spiral C) and 3 (starburst) (both from the SWIRE library) are generated from the SED of these objects using the GRASIL code (Silva et al., 1998) and improved by using IR spectra from the PHT-S spectrometer on the *Infrared Space Observatory* and from IRS on *Spitzer* (Houck et al., 2004). Template 2 is an empirical composite AGN+starburst template that fits IRAS 19254-7245. Template 4, 5, 6, 7, 8 and 9 are new, self-derived templates, with their properties described in Table 5.5. The resulting χ^2 distribution and the best χ^2 are thus derived by considering all redshifts and all templates in the final set. Note that the final χ^2 curve shows the minimum χ^2 for the template set as a function of redshift and therefore is dependent on the template set used.

Because of varying spatial coverage of the multi-wavelength data, filters are ignored for ‘out-of-field’ sources, but when a source is observed, but undetected, 3σ upper limits are taken into account by `hyperz`. We present the results of our photometric redshift estimates in Table 5.6 and show the best-fitting SEDs in Appendix C.

As mentioned above, differing error bars for the near-IR and far-IR observations introduce a bias in the fitting procedure giving the high signal-to-noise IRAC data more weight. However, by allowing a range of various ratios between the stellar (near-IR) and dust (far-IR) emission in the fitting templates we already make sure that the fits are not dependent on the IRAC data only but that also the relative contribution of the sources of emission is taken into account. To test this in more detail, we repeat the fitting procedure by relaxing the IRAC uncertainties to 20%. The best-fit redshifts are in agreement with the previously derived ones within the uncertainties. This shows that our results are not strongly biased by the IRAC data.

Greve et al. (2007) derived photometric redshifts using the $1.6 \mu\text{m}$ rest-frame stellar ‘bump’ in the observed IRAC data. They also estimate the redshift from the radio/sub-mm/mm color, but these only yield crude estimates, consistent with the redshift estimation from the stellar bump. Therefore, we only list z_{bump} in Table 5.6, which compares to our photometric redshifts and spectroscopic redshifts that exist for some of the sources. The uncertainties listed in Table 5.6 only reflect the 1σ formal uncertainties near the minimum of the χ^2 distribution and may be severely underestimated. We describe the quality of the photometric redshifts for each source in Appendix C. Figure 5.2 shows the spatial distribution of the sources, with white, open stars representing lower redshift objects ($z < 3$) and filled stars representing objects with $z > 3$.

The average redshift for these 11 sources is 2.0 ± 0.8 . This agrees with the average redshift for SPIRE $250 \mu\text{m}$ selected sources, $z = 1.8 \pm 0.2$, recently found by Mitchell-Wynne et al. (2012).

Table 5.5: Summary of the templates used for deriving photometric redshifts. Template 1-3 are from the SWIRE template library (Polletta et al., 2007). Template 4-9 are newly derived by combining the far-IR emission of 4C+41.17, the eyelash galaxy (SMM J2135-0102) and source 11, for which the spectroscopic redshift is known, with a 1 Gyr old stellar population from the Pégase.2 spectral evolution model (Fioc & Rocca-Volmerange, 1999). The far-IR and stellar emission were normalized to their peak flux densities and combined with varying ratios, as indicated.

Template ID	Description
1	Spiral C galaxy template, SWIRE template library
2	Seyfert 2+Starburst/ULIRG template for IRAS 19254-7245, SWIRE template library
3	Starburst/ULIRG template for IRAS 20551-4250, SWIRE template library
4	4C+41.17 far-IR template + old stellar population, stellar peak to dust peak ratio: 300 : 1
5	4C+41.17 far-IR template + old stellar population, stellar peak to dust peak ratio: 700 : 1
6	4C+41.17 far-IR template + old stellar population, stellar peak to dust peak ratio: 4500 : 1
7	SMM J2135-0102 far-IR template + old stellar population, stellar peak to dust peak ratio: 500 : 1
8	source 11 far-IR template + old stellar population, stellar peak to dust peakratio: 700 : 1
9	source 11 far-IR template + old stellar population, stellar peak to dust peak ratio: 1700 : 1

Table 5.6: Photometric redshifts, z_{phot} , were derived with hyperz for all sources with at least five detections. Stellar bump photometric redshifts, z_{bump} , and spectroscopic redshifts, z_{spec} are from Greve et al. (2007). Template ID's are described in Table 5.5.

Source	z_{phot}	template ID	z_{bump}	z_{spec}
2	2.5 ± 0.4	3	~ 1.8	...
5	2.4 ± 0.2	3	~ 2.6	2.672 ± 0.001
7	0.5 ± 0.1	1
9	0.6 ± 0.1	8
11	1.2 ± 0.2	9	< 1.3	1.184 ± 0.002
13	2.2 ± 0.4	5
16	4.0 ± 0.1	6
4C+41.17	3.5 ± 0.2	2	~ 4	3.792 ± 0.001
19	2.0 ± 0.1	4	< 1.3	0.507 ± 0.020
21	2.7 ± 0.2	7	~ 1.8	...
29	1.0 ± 0.1	4

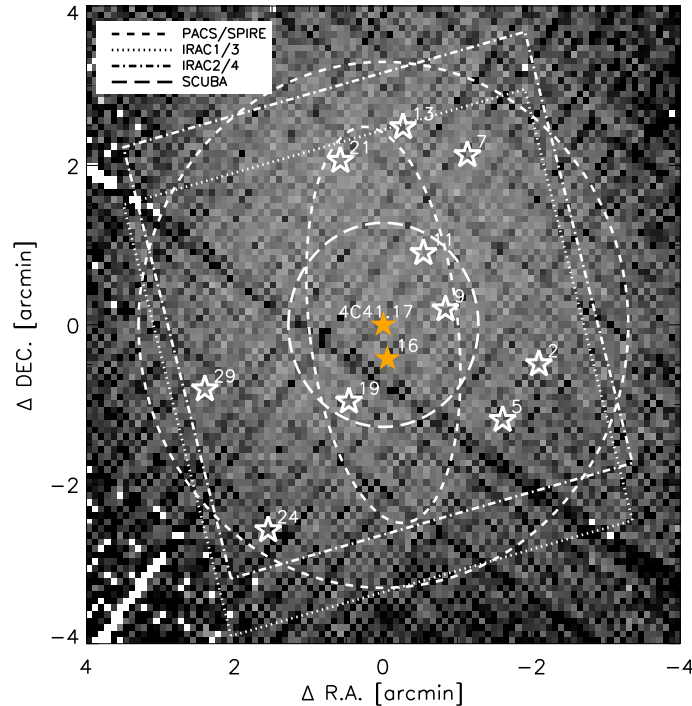


Figure 5.2: Coverage map and spatial distribution of sources with derived photometric redshifts, centered on 4C+41.17. Dark pixels indicate regions with low coverage. White, open stars indicate sources that have $z_{\text{phot}} < 3$, orange, filled stars show sources with $z_{\text{phot}} > 3$. 4C+41.17 and source 16 are very likely to be at the same redshift. The dashed circle ($r = 3.3'$)/ellipse ($a = 2.5'$, $b = 1'$) indicates the area for identifying targets in the SPIRE and PACS maps, respectively. The dotted box shows the coverage of IRAC1 and IRAC3, the dashed-dotted box shows the coverage of IRAC2 and IRAC4 and the long dashed circle shows the coverage of SCUBA. The MIPS and MAMBO images cover the whole SPIRE area and are therefore not illustrated here. The coverage/error in the region used for extraction is not homogeneous.

Most of the SPIRE-selected sources are found to be at $z < 2.5$, ruling out any physical connection with the radio galaxy and confirming that most of the far-IR sources in the vicinity of 4C+41.17 are likely foreground. Only one source, object 16, potentially lies at the same redshift as 4C+41.17. The χ^2 distribution of this source shows a clear dip at $z = 3.8$. We therefore assume that object 16 and 4C+41.17 are at the same redshift, $z = 3.8$, and adopt this assumption for our subsequent analysis.

5.4.2 Herschel non-detections

Ivison et al. (2010) report five $850 \mu\text{m}$ detected sources, of which two are described as marginal detections; for the robust subset, we find viable *Herschel* counterparts to two. We

find the same detection rate for the robust 1200- μm sources reported by Greve et al. (2007). The fact that they are not detected in any other wavelength band may suggest some of them are just statistical fluctuations. This would be especially true for those that are only marginally detected. The 1200 μm sources, however, are all observed at a significance $\geq 5\sigma$. If the sources are real they are likely very dust obscured sources belonging to the high redshift ($z > 4$) tail of sub-mm bright star-forming galaxies (Swinbank et al., 2012; Walter et al., 2012). None of these sources has significant MIPS detections or unambiguous IRAC detections and we are therefore not able to estimate a likely redshift range.

5.4.3 Far-IR Luminosities, Star-Formation Rates and Limits

For sources with more than 4 detections in the the SPIRE, MAMBO and SCUBA bands we derive dust temperatures, far-IR luminosities and star formation rates (SFR). Sources 2, 5, 11, 16, 4C+41.17 and 21 were fitted with a grey-body law of the form: $S_\nu \propto \nu^\beta B_\nu(T) = \frac{\nu^{\beta+3}}{(e^{h\nu/kT_d} - 1)}$ where S_ν is the flux density at the rest-frame frequency ν , β the grain emissivity index and T_d the dust temperature. Dust temperatures for an interstellar medium only heated by star-formation in expected to range between $\sim 20\text{--}60$ K; β can range between 1–2.5 (Casey, 2012). Far-IR luminosities were derived by integrating their SED over the wavelength range 40-1000 μm and applying the relation $L_{\text{FIR}} = 4\pi D_L^2 F_{\text{FIR}}$ where D_L is the luminosity distance computed from their photometric redshifts. Where spectroscopic redshifts were available those were applied. Source 16 was assumed to be at the redshift of the radio galaxy ($z = 3.8$). We then estimated the star formation rates by using $SFR [M_\odot] = L_{\text{FIR}}/5.8 \times 10^9 L_\odot$ (Kennicutt, 1998). The results are listed in Table 5.7.

Given the shallowness of the SPIRE images, at $z = 3.8$, we are only sensitive to the most massive starbursts. Assuming a dust emission from the starburst with $\beta = 1.5$ and $T_d = 45$ K, we find that at $z = 3.8$ we can only detect galaxies with a $SFR \gtrsim 2600 M_\odot\text{yr}^{-1}$. We therefore can only report on the presence of strongly starbursting galaxies in the field of 4C+41.17.

5.4.4 Number Density

In order compare the source density to the *Herschel* wide field surveys *Herschel*-ATLAS (Eales et al., 2010) and HerMES (Oliver et al., 2012), we restrict this analysis to a flux density limit at which our catalogs are complete. We estimate the incompleteness by placing artificial sources in our images and applying the source extraction algorithm on the modified images. The number of successful recoveries then provides us with an estimate of the incompleteness for various flux density bins. A completeness of $\sim 95\%$ is reached at $\sim 35\text{mJy}$ (corresponding to a $SFR \sim 2600 M_\odot\text{yr}^{-1}$ at $z = 3.8$) for our 250 μm catalog.

106 5. A Herschel view of the environment of the radio galaxy 4C+41.17 at $z = 3.8$

Table 5.7: Derived dust temperatures (T_d), grain emissivity indices (β), far-IR luminosities (L_{FIR}) and star formation rates (SFRs) for sources with at least 4 detections in SPIRE, MAMBO and SCUBA. Spectroscopic redshifts where used where available and are marked in italics. For source 16, we assumed the redshift of 4C+41.17 ($z = 3.8$).

Source	z	T_d [K]	β	L_{FIR} [$10^{13} L_{\odot}$]	SFR [$M_{\odot}\text{yr}^{-1}$]
2	2.6	38	1.6	0.7	1200
5	2.7	40	1.5	0.3	500
11	<i>1.2</i>	26	1.4	0.1	200
16	3.8	48	1.7	1.8	3100
4C+41.17	<i>3.8</i>	52	1.6	1.6	2800
21	2.7	32	1.7	0.4	700

We find 8 sources above that flux density limit in the extraction area of 34.2 arcmin^2 , resulting in a surface density of $\sim 0.23 \pm 0.08 \text{ arcmin}^{-2}$ for the field of 4C+41.17. The SPIRE blank field number counts at our flux density limit found by Clements et al. (2010) are $N(S_{250\text{-m}} > 36 \text{ mJy}) \sim 0.121 \pm 0.002 \text{ arcmin}^{-2}$ suggesting a marginally significant overdensity of a factor ~ 2 . On the other hand, Oliver et al. (2010) find blank field number counts of $N(S_{250\text{-m}} > 30 \text{ mJy}) \sim 0.18 \pm 0.15 \text{ arcmin}^{-2}$. We find 10 sources with flux densities above 30mJy corresponding to a surface density of $0.3 \pm 0.1 \text{ arcmin}^{-2}$. As our catalogs are not yet complete at that limit this result has to be treated with caution but still hints to a slight overdensity for the field of 4C+41.17.

Mayo et al. (2012) find a density of MIPS 24 μm sources which is ~ 2 times higher than the blank field mean density, which agrees with our *Herschel* observations. Nevertheless, this field was not counted as significantly overdense as it is still less than 3σ above the mean. Compared to the mean density of HzRG fields analyzed by Mayo et al. (2012), the field around 4C+41.17 is typical as compared to other radio galaxies in terms of density ($\delta_{4\text{C}+41.17} = 2.1 \text{ arcmin}^{-2}$, compared to $\langle \delta_{\text{HzRG}} \rangle \sim 2.2 \text{ arcmin}^{-2}$).

Selecting color-selected high-redshift IRAC sources in the fields of HzRGs, Galametz et al. (2012) finds 4C+41.17 to be overdense with a compact clump of IRAC sources identified $\sim 1'$ south of the radio galaxy. However, the IRAC color criterion applied simply identifies sources at $z > 1.2$. Given that we find an excess of galaxies at $z \sim 2.5$ (see Figure 5.2), the clump detected by Galametz et al. (2012) is likely a foreground structure, as also suggested by Greve et al. (2007).

Considering all data at hand, we therefore find no indications for a remarkable overdensity in the field of 4C+41.17.

In the 250 μm image, source 16 is found ~ 25 arcsec from the 250 μm position of 4C+41.17 (~ 180 kpc at $z = 3.8$). The probability of finding such a bright far-IR source (42 mJy at 250 μm , 48 mJy at 350 μm) at this distance to the HzRG is 4% and 8% for 250 μm and 350 μm , respectively (Oliver et al., 2010). This probability is not remarkable when considering the whole sky but is very special when the evidence points to the two sources lying at the same redshift. The probability of finding a 250 μm selected source at $z = 3.8$ is also only $\sim 5\%$ (Mitchell-Wynne et al., 2012). The probability of finding a source of that flux density at 25'' distance at $z = 3.8$ will therefore be $\ll 4\%$ and is a very unlikely event.

5.5 Summary and Conclusions

Using *Herschel* PACS and SPIRE observations combined with *Spitzer* mid-IR observations, we have carried out a multi-wavelength study of the environment of 4C+41.17, a powerful radio galaxy at $z = 3.8$. This pilot study for the HeRGÉ project clearly shows that far-IR observations combined with shorter wavelength observations improve our ability to securely distinguish overdensities found by different selection criteria (e.g. Galametz et al., 2012; Mayo et al., 2012) from truly clustered structures. The field of 4C+41.17 has long been thought to host a galaxy cluster associated with the radio galaxy (Iverson et al., 2000). Greve et al. (2007) already concluded from stellar bump photometric redshifts that most of the sources might belong to a foreground structure. Only source 16 (J065051.4 in Greve et al., 2007) appeared possibly associated with 4C+41.17. In this work we find strong indications that these two sources lie at the same redshift and thus that there is a physical association between them. Iverson et al. (2000) and Greve et al. (2007) find that the radio galaxy and source 16 appear to be connected by a faint bridge in both the SCUBA and MAMBO map increasing the likelihood that this source is part of the same system as 4C+41.17. Source 16 makes the environment of 4C+41.17 special as the probability of finding such a bright source that close (~ 25 arcsec distant, 180 kpc at $z = 3.8$) is only $\sim 5\%$.

However, close-by companion sources might actually be a common feature for HzRGs. Iverson et al. (2008) finds two clumps of emission 3.3 arcsec distant from the HzRG 4C+60.07 that are most likely merging with the $z = 3.8$ radio galaxy. Iverson et al. (2012) finds a bright sub-mm galaxy near the radio galaxy 6C 1909+72 that is most likely sharing the same node or filament of the cosmic web. Also, Nesvadba et al. (2009) find two CO-emission line components at a distance of ~ 80 kpc from the HzRG TXS0828+193 ($z = 2.6$) which may be associated with a gas-rich, low-mass satellite galaxy. Although these companions are found much closer to the HzRG than source 16 is to 4C+41.17, these observations suggest that companion sources around HzRGs may be a common feature (see also Iverson et al., 2012). We find that most of the *Herschel* far-IR sources in the vicinity of 4C+41.17 are foreground sources. However, this does not rule out the presence of a cluster around

108 5. A Herschel view of the environment of the radio galaxy 4C+41.17 at $z = 3.8$

4C+41.17 as our observations are only sensitive to galaxies with SFRs $\gtrsim 2600 M_{\odot}\text{yr}^{-1}$. Caution is needed when identifying overdensities from a single wavelength data set. With IRAC and MIPS data available for all sources being observed by the HeRGÉ project we will be able to identify likely protocluster candidates around the HzRGs. However, $850 \mu\text{m}$ data are required to constrain the Rayleigh-Jeans part of the SED. We have therefore started a systematic SCUBA-2 follow up campaign to map the full SPIRE area of the HeRGÉ fields.

Chapter 6

Outlook

The CARLA and HeRGE projects are unique pioneering surveys to systematically search for and study a large sample of high redshift galaxy clusters. The work described in this thesis are the first important steps to identify the most promising structures and a start for a more systematic study of high redshift clusters and their properties with cosmic time.

But a lot of the big questions still remain: How and when did the most massive galaxies assemble their stellar mass? How did they acquire their observed morphologies that we observe today? These need to be tackled with follow-up projects.

Pushing the Frontier of Cluster Search beyond $z > 2$

We have started the spectroscopic follow-up of some of the most promising fields with MOSFIRE@Keck and KMOS@VLT. With these data we are aiming to (i) confirm high-redshift galaxy cluster candidates, these first observations alone are expected to increase the current number of spectroscopically confirmed massive clusters at $z > 1.5$ by a factor of several, (ii) determine cluster galaxy star-formation rates (derived from [O II] and H α lines, when detected) and AGN activity and (iii) compare the high-redshift galaxies in cluster environments to field galaxy samples at the same redshift. We have also started follow-up imaging of the 30 densest CARLA fields in the i -band on the WHT. Colour magnitude diagrams will measure the color of the red sequence and the fraction of red galaxies to identify the formation redshift of the massive galaxies and to measure how rapidly massive cluster galaxies quench their star formation. Fig. 6.1 shows a three-color (IRAC1, IRAC2, i -band) image of one of our high-priority CARLA targets, 7C1753 at $z = 1.9$, a prominent clump of red sequence galaxies is visible in the centre. Spectroscopic confirmation is planned. Many of the CARLA fields are as dense or even denser than this one and confirmed clusters will likely become the targets of future observations, including deep Hubble imaging and HST slitless spectroscopy.

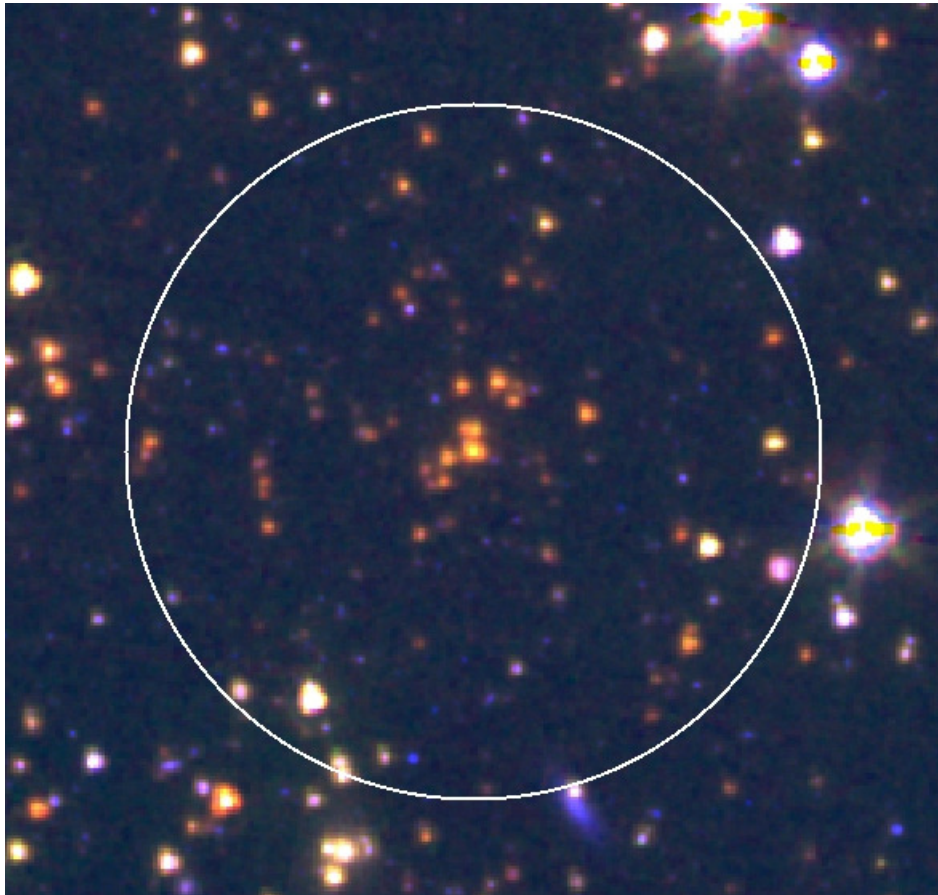


Figure 6.1: Three-color image (IRAC1, IRAC2, i-band) of the field of 7C1753 at $z = 1.9$. The white circle has a radius of $r = 1$ arcmin which corresponds to ~ 500 kpc at this redshift. The cluster candidate is clearly visible as a red overdensity. Many of the CARLA fields are as dense and even denser than this high-priority target.

Tracing the Origin and Fate of Clusters with Simulations

One of the immediate questions that arises from the results presented in this thesis is what is the fate of these rich CARLA galaxy overdensities? What kind of clusters will they evolve into at $z = 0$? Recently, Chiang et al. (2013) studied the progenitors of 2,832 galaxy clusters at $z = 0$ across cosmic history using the Λ CDM Millennium Run and semi-analytic simulations. They showed that the properties of a galaxy cluster (e.g. size, mass, galaxy overdensity) at $z = 0$ are closely related to its properties at all redshifts and that the mass of present-day clusters can be ‘predicted’ from the observed galaxy overdensity. Rare progenitors of the most massive clusters formed as early as $z \sim 2.3$. We are planning to compare the CARLA cluster candidates to simulations like the ones above adapting the analysis to our selection. This analysis will show which kind of clusters the overdensities around radio-loud AGN will evolve into. As radio-loud AGN belong to the most massive galaxies in the Universe and likely reside in the largest dark matter halos, we expect the most extreme CARLA overdensities to evolve into the most massive systems at $z = 0$.

Recently, much attention has been given to the question of whether the most distant, highest mass clusters are consistent with a standard Gaussian power spectrum Λ CDM cosmology, or whether one must invoke non-Gaussian initial density fluctuations from inflation to seed structure formation. This apparent discrepancy between the number of rich clusters known at high redshift and the predictions of ‘vanilla’ Λ CDM remains controversial, in part due to the small number of confirmed clusters at high redshift. Tracing the progenitors of the most massive systems with CARLA will improve our census of massive, high-redshift ($z > 1.3$) clusters and will finally allow to compare a large sample of massive high-redshift clusters to predictions from simulations.

A multi-wavelength Analysis of the dusty Starbursts in high-redshift Galaxy Clusters

While finding and confirming clusters at high-redshift is essential, an important next step is to study the various galaxy populations within these special environments to get insights about how cluster galaxies formed. How is the cluster population different from the field? When are clusters actively forming stars and when and why does this star formation get quenched? To answer these questions we need to (i) obtain a full census of the active galaxy population in galaxy clusters: the dusty starbursts and AGN and (ii) also focus on the central active galaxy that is the most likely progenitor of the dominant brightest cluster galaxy (BCG) at $z = 0$.

With HERGE, we recently obtained 10-band (3.6 to 500 μm) imaging of a represen-

tative sample of the fields of 71 high-redshift radio galaxies uniformly distributed across $1.0 < z < 5.2$. CARLA (Wylezalek et al., 2013a) and other work (e.g. Ivison et al., 2012) have shown that the overdensities are concentrated within a region of 1 – 2 Mpc. The single HERGE *Herschel* pointings are therefore of sufficient areal coverage to identify a significant fraction of dusty star-forming cluster members and AGN. Existing *Spitzer*/4-band IRAC data will be a measure for the fraction of the old stellar population and *Spitzer*/MIPS data will be important to derive the fraction of AGN in these clusters. We will derive photometric redshifts with these ancillary data to identify cluster members (see Chapter 5). Based on a sample of 16 spectroscopically confirmed clusters at $1 < z < 1.6$, Brodwin et al. (2013) have recently shown that beyond $z > 1.3$ the fraction of star-forming cluster members increases monotonically toward the cluster centers, indicating that at $z > 1.4$ environment-dependent quenching had not yet been established. With the HERGE data set we will be able to extend this work and test how the star-formation activity evolves in some of the densest environments.

Complementary to studying the fields of the HERGE sources, we are planning to investigate the central radio-loud AGN that will most likely evolve into the BCG, dominating the cluster core. In Ivison et al. (2012) and Wylezalek et al. (2013b) we have shown, that many radio-loud AGN have close-by companions and that complex morphologies are commonplace amongst high-redshift radio galaxies. These preliminary results do suggest that the starburst activity in high-redshift radio galaxies is driven by the interaction of two (or more) gas-rich systems, rather than by a steady accretion of cold gas. Complementary to the *Herschel* data, we have started a sub-mm follow-up of the HERGE sources with ALMA (accepted Cycle 1 filler program) and CARMA that will resolve the dust continuum emission on 8-kpc scales to determine the prevalence of close companions and that will provide an essential data point on the Rayleigh-Jeans side of the spectral energy distributions (SEDs) to complement our *Herschel* SEDs. Systematically studying these sources and fields in this wide redshift range ($1 < z < 5$) and with this rich of a data set will provide a unique, detailed multi-component analysis of some of the richest and most active high-redshift clusters.

Systematically studying galaxy cluster formation and evolution with various observational techniques, simulations and the combination of the two as outlined and planned above will make a significant impact on understanding the formation of the most massive structures over several Gyrs. CARLA and HeRGE are unique surveys to accomplish these goals.

Appendix **A**

The full CARLA sample

Table A.1: The CARLA sample (in R.A. order).

Name	R.A. (J2000)	Dec. (J2000)	z	$\log(L_{500\text{MHz}})$ (W Hz ⁻¹)	Σ (arcmin ⁻²)	AGN Type
USS0003-019	00:06:11.20	-01:41:50.2	1.54	27.86	11.2	HzRG
PKS_0011-023	00:14:25.50	-02:05:56.0	2.08	28.15	12.1	HzRG
MRC_0015-229	00:17:58.20	-22:38:3.8	2.01	28.32	17.9	HzRG
BRL0016-129	00:18:51.40	-12:42:34.6	1.59	29.02	17.2	HzRG
MG0018+0940	00:18:55.20	+09:40:6.9	1.59	28.39	14.7	HzRG
6CS_0020p440	00:23:8.50	+44:48:23.0	2.99	28.49	7.7	HzRG
NVSS_J002402-325253	00:24:2.30	-32:52:54.1	2.04	27.93	14.3	HzRG
NVSSJ002431-303330	00:24:32.00	-30:33:29.2	2.42	27.86	10.2	HzRG
6CS_0024p356	00:26:52.00	+35:56:24.0	2.16	28.04	17.5	HzRG
4C_40.02	00:30:49.00	+41:10:49.1	2.43	28.64	18.5	HzRG
MRC_0030-219	00:33:23.90	-21:42:1.1	2.17	28.14	11.2	HzRG
4C_p44.02	00:36:53.50	+44:43:21.0	2.79	28.98	14.0	HzRG
WN_J0040p3857	00:40:56.21	+38:57:29.9	2.61	27.80	12.1	HzRG
MG0046+1102	00:46:41.40	+11:02:52.4	1.81	28.27	16.9	HzRG
MRC_0052-241	00:54:29.81	-23:51:29.9	2.86	28.77	16.3	HzRG
J005716.99-002433.2	00:57:16.99	-00:24:33.2	2.73	27.99	13.1	RLQ
J010826.84-00372	01:08:26.83	-00:37:24.0	1.37	28.23	13.7	RLQ
6CS_0106p397	01:09:25.39	+40:00:1.1	2.28	28.11	12.7	HzRG
6CS_0112p372	01:14:50.21	+37:32:33.0	2.54	28.22	9.3	HzRG
MRC0114-211	01:16:51.41	-20:52:6.6	1.41	29.18	20.4	HzRG
6CS_0115p394	01:17:55.30	+39:44:33.0	2.24	27.93	13.4	HzRG
6CS_0118p486	01:21:16.30	+48:57:40.0	2.35	27.83	13.4	HzRG
MG0122+1923	01:22:30.00	+19:23:39.1	1.60	28.37	16.3	HzRG
J012517.14-001828.9	01:25:17.14	-00:18:28.9	2.28	28.28	12.4	RLQ
NVSSJ012932-385433	01:29:33.00	-38:54:34.9	2.19	27.99	15.6	HzRG
6C_0132+330	01:35:30.41	+33:17:1.0	1.71	27.64	14.3	HzRG
TXS_0134p251	01:37:7.01	+25:21:19.1	2.90	28.57	14.4	HzRG
6CS_0135p313	01:38:6.60	+31:32:42.0	2.20	27.97	14.0	HzRG
MRC0139-273	01:41:27.10	-27:06:10.4	1.44	28.78	15.7	HzRG
MRC_0140-257	01:42:41.21	-25:30:33.8	2.64	28.44	10.5	HzRG
6CS_0142p427	01:45:28.99	+42:57:42.1	2.23	28.10	9.9	HzRG
MG_0148p1028	01:48:28.90	+10:28:21.0	2.85	28.56	12.7	HzRG

MRC0152-209	01:54:55.80	-20:40:26.4	1.92	28.56	18.8	HzRG
6CS_0152p463	01:55:45.60	+46:37:10.9	2.28	27.97	15.3	HzRG
J015832.51-004238.2	01:58:32.52	-00:42:38.2	2.61	28.12	12.1	RLQ
J015856.26+13070	01:58:56.26	+13:07:1.9	1.89	28.11	14.3	RLQ
6C_0158+315	02:00:55.80	+31:46:16.0	1.51	27.86	N	HzRG
TXS_0200p015	02:02:42.89	+01:49:11.0	2.23	28.07	11.8	HzRG
6C_0201+499	02:04:22.80	+50:08:59.6	1.98	28.00	5.7	HzRG
TXS_0211-122	02:14:17.40	-11:58:46.9	2.34	28.48	15.3	HzRG
TXS_0214p183	02:17:25.80	+18:37:3.0	2.13	28.46	14.3	HzRG
5C6.217	02:19:48.79	+33:48:18.4	1.41	28.19	15.0	HzRG
WN_J0231p3600	02:31:11.50	+36:00:27.0	3.08	28.20	13.1	HzRG
MRC_0251-273	02:53:16.70	-27:09:10.1	3.16	28.54	11.5	HzRG
J025928.51-001959.9	02:59:28.51	-00:20:00.0	2.00	27.99	16.9	RLQ
WN_J0303p3733	03:03:25.99	+37:33:42.1	2.51	28.44	12.1	HzRG
NVSSJ030431-315308	03:04:31.99	-31:53:8.2	2.24	27.79	12.7	HzRG
4C04+11	03:11:48.00	+05:08:3.0	4.15	29.49	N	HzRG
MG0311+1532	03:11:56.90	+15:32:55.0	1.99	28.35	12.4	HzRG
BRL0310-150	03:12:46.39	-14:49:51.6	1.77	29.17	11.8	HzRG
MRC0324-228	03:27:4.39	-22:39:42.5	1.89	28.59	10.8	HzRG
MP_J0340-6507	03:40:44.59	-65:07:12.0	2.29	28.82	12.8	HzRG
MRC_0349-211	03:51:11.81	-20:58:0.1	2.33	28.28	11.5	HzRG
MRC0350-279	03:52:51.60	-27:49:22.4	1.90	28.40	14.3	HzRG
TXS_0355-037	03:57:48.00	-03:34:8.0	2.15	28.34	13.1	HzRG
TXS_0417-181	04:19:43.61	-18:01:55.9	2.77	28.64	14.0	HzRG
TXS_0448p091	04:51:14.59	+09:14:29.0	2.04	28.11	15.0	HzRG
TN_J0452-1737	04:52:26.71	-17:37:54.1	2.26	28.09	11.2	HzRG
MRC0457-235	04:59:17.30	-23:30:57.2	1.99	28.38	14.0	HzRG
PKS_0529-549	05:30:25.39	-54:54:20.9	2.58	29.16	15.0	HzRG
MRC0600-219	06:02:17.30	-21:58:21.4	1.71	28.22	13.1	HzRG
WN_J0617p5012	06:17:39.41	+50:12:55.1	3.15	28.02	11.5	HzRG
6C_0629p53	06:33:52.01	+53:16:31.1	2.25	28.35	9.6	HzRG
J073320.48+272103.4	07:33:20.40	+27:21:3.6	2.94	28.37	14.0	RLQ
B3_0731p438	07:35:21.84	+43:44:21.1	2.43	28.89	9.2	HzRG
J074155.64+420817.7	07:41:55.68	+42:08:17.9	2.23	27.90	12.1	RLQ
J074309.88+39413	07:43:9.84	+39:41:30.1	1.71	28.16	17.5	RLQ
PKS_0742p10	07:45:32.88	+10:11:12.8	2.62	28.74	14.3	HzRG
J074625.87+254902.1	07:46:25.92	+25:49:2.3	2.98	28.63	12.4	RLQ
WN_J0747p3654	07:47:29.28	+36:54:38.2	2.99	28.14	10.8	HzRG
B3_0744p464	07:47:43.68	+46:18:58.0	2.93	28.87	11.5	HzRG
J074756.22+351701.1	07:47:56.16	+35:17:1.0	2.23	27.67	13.7	RLQ
J074922.97+225511.8	07:49:23.04	+22:55:12.0	2.17	27.66	14.6	RLQ
J075019.54+363002.8	07:50:19.44	+36:30:2.9	2.03	27.75	8.6	RLQ
J075020.43+48145	07:50:20.40	+48:14:53.2	1.96	28.46	12.4	RLQ
6CSS0746p5445	07:50:24.96	+54:38:7.1	2.16	27.64	16.6	HzRG
TXS_0748p134	07:51:1.20	+13:19:27.1	2.42	28.31	10.2	HzRG
J075458.32+294154.2	07:54:58.32	+29:41:54.2	2.11	28.29	16.3	RLQ
J075821.52+143719.0	07:58:21.60	+14:37:19.2	2.40	28.08	12.1	RLQ
6CSS0743p5019	07:58:6.00	+50:11:3.1	3.00	28.41	12.8	HzRG
4C_p39.21	07:58:8.88	+39:29:28.0	2.12	28.51	17.9	HzRG
J080016.10+402955.6	08:00:16.08	+40:29:55.7	2.02	27.92	23.0	RLQ
J080442.23+30123	08:04:42.24	+30:12:37.1	1.45	28.42	12.8	RLQ
J080749.05+451550.3	08:07:48.96	+45:15:50.4	3.19	28.24	12.1	RLQ
J081100.93+21413	08:11:0.96	+21:41:37.0	1.52	28.00	12.7	RLQ
5C_7.10	08:11:26.40	+26:18:19.1	2.19	28.21	7.3	HzRG
5C_7.15	08:12:19.20	+26:30:18.0	2.43	28.12	12.4	HzRG
J081303.83+254211.0	08:13:3.84	+25:42:11.2	2.02	28.23	10.5	RLQ
B3_0811p391	08:14:30.72	+38:58:35.0	2.62	27.84	16.9	HzRG

J081534.16+330529.0	08:15:34.08	+33:05:29.0	2.43	28.34	10.8	RLQ
J082107.61+310751.1	08:21:7.68	+31:07:51.2	2.63	27.83	12.1	RLQ
6CE0820+3642	08:23:48.00	+36:32:46.3	1.86	28.27	9.6	HzRG
J082428.02+234107.9	08:24:28.08	+23:41:7.8	2.57	28.08	7.3	RLQ
J082447.24+55524	08:24:47.28	+55:52:41.9	1.42	28.45	14.7	RLQ
5C_7.223	08:24:6.48	+26:28:12.0	2.09	27.71	12.4	HzRG
6CSS0824p5344	08:27:59.04	+53:34:14.9	2.82	28.27	18.2	HzRG
J082706.51+105224.2	08:27:6.48	+10:52:24.2	2.28	27.98	15.1	RLQ
6CE0825+3452	08:28:26.64	+34:42:50.0	1.46	28.08	17.2	HzRG
5C_7.269	08:28:39.60	+25:27:29.9	2.22	27.78	15.0	HzRG
5C_7.271	08:28:59.52	+24:54:0.0	2.22	27.97	12.4	HzRG
J083031.93+052006.7	08:30:31.92	+05:20:6.8	2.22	27.81	10.8	RLQ
TXS_0828p193	08:30:53.04	+19:13:16.0	2.57	28.44	N	HzRG
J083249.39+155408.6	08:32:49.44	+15:54:8.6	2.42	28.27	9.6	RLQ
J083314.36+112336.3	08:33:14.40	+11:23:36.2	2.98	28.64	11.8	RLQ
J083636.88+41255	08:36:36.96	+41:25:54.1	1.30	27.89	16.4	RLQ
J083722.41+582501.8	08:37:22.32	+58:25:1.9	2.10	28.49	16.0	RLQ
6CSS0834p4129	08:37:48.96	+41:19:54.1	2.44	27.80	13.4	HzRG
J083910.89+200207.3	08:39:10.80	+20:02:7.4	3.04	28.13	12.1	RLQ
J084538.59+585232.3	08:45:38.64	+58:52:32.5	2.15	27.97	11.5	RLQ
J084506.24+425718.4	08:45:6.24	+42:57:18.4	2.10	28.01	N	RLQ
J084713.03+083021.8	08:47:12.96	+08:30:21.8	2.04	28.04	12.8	RLQ
J084715.16+383109.9	08:47:15.12	+38:31:9.8	3.17	28.34	16.0	RLQ
J085051.80+152215.0	08:50:51.84	+15:22:15.2	2.02	28.35	N	RLQ
BRL0851-142	08:53:48.96	-14:27:53.6	1.67	29.03	12.1	HzRG
J085442.00+57572	08:54:42.00	+57:57:29.2	1.32	28.26	18.2	RLQ
4C_12.32	08:55:20.88	+12:17:26.9	2.47	28.56	13.4	HzRG
J085555.50+094154.2	08:55:55.44	+09:41:54.3	2.19	27.77	15.0	RLQ
6CSS0854p3500	08:57:16.08	+34:48:24.1	2.38	27.92	12.7	HzRG
4C_40.22	08:59:59.52	+40:24:36.0	2.28	28.39	14.4	HzRG
4C_p03.16	09:00:14.40	+03:24:8.0	2.81	28.48	15.0	HzRG
6CE0901+3551	09:04:32.40	+35:39:3.2	1.91	28.25	10.2	HzRG
J090444.33+233354.0	09:04:44.40	+23:33:54.0	2.26	27.77	13.1	RLQ
6C_0901p54	09:05:24.24	+54:05:42.0	2.25	28.11	14.7	HzRG
J090527.46+485049.9	09:05:27.36	+48:50:49.9	2.69	28.62	14.0	RLQ
J090549.05+041010.1	09:05:48.96	+04:10:10.2	3.15	28.34	8.0	RLQ
6CE0905+3955	09:08:16.80	+39:43:26.0	1.88	28.27	18.2	HzRG
J091054.17+375915.0	09:10:54.24	+37:59:15.0	2.16	28.11	14.4	RLQ
J091055.23+253921.4	09:10:55.20	+25:39:21.6	2.75	28.25	18.6	RLQ
J091207.02+33482	09:12:6.96	+33:48:29.2	1.87	27.98	11.8	RLQ
TN_J0920-0712	09:20:22.32	-07:12:18.0	2.76	28.48	8.3	HzRG
J092035.80+002330.6	09:20:35.76	+00:23:30.7	2.49	27.89	15.9	RLQ
J092058.46+444154.0	09:20:58.56	+44:41:53.9	2.19	28.75	19.8	RLQ
J092507.81+00191	09:25:7.92	+00:19:13.0	1.72	28.35	15.0	RLQ
J092824.13+44460	09:28:24.24	+44:46:4.1	1.90	27.81	12.8	RLQ
J093035.08+464408.6	09:30:35.04	+46:44:8.5	2.03	28.15	14.0	RLQ
6C_0930p389	09:33:6.96	+38:41:48.1	2.40	28.41	10.2	HzRG
J093531.83+363317.6	09:35:31.92	+36:33:17.6	2.86	28.43	11.8	RLQ
J094014.50+254713.6	09:40:14.40	+25:47:13.6	3.19	28.55	11.5	RLQ
J094113.55+114532.2	09:41:13.44	+11:45:32.4	3.20	28.41	13.4	RLQ
TNJ0941-1628	09:41:7.44	-16:28:3.0	1.64	28.18	19.5	HzRG
J094442.31+255443.3	09:44:42.24	+25:54:43.2	2.92	28.86	13.1	RLQ
MRC_0943-242	09:45:32.88	-24:28:50.2	2.92	28.62	N	HzRG
J095033.62+274329.9	09:50:33.60	+27:43:30.0	2.36	27.94	18.8	RLQ
TXS_0952-217	09:54:29.04	-21:56:53.2	2.95	28.08	12.8	HzRG
J095552.24+500131.6	09:55:52.32	+50:01:31.4	2.12	27.68	N	RLQ
NVSS_J095751-213321	09:57:51.36	-21:33:20.9	3.13	28.11	15.3	HzRG

J095819.66+47250	09:58:19.68	+47:25:7.0	1.88	28.35	13.1	RLQ
MRC0955-288	09:58:4.80	-29:04:7.3	1.40	28.65	20.1	HzRG
J095858.94+294804.1	09:58:59.04	+29:48:4.3	2.07	27.67	12.4	RLQ
J100120.84+55534	10:01:20.88	+55:53:48.8	1.41	28.03	12.1	RLQ
J100157.73+10154	10:01:57.84	+10:15:49.0	1.53	27.85	11.5	RLQ
J100515.99+480533.3	10:05:16.08	+48:05:33.4	2.39	28.12	8.9	RLQ
J100741.50+135629.6	10:07:41.52	+13:56:29.8	2.72	28.87	11.2	RLQ
NVSS_J101008-383629	10:10:7.92	-38:36:29.2	2.24	28.30	9.2	HzRG
3C239	10:11:45.36	+46:28:19.9	1.78	28.98	12.8	HzRG
J101211.44+330926.4	10:12:11.52	+33:09:26.3	2.25	27.99	12.7	RLQ
J101302.29+352605.7	10:13:2.40	+35:26:5.6	2.65	28.22	15.0	RLQ
J101329.93+491840.9	10:13:30.00	+49:18:41.0	2.20	28.15	12.1	RLQ
J101515.63+01585	10:15:15.60	+01:58:53.0	1.38	28.12	11.8	RLQ
J101644.31+203747.2	10:16:44.40	+20:37:47.3	3.12	28.90	13.7	RLQ
J101725.88+611627.5	10:17:25.92	+61:16:27.5	2.81	28.63	23.6	RLQ
J101827.85+05303	10:18:27.84	+05:30:30.0	1.94	28.04	20.1	RLQ
MG_1019p0534	10:19:33.36	+05:34:35.0	2.77	28.57	15.9	HzRG
MRC1017-220	10:19:48.96	-22:19:58.1	1.77	28.89	13.1	HzRG
6CE1016+3637	10:19:53.52	+36:22:46.2	1.86	28.62	17.2	HzRG
J102117.47+34372	10:21:17.52	+34:37:21.0	1.41	27.94	18.5	RLQ
J102230.30+30410	10:22:30.24	+30:41:4.9	1.32	28.20	15.6	RLQ
J102429.58-005255.4	10:24:29.52	-00:52:55.4	2.56	28.88	16.9	RLQ
J102631.96+06273	10:26:31.92	+06:27:33.0	1.71	28.41	17.5	RLQ
TN_J1033-1339	10:33:10.80	-13:39:51.8	2.43	28.35	10.2	HzRG
6CE1031+3405	10:34:35.04	+33:49:20.6	1.83	28.49	11.5	HzRG
NVSS_J103615-321659	10:36:15.36	-32:16:57.0	2.14	27.82	12.8	HzRG
J103641.96+250236.3	10:36:42.00	+25:02:36.2	2.02	27.63	11.8	RLQ
J104148.89+523355.5	10:41:48.96	+52:33:55.4	2.30	27.78	13.7	RLQ
8C_1039p681	10:42:37.44	+67:50:24.0	2.53	28.56	16.3	HzRG
J104257.58+074850.5	10:42:57.60	+07:48:50.5	2.67	28.48	11.2	RLQ
6CE1042+3912	10:45:14.88	+38:56:37.7	1.77	28.64	16.0	HzRG
6CE1045+3403	10:48:12.24	+33:47:46.0	1.82	28.32	16.6	HzRG
J104830.20+265808.2	10:48:30.24	+26:58:8.4	2.76	28.46	13.7	RLQ
6CSS1045p4459	10:48:31.92	+44:44:28.0	2.57	28.05	19.4	HzRG
J104833.69+60084	10:48:33.60	+60:08:44.9	1.73	28.50	12.4	RLQ
J104941.09+133255.6	10:49:41.04	+13:32:55.7	2.77	27.88	12.1	RLQ
MRC1048-272	10:50:42.48	-27:33:8.3	1.56	28.71	10.5	HzRG
J105231.82+08060	10:52:31.92	+08:06:8.0	1.64	28.05	19.5	RLQ
WN_J1053p5424	10:53:36.24	+54:24:42.1	3.08	28.55	13.7	HzRG
J105726.62+032448.0	10:57:26.64	+03:24:48.1	2.83	28.11	15.0	RLQ
B2_1056p39	10:59:11.52	+39:25:0.8	2.17	28.20	13.4	HzRG
J110020.21+09493	11:00:20.16	+09:49:35.0	1.32	27.81	16.6	RLQ
TN_J1102-1651	11:02:47.04	-16:51:33.8	2.11	28.07	13.7	HzRG
6CE1100+3505	11:03:26.40	+34:49:46.9	1.44	28.10	23.0	HzRG
J110344.53+023209.9	11:03:44.64	+02:32:9.9	2.51	28.07	18.2	RLQ
6CSS1102p4329	11:05:42.96	+43:13:25.0	2.73	28.17	12.8	HzRG
MRC_1106-258	11:08:30.24	-26:05:6.0	2.43	28.48	11.5	HzRG
6C_1106p380	11:09:28.80	+37:44:30.8	2.29	28.44	16.6	HzRG
J110903.88+202857.5	11:09:3.84	+20:28:57.7	2.58	27.86	14.3	RLQ
TN_J1112-2948	11:12:24.00	-29:48:6.1	3.09	28.76	N	HzRG
WN_J1115p5016	11:15:6.96	+50:16:23.9	2.54	27.82	11.5	HzRG
TXS_1113-178	11:16:14.64	-18:06:23.0	2.24	28.46	16.6	HzRG
4C_34.34	11:16:30.48	+34:42:24.1	2.40	28.46	14.7	HzRG
J111857.29+123441.7	11:18:57.36	+12:34:41.9	2.13	29.02	15.9	RLQ
J111914.33+600457.1	11:19:14.40	+60:04:57.4	2.65	28.17	8.9	RLQ
NVSS_J111921-363139	11:19:21.84	-36:31:39.0	2.77	29.39	14.0	HzRG
3C256.0	11:20:42.96	+23:27:54.7	1.82	28.97	13.4	HzRG

J112338.14+052038.5	11:23:38.16	+05:20:38.5	2.18	27.88	15.8	RLQ
3C_257	11:23:9.36	+05:30:18.0	2.47	29.16	13.7	HzRG
J112553.70+261019.9	11:25:53.76	+26:10:19.9	2.35	28.75	15.3	RLQ
J112657.65+45160	11:26:57.60	+45:16:5.9	1.81	28.14	12.8	RLQ
J112851.69+232617.3	11:28:51.60	+23:26:17.2	3.05	28.22	11.2	RLQ
J112914.10+09515	11:29:14.16	+09:51:59.0	1.52	28.12	22.9	RLQ
J113053.28+38151	11:30:53.28	+38:15:18.0	1.74	28.34	10.8	RLQ
MRC1128-268	11:31:3.84	-27:05:18.2	1.43	28.08	18.8	HzRG
MRC1131-269	11:33:31.44	-27:15:23.4	1.71	28.37	13.4	HzRG
B2_1132p37	11:35:6.00	+37:08:40.9	2.88	28.71	22.0	HzRG
6C_1134p369	11:37:7.68	+36:39:54.0	2.13	28.31	8.3	HzRG
J114054.56+264335.0	11:40:54.48	+26:43:35.0	2.13	28.11	8.9	RLQ
BRL1140-114	11:42:35.04	-11:41:48.1	1.94	29.03	16.9	HzRG
6CE1141+3525	11:43:51.12	+35:08:22.6	1.78	28.29	19.1	HzRG
J114705.24+08390	11:47:5.28	+08:39:1.3	1.60	27.76	16.9	RLQ
J115043.87-00235	11:50:43.92	-00:23:54.0	1.98	29.06	17.2	RLQ
J115129.37+38255	11:51:29.28	+38:25:52.0	1.30	28.02	17.2	RLQ
J115201.12+102322.8	11:52:1.20	+10:23:22.9	2.09	27.88	18.5	RLQ
J115249.18+181846.8	11:52:49.20	+18:18:46.8	2.72	28.01	13.7	RLQ
J115901.74+065619.0	11:59:1.68	+06:56:19.1	2.19	27.79	15.6	RLQ
J115944.82+011206.9	11:59:44.88	+01:12:7.0	2.00	28.06	14.1	RLQ
B2_1159p39A	12:01:49.92	+39:19:10.9	2.37	28.22	7.6	HzRG
J120301.00+063441.5	12:03:0.96	+06:34:41.6	2.18	28.24	9.9	RLQ
J120436.80+522841.7	12:04:36.72	+52:28:41.9	2.73	28.32	13.4	RLQ
J120727.90+275458.8	12:07:27.84	+27:54:58.7	2.18	28.49	16.9	RLQ
6CE1204+3519	12:07:31.92	+35:03:6.5	1.37	28.21	12.1	HzRG
B3_1204p401	12:07:6.24	+39:54:38.9	2.07	28.33	11.8	HzRG
J120913.61+43392	12:09:13.68	+43:39:20.2	1.40	28.57	15.9	RLQ
J121255.81+245332.3	12:12:55.92	+24:53:32.3	2.37	27.90	12.4	RLQ
J121205.91+204320.1	12:12:6.00	+20:43:20.3	2.31	28.26	17.5	RLQ
J121303.80+324736.8	12:13:3.84	+32:47:37.0	2.51	27.96	9.9	RLQ
MRC1211-272	12:14:24.48	-27:30:48.6	1.89	28.39	12.5	HzRG
J121404.11+33094	12:14:4.08	+33:09:45.0	1.60	28.56	15.3	RLQ
J121604.72+58433	12:16:4.80	+58:43:32.9	1.45	27.96	12.4	RLQ
J121711.02+583526.3	12:17:11.04	+58:35:26.2	2.55	28.60	11.5	RLQ
J121715.16+343538.2	12:17:15.12	+34:35:38.4	2.65	28.09	13.4	RLQ
J121740.83+64070	12:17:40.80	+64:07:7.0	1.30	28.09	13.7	RLQ
J121911.23-004345.5	12:19:11.28	-00:43:45.6	2.29	27.73	13.7	RLQ
MRC1217-276	12:20:21.12	-27:53:1.0	1.90	28.23	19.1	HzRG
J122033.87+33431	12:20:33.84	+33:43:12.0	1.53	28.82	17.6	RLQ
J122419.81+11072	12:24:19.92	+11:07:23.2	1.76	28.07	9.6	RLQ
J122836.88+101841.9	12:28:36.96	+10:18:42.1	2.31	28.40	10.8	RLQ
J122847.42+37061	12:28:47.52	+37:06:11.9	1.52	27.94	8.6	RLQ
J122851.76+48580	12:28:51.84	+48:58:0.8	1.72	28.07	N	RLQ
J123212.63+335540.9	12:32:12.72	+33:55:40.8	2.49	28.16	8.3	RLQ
4C_26.38	12:32:23.52	+26:04:7.0	2.61	28.41	12.8	HzRG
B2_1230+349	12:32:41.52	+34:42:50.8	1.53	28.35	16.6	HzRG
J123603.91+242443.0	12:36:3.84	+24:24:43.2	2.94	28.00	10.2	RLQ
J124129.58+602041.3	12:41:29.52	+60:20:41.3	2.07	28.30	15.0	RLQ
WN_J1242p3915	12:42:53.04	+39:15:49.0	2.13	28.03	11.8	HzRG
J124857.33+470344.4	12:48:57.36	+47:03:44.3	2.05	28.14	15.9	RLQ
MG_1251p1104	12:51:0.00	+11:04:19.9	2.32	28.42	11.2	HzRG
J130033.30+40090	13:00:33.36	+40:09:6.8	1.67	28.59	19.8	RLQ
J130121.01+190421.4	13:01:21.12	+19:04:21.4	3.07	28.18	13.4	RLQ
BRL1303+091	13:05:36.00	+08:55:15.5	1.41	28.72	19.1	HzRG
J131718.64+39252	13:17:18.72	+39:25:27.8	1.56	28.19	19.8	RLQ
J131907.48+621721.3	13:19:7.44	+62:17:21.1	3.07	28.36	14.0	RLQ

J132118.83+110649.9	13:21:18.72	+11:06:50.0	2.18	28.93	8.3	RLQ
J132255.66+391207.9	13:22:55.68	+39:12:7.9	2.99	28.02	16.1	RLQ
J132529.71+65151	13:25:29.76	+65:15:13.0	1.63	28.28	15.5	RLQ
J132720.98+432627.9	13:27:20.88	+43:26:28.0	2.08	28.44	18.2	RLQ
J133335.78+164903.9	13:33:35.76	+16:49:4.1	2.09	28.29	13.7	RLQ
J133521.96+454238.2	13:35:22.08	+45:42:38.2	2.45	28.25	10.2	RLQ
WNR_J1338p3532	13:38:15.12	+35:32:3.8	2.77	28.42	13.7	HzRG
J133923.77+632858.4	13:39:23.76	+63:28:58.4	2.56	28.56	10.5	RLQ
J133932.66-031706.3	13:39:32.64	-03:17:6.3	2.31	28.20	16.6	RLQ
J134022.94+375443.8	13:40:23.04	+37:54:43.9	3.11	28.49	14.7	RLQ
J134224.31+511012.5	13:42:24.24	+51:10:12.4	2.60	28.04	13.1	RLQ
J134425.53+38413	13:44:25.44	+38:41:30.1	1.54	27.83	13.4	RLQ
J134536.94+38231	13:45:36.96	+38:23:12.1	1.85	28.51	13.1	RLQ
J134723.49+183537.5	13:47:23.52	+18:35:37.7	2.18	28.28	13.7	RLQ
4C_24.28	13:48:14.88	+24:15:50.0	2.89	29.05	15.6	HzRG
4C_p43.31	13:52:28.56	+42:59:22.9	2.15	28.43	13.7	HzRG
J135351.5+015153	13:53:51.60	+01:51:53.0	1.61	27.96	10.8	RLQ
J135817.60+57520	13:58:17.52	+57:52:4.1	1.37	28.01	22.7	RLQ
J135927.15+01595	13:59:27.12	+01:59:54.0	1.33	28.13	11.2	RLQ
PKS_1357p007	14:00:21.36	+00:30:19.0	2.67	28.72	10.2	HzRG
MG_1401p0921	14:01:18.24	+09:21:24.0	2.09	28.26	9.6	HzRG
NVSS_J140223-363539	14:02:23.52	-36:35:42.0	2.80	28.34	15.3	HzRG
J140432.99+072846.9	14:04:32.88	+07:28:47.0	2.86	28.10	18.2	RLQ
J140445.88-013021.8	14:04:45.84	-01:30:21.9	2.50	28.53	15.3	RLQ
3C294.0	14:06:43.92	+34:11:25.4	1.79	28.91	10.6	HzRG
J140653.84+343337.3	14:06:53.76	+34:33:37.4	2.57	28.09	16.6	RLQ
J140744.20+140620.8	14:07:44.16	+14:06:20.9	2.18	27.69	11.5	RLQ
J140812.95+561332.5	14:08:12.96	+56:13:32.5	2.02	28.09	11.8	RLQ
J141030.99+614136.9	14:10:30.96	+61:41:37.0	2.25	27.81	15.0	RLQ
4C_-00.54	14:13:15.12	-00:23:00.0	2.36	28.41	11.8	HzRG
J141318.86+450523.0	14:13:18.96	+45:05:22.9	3.11	28.19	8.7	RLQ
J141528.47+370621.2	14:15:28.56	+37:06:21.2	2.37	28.41	10.8	RLQ
J141708.16+46070	14:17:8.16	+46:07:5.2	1.56	28.40	10.8	RLQ
J141906.82+055501.9	14:19:6.72	+05:55:1.9	2.29	27.69	19.1	RLQ
J141908.18+06283	14:19:8.16	+06:28:34.0	1.44	29.09	12.4	RLQ
J142330.09+11595	14:23:30.00	+11:59:51.0	1.61	28.41	14.7	RLQ
BRL1422-297	14:25:29.28	-29:59:56.0	1.63	29.11	16.9	HzRG
J142950.91+260750.2	14:29:50.88	+26:07:50.2	2.92	28.55	12.8	RLQ
J143009.74+10432	14:30:9.84	+10:43:26.0	1.71	27.94	11.5	RLQ
J143243.29+41032	14:32:43.20	+41:03:27.0	1.97	28.03	15.9	RLQ
J143331.87+190711.6	14:33:31.92	+19:07:11.6	2.36	27.74	11.5	RLQ
J143645.80+633637.9	14:36:45.84	+63:36:37.8	2.07	28.60	16.6	RLQ
J143737.05+094847.7	14:37:36.96	+09:48:47.7	2.16	27.94	N	RLQ
TXS_1436p157	14:39:5.04	+15:31:18.8	2.54	28.24	16.6	HzRG
J144358.60+63322	14:43:58.56	+63:32:26.2	1.38	28.11	16.0	RLQ
NVSS_J144932-385657	14:49:32.88	-38:56:57.8	2.15	28.07	11.2	HzRG
J145301.48+103617.1	14:53:1.44	+10:36:17.3	2.28	28.08	12.1	RLQ
J145554.12+443137.6	14:55:54.24	+44:31:37.6	2.67	28.24	15.0	RLQ
J145629.16+543915.8	14:56:29.28	+54:39:15.8	2.26	27.93	8.9	RLQ
J145722.53+051921.8	14:57:22.56	+05:19:21.8	3.18	28.15	10.5	RLQ
J150426.69+285430.5	15:04:26.64	+28:54:30.6	2.28	28.50	10.5	RLQ
J150823.71+334700.7	15:08:23.76	+33:47:0.6	2.21	27.85	14.7	RLQ
NVSS_J151020-352803	15:10:20.88	-35:28:3.0	2.94	28.35	12.7	HzRG
J151005.88+59585	15:10:6.00	+59:58:53.0	1.72	27.96	21.4	RLQ
J151508.59+213345.9	15:15:8.64	+21:33:46.1	2.25	27.73	18.5	RLQ
J152043.59+473249.3	15:20:43.68	+47:32:49.2	2.81	27.93	12.8	RLQ
J152117.57+175601.0	15:21:17.52	+17:56:1.0	3.05	28.18	8.0	RLQ

J152149.61+433639.3	15:21:49.68	+43:36:39.2	2.17	28.04	N	RLQ
NVSS_J152435-352623	15:24:35.52	-35:26:21.8	2.76	28.48	13.4	HzRG
J153124.07+075431.1	15:31:24.00	+07:54:31.1	2.46	27.76	10.2	RLQ
J153514.65+483659.7	15:35:14.64	+48:36:59.8	2.54	27.89	13.7	RLQ
J153727.68+231826.1	15:37:27.60	+23:18:26.3	2.26	27.74	N	RLQ
8C_1536p620	15:37:9.12	+61:55:36.1	2.45	28.25	16.7	HzRG
J153925.10+160400.2	15:39:25.20	+16:04:0.1	2.54	28.48	14.2	RLQ
J154125.46+534813.0	15:41:25.44	+53:48:13.0	2.53	28.23	11.8	RLQ
J154459.42+040746.3	15:44:59.52	+04:07:46.4	2.18	28.60	14.4	RLQ
J154502.81+51350	15:45:2.88	+51:34:59.9	1.93	28.38	9.9	RLQ
J154534.34+200640.5	15:45:34.32	+20:06:40.3	2.13	27.85	11.5	RLQ
TXS_1545-234	15:48:17.52	-23:37:1.9	2.75	28.74	11.2	HzRG
J154827.92+073811.5	15:48:27.84	+07:38:11.5	2.85	27.91	12.8	RLQ
J154917.47+503805.7	15:49:17.52	+50:38:5.6	2.17	28.56	14.5	RLQ
J155538.83+110643.5	15:55:38.88	+11:06:43.6	2.68	28.06	14.4	RLQ
J160016.98+183830.0	16:00:17.04	+18:38:30.1	2.40	28.12	14.0	RLQ
TXS_1558-003	16:01:17.28	-00:28:46.0	2.52	28.82	14.7	HzRG
J160154.53+135710.6	16:01:54.48	+13:57:10.8	2.24	28.56	11.8	RLQ
J160212.60+241010.5	16:02:12.72	+24:10:10.6	2.53	28.31	11.2	RLQ
J161022.33+32382	16:10:22.32	+32:38:24.0	1.52	27.93	17.2	RLQ
J161005.28+181143.4	16:10:5.28	+18:11:43.4	3.12	28.31	10.2	RLQ
J161341.06+34124	16:13:41.04	+34:12:47.2	1.40	28.88	11.8	RLQ
J161526.65+431258.2	16:15:26.64	+43:12:58.3	3.16	28.02	7.3	RLQ
J161602.57+302339.8	16:16:2.64	+30:23:39.8	2.45	28.23	10.5	RLQ
J161655.57+362134.5	16:16:55.68	+36:21:34.6	2.26	28.24	14.3	RLQ
J161903.68+061302.2	16:19:3.60	+06:13:2.3	2.10	28.54	9.3	RLQ
J162014.19+103621.0	16:20:14.16	+10:36:21.2	2.10	27.82	19.2	RLQ
J162307.62+39093	16:23:7.68	+39:09:32.0	1.98	27.87	10.5	RLQ
J163221.05+264353.4	16:32:21.12	+26:43:53.4	2.68	28.39	16.3	RLQ
J163412.78+320335.4	16:34:12.72	+32:03:35.3	2.34	28.03	15.0	RLQ
J163515.50+38080	16:35:15.60	+38:08:3.8	1.81	28.97	12.8	RLQ
J164125.22+225704.0	16:41:25.20	+22:57:4.0	2.06	28.08	11.8	RLQ
J164240.41+25230	16:42:40.32	+25:23:7.1	1.73	28.18	12.7	RLQ
TXS_1647p100	16:50:5.04	+09:55:11.0	2.51	28.53	9.6	HzRG
J165519.22+324241.0	16:55:19.20	+32:42:41.0	3.19	28.27	12.7	RLQ
J165801.42+34432	16:58:1.44	+34:43:27.8	1.94	28.25	16.4	RLQ
J165913.85+171415.0	16:59:13.92	+17:14:15.0	2.02	27.90	12.7	RLQ
J170306.10+61524	17:03:6.00	+61:52:44.0	1.92	27.78	16.9	RLQ
TXS_1707p105	17:10:6.96	+10:31:9.1	2.35	28.63	11.8	HzRG
WNH_1717p6827	17:16:56.40	+68:24:2.2	2.84	27.98	12.4	HzRG
7C_1736p650	17:36:37.44	+65:02:28.0	2.40	27.65	N	HzRG
WNH_1736p6504	17:36:37.44	+65:02:35.2	2.60	27.74	N	HzRG
7C_1740p6640	17:40:42.24	+66:38:44.2	2.10	27.77	16.3	HzRG
MG_1747p1821	17:47:6.96	+18:21:11.2	2.28	28.86	N	HzRG
7C1751+6809	17:50:49.92	+68:08:25.8	1.54	27.80	16.3	HzRG
7C1753+6311	17:53:35.28	+63:10:49.1	1.96	27.96	19.1	HzRG
MP_J1755-6916	17:55:29.76	-69:16:54.1	2.55	28.95	14.0	HzRG
7C1756+6520	17:57:5.28	+65:19:53.0	1.48	27.78	18.8	HzRG
7C_1758p6719	17:58:47.28	+67:19:45.8	2.70	27.99	8.9	HzRG
WNH_1758p5821	17:58:48.00	+58:21:41.0	2.96	27.98	15.0	HzRG
MP_J1758-6738	17:58:52.80	-67:38:34.1	2.03	28.99	13.4	HzRG
7C_1802p6456	18:02:22.08	+64:56:44.9	2.11	28.18	15.0	HzRG
8C1803+661	18:03:50.88	+66:05:19.0	1.61	00.00	9.2	HzRG
7C1805+6332	18:05:56.88	+63:33:13.0	1.84	27.92	12.4	HzRG
7C_1807p6719	18:07:13.44	+67:19:41.9	2.78	27.99	12.9	HzRG
4C_40.36	18:10:55.68	+40:45:23.0	2.27	28.79	12.4	HzRG
WNH_1821p6117	18:22:18.72	+61:18:37.1	2.81	27.94	12.4	HzRG

BRL1859-235	19:02:49.20	-23:29:51.4	1.43	29.14	6.1	HzRG
4C_48.48	19:33:5.52	+48:11:46.0	2.34	28.29	12.4	HzRG
TN_J1941-1952	19:41:0.00	-19:52:14.2	2.67	28.85	14.2	HzRG
NVSSJ201943-364542	20:19:43.92	-36:45:42.8	2.12	27.69	11.5	HzRG
MRC_2025-218	20:27:59.04	-21:40:57.0	2.63	28.74	14.8	HzRG
TXS_2034p027	20:36:34.80	+02:56:55.0	2.13	28.45	N	HzRG
MG2037-0011	20:37:13.44	-00:10:58.5	1.51	28.37	9.6	HzRG
MRC_2036-254	20:39:24.48	-25:14:30.8	2.00	28.52	26.4	HzRG
NVSSJ204601-335656	20:46:0.96	-33:56:57.1	2.50	27.89	17.5	HzRG
MRC_2048-272	20:51:3.36	-27:03:5.0	2.06	28.72	13.1	HzRG
MRC_2052-253	20:55:1.44	-25:09:52.9	2.60	28.77	14.7	HzRG
MG2058+0542	20:58:29.04	+05:42:51.0	1.38	28.65	11.8	HzRG
NVSSJ210626-314003	21:06:25.92	-31:40:1.9	2.11	28.03	12.1	HzRG
4C_23.56	21:07:14.88	+23:31:45.1	2.48	28.93	15.3	HzRG
MG2109+0326	21:09:21.60	+03:26:52.7	1.63	28.21	13.4	HzRG
MG2121+1839	21:21:25.44	+18:39:8.6	1.86	28.25	16.3	HzRG
NVSS_J213238-335318	21:32:39.12	-33:53:19.0	2.90	28.60	16.6	HzRG
NVSS_J213510-333703	21:35:10.56	-33:37:4.1	2.52	27.90	9.9	HzRG
NVSS_J213637-340318	21:36:38.40	-34:03:20.9	2.77	28.39	17.3	HzRG
J213638.58+00415	21:36:38.64	+00:41:54.0	1.94	29.14	21.7	RLQ
MRC2135-257	21:38:0.96	-25:31:49.4	1.31	28.21	9.2	HzRG
TXS_2202p128	22:05:14.40	+13:05:34.1	2.70	28.54	15.3	HzRG
MRC2204-202	22:07:16.08	-20:03:26.6	1.62	28.60	14.0	HzRG
J221509.31+13223	22:15:9.36	+13:22:36.8	1.90	28.59	10.2	RLQ
MRC2224-273	22:27:43.20	-27:05:1.7	1.68	28.17	20.7	HzRG
J222940.08-08325	22:29:40.08	-08:32:54.0	1.56	28.37	11.2	RLQ
MRC2247-232	22:50:29.76	-23:01:10.6	1.33	28.49	13.7	HzRG
USS2251-089	22:53:40.32	-08:40:43.6	1.99	28.60	15.0	HzRG
TNR_2254p1857	22:54:53.76	+18:57:4.0	2.15	27.80	21.4	HzRG
J230011.73-102144.4	23:00:11.76	-10:21:44.3	2.30	27.99	8.9	RLQ
4C_p40.49	23:07:53.52	+40:41:48.8	2.14	28.46	16.2	HzRG
NVSS_J231144-362215	23:11:45.12	-36:22:14.9	2.53	27.83	21.1	HzRG
J231607.25+010012.9	23:16:7.20	+01:00:12.9	2.63	27.85	16.9	RLQ
BRL2318-166	23:21:1.92	-16:23:5.6	1.41	28.93	13.7	HzRG
TXS_2319p223	23:21:42.48	+22:37:54.8	2.55	28.46	14.3	HzRG
NVSS_J232651-370909	23:26:51.60	-37:09:11.2	2.36	28.02	12.8	HzRG
B3_J2330p3927	23:30:24.96	+39:27:11.2	3.09	28.33	11.2	HzRG
NVSS_J233034-330009	23:30:34.56	-33:00:11.9	2.68	28.23	15.0	HzRG
TXS_2332p154	23:34:58.08	+15:45:50.0	2.48	28.36	12.7	HzRG
MG_2348p0507	23:48:31.92	+05:07:33.0	2.02	28.58	12.1	HzRG
TXJ2351+1034	23:51:26.88	+10:34:54.1	1.33	27.93	12.4	HzRG
4C_28.58	23:51:59.04	+29:10:28.9	2.91	28.91	16.0	HzRG
TXS_2353-003	23:55:36.96	-00:02:58.0	2.59	28.76	21.4	HzRG
J235553.53+15412	23:55:53.52	+15:41:26.2	1.80	28.57	15.6	RLQ
J235718.38+14460	23:57:18.48	+14:46:9.1	1.81	28.54	15.3	RLQ
MRC2355-214	23:57:35.28	-21:13:24.2	1.41	28.22	11.2	HzRG

Appendix B

Results for 3.6 μm luminosity functions

Figure B.1 shows the results of Schechter fits to cluster member candidates detected above the IRAC1 95% completeness limit of 3.45 μJy for CARLA clusters with $\Sigma_{\text{CARLA}} > 2\sigma$. Table B.1 lists the results for all redshifts for both the α free and α fixed to $\alpha = -1$. The background subtraction and fitting procedure are identical to the analysis for IRAC2 detected sources (see Section 3). Similar to the results of the 4.5 μm Schechter fits, the IRAC1 luminosity functions are well described by $\alpha = -1$. Note that due to the shallower IRAC1 observations, the uncertainties on α for the free α fits are about two times larger than for the IRAC2 luminosity functions. Therefore, the fixed- α -fits probably constrain $m_{3.6\mu\text{m}}^*$ better than the free- α fits.

Table B.1: Schechter fit results for both α free and α fixed fits to the 3.6 μm luminosity function.

Σ_{CARLA}	$\langle z \rangle$	$m_{3.6\mu\text{m}}^*$	α	$m_{3.6\mu\text{m},\alpha=-1}^*$	N
$>2\sigma$	1.45	$20.30^{+0.30}_{-0.20}$	$-0.42^{+0.25}_{-0.20}$	$19.62^{+0.25}_{-0.20}$	28
$>2\sigma$	1.77	$20.05^{+0.30}_{-0.20}$	$-1.14^{+0.20}_{-0.20}$	$20.22^{+0.25}_{-0.20}$	30
$>2\sigma$	2.05	$19.98^{+0.30}_{-0.20}$	$-0.99^{+0.20}_{-0.15}$	$19.97^{+0.25}_{-0.20}$	30
$>2\sigma$	2.26	$19.64^{+0.25}_{-0.25}$	$-1.30^{+0.20}_{-0.20}$	$20.14^{+0.25}_{-0.25}$	29
$>2\sigma$	2.51	$20.03^{+0.30}_{-0.20}$	$-0.91^{+0.25}_{-0.20}$	$19.92^{+0.25}_{-0.20}$	30
$>2\sigma$	2.92	$19.70^{+0.30}_{-0.25}$	$-1.06^{+0.25}_{-0.20}$	$19.79^{+0.30}_{-0.20}$	30

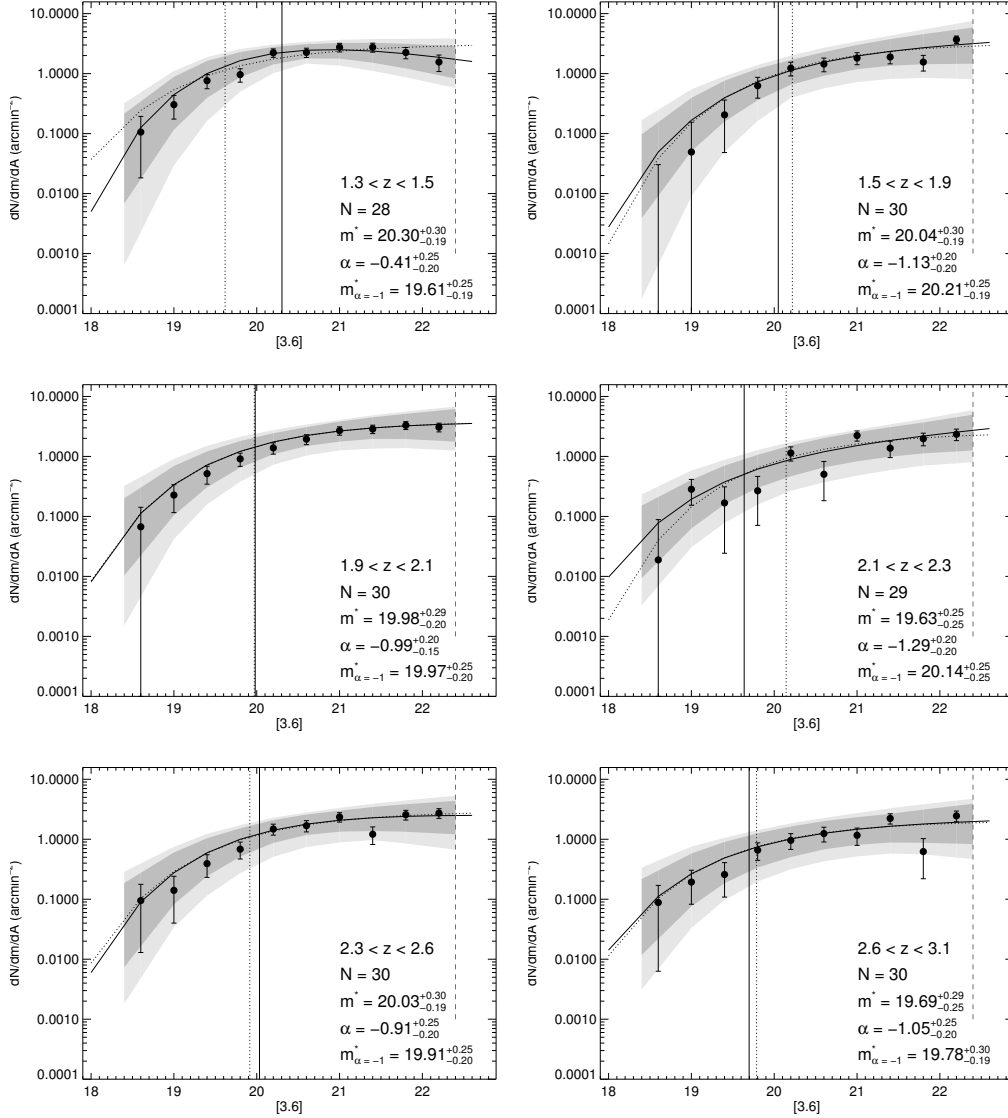


Figure B.1: Schechter fits to the $3.6\mu\text{m}$ cluster luminosity function in each redshift bin for CARLA cluster members with $\Sigma_{\text{CARLA}} > 2\sigma$. The redshift bins were chosen to contain similar numbers of objects, N . The solid circles are the binned differences between the luminosity function for all IRAC-selected sources in the clusters and the background luminosity function derived from the SpUDS survey. The solid curve shows the fit to the data for a free α while the dotted curve shows the fit for $\alpha = -1$. The vertical solid and dotted lines show the fitted values for m^* with free and fixed α , respectively. The dark and light grey shaded regions show the 1σ and 2σ confidence regions for the α -free-fit derived from Markov-Chain Monte Carlo simulations. The vertical dashed line shows the apparent magnitude limit.

Appendix C

Notes on individual sources in the field of 4C41.17

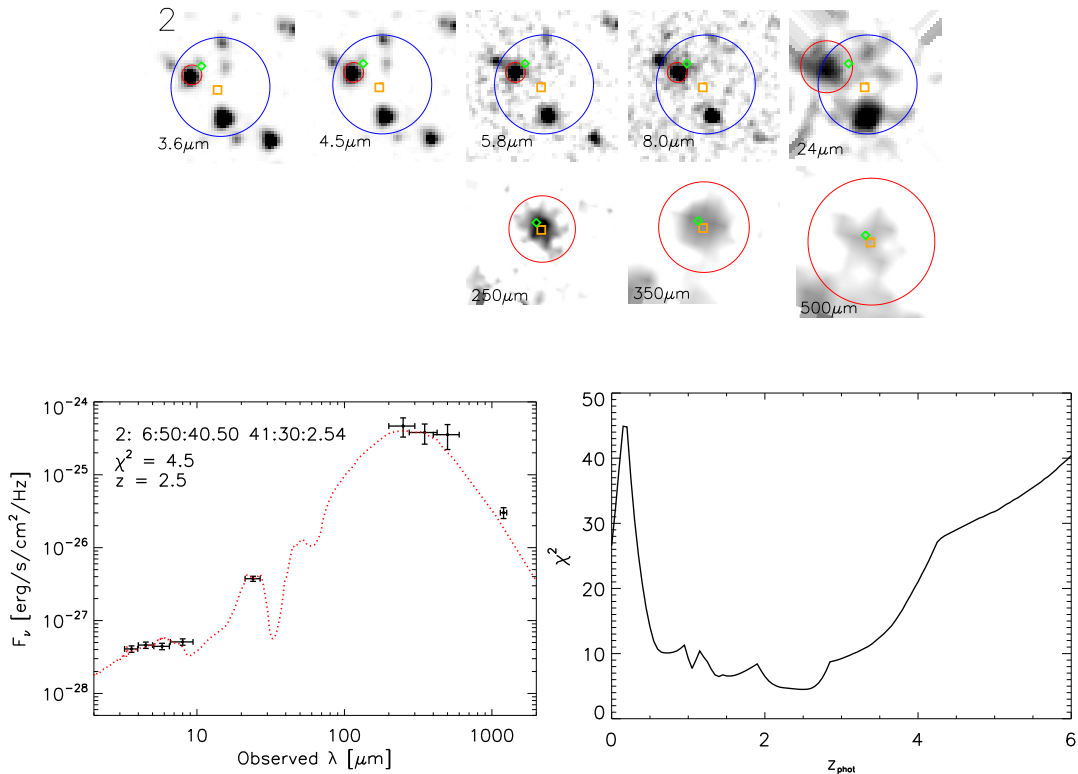


Figure C.1: This source is found to be at $z_{\text{phot}} = 2.5$ and best fit with a starburst template (I20551). The dust peak is very well observed and well fit. The χ^2 distribution shows a clear dip at this redshift, placing this source foreground to the radio galaxy.

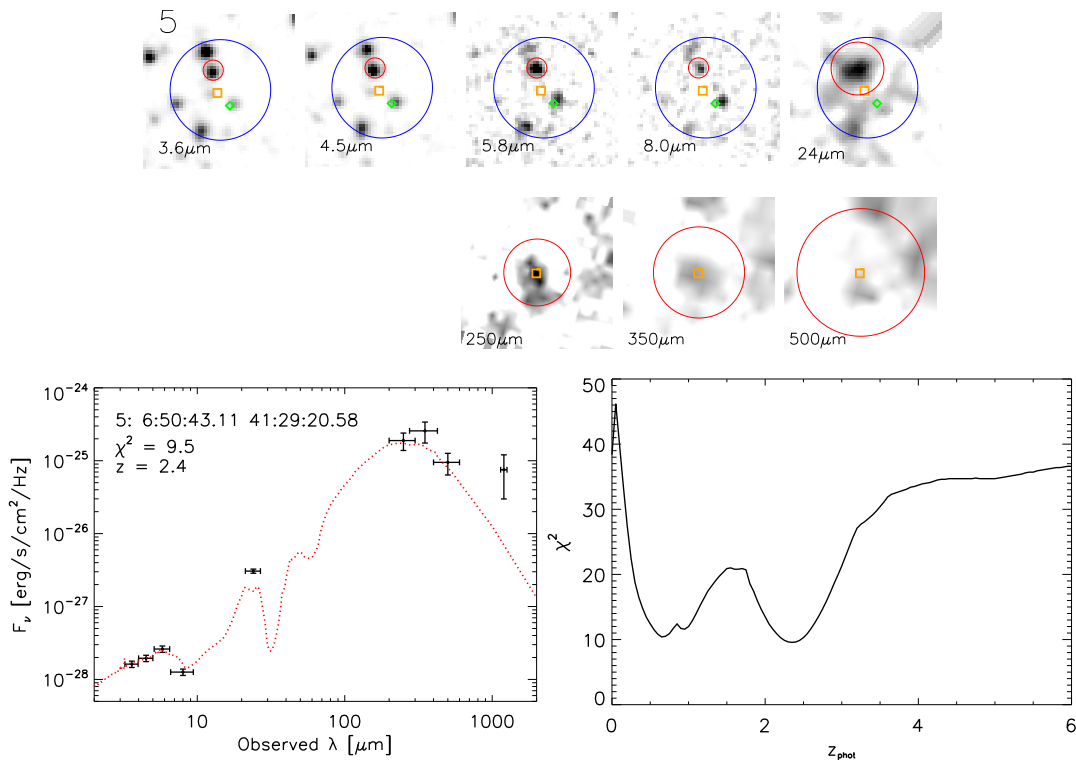


Figure C.2: The IRAC photometry of this source shows a very prominent stellar bump that is well fit by the starburst template, leaving, no doubt on the low redshift ($z_{\text{phot}} \sim 2.4$) of this source. This is also confirmed by its spectroscopic redshift ($z_{\text{spec}} = 2.672$) consistent with our photometric redshift. Greve et al. (2007) finds a very extended Ly α halo extending 50 kpc from this source.

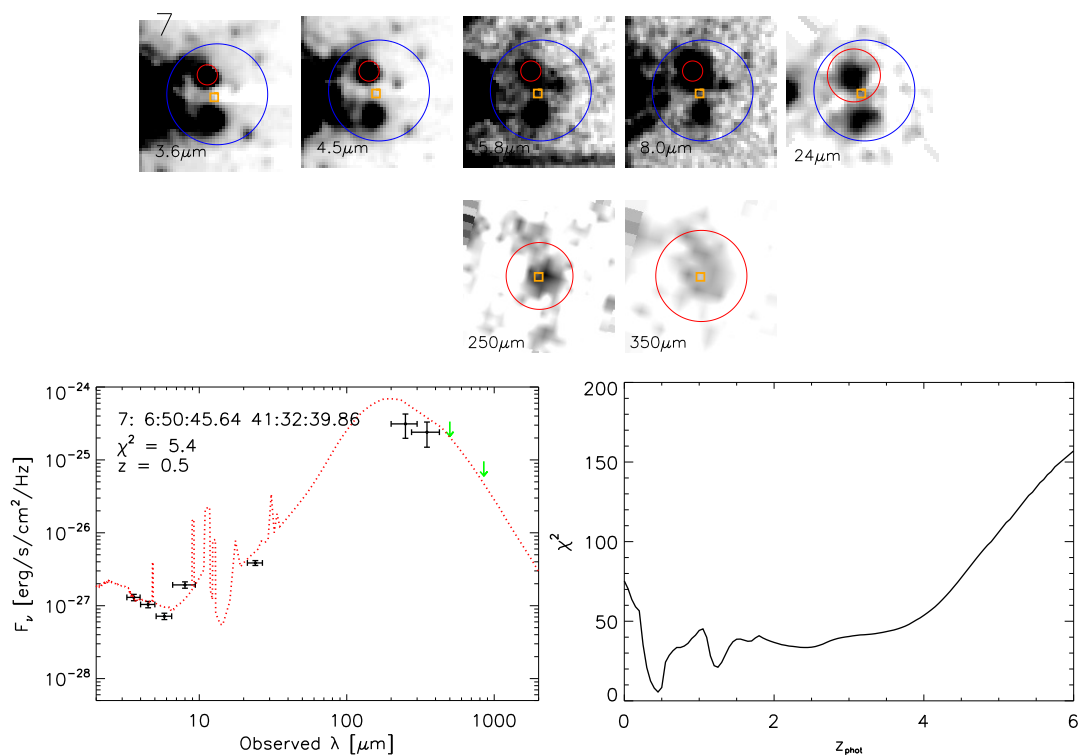


Figure C.3: Although the far-IR photometric observations are not well fit by `hyperz`, the upper limit at 850 μm is very constraining and places the dust peak at $\sim 200 \mu\text{m}$. The IRAC and MIPS photometric points can only be fit with a spiral template. The χ^2 distribution places the source unambiguously at low redshift ($z_{\text{phot}} = 0.5$).

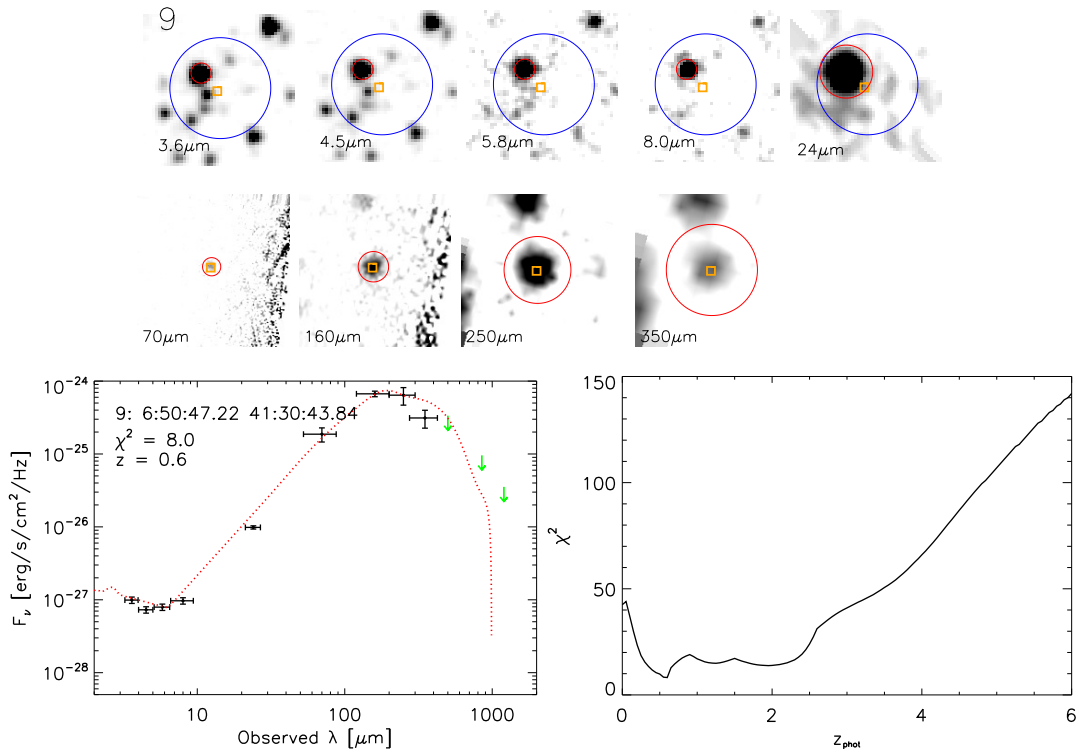


Figure C.4: The hyperz fit (source 11 dust template + old stellar population) fits the far-IR emission very well. The IRAC observations show the long wavelength tail of the stellar bump (at 1.6 μm restframe wavelength) indicating a low redshift. We find no secondary prominent dips in the χ^2 distribution and this source is thus found to be at lower redshift ($z_{\text{phot}} = 0.6$) than the radio galaxy.

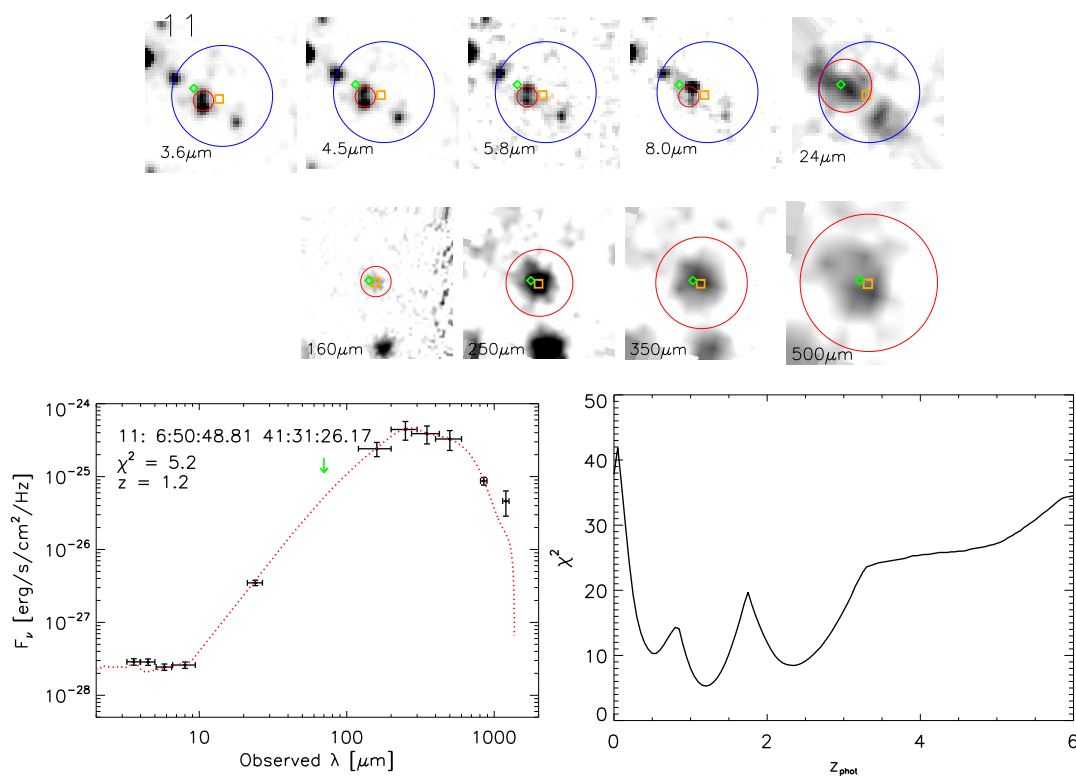


Figure C.5: This source is detected in all far-IR bands (160-1200 μm). The best χ^2 is found with template 9 (this source + old stellar population) and gives a redshift of 1.2, matching the spectroscopic redshift of 1.184.

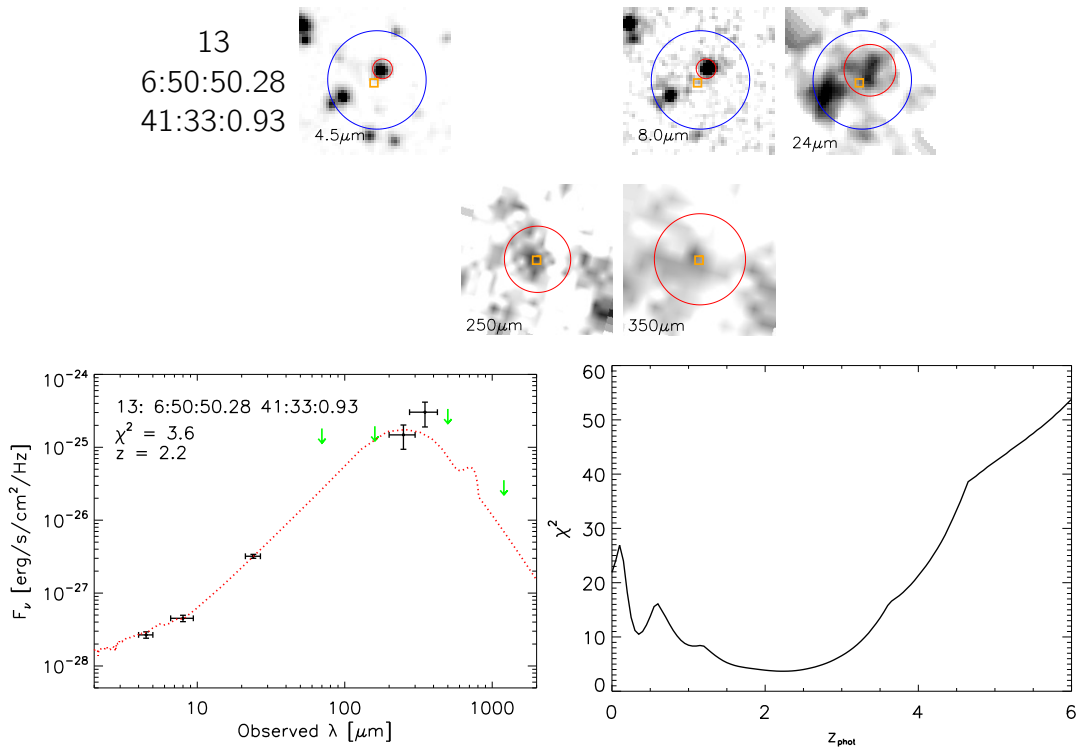


Figure C.6: Only five photometric points are available for fitting the SED of this source. The increasing emission towards 350 μm is not well fit and the best χ^2 solution gives a redshift of 2.2. Blending of other sources in close proximity may cause this increasing flux at 350 μm .

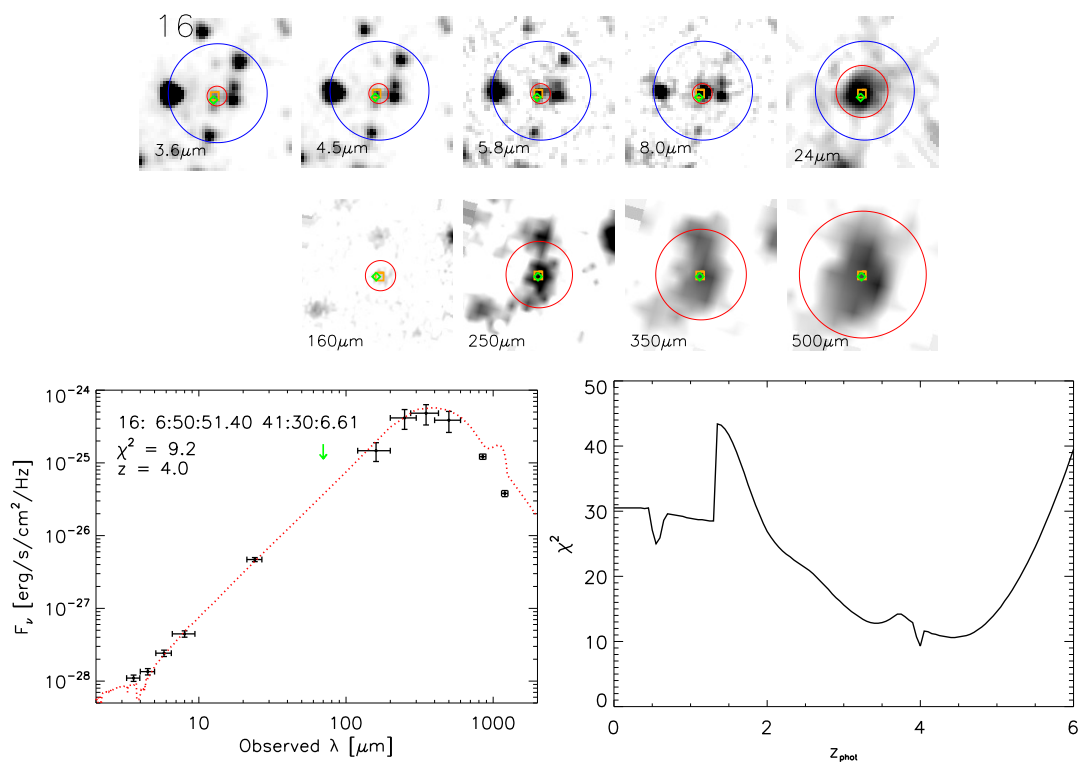


Figure C.7: This source is nicely fit by an AGN dominated template, similar to the SED of 4C+41.17. The χ^2 distribution shows a clear and prominent dip at the redshift of the radio galaxy. This source is therefore our most likely candidate to be associated with the radio galaxy.

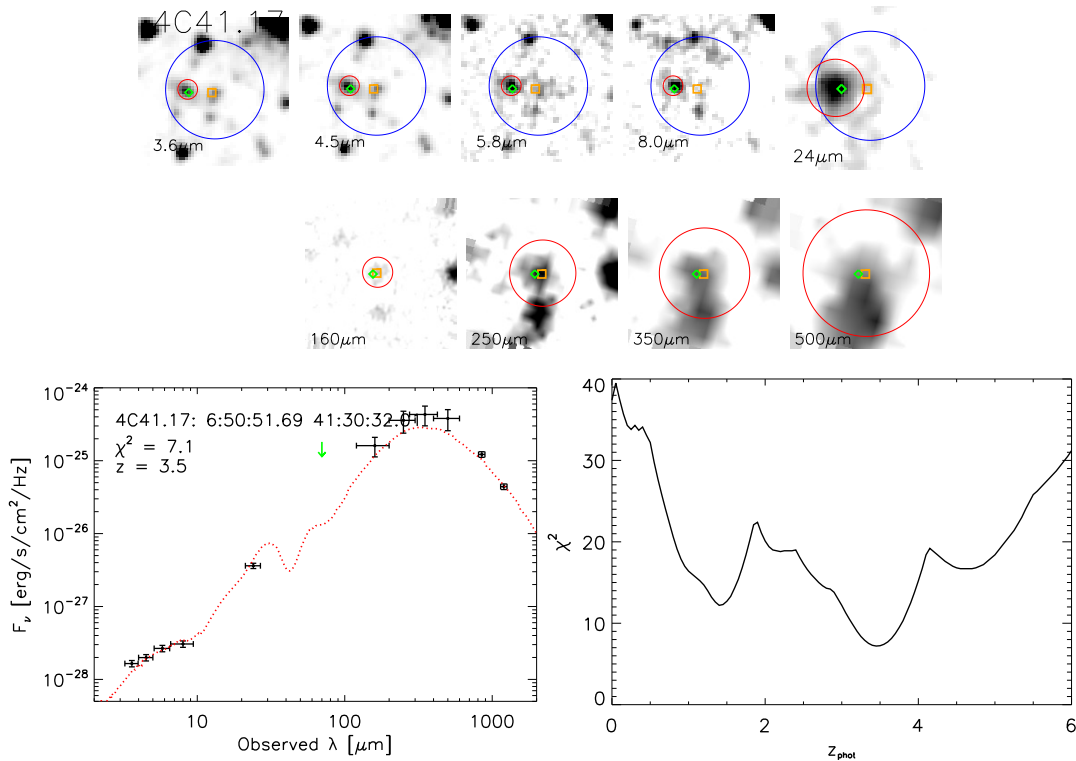


Figure C.8: The redshift of the radio galaxy is well constrained by the photometric redshift fitting using a composite AGN+starburst template (I19254). A single significant dip appears at a redshift of ~ 3.5 in the χ^2 distribution which is consistent with the spectroscopic redshift of 3.792. Note that this source is not fit by its own template as the stellar to dust peak ratio in those templates is not as optimal as in template 2.

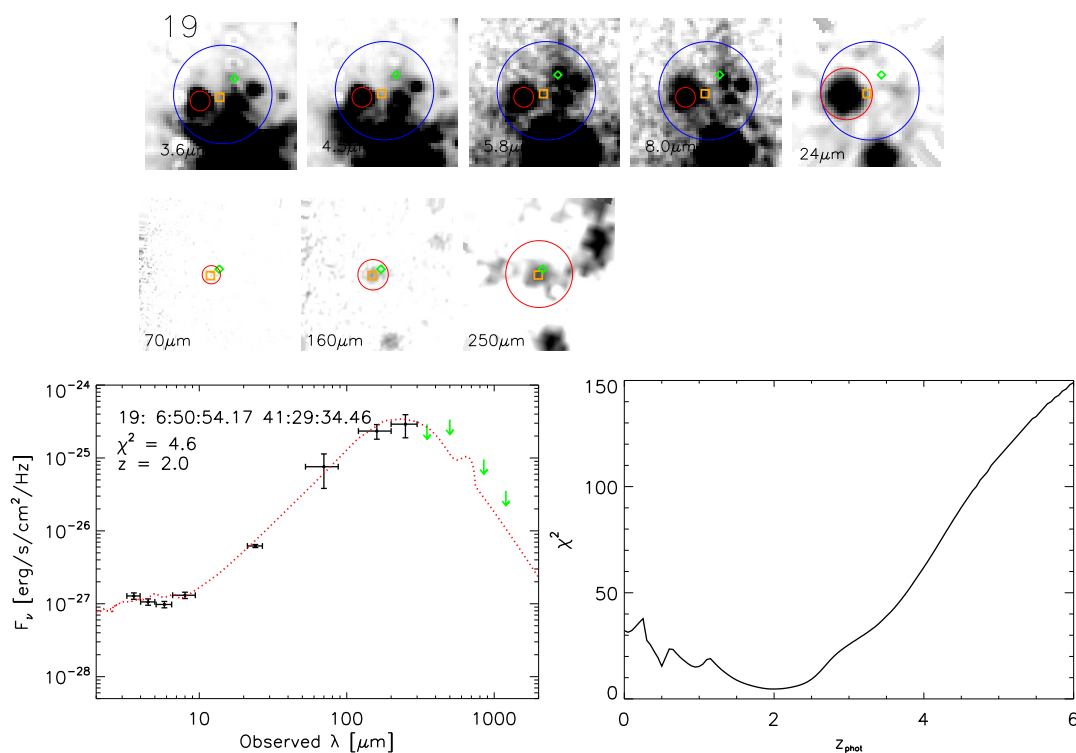


Figure C.9: The best χ^2 for this source is $z \sim 2.0$, but secondary peaks are more consistent with its spectroscopic redshift ($z_{\text{spec}} = 0.507$). Longer wavelength data (e.g. at 850 μm) are needed to constrain the redshift more accurately. The dust peak at $\sim 200 \mu\text{m}$ and the upper limits at longer wavelengths strongly constrain the source to be at $z_{\text{phot}} < 3.8$.

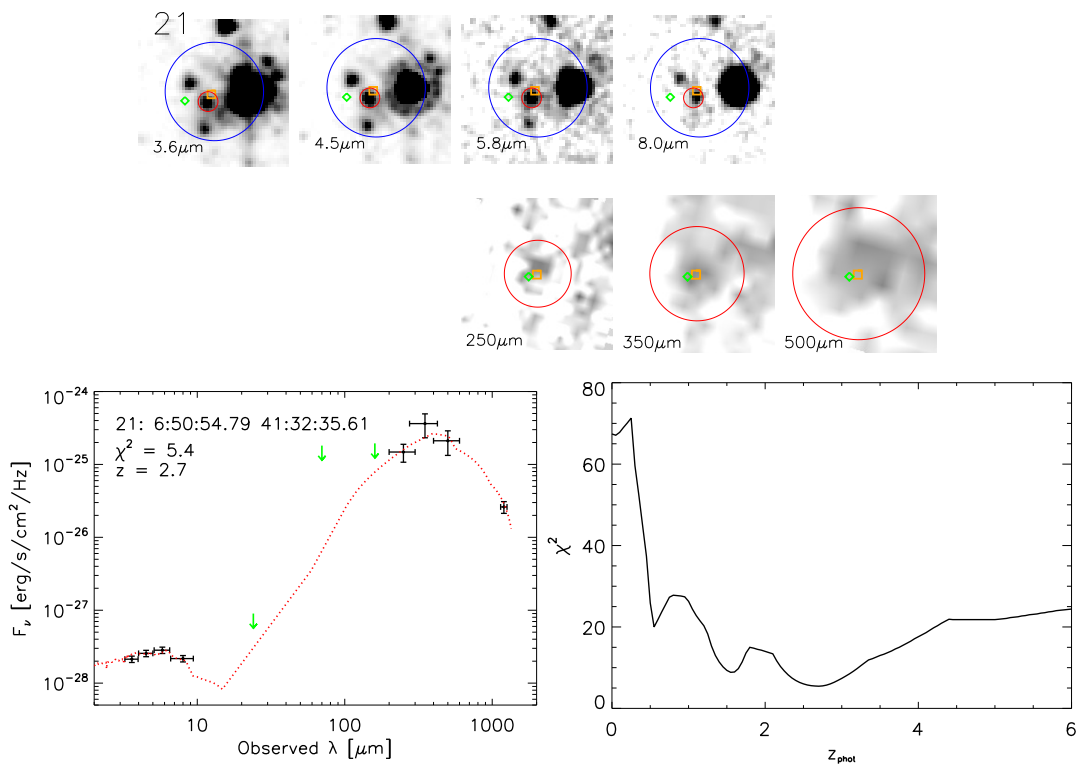


Figure C.10: The stellar bump is clearly observed peaking between the IRAC2 and IRAC3 band. Hyperz nicely fits this peak and puts this source at $z_{\text{phot}} \sim 2.7$.

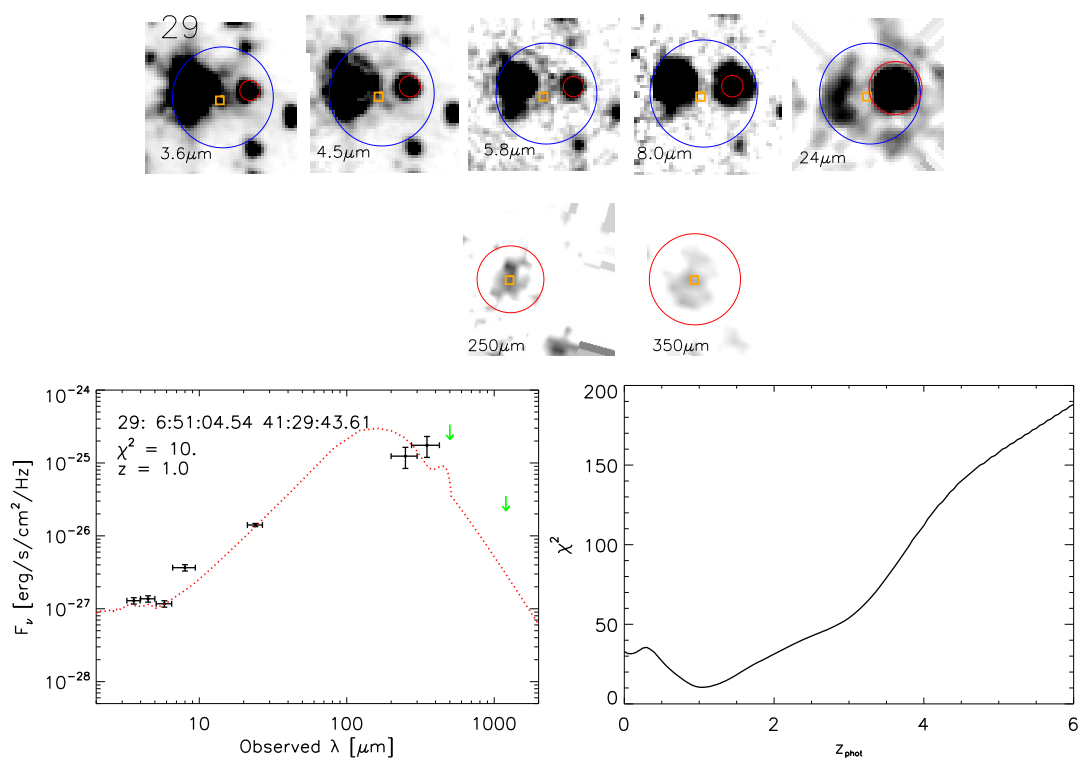


Figure C.11: A weak stellar bump peaking between the IRAC1 and IRAC2 bands is observed for this source. The overall SED is very similar to source 7 suggesting a low redshift. This is also found by the photometric redshift fitting procedure. The far-IR observations are not well fit but may be due to confusion with another source very bright at 24 μm and very close (~ 6 arcsec) to the center of detections. The IRAC photometry, however, is very constraining and the χ^2 distribution also confirms a clear low redshift for this source.

Bibliography

- Abell, G. O. 1958, ApJS, 3, 211
- Alberts, S., Pope, A., Brodwin, M., et al. 2014, MNRAS, 437, 437
- Allen, S. W., Evrard, A. E., & Mantz, A. B. 2011, ARA&A, 49, 409
- Allen, S. W., Rapetti, D. A., Schmidt, R. W., et al. 2008, MNRAS, 383, 879
- Archibald, E. N., Dunlop, J. S., Hughes, D. H., et al. 2001, MNRAS, 323, 417
- Ashby, M. L. N., Stern, D., Brodwin, M., et al. 2009, ApJ, 701, 428
- Barthel, P., Haas, M., Leipski, C., & Wilkes, B. 2012, ApJL, 757, L26
- Barthel, P. D., & Arnaud, K. A. 1996, MNRAS, 283, L45
- Benford, D. J., Cox, P., Omont, A., Phillips, T. G., & McMahon, R. G. 1999, ApJL, 518, L65
- Bertin, E., & Arnouts, S. 1996, A&AS, 117, 393
- Best, P. N. 2000, MNRAS, 317, 720
- Best, P. N., Kauffmann, G., Heckman, T. M., et al. 2005, MNRAS, 362, 25
- Best, P. N., Longair, M. S., & Roettgering, H. J. A. 1998, MNRAS, 295, 549
- BICEP2 Collaboration, Ade, P. A. R., Aikin, R. W., et al. 2014, ArXiv e-prints
- Blain, A. W., Smail, I., Ivison, R. J., Kneib, J.-P., & Frayer, D. T. 2002, PhR, 369, 111
- Blundell, K. M., & Rawlings, S. 1999, Nature, 399, 330
- Bolzonella, M., Miralles, J.-M., & Pelló, R. 2000, A&A, 363, 476
- Borgani, S., Governato, F., Wadsley, J., et al. 2001, ApJL, 559, L71
- Brodwin, M., Gonzalez, A. H., Moustakas, L. A., et al. 2007, ApJL, 671, L93
- Brodwin, M., Brown, M. J. I., Ashby, M. L. N., et al. 2006, ApJ, 651, 791
- Brodwin, M., Ruel, J., Ade, P. A. R., et al. 2010, ApJ, 721, 90

- Brodwin, M., Stern, D., Vikhlinin, A., et al. 2011, *ApJ*, 732, 33
- Brodwin, M., Stanford, S. A., Gonzalez, A. H., et al. 2013, *ArXiv e-prints*
- Bruzual, G., & Charlot, S. 2003, *MNRAS*, 344, 1000
- Bryant, J. J., Johnston, H. M., Broderick, J. W., et al. 2009, *MNRAS*, 395, 1099
- Carlstrom, J. E., Holder, G. P., & Reese, E. D. 2002, *ARA&A*, 40, 643
- Casey, C. M. 2012, *arXiv:1206.1595*
- Chabrier, G. 2003, *PASP*, 115, 763
- Chambers, K. C., Miley, G. K., & van Breugel, W. J. M. 1990, *ApJ*, 363, 21
- Chiang, Y.-K., Overzier, R., & Gebhardt, K. 2013, *ArXiv e-prints*
- Chung, S. M., Eisenhardt, P. R., Gonzalez, A. H., et al. 2011, *ApJ*, 743, 34
- Clements, D. L., Rigby, E., Maddox, S., et al. 2010, *A&A*, 518, L8
- Cohen, A. S., Lane, W. M., Cotton, W. D., et al. 2007, *AJ*, 134, 1245
- Coil, A. L. 2013, *The Large-Scale Structure of the Universe*, ed. T. D. Oswalt & W. C. Keel, 387
- Condon, J. J., Cotton, W. D., Greisen, E. W., et al. 1998, *AJ*, 115, 1693
- Croom, S. M., Smith, R. J., Boyle, B. J., et al. 2004, *MNRAS*, 349, 1397
- Dawson, K. S., Aldering, G., Amanullah, R., et al. 2009, *AJ*, 138, 1271
- De Breuck, C., Downes, D., Neri, R., et al. 2005, *A&A*, 430, L1
- De Breuck, C., van Breugel, W., Röttgering, H., et al. 2001, *AJ*, 121, 1241
- De Breuck, C., Seymour, N., Stern, D., et al. 2010, *ApJ*, 725, 36
- de Propris, R., Eisenhardt, P. R., Stanford, S. A., & Dickinson, M. 1998, *ApJl*, 503, L45
- Diolaiti, E., Bordinelli, O., Bonaccini, D., et al. 2000, *A&AS*, 147, 335
- Doherty, M., Tanaka, M., De Breuck, C., et al. 2010, *A&A*, 509, A83
- Donoso, E., Li, C., Kauffmann, G., Best, P. N., & Heckman, T. M. 2010, *MNRAS*, 407, 1078

- Dowell, C. D., Allen, C. A., Babu, R. S., et al. 2003, in Society of Photo-Optical Instrumentation Engineers (SPIE) Conference Series, Vol. 4855, Society of Photo-Optical Instrumentation Engineers (SPIE) Conference Series, ed. T. G. Phillips & J. Zmuidzinas, 73–87
- Dressler, A. 1980, *ApJ*, 236, 351
- Drouart, G., De Breuck, C., Vernet, J., et al. 2014, *A&A*, in press
- Dunlop, J. S., Hughes, D. H., Rawlings, S., Eales, S. A., & Ward, M. J. 1994, *Nature*, 370, 347
- Dunlop, J. S., & Peacock, J. A. 1990, *MNRAS*, 247, 19
- Eales, S., Dunne, L., Clements, D., et al. 2010, *PASP*, 122, 499
- Einstein, A. 1936, *Science*, 84, 506
- Eisenhardt, P. R. M., Brodwin, M., Gonzalez, A. H., et al. 2008, *ApJ*, 684, 905
- Elston, R. J., Gonzalez, A. H., McKenzie, E., et al. 2006, *ApJ*, 639, 816
- Erlund, M. C., Fabian, A. C., & Blundell, K. M. 2008, *MNRAS*, 386, 1774
- Erlund, M. C., Fabian, A. C., Blundell, K. M., Celotti, A., & Crawford, C. S. 2006, *MNRAS*, 371, 29
- Fabian, A. C. 1994, *ARA&A*, 32, 277
- Falder, J. T., Stevens, J. A., Jarvis, M. J., et al. 2010, *MNRAS*, 405, 347
- Fan, X. 2006, *NewAR*, 50, 665
- Fanaroff, B. L., & Riley, J. M. 1974, *MNRAS*, 167, 31P
- Fanidakis, N., Baugh, C. M., Benson, A. J., et al. 2011, *MNRAS*, 410, 53
- Fassbender, R., Nastasi, A., Böhringer, H., et al. 2011, *A&A*, 527, L10
- Fazio, G. G., Hora, J. L., Allen, L. E., et al. 2004, *ApJS*, 154, 10
- Ferrarese, L., & Merritt, D. 2000, *ApJl*, 539, L9
- Fioc, M., & Rocca-Volmerange, B. 1999, arXiv:astro-ph/9912179
- Furusawa, H. e. a. 2008, *ApJs*, 176, 1

- Galametz, A., Stern, D., Stanford, S. A., et al. 2010a, *A&A*, 516, A101
- Galametz, A., Stern, D., Eisenhardt, P. R. M., et al. 2009, *ApJ*, 694, 1309
- Galametz, A., Vernet, J., De Breuck, C., et al. 2010b, *A&A*, 522, A58
- Galametz, A., Stern, D., De Breuck, C., et al. 2012, *ApJ*, 749, 169
- Galametz, A., Stern, D., Pentericci, L., et al. 2013, *A&A*, 559, A2
- Gettings, D. P., Gonzalez, A. H., Stanford, S. A., et al. 2012, *ApJL*, 759, L23
- Gobat, R., Daddi, E., Onodera, M., et al. 2011, *A&A*, 526, A133
- Greve, T. R., Stern, D., Ivison, R. J., et al. 2007, *MNRAS*, 382, 48
- Griffin, M. J., Abergel, A., Abreu, A., et al. 2010, *A&A*, 518, L3
- Griffith, R. L., & Stern, D. 2010, *AJ*, 140, 533
- Häring, N., & Rix, H.-W. 2004, *ApJL*, 604, L89
- Hartley, W. G., Almaini, O., Mortlock, A., et al. 2013, *MNRAS*, 431, 3045
- Hatch, N. A., Kurk, J. D., Pentericci, L., et al. 2011a, *MNRAS*, 415, 2993
- Hatch, N. A., Overzier, R. A., Kurk, J. D., et al. 2009, *MNRAS*, 395, 114
- Hatch, N. A., De Breuck, C., Galametz, A., et al. 2011b, *MNRAS*, 410, 1537
- Herschel, W. 1785, *Royal Society of London Philosophical Transactions Series I*, 75, 213
- Herzog, E., Wild, P., & Zwicky, F. 1957, *PASP*, 69, 409
- Hickox, R. C., Jones, C., Forman, W. R., et al. 2009, *ApJ*, 696, 891
- Hill, G. J., & Lilly, S. J. 1991, *ApJ*, 367, 1
- Holden, B. P., Stanford, S. A., Eisenhardt, P., & Dickinson, M. 2004, *AJ*, 127, 2484
- Holland, W. S., Robson, E. I., Gear, W. K., et al. 1999, *MNRAS*, 303, 659
- Hopkins, P. F., Hernquist, L., Cox, T. J., et al. 2006, *ApJs*, 163, 1
- Houck, J. R., Roellig, T. L., van Cleve, J., et al. 2004, *ApJS*, 154, 18
- Hubble, E. P. 1925, *ApJ*, 62, 409

- . 1926, *ApJ*, 64, 321
- Humphrey, A., Zeballos, M., Aretxaga, I., et al. 2011, *MNRAS*, 418, 74
- Husband, K., Bremer, M. N., Stanway, E. R., et al. 2013, *MNRAS*, 432, 2869
- Hutchings, J. B., Crampton, D., Morris, S. L., Durand, D., & Steinbring, E. 1999, *AJ*, 117, 1109
- Hutchings, J. B., Scholz, P., & Bianchi, L. 2009, *AJ*, 137, 3533
- Ilbert, O., Salvato, M., Le Floc'h, E., et al. 2010, *ApJ*, 709, 644
- Iverson, R. J., Dunlop, J. S., Smail, I., et al. 2000, *ApJ*, 542, 27
- Iverson, R. J., Morrison, G. E., Biggs, A. D., et al. 2008, *MNRAS*, 390, 1117
- Iverson, R. J., Swinbank, A. M., Swinyard, B., et al. 2010, *A&A*, 518, L35
- Iverson, R. J., Smail, I., Amblard, A., et al. 2012, arXiv:1206.4046
- John, T. L. 1988, *A&A*, 193, 189
- Johnson, O., Almaini, O., Best, P. N., & Dunlop, J. 2007, *MNRAS*, 376, 151
- Kauffmann, G., Heckman, T. M., & Best, P. N. 2008, *MNRAS*, 384, 953
- Kauffmann, G., White, S. D. M., Heckman, T. M., et al. 2004, *MNRAS*, 353, 713
- Kennicutt, Jr., R. C. 1998, *ApJ*, 498, 541
- Kravtsov, A. V., & Borgani, S. 2012, *ARA&A*, 50, 353
- Kreysa, E., Gemuend, H.-P., Gromke, J., et al. 1998, in *Society of Photo-Optical Instrumentation Engineers (SPIE) Conference Series*, Vol. 3357, *Society of Photo-Optical Instrumentation Engineers (SPIE) Conference Series*, ed. T. G. Phillips, 319–325
- Krick, J. E., Surace, J. A., Thompson, D., et al. 2008, *ApJ*, 686, 918
- Kroupa, P. 2001, *MNRAS*, 322, 231
- Kurk, J., Cimatti, A., Zamorani, G., et al. 2009, *A&A*, 504, 331
- Kurk, J. D., Pentericci, L., Röttgering, H. J. A., & Miley, G. K. 2004, *A&A*, 428, 793
- Lacy, M., Wilson, G., Masci, F., et al. 2005, *ApJs*, 161, 41

- Lidman, C., Suherli, J., Muzzin, A., et al. 2012, MNRAS, 427, 550
- Lilly, S. J., & Longair, M. S. 1984, MNRAS, 211, 833
- Lin, Y.-T., Mohr, J. J., Gonzalez, A. H., & Stanford, S. A. 2006, ApJ, 650, L99
- Magnelli, B., Lutz, D., Santini, P., et al. 2012, A&A, 539, A155
- Makovoz, D., & Khan, I. 2005, in Astronomical Society of the Pacific Conference Series, Vol. 347, Astronomical Data Analysis Software and Systems XIV, ed. P. Shopbell, M. Britton, & R. Ebert, 81
- Mancone, C. L., & Gonzalez, A. H. 2012, PASP, 124, 606
- Mancone, C. L., Gonzalez, A. H., Brodwin, M., et al. 2010, ApJ, 720, 284
- Mancone, C. L., Baker, T., Gonzalez, A. H., et al. 2012, ApJ, 761, 141
- Mandelbaum, R., Li, C., Kauffmann, G., & White, S. D. M. 2009, MNRAS, 393, 377
- Martini, P., Miller, E. D., Brodwin, M., et al. 2013, ApJ, 768, 1
- Matsuda, Y., Smail, I., Geach, J. E., et al. 2011, MNRAS, 416, 2041
- Matthews, T. A. 1965, AJ, 70, 144
- Mauduit, J.-C., Lacy, M., Farrah, D., et al. 2012, PASP, 124, 714
- Mayo, J. H., Vernet, J., De Breuck, C., et al. 2012, A&A, 539, A33
- Mei, S., Holden, B. P., Blakeslee, J. P., et al. 2006, ApJ, 644, 759
- Mei, S., Stanford, S. A., Holden, B. P., et al. 2012, ApJ, 754, 141
- Messier, C. 1781, Catalogue des Nebuleuses et des amas d'etoiles (Catalog of Nebulae and Star Clusters), Tech. rep.
- Miley, G., & De Breuck, C. 2008, A&ARv, 15, 67
- Minkowski, R. 1960, ApJ, 132, 908
- Mitchell-Wynne, K., Cooray, A., Gong, Y., et al. 2012, arXiv: 1203.0063
- Mocz, P., Fabian, A. C., & Blundell, K. M. 2013, MNRAS, 432, 3381
- Moran, S. M., Ellis, R. S., Treu, T., et al. 2007, ApJ, 671, 1503

- Mortlock, A., Conselice, C. J., Hartley, W. G., et al. 2013, MNRAS, 433, 1185
- Mortonson, M. J., Hu, W., & Huterer, D. 2011, Phys. Rev. D, 83, 023015
- Mullis, C. R., Rosati, P., Lamer, G., et al. 2005, ApJ, 623, L85
- Muzzin, A., Wilson, G., Demarco, R., et al. 2013, ApJ, 767, 39
- Muzzin, A., Wilson, G., Lacy, M., Yee, H. K. C., & Stanford, S. A. 2008, ApJ, 686, 966
- Muzzin, A., Yee, H. K. C., Hall, P. B., Ellingson, E., & Lin, H. 2007, ApJ, 659, 1106
- Myers, S. T., Baker, J. E., Readhead, A. C. S., Leitch, E. M., & Herbig, T. 1997, ApJ, 485, 1
- Navarro, J. F., Frenk, C. S., & White, S. D. M. 1995, MNRAS, 275, 720
- Nelan, J. E., Smith, R. J., Hudson, M. J., et al. 2005, ApJ, 632, 137
- Nesvadba, N. P. H., De Breuck, C., Lehnert, M. D., et al. 2011, A&A, 525, A43
- Nesvadba, N. P. H., Neri, R., De Breuck, C., et al. 2009, MNRAS, 395, L16
- Oegerle, W. R., Fitchett, M. J., & Danly, L. 1990, Science, 250, 1023
- Oliver, S. J., Wang, L., Smith, A. J., et al. 2010, A&A, 518, L21
- Oliver, S. J., Bock, J., Altieri, B., et al. 2012, MNRAS, 3269
- Ott, S. 2010, in Astronomical Society of the Pacific Conference Series, Vol. 434, Astronomical Data Analysis Software and Systems XIX, ed. Y. Mizumoto, K.-I. Morita, & M. Ohishi, 139
- Papovich, C. 2008, ApJ, 676, 206
- Papovich, C., Dole, H., Egami, E., et al. 2004, ApJS, 154, 70
- Papovich, C., Momcheva, I., Willmer, C. N. A., et al. 2010, ApJ, 716, 1503
- Peebles, P. J. E. 1980, The large-scale structure of the universe
- Peng, Y.-j., Lilly, S. J., Kovač, K., et al. 2010, ApJ, 721, 193
- Pentericci, L., Kurk, J. D., Röttgering, H. J. A., et al. 2000, A&A, 361, L25
- Pilbratt, G. L., Riedinger, J. R., Passvogel, T., et al. 2010, A&A, 518, L1

- Poglitsch, A., Waelkens, C., Geis, N., et al. 2010, *A&A*, 518, L2
- Polletta, M., Tajer, M., Maraschi, L., et al. 2007, *ApJ*, 663, 81
- Ramos Almeida, C., Bessiere, P. S., Tadhunter, C., et al. 2013a, *ArXiv e-prints*
- Ramos Almeida, C., Bessiere, P. S., Tadhunter, C. N., et al. 2013b, *MNRAS*
- Rawlings, S., & Jarvis, M. J. 2004, *MNRAS*, 355, L9
- Rawlings, S., & Saunders, R. 1991, *Nature*, 349, 138
- Reichardt, C. L., Stalder, B., Bleem, L. E., et al. 2012, *ArXiv e-prints*
- Rettura, A., Mei, S., Stanford, S. A., et al. 2011, *ApJ*, 732, 94
- Rieke, G. H., Young, E. T., Engelbracht, C. W., et al. 2004, *ApJS*, 154, 25
- Rigby, E. E., Best, P. N., Brookes, M. H., et al. 2011, *MNRAS*, 416, 1900
- Rocca-Volmerange, B., Le Borgne, D., De Breuck, C., Fioc, M., & Moy, E. 2004, *A&A*, 415, 931
- Rocca-Volmerange, B., Drouart, G., De Breuck, C., et al. 2013, *ArXiv e-prints*
- Roche, N., Eales, S., & Hippelein, H. 1998, *MNRAS*, 295, 946
- Röttgering, H. J. A., van Ojik, R., Miley, G. K., et al. 1997, *A&A*, 326, 505
- Sarazin, C. L. 1988, *S&T*, 76, 639
- Schechter, P. 1976, *ApJ*, 203, 297
- Schneider, D. P., Richards, G. T., Hall, P. B., et al. 2010, *AJ*, 139, 2360
- Seymour, N., Stern, D., De Breuck, C., et al. 2007, *ApJS*, 171, 353
- Seymour, N., Altieri, B., De Breuck, C., et al. 2012, *ApJ*, 755, 146
- Shen, Y., Richards, G. T., Strauss, M. A., et al. 2011, *ApJs*, 194, 45
- Sikora, M., Stawarz, Ł., & Lasota, J.-P. 2007, *ApJ*, 658, 815
- Silva, L., Granato, G. L., Bressan, A., & Danese, L. 1998, *ApJ*, 509, 103
- Simpson, C., & Eisenhardt, P. 1999, *PASP*, 111, 691

- Simpson, C., Martínez-Sansigre, A., Rawlings, S., et al. 2006, MNRAS, 372, 741
- Skibba, R. A., Engelbracht, C. W., Dale, D., et al. 2011, ApJ, 738, 89
- Smith, E. P., & Heckman, T. M. 1990, ApJ, 348, 38
- Snyder, G. F., Brodwin, M., Mancone, C. M., et al. 2012, ApJ, 756, 114
- Sorba, R., & Sawicki, M. 2010, ApJ, 721, 1056
- Stalder, B., Ruel, J., Šuhada, R., et al. 2013, ApJ, 763, 93
- Stanford, S. A., Eisenhardt, P. R., & Dickinson, M. 1998, ApJ, 492, 461
- Stanford, S. A., Eisenhardt, P. R., Brodwin, M., et al. 2005, ApJ, 634, L129
- Stanford, S. A., Brodwin, M., Gonzalez, A. H., et al. 2012, ApJ, 753, 164
- Stern, D., Holden, B., Stanford, S. A., & Spinrad, H. 2003, AJ, 125, 2759
- Stern, D., Jimenez, R., Verde, L., Stanford, S. A., & Kamionkowski, M. 2010, ApJS, 188, 280
- Stern, D., Eisenhardt, P., Gorjian, V., et al. 2005, ApJ, 631, 163
- Stern, D., Kirkpatrick, J. D., Allen, L. E., et al. 2007, ApJ, 663, 677
- Stevens, J. A., Jarvis, M. J., Coppin, K. E. K., et al. 2010, MNRAS, 405, 2623
- Stevens, J. A., Ivison, R. J., Dunlop, J. S., et al. 2003, Nature, 425, 264
- Strazzullo, V., Rosati, P., Pannella, M., et al. 2010, A&A, 524, A17
- Sunyaev, R. A., & Zeldovich, I. B. 1980, ARA&A, 18, 537
- Sutherland, W., & Saunders, W. 1992, MNRAS, 259, 413
- Suzuki, N., Rubin, D., Lidman, C., et al. 2012, ApJ, 746, 85
- Swinbank, A. M., Smail, I., Longmore, S., et al. 2010, Nature, 464, 733
- Swinbank, M., Karim, A., Smail, I., et al. 2012, ArXiv e-prints
- Targett, T. A., Dunlop, J. S., & McLure, R. J. 2012, MNRAS, 420, 3621
- Thomas, D., Maraston, C., Schawinski, K., Sarzi, M., & Silk, J. 2010, MNRAS, 404, 1775

- Ueda, Y., Watson, M. G., Stewart, I. M., et al. 2008, *ApJs*, 179, 124
- Urry, C. M., & Padovani, P. 1995, *PASP*, 107, 803
- van der Burg, R. F. J., Muzzin, A., Hoekstra, H., et al. 2013, *A&A*, 557, A15
- van Dokkum, P. G., & Stanford, S. A. 2003, *ApJ*, 585, 78
- Vanderlinde, K., Crawford, T. M., de Haan, T., et al. 2010, *ApJ*, 722, 1180
- Venemans, B. P., Kurk, J. D., Miley, G. K., et al. 2002, *ApJL*, 569, L11
- Venemans, B. P., Röttgering, H. J. A., Miley, G. K., et al. 2007, *A&A*, 461, 823
- Vernet, J., Fosbury, R. A. E., Villar-Martín, M., et al. 2001, *A&A*, 366, 7
- Vikhlinin, A., Kravtsov, A. V., Burenin, R. A., et al. 2009, *ApJ*, 692, 1060
- Walter, F., Decarli, R., Carilli, C., et al. 2012, *Nature*, 486, 233
- White, R. L., Becker, R. H., Helfand, D. J., & Gregg, M. D. 1997, *ApJ*, 475, 479
- White, S. D. M., & Rees, M. J. 1978, *MNRAS*, 183, 341
- Willott, C. J., Rawlings, S., Blundell, K. M., Lacy, M., & Eales, S. A. 2001, *MNRAS*, 322, 536
- Wilson, A. S., & Colbert, E. J. M. 1995, *ApJ*, 438, 62
- Wilson, G., Muzzin, A., Yee, H. K. C., et al. 2009, *ApJ*, 698, 1943
- Wylezalek, D., Galametz, A., Stern, D., et al. 2013a, *ApJ*, 769, 79
- Wylezalek, D., Vernet, J., De Breuck, C., et al. 2013b, *MNRAS*, 428, 3206
- . 2014, *ApJ*, 786, 17
- Yates, M. G., Miller, L., & Peacock, J. A. 1989, *MNRAS*, 240, 129
- Zeimann, G. R., Stanford, S. A., Brodwin, M., et al. 2012, *ApJ*, 756, 115
- Ziparo, F., Popesso, P., Finoguenov, A., et al. 2014, *MNRAS*, 437, 458
- Zwicky, F. 1933, *Helvetica Physica Acta*, 6, 110

Curriculum Vitae

Personal

Name	Dominika Wylezalek
Birth	2 May 1988 in Aschaffenburg, Germany

Education

Sep 2011 – present	PhD in Astrophysics <i>European Southern Observatory/Ludwig Maximilian University of Munich</i> Supervisor: Carlos De Breuck (ESO), Joël Vernet (ESO), Prof. Andreas Burkert (LMU)
Sep 2012 – Feb 2013	Visiting PhD Student <i>California Institute of Technology/Jet Propulsion Laboratory, US</i> As part of the 'JPL Visiting Student Researchers Program' Host and Supervisor: Daniel Stern (Caltech/JPL)
Oct 2010 – July 2011	Master of Advanced Study in Physics <i>University of Cambridge, UK, mark: merit</i> Thesis: A multi-wavelength search for distant accreting supermassive black holes Supervisor: Prof. Richard McMahon (Institute of Astronomy, Cambridge)
Sep 2007 – July 2010	Bachelor of Science in Physics <i>University of Heidelberg, Germany, mark: 1.4; range 1 to 6 (1: highest, 6: lowest)</i> Thesis: Polarization Variability of radio-loud AGN Supervisor: Prof. Jochen Heidt (Heidelberg Observatory)

Awards

2011 – present	PhD Fellowship From the 'International Max-Planck Research School on Astrophysics' (IMPRS)
2007–2011	Scholarship From the 'German National Academic Foundation' ('Studienstiftung des Deutschen Volkes')
2007	Award of the German Association for Physics For excellent achievements in exams

Acknowledgements – Danksagung

I consider myself very lucky to have been able to work on such exciting projects and to have had all the support I needed. I would therefore like to first thank **Carlos De Breuck** and **Joël Vernet**, the best supervisors in the world! Thanks a lot for your time, for productive meetings, useful discussions, for teaching me how to do science and for the chit-chat that taught me a lot about what's going on behind the curtain. Thanks for introducing me to your beer/wine cellars (Carlos, German beer is still the best ☺) to APEX, MUSE and for becoming my friends. After working with you and learning from you, I feel well prepared for the next steps and am looking forward to many years of collaboration.

I also thank **Dan Stern**, my quasi third supervisor, so much for his support, for giving me the chance to work with him for six months at Caltech/JPL (in sunny California), for introducing me to many people that enabled me to join exciting collaborations, for his careful reads of my papers, proposals and abstracts and for giving me many opportunities to go observing. I am very inspired by how you can handle so many tasks while always being happy and calm and while never seeming to be stressed.

Big thanks to **Andi Burkert**, my supervisor at the LMU, for supporting my thesis and defense and for useful input during our committee meetings.

I further want to thank **Audrey Galametz** for being a great collaborator and friend, for sharing your experiences with me and for an amazing day at Disneyland.

A lot of the work would not have been possible with the help and input from my wonderful collaborators, especially **Alessandro, Anthony, Mark, Matt, Nick, Nina** and **Roberto!** Thank you!

I would also like to thank **ESO** for its great support whenever I wanted to go on observing trips, to conferences or on science visits and for the great scientific environment they provided. Thanks to the amazing group of **ESO students** and **fellows**, for endless coffees, dinners and beers. I especially thank **Carlo, Anna** and **Margherita** for becoming such good friends and for keeping me motivated (and also sometimes freaked out... yes Carlo, I mean you ☺)!

Ein riesengroßes Danke geht an **Casimir**, der in den letzten drei Jahren an meiner Seite stand, mich unterstützt hat wo und wann er konnte, der immer an meine Träume geglaubt hat und der viel auf sich nimmt, damit wir sie zusammen weiterträumen können. Danke für die wunderschöne Zeit mit dir in München, für die vielen Stunden in den Alpen, für unsere tollen Reisen und deine Geduld. Ich freue mich sehr auf unser weiteres gemeinsames Abenteuer! :-*

Ein weiteres riesengroßes Danke möchte ich an meine **Eltern, Monika & Lucian**, richten, die immer für mich da waren, an mich geglaubt haben, die immer neugierig geblieben sind und mir regelmäßig Fragen stellen, über die ich grübeln muss. Allerdings habe ich nach 20 Jahren lernen und forschen an vorderster Front leider immer noch nicht die Antwort auf DIE Frage gefunden. Ich schätze, da muss ich einfach weiter forschen oder doch irgendwann ∞ akzeptieren...

Danke auch an meine Freunde und Freundinnen, ganz besonders an meine Münchener Mädels **Anne-Lena, Esther, Tatjana** und **Tessa**. Für unsere wöchentlichen Mädelsabende, leckere Dinner, Käffchenkränze, Shoppingtouren, Parties und endlose Gespräche. Danke an **Melanie**, dass wir uns nie aus den Augen verloren haben und dass du seit über 15 Jahren meine Freundin bist, die mich versteht und mir immer zuhört.

Vieles, was in den letzten Jahren passiert ist, wäre nicht ohne die Unterstützung und die Freundschaften all dieser Personen möglich gewesen und ich bin unheimlich dankbar dafür, so viele tolle Freunde und Kollegen zu haben. Ich freue mich sehr auf die nächsten Jahre, die - wie ich glaube - ziemlich spannend werden!